Macrocyclic Poly-Pyridyl Based Transition Metal Complexes for Photocatalytic Water Splitting

---

Dissertation

zur

Erlangung der naturwissenschaftlichen Doktorwürde
(Dr. sc. nat.)

vorgelegt der

Mathematisch-naturwissenschaftlichen Fakultät

der

Universität Zürich

von

Stephan Schnidrig

aus

Grächen VS

Promotionskommission

Prof. Dr. Roger Alberto (Vorsitz)

Dr. Benjamin Probst (Leitung der Dissertation)

Prof. Dr. Greta Patzke

Prof. Dr. Jürg Osterwalder

Zürich, 2017

To my beloved family

I. Table of Contents

II. Zusammenfassung

Der Fokus dieser Doktorarbeit war die Herstellung und Untersuchung von neuen, makrozyklischen poly-pyridyl Liganden und ihren Komplexen. Es galt insbesondere, deren Aktivität als Wasser Reduktions Katalysatoren für die photokatalytische Wasserspaltung zu ermitteln. Komplexe mit makrozyklischen poly-pyridyl Liganden wurden bisher nicht auf deren Aktivität als Wasser Reduktions Katalysatoren untersucht, obwohl Cobalt-Komplexe, basierend auf poly-pyridyl Liganden, zu den besten Katalysatoren für photokatalytische Wasserspaltung gehören. Ein Portfolio von verschiedenen makrozyklischen Liganden wurde erstellt mit Kohlenstoff, Stickstoff oder Schwefel verbrückten Bipyridyl und Phenanthrolyl Einheiten. Die Liganden konnten durch Derivatisierung am verbrückenden Atom auf spezifische Anforderungen angepasst werden. Verschiedenste Metalle wurden für die Komplexierung dieser Liganden verwendet. Der Fokus lag dabei auf den Cobalt und Nickel Komplexen, welche auf ihre Aktivität als Katalysatoren für die photokatalytische Wasserspaltung geprüft wurden. Alle Cobalt Katalysatoren zeigten katalytische Aktivität und Umsatzzahlen von bis zu 20‘000 H_2/Co konnten ermittelt werden.

Ein weiterer Schwerpunkt war die Ermittlung der physikochemischen Eigenschaften, um einen tieferen Einblick in den Mechanismus der Katalyse zu erhalten. Die verbrückenden Atome in diesen Makrozyklen haben sehr spezielle Eigenschaften und ermöglichen unter anderem die selektive Synthese neutraler oder anionischer Liganden.

Ausführliche elekrochemische Untersuchungen verschiedenster Katalysatoren wurde durchgeführt und mit den katalytischen Daten verglichen, um Trends zu ermitteln und neue bessere Katalysatoren zu entwickeln. Das ermittelte katalytische „onset“ Potential aus der cyclischen Voltammetrie deckt sich mit der beobachteten Wasserstoff Entwicklung in der „Linear Sweep“ Voltammetrie. Trends für sehr ähnliche Katalysatoren konnten ermittelt werden. Höhere katalytische „onset“ Potentiale zeigten für sehr ähnliche Komplexe tiefere Umsatzzahlen. Stickstoff verbrückte Komplexe zeigten generell tiefere maximale Wasserstoffraten (H_2/s) als deren Kohlenstoffverbrückte Gegenstücke. Langsame Katalysatoren führen indes nicht zwingend zu tieferen Umsatzzahlen. Globale Trends beim Vergleichen unterschiedlicher Katalysatoren waren schwierig zu ermitteln, da sich die Systeme elektronisch zu stark unterscheiden.

III. Summary

The main goal of this thesis was the synthesis and investigation of nouvelle macrocyclic poly-pyridyl based complexes for photocatalytic water reduction. While poly-pyridyl based cobalt complexes showed promising results as catalysts for photocatalytic water splitting, their macrocyclic counterparts were never investigated.

A series of macrocyclic poly-pyridyl ligands was developed with bipyridine or phenanthroline as building blocks, connected by a carbon, nitrogen or sulphur atom. Derivatisation at the bridging atom of this ligand frameworks was performed to tune the scaffold to the desired needs. Various metal complexes were prepared with this ligand. Focusing mainly on cobalt and nickel complexes which were tested for their catalytic activity as water reduction catalysts. All cobalt catalysts showed promising catalytic activity and turnover numbers of up to 20’000 H_2/Co could be achieved, thus being some of the best catalysts known for water reduction.

A further focus was the investigation of the physicochemical properties of these complexes and get further insight into the reaction mechanism. The bridging atoms in these macrocyclic complexes have unique properties, enabling a selective access to neutral or anionic ligands.

Finally, an in depth electrochemical study with a library of water reduction catalysts was conducted. The results were compared to the photocatalytic performance and trends were deduced to designing better performing catalysts. The proposed catalytic onset potentials in cyclic voltammetry was supported by detection of hydrogen in linear sweep voltammetry. Trends could be observed for very similar catalysts. The difference in molecular electronics between the catalyst scaffolds made the identification of global trends difficult. The maximal hydrogen evolution (H_2/s) was considerable lower for nitrogen bridged complexes as compared to their carbon analogues. Very similar catalysts with higher catalytic onset potentials showed generally lower turnover numbers. However, slower catalysts did not necessary lead to overall lower turnover numbers.

IV. Acknowledgements

Research is never solely based on the work of an individual person. Thus, I would like to thank several persons without whom this work would not have been possible.

First of all, I thank Prof. Dr. Roger Alberto for the possibility to perform my Master thesis and my PhD study in his group. His continuous flow of insightful new ideas to advance the research was very helpful and lead to a challenging but very interesting working environment.

A special thanks to Dr. Benjamin Probst for his strong support as supervisor of the hydrogen evolution group and his guidance throughout the thesis.

Thanks to Prof. Dr. Greta Patzke and Prof. Dr. Jürg Osterwalder for being co-examiner of this thesis as well as for their support regarding measurements or joint projects.

Thanks to Prof. Dr. Philipp Kurz for being the external examiner. His willingness and spent time is greatly appreciated.

A very big thanks to Evelyne Joliat for her contribution in the research of pyrphyrins, for the interesting discussions and for being a great lab colleague. Her research in the field of pyrphyrins contributed strongly to this thesis. At several instances, comparison between her and my work are drawn and are highlighted. Her work was crucial to draw a more complete picture.

Special thanks for the investigation of the pyrphyrin molecule and its corresponding metal complexes goes to Dr. Gerson Mette, Dominik Leuenberger, Wolf-Dietrich Zabka, Manuel Graf and Denys Sutter from the group of Prof. Dr. Ostwerwalder, Yeliz Gürdal and Marcella Ianuzzi from the group of Prof. Dr. Hutter and Christian Wäckerlin from the group of Prof. Dr. Karl-Heinz Ernscht.

Thanks to Prof. Dr. Kim Baldridge for her collaboration by performing calculations of pyrphyrin molecules and pyrphyrin complexes.

Special thanks to Dr. Cyril Bachmann for supervising my Master thesis and the numerous interesting discussions. Additional thanks to his work in the field of homogenous water splitting. The electrochemical study was a result of a joint project and would not have been possible, in this form, without him.

IV. Acknowledgements

Thanks to Christian Bünzli for his contribution to the research field of this thesis by investigating phenphyrins in our group during his Master thesis. He increased the library of macrocyclic poly-pyridyl complexes by an additional catalytically active catalyst.

Many thanks to our apprentices Lara Pestrin and David Meyer as well as to the students Yannick Schönauer and Liliane Suter who worked in our group and strongly contributed to the work.

I would also like to thank all current and former members of the hydrogen group: Dr. Benjamin Probst, Evelyne Joliat, Mathias Mosberger, Dr. Johannes Windisch, Dr. Cyril Bachmann, Dr. Miriam Oberholzer, Dr. Miguel Guttentag, Dr. Craig Richmond, Dr. Chunhua Cui, Nicola Weder and Peter Müller. Everyone contributed to a very pleasant working environment and we had many fruitful discussions.

Special thanks to my former lab colleagues Evelyne Joliat, Samer Suleiman, Hernández Valdés and Christian Bünzli for providing a great working environment as well as for all the interesting discussions and ideas.

Thanks to the rest of the Alberto group members for their support and for creating a pleasant working atmosphere.

Many thanks to the following people for their support regarding measurements, interpretation of measurements and system development:
Prof. Dr. Bernhard Spingler and Dr. Olivier Blacque for their help in single crystal X-ray measurements and interpretation.
Heinz Spring and Irène Lehmann for elemental analysis.
Dr. Thomas Fox for NMR support, measurements, discussions as well as the help regarding EPR interpretation.
Prof. Dr. Gunnar Jeschke for the EPR measurements.
Dr. Ferdinand Wild for TGA measurements and the infrastructural support.
Dr. Fabian von Rohr for SQUID measurements.
Dr. Laurent Bigler, Urs Stalder and Rahel Bucher for HR-ESI support and measurements.
Hanspeter Stalder and Serkan Sariyildiz from the workshop, who professionally built and repaired many of our custom setups.
The glassblowers Daniel Schnarwiler and Guido Stadelmann for fabrication of highly specific glassware.

Thanks to the administrative staff which was always of great help, especially Dr. Valeria Mozzetti Rohrseitz, who organised all things concerning the LightChEC consortium, as well as Ramona Erni.

For financial support, I would like to thank the University of Zurich, the URPP LightChEC and the graduate school CMSZH.

A very special thanks goes to my parents Marius and Elisabeth Schnidrig and my brother Patrick Schnidrig as well as my Sister in law Evgenyia Schnidrig for their great mental and financial support over the course of the education.

Finally, I also wanted to thank all my friends for their mental support during all this time.

V. Abbreviations

AcO^- (ac)/AcOH	acetate anion/ acetic acid	
$AscO^-$/AscOH	ascorbate anion/ ascorbic acid	
appy	alternative pentapyridine	
aza-pyr	*aza*-bridged pyrphyrin	
aza-phyr	*aza*-bridged phenphyrin	
BTOE	Billion tons of oil equivalent	
bpy	2,2'-bipyridine	
BRB	Britton Robinson buffer	
C-appy	alternative pentapyridine with an additional carbon atom	
CE	counter electrode	
COP	catalytic onset potential	
COSY (NMR)	correlated spectroscopy	
CV	cyclic voltammetry	
DCM	dichloromethane	
DEPT (NMR)	distortionless enhancement of polarisation transfer	
DHA	dehydroascorbic acid	
dmf	N, N-dimethylformamide	
dmso	dimethyl sulfoxide	
dmtpy	dimethyl-tetrapyridine	
DP	differential pulse	
E_{pa}	peak anodic potential	[V]
E_{pc}	peak cathodic potential	[V]
EA	elemental analysis	
EPR	electron paramagnetic resonance (spectroscopy)	
eq	equivalent	
ESI	electrospray ionisation	
Fc/Fc^+	ferrocene/ferrocenium ion	
FT-IR	Fourier transform infrared (spectroscopy)	
GC	gas chromatography	
GCE	glassy carbon electrode	
GDP	gross domestic product	
HMDE	hanging mercury drop electrode	
HPLC	high performance liquid chromatography	
hpy	hexapyridine	
HR	high resolution	
IR	infrared (spectroscopy)	
LED	light emitting diode	

LDA	lithium diisopropylamide	
LSV	linear sweep voltammetry	
mCPBA	*meta*-chloroperoxybenzoic acid	
MS	mass spectroscopy	
MTOE	million tons of oil equivalent	
N-appy	nitrogen bridged alternative pentapyridine	
NCS	thiocyanat	
NHE	normal hydrogen electrode	
NMR	nuclear magnetic resonance (spectroscopy)	
NOE (NMR)	nuclear Overhauser effect	
OPV	overpressure valve	
$^{-}$OTf/TfO^{-}	deprotonated trifluoromethanesulfonic acid	
PCET	proton coupled electron transfer	
PEG	polyethylene glycol	
phen	phenanthroline	
PS	photosensitiser	
pyr	pyrphyrin	
pyr-bu	*mono*-butylpyrphyrin	
pyr-bu$_2$	*di*-butylpyrphyrin	
pyr-MePEG	*mono*-methyl-polyethylene-glycolpyrphyrin	
pyr-pent	*mono*-pentylpyrphyrin	
phyr	phenphyrin	
rt	room temperature (20-30 °C)	[°C]
SEA	sacrificial electron acceptor	
SED	sacrificial electron donor	
Sol	solvent molecule	
SQUID	superconducting quantum interference device (spectroscopy)	
TBAPF$_6$	tetrabutylammonium hexafluorophosphate	
TCEP	tris(2-carboxyethyl)phosphine	
TCEPO	tris(2-carboxyethyl)phosphine oxide	
TCD	thermal conductivity detector	
TEOA	triethanolamine	
TFA	trifluoroacetic acid	
TfOH	trifluoromethanesulfonic acid	
TGA	thermogravimetric analysis	
THF	tetrahydrofuran	
thia-phyr	thia bridged phenphyrin	
TMEDA	tetramethylethylenediamine	
TOE	tons of oil equivalent	

V. Abbreviations

TOF_M	turn over frequency (mol H_2 formed per mol M per time)	[s^{-1}]
TON_M	turn over number (mol H_2 per mol M)	
tpy	tetrapyridine	
TpyP	tetraphenylporphyrin	
UPLC	ultra performance liquid chromatography	
UV/Vis	ultraviolet / visible (spectroscopy)	
WE	working electrode	
WOC	water oxidation catalyst	
WRC	water reduction catalyst	

VI. Main Compounds

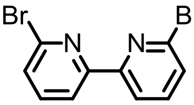

6,6'-dibromo-2,2'-bipyridine
(**1**)

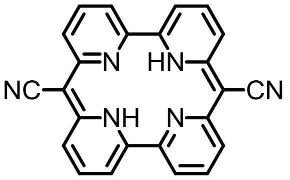

pyrphyrin
pyr
(**2**)

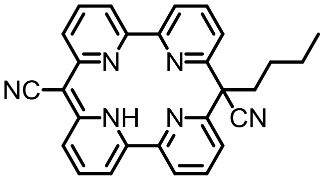

mono-butylpyrphyrin
pyr-bu
(**3**)

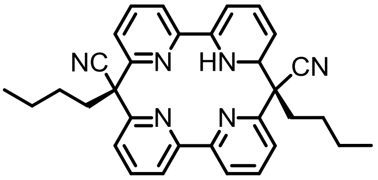

Synthesised by E. Joliat
cis-*di*-butylpyrphyrin
cis-pyr-bu$_2$
(**4**)

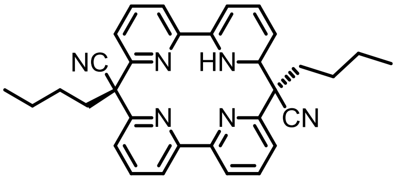

Synthesised by E. Joliat
trans-*di*-butylpyrphyrin
trans-pyr-bu$_2$
(**5**)

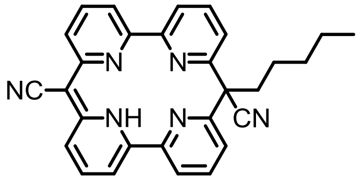

mono-pentylpyrphyrin
pyr-pent
(**6**)

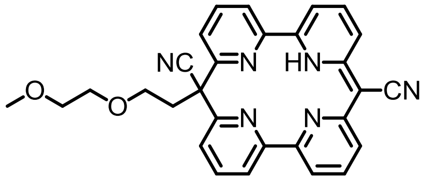

mono-methyl-PEG-pyrphyrin
pyr-MePEG
(**7**)

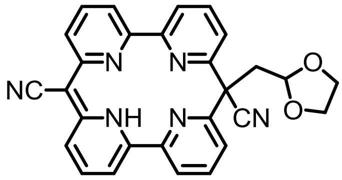

mono-methyldioxolane-pyrphyrin
pyr-dioxolane
(**8**)

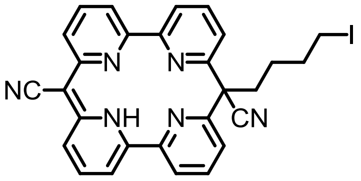

mono-iodobutyl-pyrphyrin
pyr-Ibu
(**9**)

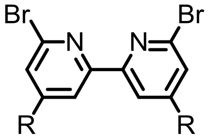

(**13**) R = NO_2, 6,6'-dibromo-4,4'-dinitro-2,2'-bipyridine
(**14**) R = OMe, 6,6'-dibromo-4,4'-dimethoxy-2,2'-bipyridine, C. Bachmann
(**15**) R = Me, 6,6'-dibromo-4,4'-dimethyl-2,2'-bipyridine, i^{2}CNS

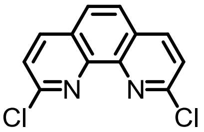

2,9-dichloro-1,10-phenanthroline
(**19**)

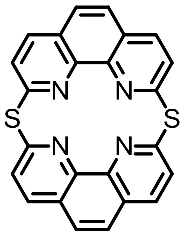

thia-phenphyrin
thia-phyr
(**21**)

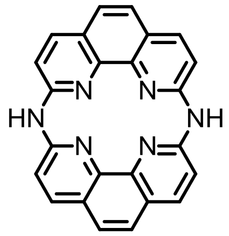

aza-phenphyrin
aza-phyr
(**22**)

VI. Main Compounds

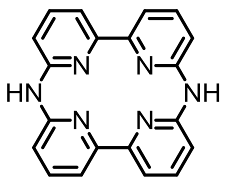

aza-pyrphyrin
aza-pyr
(**24**)

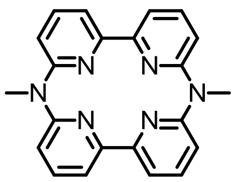

dimethyl-*aza*-pyrphyrin
Me$_2$aza-pyr
(**25**)

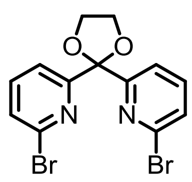

6,6'-(1,3-dioxolane-2,2-diyl)bis(2-bromopyridine)
(**27**)

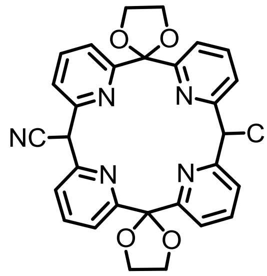

(**28**)

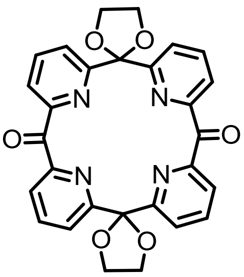

(**29**)

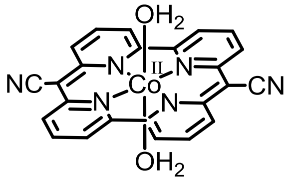

[Co^{II}(OH$_2$)$_2$(pyr)] (**41**)

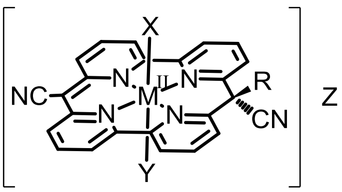

(**42**) M = Co^{II}, R = MePEG, X = MeOH, Y = Br, Z = none
(**43**) M = Co^{II}, R = MePEG, X, Y = H_2O, Z = ClO_4^-
(**44**) M = Co^{II}, R = butyl, X = MeOH, Y = Br, Z = none
(**45**) M = Co^{II}, R = butyl, X = none, Y = THF, Z = ClO_4^-
(**46**) M = Ni^{II}, R = butyl, X = none, Y = none, Z = ClO_4^-
(**47**) M = Cu^{II}, R = butyl, X = none, Y = MeOH, Z = ClO_4^-
(**48**) M = Fe^{II}, R = butyl, X,Y = H_2O, Z = ClO_4^-
(**49**) M = Zn^{II}, R = MePEG, X = pyridine, Y = none, Z = TfO$^-$

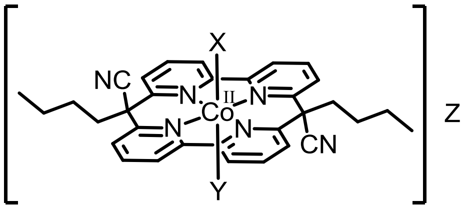

Synthesised by Evelyne Joliat:
(**50**) configuration: *cis*, X,Y = Br, Z = none
(**51**) configuration: *cis*, X,Y = H_2O, Z = 2 ClO_4^-
(**52**) configuration: *trans*, X,Y = Br, Z = none
(**53**) configuration: *trans*, X,Y = H_2O, Z = 2 ClO_4^-

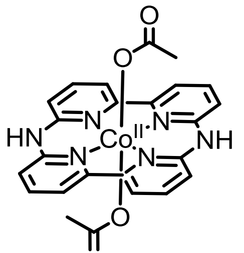

[Co^{II}(ac)$_2$(aza-pyr)]
(**55**)

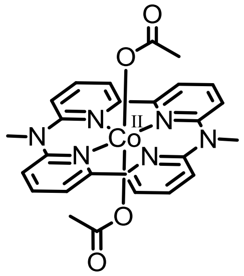

[Co^{II}(ac)$_2$(Me$_2$aza-pyr)]
(**56**)

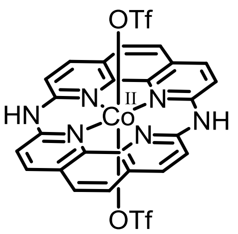

Synthesised by C. Bünzli
[Co^{II}(TfO)$_2$(aza-phyr)]
(**57**)

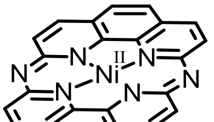

[Ni^{II}$_2$(aza-phyr)] (**58**)

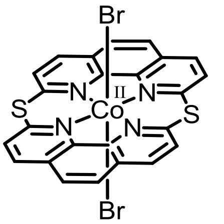

[Co^{II}Br$_2$(thia-phyr)] (**59**)

1. Introduction

1.1 The World's energy demand

The world's energy demand has been rapidly increasing over the last century due to the growth in the world economy and the ever growing world population (Figure 1).[4] Mainly driven by the fast growth of the emerging markets which lifted over two billion people from low income. This growth is thought to remain strong for the foreseeable future.[4,5] As a consequence, since 1965 the energy consumption of the world has more than tripled to a staggering 13'100 MTOE (million tons of oil equivalent, $5.5*10^{20}$ J).[6] Over 80 % of the global energy demand is still covered by non-renewable fossil fuels. Apart from their ultimately limited availability, severe environmental problems are caused by the extraction and combustion of fossil fuels.[7]

Alternative renewable energy resources are needed to ensure a sustainable economic growth. Energy produced by nuclear power plants is not a feasible solution, because the production is still based on a shrinking resource pool. Additionally, the costs for possible accidents, waste disposal and reactor shutdowns are, most likely, often severely underestimated.[8,9] Energy produced by hydroelectricity, wind, solar irradiation, geothermal power, biomass and biofuels could cover our energy demand and substitute fossil fuels in the future, while causing less harm to the environment. Figure 1 shows a clear recent trend, where fossil fuels might finally be substituted by renewable energies. A steep decline in the oil share of the produced primary energy is observed since the 1980. However, in this period an almost equal amount of gain in shares for gas is observed which will continue to rise in the transition phase to a sustainable energy production. The energy production via gas combustion is additionally boosted by the anti-nuclear energy movement from many western countries which would otherwise lead to critical shortages of electricity.[4]

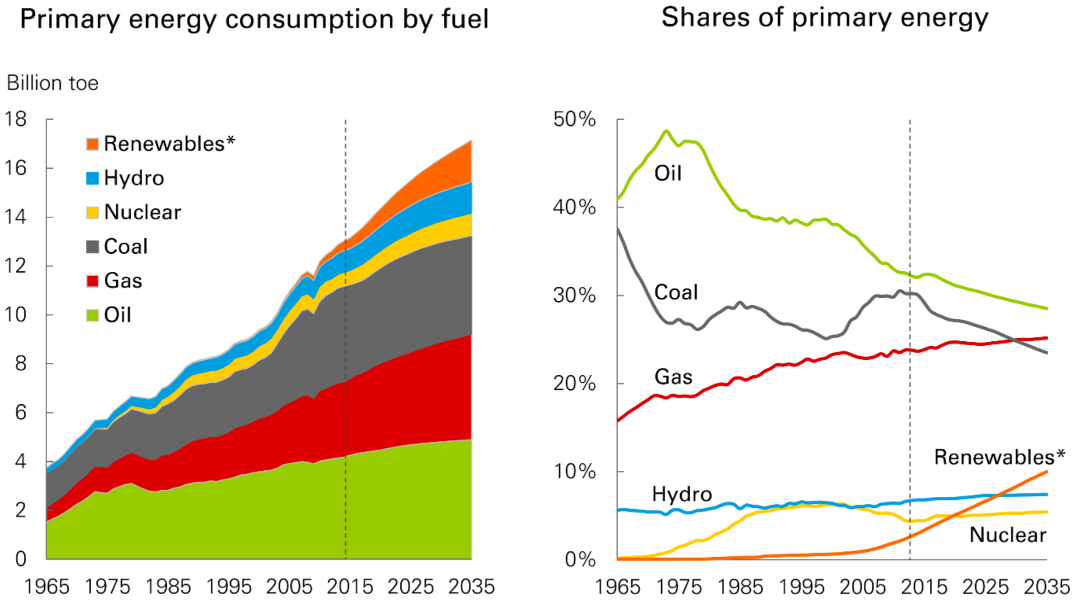

***Figure 1**: Left: Chart of the increasing energy demand in BTOE (billion tons of oil equivalent) Right: Chart of the percentage each energy source counted and counts towards the total energy consumption at the given time.*[4]
**Renewables includes wind, solar, geothermal, biomass, and biofuels*

Different economic projections show that the primary energy demand growth per capita might peak before 2030. This is earlier than previously expected and mainly attributed to unprecedented efficiencies, created by new technologies and more stringent energy policies (Figure 2).[10] This is crucial for the long-term coverage of the energy demand in a capita based economy. The saturation and decline in energy demand per capita is strongly supported by the continuing unprecedented rise of wind and solar energy.

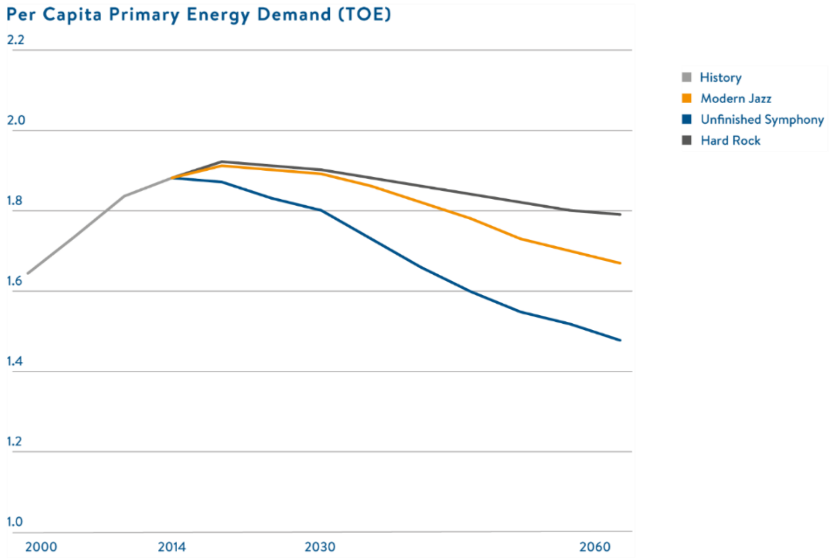

***Figure 2**: Primary energy demand prediction in TOE for three different economic forecasts. Source: World Energy Council, Paul Scherrer Institute, Accenture Strategy Modern Jazz: GDP 3.3 % (economics focused international governance) Unfinished Symphony: 2.9 % (broad-based international governance) Hard Rock: 1.7 % (fractured and weak international system)*[10]

Solar energy is indeed one of the most promising renewable energy resources by exhibiting the highest abundancy. Within one hour more solar energy reaches our planet than humanity needed for a whole year back in 2002.[7,11] Thus, even utilising only a fraction of this energy potential would be sufficient to cover the increasing energy demand and replace the non-renewable energy resources. The small fraction of energy removed from the ecosystem should also cause less severe environmental problems compared to other renewable energies such as hydroelectricity.

Solar energy can already be converted to usable energy sources by various means. Photovoltaic cells that directly generate electricity or solar power plants that drive a turbine by steam to generate electricity are already used in large scale production. Over 80 % of our energy demand is still comprised of non-electric energy.[7,12] Notably, due to most energy needed for transportation and heating purposes being covered by combustion of fossil fuels. On the bright side, electricity has been by far the fastest growing form of end-use energy consumption for the last few decades and is destined to increase even further due to being strongly linked to the economic growth.[13] Main drawback of solar energy is its fluctuating availability, arising from the day/night cycle, the inconsistent weather conditions and the difficulty of long-term storage of electricity.[14,15] It is thus essential to find solutions for the short and long-term storage of energy.

One of the most promising prospects is the production of solar fuels by artificial photosynthesis, thus storing energy in chemical bonds.[16] Photocatalytic water splitting where water is split into oxygen and hydrogen would be a suitable way to store energy. Hydrogen is a good energy carrier and the stored energy can be released by non-polluting combustion according to the actual energy demand.[17] Hydrogen has a very high energy density per mol and weight, but exhibits a very low density per volume, making storage and handling in smaller amounts rather difficult (Figure 3).[1] Thus, direct conversion of hydrogen to a better suited chemical storage molecule might be favourable, especially for supplying transportation energy (cars, planes, boats). Hydrogen could also be used for chemical reactions, such as the synthesis of ammonia by the Haber-Bosch process or hydrogenations. Hydrogen can be converted to hydrocarbons by the Fischer-Tropsch process using biogas derived syn-gas.[18]. Alternatively, H_2 can be reacted with CO_2 to form methanol.[19] The obtained hydrocarbons or methanol are easier to handle (liquid, higher volumetric energy density) and can be used in normal combustion engines with only minor adaptations. The possibility to reuse the already established infrastructure would save costs. Indecently, methanol is already used in the combustion engines for the IndyCar races in America.

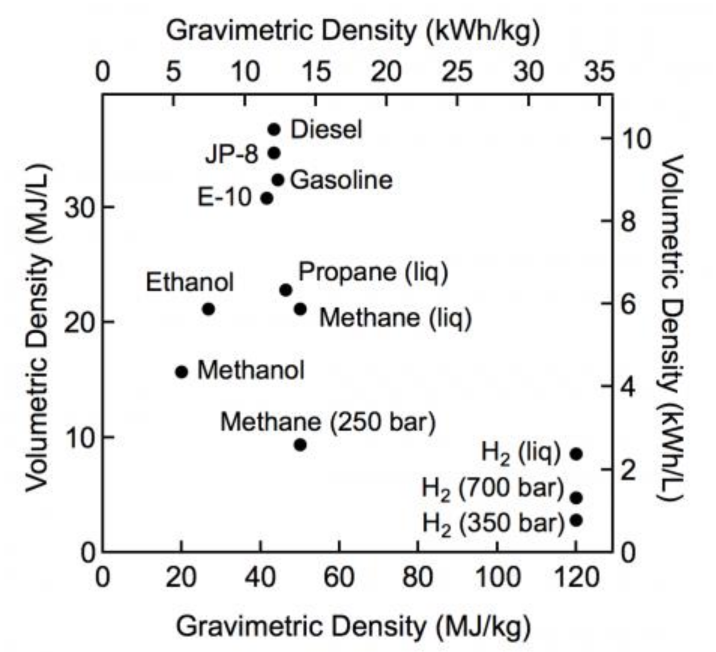

Figure 3*: Comparison of specific energy (energy per mass or gravimetric density) and energy density (energy per volume or volumetric density) for several fuels based on lower heating values.*[1]

1.2 Photocatalytic water splitting

Storing of chemical energy by using solar power to form molecular bonds is often referred to as artificial photosynthesis, since it essentially tries to imitate nature.[7] Photocatalytic water splitting, where water is decomposed into hydrogen and oxygen, is a complicated multi-electron process and consist of several reaction steps (Figure 4).[16] The total reaction can be divided into a photosensitiser (PS), water oxidation catalyst (WOC) and water reduction catalyst (WRC) based subsystems which is schematically described in Figure 4. The photosensitiser (PS) subsystem absorbs the solar energy by excitation of the PS to *PS followed by an electron uptake to form PS^- by oxidation of the water oxidation catalyst (WOC → WOC^+). The reduced photosensitiser (PS^-) then transfers the electron onto the WRC (WRC → WRC^-), thus ensuring a continuous electron transfer from the WOC to the WRC. In the WOC pathway, H_2O gets oxidised to O_2 and 2 H^+ via a WOC. On the other hand, the WRC reduces the released protons from the water oxidation to form H_2.[20] Due to the complexity of the total system, various back electron transfers between the oxidative (WOC) and reductive (WRC) half reaction can occur and inhibit catalysis.[21] A purely homogenous system to split water into hydrogen and oxygen has thus not yet been described. Only combinations with heterogeneous electrodes or semiconductors applied in so called artificial leafs are able to drive the total reaction.[22] Therefore, the total process is separated into two individual segments (blue and red framing shown in Figure 4) for research in purely homogenous catalysis. This is achieved by either exchanging the WOC by a sacrificial electron donor (SED) in the reductive half reaction (red box) or the exchange of the WRC by a sacrificial electron acceptor (SEA) in the oxidative half reaction.

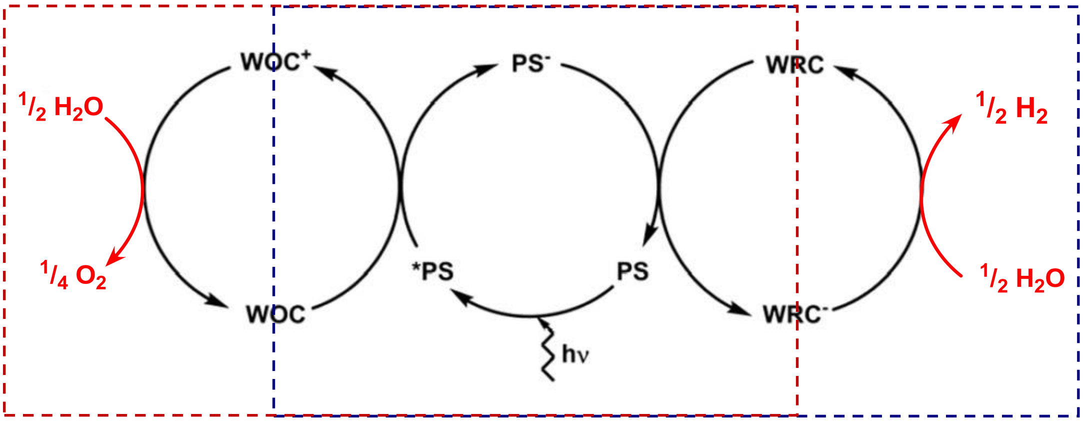

Figure 4: *Schematic representation of the overall photocatalytic water splitting reaction consisting of three subsystems: oxidation of water (WOC cycle), reduction of water (WRC cycle) and light absorption via the photosensitiser (PS).*

1.2.1 Water oxidation catalysis

Water oxidation gives oxygen in a four electron and four proton process, thus being considerably more demanding than the corresponding water reduction, where two electrons and two protons are involved. Magnesium, ruthenium or iridium based molecular catalysts have shown to be working catalysts. They are often limited by the harsh oxidative reaction condition leading to the decomposition of the ligand framework.[23] Alternatively, oxidative more robust metal oxides, polyoxometalates or spinels were successfully used as heterogeneous WOC.[23-25] Benchmarking of the various WOCs is usually performed by electrocatalysis or chemical oxidation with $Ce(NH_4)_2(NO_3)_6$ at pH values below 2. Photocatalytic oxygen evolution is mostly investigated by using $[Ru(bpy)_3]^{2+}$ as a photosensitiser and peroxodisulfate ($S_2O_8^{2-}$) as sacrificial electron acceptor.

1.2.2 Homogenous water reduction catalysis

Main focus of this dissertation was the investigation of the homogenous photocatalytic water reduction. In this process hydrogen is produced by the reduction of two protons with two electrons (Figure 4, blue box).

First functional WRCs for proton reduction were already described in 1979 and 1983 by Sutin and Lehn.[26,27] While they relied on organic solvents, a still ongoing rapid development of new WRCs lead to highly active catalysts even under purely aqueous conditions.[28]

$[Ru(bipy)_3]^{2+}$ was one of the first PS in use for homogeneous photocatalytic proton reduction.[25] In the following decades many examples of new PSs were reported: Bipyridine complexes based on platinum group elements, diimines based PSs (e.g. $[Ru(diimine)_3]^{2+}$, $[Ir(ppy)(diimine)]^+$, $[Ir(ppy)_2(diimine)]$), carbonyl based complexes of rhenium (e.g. $[ReBr(CO)_3phen]$, $[ReBr(bipy)(CO)_3]$).[29-32] Exchanging the bromide ligand in $[ReBr(bipy)(CO)_3]$ by thiocyanate gave $[Re(NCS)(bipy)(CO)_3]$ which lead to improved performances in DMF.[32] Exchanging the thiocyanate by a pyridine lead to $[Re(bipy)(CO)_3(py)][TfO]$, a very efficient water soluble PS.[33].Photosensitisers based on more abundant elements (e.g. Cu, Zn, Sn), quantum dots or purely organic molecules (e.g. Eosin Y) were also strongly investigated and a vast variety of functional photosensitisers were reported.[34-39] Despite the intense efforts to design better suited photosensitisers over the last few decades, $[Ru(bipy)_3]^{2+}$ and other *tris*-bipyridine metal complexes remain to date amongst the most effective PS to drive proton reduction.[28,40] In this thesis, $[Re(bipy)(CO)_3(py)][TfO]$ and $[Ru(bipy)_3]Cl_2$ were used as PS for photocatalytic hydrogen evolution.

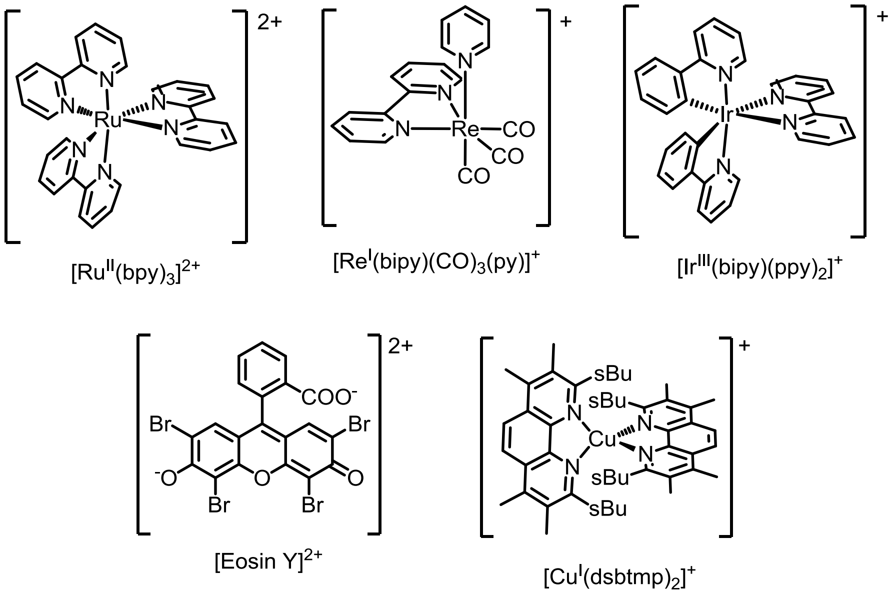

$[Ru^{II}(bpy)_3]^{2+}$ $[Re^{I}(bipy)(CO)_3(py)]^+$ $[Ir^{III}(bipy)(ppy)_2]^+$

$[Eosin\ Y]^{2+}$ $[Cu^{I}(dsbtmp)_2]^+$

***Figure 5**: Selected examples of photosensitisers showing the two photosensitisers applied in this thesis ($[Ru^{II}(bipy)_3]Cl_2$[41] and $[Re^{I}(bipy)(CO)_3(py)][TfO]$)[42], the noble-metal based $[Ir^{III}(bipy)(ppy)_2]^+$ [43], the purely organic dye Eosin Y[44] and the cupper PS $[Cu^{I}(dsbtmp)_2]^+$ [35].*

Originally, Sutin et al. used a macrocyclic cobalt ($Co^{I}(Me_4[14]tetraeneN_4)^+$) as WRC in presence of $[Ru(bipy)_3]^{2+}$ as PS and ascorbic acid as sacrificial electron donor (SED) and proton source.[25] To date, $[Ru(bipy)_3]^{2+}$ remains still one of the most versatile PS and ascorbic acid is still widely used as SED for photocatalytic water reduction. That said, continuous research in the field over the last decades lead to a steady performance increase in photocatalysis by development of a vast library of new WRCs consisting of noble and earth abundant metal complexes (Figure 6). Earth abundant cobalt complexes[20,28,40,45-49] show some of the most promising results in proton reduction, next to nickel[48,50], molybdenum[51,52] and iron[53] complexes. The structure of one of the first cobalt catalysts was ill defined and was later improved by cobaloximes which were researched for many years.[30-33] WRCs with bipyridine ligands like $[Co(bipy)_3]^{3+}$ and $[Rh(bipy)_3]^{3+}$ reported by Bernhard et al. showed also catalytic activity.[43,54] Generally, the most efficient WRCs were comprised of pyridine, pyridine derivatives or bipyridine based ligand systems. However, when application moved from organic solvents (mostly triethanolamine) into water, severe limitations were observed, because of the instability of most WRCs under reductive aqueous conditions.[32,33] Searching for better ligand systems, which remained stable towards reduction, lead to the discovery of poly-pyridyl ligand systems.[20,28,40,49] This new class of WRCs showed drastically increased performance, showing equal or even superior performance than noble metal catalysts.

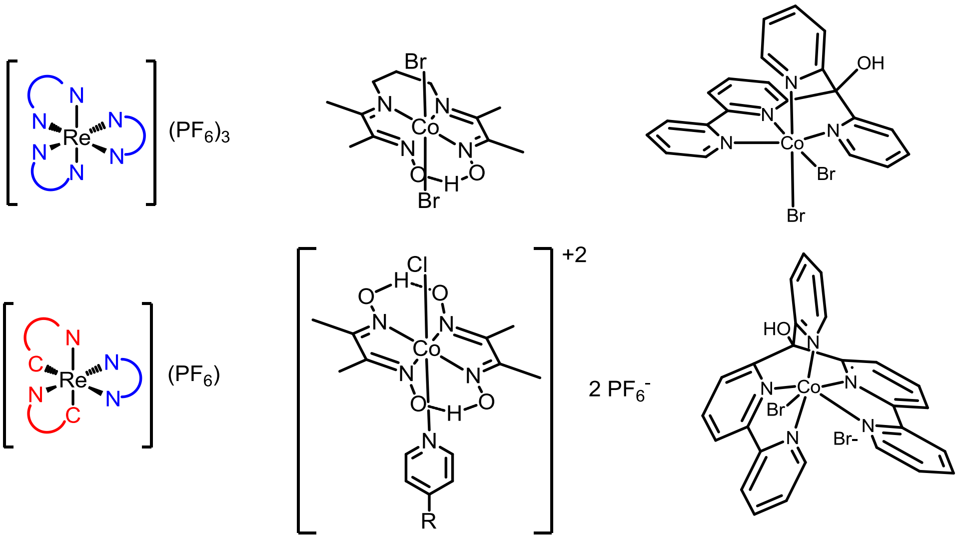

Figure 6: *Selected examples of reported WRCs for proton reduction. Left row: general structure of Re based catalysts[43]; Middle row: cobaloxime and derivative (top, Alberto et al.[33]; bottom, Artero et al.[31]); Right row: poly-pyridyl cobalt WRCs[20,49]*

Only a few suitable sacrificial electron donors (SEDs) have been reported and ascorbate is still the most widely used SED in acidic aqueous media. For slightly basic pH values, triethanolamine (TEOA) and trialkylamines proved to be functional SEDs. While TEOA and trialkylamines are irreversibly oxidised and do not interfere with the catalytic cycle, ascorbate converts to dihydroascorbic acid (DHA). DHA has been shown to inhibit catalysis by short-cutting the catalytic cycle.[55]

1.3 Porphyrins

Porphyrins are naturally occurring heterocycles that consist of four pyrrole subunits which are interconnected over methylene groups (Figure 7).[56] Porphyrins follow the Hückel rule (4n + 2) and are aromatic structures with 22 delocalised π-electrons, respectively 26 after complexation.[57,58] Nature uses porphyrins and its derivatives (e.g. chlorins) with abundant metal centres such as Fe, Mg in a broad variety. For instance as photosensitiser in chlorophyll, as catalyst in various reactions or as transporter for oxygen in blood.[59] Vitamin B12, which is important for the amino acid metabolism in humans, is a cobalt based derivative of a tetra-pyrrole ligand (corrin systems).[59] Porphyrins can bind metal atoms in their cavity, usually in a 2+ or 3+ state and act as doubly negatively charged anionic ligand system (Figure 7). Complexation of porphyrins often leads to extremely stable complexes.[56]

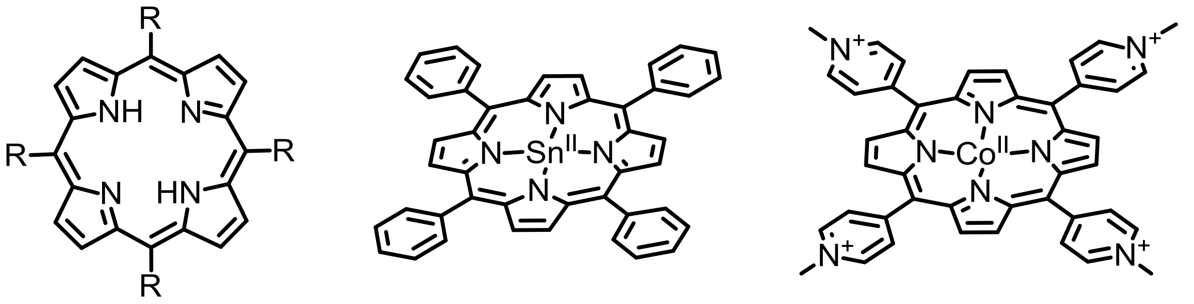

***Figure 7**: General structure of porphyrins (left, R = H, porphin), a reported PS (SnTPP[60], middle) and a porphyrin based WRC (Co(NMeTPyP^{4+})[61], right).*

Porphyrins became a research focus due to their unique physiochemical properties (photochemistry, metal complexation, electron and radical uptake and distribution). The often very low solubility of porphyrins severely limits application and extensive research was mandatory to increase the solubility of this class of structure.[62] Porphyrin metal complexes showed very good capabilities as photosensitisers and have even been reported to work as PS in photocatalytic hydrogen and oxygen evolution.[60,63,64] Artificial metallo-porphyrins have been shown as early as 1985 to act as catalysts for the electrochemical reduction of protons to hydrogen.[65-67] In addition, $[Co(NMeTPyP)]^{4+}$ has recently been reported to work as WRC in photocatalytic proton reduction which was supported by other catalytic active cobalt porphyrins in our group.[61]

1.4 From porphyrins to pyrphyrins and phenphyrins

The robustness of macrocyclic porphyrins and their potential for catalytic activity towards proton reduction, combined with the proven exceptional catalytic performance of cobalt poly-pyridyl WRCs could result in a highly active and stable new class of WRCs. Thus, the reported macrocycles based on two bipyridine or phenanthroline subunits interlinked by carbon, sulphur or nitrogen atoms became promising candidates for catalytic investigations (Figure 8).[68-71] For the most part, only superficial investigations were performed and just a few metal complexes based on this macrocycles have been reported.[72-75] Even though the ligand frameworks are known for several decades. These macrocycles (**2**, **3**, **5**, **8**, **15**, **53**) share some similarities to porphyrins, but contain pyridine subunits instead of pyrrole. Trivial names for **2** (pyrphyrin, pyr), **8** (*aza*-pyrphyrin, *aza*-pyr) and **15** (*aza*-phenpyrin, *aza*-phyr) were assigned due to the repeated mentioning of these heterocycles.

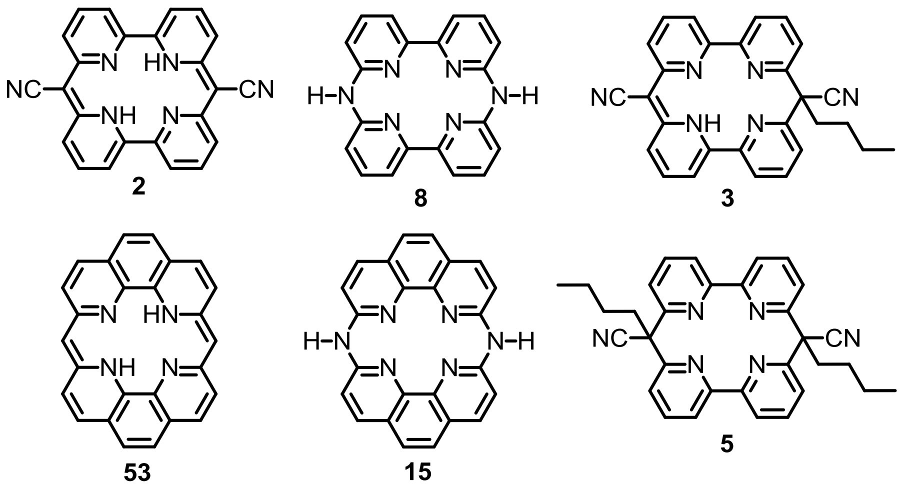

***Figure 8**: Poly-pyridyl based macrocycles **2**, **3**, **5**, **8**, **15** and **53**.*

Ligands **2**, **8**, **15** and **53** display two tautomeric forms in which the hydrogen atom is either located at the bridging atom or on the pyridyl nitrogen atom (Figure 9). While **2** and **53** are thought to be mainly present in their conjugated structure, compound **8** and **15** should be favouring the open structured form. Alkylation at the bridging carbon atom as shown for **3** and **5** removes the possibility of deprotonation, thus making tautomerisation at that centre impossible. Concluding, ligand **2** and **53** mostly act as anionic ligands with a charge of minus two, should exhibit a planar structure and be able to strongly bind metals. *Mono*-alkylated compound **3** can be considered as an anionic ligand with a charge of minus one and the *di*-alkylated ligand **5** acts as a neutral ligand. Ligand **8** and **15** are also considered neutral ligands due to them disfavouring conjugation over the *aza*-bridge. The structural similarities between porphyrin and pyrphyrin indicate a high stability of the molecule and the corresponding complexes due to the charge, conjugation, planarity and cyclic nature of pyrphyrin.

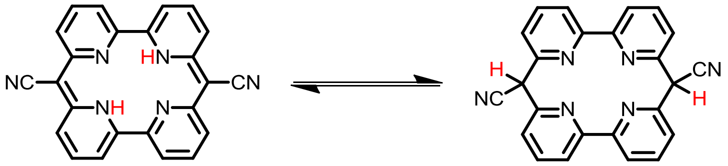

***Figure 9**: Tautomeric forms of open structured (right) and conjugated (left) pyrphyrin*

Porphyrins are with 22 and 26 conjugated electrons a clear aromatic system regarding the Hückel rule ((4n+2) electrons), whereas pyrphyrins with 28 electrons don't fulfil this rule. In fact, unhindered conjugation is strictly speaking only possible within the bipyridine or phenanthroline moiety. However, the physiochemical data and calculations for known ligands and complexes strongly imply delocalisation over the complete ligand backbone.

1.5 Objectives

The main goal of the dissertation was the synthesis and investigation of new macrocyclic poly-pyridyl based complexes with the ligand frameworks shown in Figure 8. Their possible applications as photocatalytic WRCs was our main interest in the compounds. Complexes based on these ligands show structural similarities to cobaloximes (four nitrogen in a plane), thus such complexes might also show catalytic activity as WRCs and could potentially exhibit a low overpotential as observed for cobaloximes. Macrocyclic complexes should also be considerably more stable towards ligand reduction and subsequent deactivation as seen in cobaloximes. Additionally, all ligands contain pyridine subunits in form of bipyridine or phenanthroline. Thus, being similar to the reported cobalt poly-pyridine catalysts which showed remarkable catalytic performance as WRCs at high overpotentials. The complexes based on these macrocyclic ligands might lead to very robust and highly active WRCs exhibiting a low overpotential. Interesting photochemical properties seen in porphyrins made complexes based on these ligands also promising for the development of new potential PS. Functionalisation at the ligand backbone by alkylation or by other means was a further focus to change and tune the electronics of the complexes, leading ideally to better performing catalysts. Additionally, these investigations should sharpen our understanding of the WRCs by thorough electrochemical and photocatalytic investigations.

2. Results and Discussion

This section gives an overview of the main results of the thesis. Starting with the synthesis and the physiochemical properties of the organic macrocyclic ligands (2.1) wherein the synthesis of pyrphyrin based macrocycles (2.1.1), *aza*- and *thia*-bridged macrocycles (2.1.2) and the tetra-pyridyl macrocycle (2.1.3) are described. In chapter (2.2) the synthesis of the corresponding metal complexes is described, subdivided into pyrphyrin based complexes (2.2.1) and *aza*- and *thia*-bridged macrocyclic complexes (2.2.2).

Following, the investigation and comparison of the physicochemical properties of the metallocomplexes are described (2.3). Firstly, the crystal structures of selected complexes is discussed (2.3.1). Later on, an in depth analysis of the spectroscopy (2.3.2), UV/Vis titration (2.3.3) and electrochemistry (2.3.4) of the complexes is described.

Photocatalysis of the metal complexes is specified in chapter (2.4). Seperated into a chapter about pyrphyrin based catalysts (2.4.1) and *aza*-bridged macrocyclic complexes (2.4.2).

In the last subchapter (2.5), a general approach to benchmark the various catalysts by electrochemistry is described and general trends are discussed. For that, the photocatalytic activity of various WRCs are compared (2.5.1). Electrochemical investigations of the same catalysts are performed (2.5.2). Finally, the data is supported by selected examples of in-line GC measurements (2.5.3).

Scheme 1 on the next page illustrates the general scheme of synthesis for the poly-pyridyl based macrocyclic cobalt complexes. Synthesis of **30**, **31** and **50**-**54** was performed by Evelyne Joliat[3] in our group while complex **57** was synthesised by Christian Bünzli[76]. Highlighted in blue is the ligand framework. Reaction conditions I - VI are as follows: I) $Co(ac)_2 \cdot 4\ H_2O$, MeOH, rt, 90 % II) $CoBr_2$ hydrate, NaOH, MeOH, reflux, 2 d, 80 %; III) $Co(ac)_2$ tetrahydrate, KO^tBu, pyridine reflux, 2 h, 90 %; IV) $CoBr_2$ hydrate, EtOH, reflux, 2 h, 65 %; V) $CoBr_2$, $CHCl_3$, MeOH, 25 °C, 15 min, 10 %[3]; VI) $Co(OTf)_2$, MeCN, reflux, 2 h, 40 %; $X = Br^-, I^-$; X_1, X_2 = ac^- or H_2O; $X_3 = CH_3OH$; X_{4-8}, Br^-; $X_9 = TfO^-$

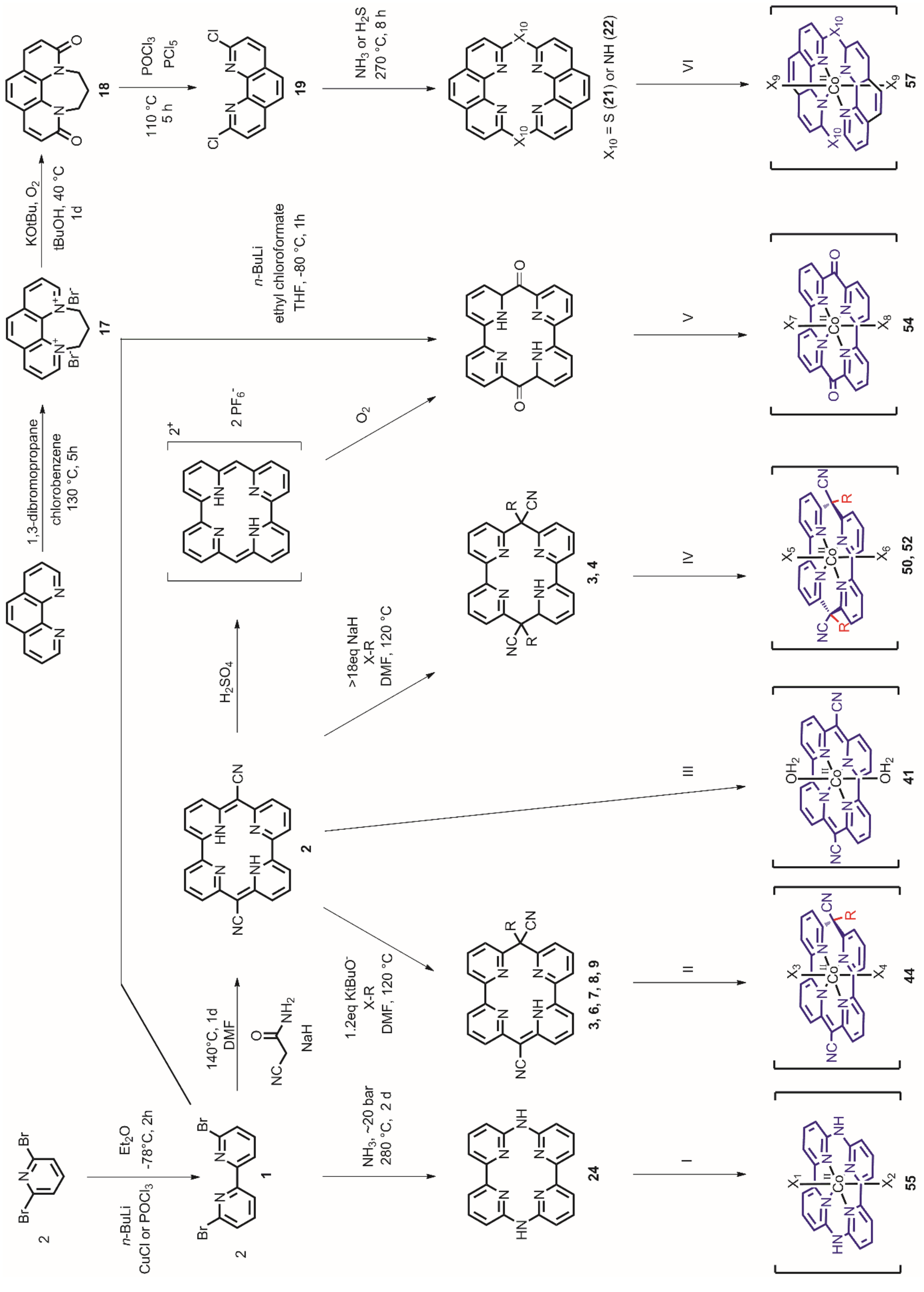
2
Br
N
Br
n-BuLi
CuCl or POCl3
Et2O
-78°C, 2h
2
1
140°C, 1d
DMF
NaH
NH3, ~20 bar
280 °C, 2 d
24
1.2eq KtBuO-
X-R
DMF, 120 °C
3, 6, 7, 8, 9
2
H2SO4
>18eq NaH
X-R
DMF, 120 °C
3, 4
2+
2 PF6-
O2
1,3-dibromopropane
chlorobenzene
130 °C, 5h
17
KOtBu, O2
tBuOH, 40 °C
1d
18
POCl3
PCl5
110 °C
5 h
19
n-BuLi
ethyl chloroformate
THF, -80 °C, 1h
NH3 or H2S
270 °C, 8 h
X10 = S (21) or NH (22)
I
II
III
IV
V
VI
55
44
41
50, 52
54
57
Co
II
X1
X2
X3
X4
X5
X6
X7
X8
X9
X10
OH2
NC
CN
R
HN
NH
Cl
O

2.1 Syntheses and physicochemical properties of the ligands

2.1.1 Pyrphyrin based macrocycles

*(6E,17E)-23,24,25,26-tetraazapentacyclo[17.3.1.1^{2,6}.1^{8,12}.1^{13,17}] hexacosa-1(23),2,4,6,8(25),9,11,13,15,17,19,21-dodecaene-7,18-dicarbonitrile (**2**, **pyrphyrin**, **pyr**)*

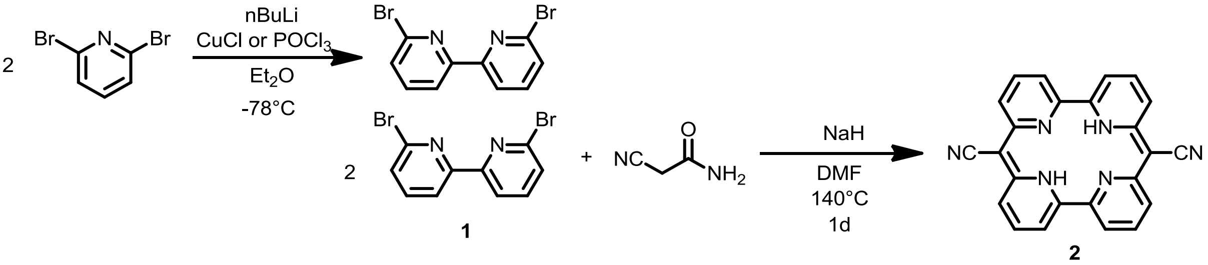

Scheme 2: *Synthesis of the pyrphyrin ligand system*

The synthesis of 6,6'-dibromo-2,2'-bipyridine (**1**) was performed via lithiation of 2,6-dibromopyridine in diethyl ether at -78 °C followed by oxidative coupling with $POCl_3$ to afford **1** as a white crystalline solid in 40 % yield.[77] $POCl_3$ could be interchanged by $SOCl_2$ with similar results.[77] The described purification by column chromatography could be replaced by crystallisation from CH_2Cl_2 and heptane. Therefore, the reaction could easily be scaled up to 100 g starting material. The improved workup was especially important for synthesis of larger amounts, since ligand **1** shows rather low solubility in organic liquids (~10 g per litre CH_2Cl_2). Recrystallisation of the mother liquor after removal of the first crystallised batch of **2** did not yield crystals with sufficient purity. CuCl could be used as coupling reagent, but the obtained yield (~16 %) was considerably lower. Copper induced oxidative coupling by using $CuCl_2$ was also possible.[78] In all cases, the $CuCl_2$, $SOCl_2$ and $POCl_3$ seemed to induce the coupling reaction by forming an activated C-Cu, C-S or C-P bond respectively. However, when copper sources were used, the formed impurities could only be removed by silica gel chromatography (CH_2Cl_2:MeOH, 99:1). Various crystallisation trials showed co-crystallisation of side products. Thus, for larger scale reactions no copper was used.

Reaction of **1** with cyanoacetamide, using NaH in hot DMF, gave **2** (pyrphyrin, pyr) in modest yields (~16 %) according to a reported procedure.[68,73] The reaction most likely proceeds through two subsequent deprotonations of cyanoacetamide and addition of the carbanion to form **2** accompanied by CO_2 elimination. The reaction was unique to cyanoacetamide, as no corresponding product formation was observed if other conjugation stabilised amides or MeCN were reacted with **1**. One of many side products could be crystallised and analysed by X-ray crystallography (Figure 10). A reaction of DMF with the bipyridine backbone was observed.

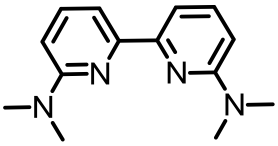

***Figure 10**: Side product of the pyrphyrin synthesis*

Pyrphyrin exhibits a very dark wine red colour and shows a specific CN band stretch frequency at 2185 cm^{-1}. Normal CN stretch frequencies show a weak to medium absorption.[79] In the case of pyrphyrin, the band is very pronounced due to its direct link to a conjugated system and the overlapping of the two equivalent CN stretch frequencies. The conjugated system also leads to the intense colouring. Pyrphyrin showed extremely low solubility in almost all solvents. Partial solubility in hot DMF and DMSO was observed as well as good solubility at room temperature in TFA and H_2SO_4 by reversible protonation. Precipitation of **2** was observed if the strongly acidic solutions were diluted by water.

Analysis of pyrphyrin relied on solid state IR and elemental analysis (EA), as alternative analytical techniques were difficult due to the solubility. Detection by mass spectrometry (MS) for instance was not possible. Purification of pyrphyrin by soxhlet, dissolving in acid followed by precipitation or washing with large amounts of various solvents did not lead to a matching elemental analysis for pyrphyrin. Nevertheless, in most cases it was enough to thoroughly wash the pyrphyrin with organic solvents and use it directly for the next reaction step.

It was, however, possible to obtain pyrphyrin in high purity (according to elemental analysis (EA)) by extensively washing the crude pyrphyrin with DMF and MeOH, followed by sublimation at 1*10^{-6} mbar and 350 °C. This purification was only partially reproducible and normally several attempts were needed to obtain pure product according to EA. Attributed to the different porosity of the obtained pyrphyrin, distribution of the side products, encapsulation of **2** by polymeric side products as well as the slow degradation of pyrphyrin under the sublimation conditions. A bright red impurity was often sublimated first and only thereafter pure pyrphyrin was sublimated. Said impurity was soluble in organic solvents. Thus, the hypothesis of the encapsulation of impurities by insoluble pyrphyrin or their corresponding polymeric side products was corroborated. Partial decomposition was observed after sublimation (350 °C, 1*10^{-6} mbar, 3 d) and a considerable amount of a black insoluble residue was formed which did no longer exhibit a cyanide IR band.

^{1}H NMR analysis in d-TFA did not show the expected signals, suggesting strong interaction of pyrphyrin with TFA. A solid state ^{13}C NMR of pure pyrphyrin gave rise to eight signals between 75 and 160 ppm (Figure 11). On the basis of the equilibria shown in Scheme 3 as proposed by Ogawa et al.[69] 12 (conjugated form, left) respectively 7 (open structure form, right) signals would be expected. All signals are relatively broad and, except for one, positioned in the region expected for aromatic and nitrile carbon atoms. The first signal at 76 ppm is considerably less downfield shifted than the other signals (110 ppm – 160 ppm) showing a non-aromatic character. ChemDraw simulations and comparison with ^{13}C NMR shift tables[79] highly support the hypothesis that the signal at 76 ppm corresponds to the bridging carbon atom of the conjugated pyrphyrin form (expected at around 85 ppm). One would estimate a significantly lower signal at around 40 ppm for the bridging carbon in the open structure form.[79] The remaining 10 aromatic and the nitrile signals seem to overlap. Hence, in solid form, pyrphyrin seems to be present in its conjugated form. This assignment is in-line with the colour and the calculations as detailed below.[40]

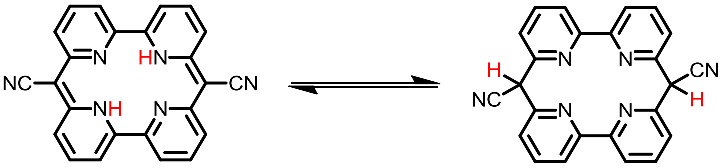

***Scheme 3**: Tautomeric forms of conjugated (left) and open structured (right) pyrphyrin (**2**)*

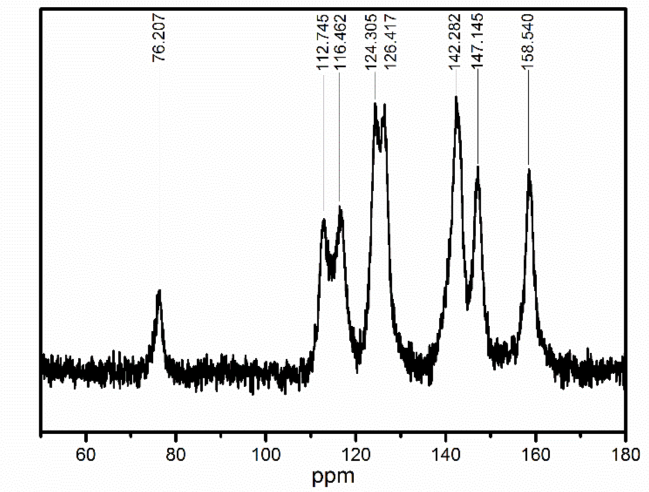

***Figure 11**: Solid state ^{13}C NMR of pyrphyrin (**2**) at 25 kHz*

Since underivatised pyrphyrin could not be crystallised and subjected to X-ray diffraction analysis for structure determination, computational methods (B97D/Def2-TZVPP (DMF)) were employed to obtain structural information and relative energies for the conjugated and open forms (Figure 12).[40] Calculation do indeed show that pyrphyrin is completely planar in gas phase, thus residing in the conjugated form. Only a very slight out of plane twist in the pyridyl subunits in solution was calculated while the molecule stayed planar around the –C–CN moiety. The two cyano-substituents are aligned in an anti-parallel fashion.

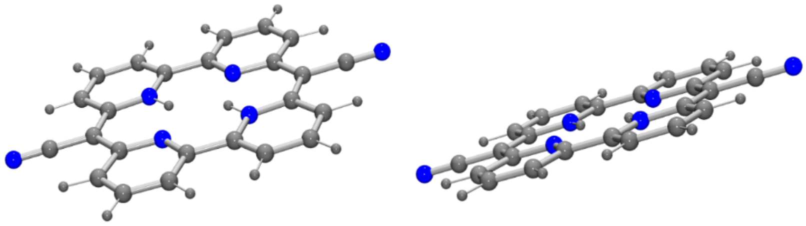

***Figure 12**: B97D/Def2-TZVPP (DMF) calculated structure of pyrphyrin[40]; Grey large: carbon, Grey small: hydrogen, Blue: nitrogen*

Alkylation of pyrphyrin (**2**, **pyr**)

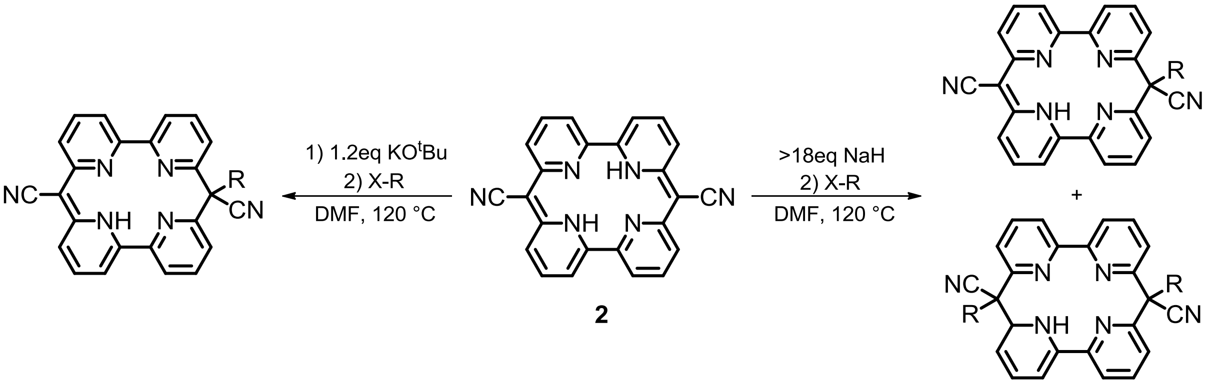

***Scheme 4**: Synthesis scheme for the mono- and di-alkylation of pyrphyrin, X = Br, I*

The solubility of **2** and its corresponding metal complexes could be improved by alkylation of pyrphyrin.[40,68,73] Depending on the reaction conditions, formation of mono- or di-alkylated product was achieved. In all cases, pyrphyrin needed to be pre-treated by a strong base (NaH, KO*t*Bu) in hot DMF, followed by the dropwise addition of the alkylation agent. Activation of pyrphyrin by deprotonation with NaH seemed to be crucial, but exact reproduction was impossible due to the variable deprotonation rates arising from the different particle sizes and trace impurities. Deprotonation of pyrphyrin to form the active species for the subsequent reaction lead to an intense red colour and an almost complete dissolution of the starting material in DMF. Over time, the colour intensity gradually degraded to a dark wine brown suspension. A slow deactivation of pyrphyrin by the prolonged reaction time might be the origin of this observation. Originating from reaction of DMF with NaH, deprotonation of pyrphyrin or the formation of side products. The reaction rate with alyklhalides was substantially increased if the deprotonated pyrphyrin exhibited a strong red colouration which is in support of the hypothesis.

Mainly doubly alkylated products were formed when pyrphyrin and NaH in DMF were sonicated for 1 h at 70 °C prior to the addition of the electrophile (R-X). On the other hand, stirring for 2 h at 60 °C lead to higher yields of mono-alkylated product. While a very bright red suspension after sonication was obtained, a far darker suspension was observed when only heating (60°C) was applied. The colour changed back to dark red within five minutes upon addition of the alkylation agent. It was not possible to observe the starting material by HPLC or TLC and therefore conversion could only be checked by the formation of the product peaks. Using sublimated pyrphyrin improves the robustness of the synthesis, but consumes a considerable larger amount of starting material due to the low yield of sublimated pyrphyrin. Lower purity pyrphyrin was used since alkylated pyrphyrins are easily purified by column chromatography, thus giving far larger overall yields of the desired products.

Addition of 1-iodo-butane to deprotonated pyrphyrin resulted in a mixture of *mono*-butyl-pyrphyrin (pyr-bu, **3**), *cis*- and *trans*-dibutyl-pyrphyrin (*cis*-pyr-bu$_2$, **4** and *trans*-pyr-bu$_2$, **5**)[3,68] which could be separated by column chromatography (SiO$_2$, CH$_2$Cl$_2$/MeOH (10:0) to CH$_2$Cl$_2$/MeOH (9:1)). Compound **3** was eluted first and could be isolated pure, while the second fraction (*cis*-pyr-bu$_2$, (**4**)) was contaminated with **3**. *trans*-pyr-bu$_2$ (**5**) was collected as third fraction with an unidentifiable impurity. A fourth fraction was eluted, which E. Joliat identified as the triiodide salt of protonated **4**.[3] *cis*- and *trans*-dibutyl pyrphyrin were purified (by E. Joliat[3]) by repeated recrystallisation in acetone and EtOH. On reversed phase (C$_{18}$) HPLC, the order of elution was inverted and **5** was eluted before **4** which was finally followed by **3**. The triiodide salt of **4** was not observed as separate fraction under HPLC measurement conditions. Detailed synthesis and isolation of compound **4** and **5** was described by E. Joliat in our group.[3]

Mono-alkylated product was formed in all cases due to the instability of the bromide and iodide sources in strong base. NaH needed to be used in large excess (>20 eq) even for the targeting of the mono-alkylated products. Under this conditions selective *mono*-alkylation was difficult, showing either incomplete conversion or too much doubly alkylated species under very similar conditions. The huge excess of alkylation agent (>30 eq) needed made the synthesis of more complicated derivatives very pricy. The usage of alkyl-bromide instead of alkyl-iodide (e.g. 1-bromo-pentane or -butane) especially in combination with KO^{t}Bu as base suppressed di-alkylation completely. The lower reactivity of the bromides lead to a more controlled conversion to the mono-alkylated product by trading conversion rate with selectivity. Noteworthy, KO^{t}Bu could be applied in a slight excess (1.3 eq) instead of the >20 eq needed with NaH and simplified workup. The requirement of the alkylation agent could also be reduced to a near stoichiometric amount (1.2 eq). This allowed the alkylation with a larger library of reagents. For instance, close to stoichiometric amounts of KO^{t}Bu and 1-iodo-butane yielded exclusive formation of *mono*-butyl-pyrphyrin (**3**) in approximately 30 % yield after purification. Derivatisation of **2** to the desired mono-alkylated products was achieved with a variety of alkylation agents as seen in Table 1.

R-X	Yield	compound
	**28 %**	**3**
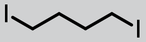	**15 %**	**9**
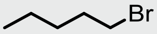	**32 %**	**6**
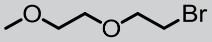	**52 %**	**7**
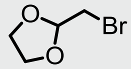	**28 %**	**8**

Table 1**: Summary of alkylation reagents and corresponding yields for the mono-alkylation of **2

Alkylation of the pyrphyrin ligand framework increased the solubility in organic solvents while the products remained insoluble in water. In all cases the colour changed from a dark wine red colour to a bright luminous red, while *di*-alkylation gave rise to pale red solids. This was expected, given the reduced conjugation and planarity upon alkylation. Ligand **7** showed the best solubility of the *mono*-alkylated ligands, especially in MeOH.

Dimerisation of deprotonated pyrphyrin (1 eq KO^{t}Bu) was observed when alkylation was performed with a slight excess of 1,4-diiodobutane (1.2 eq) to form the dimer **10**. Mainly *mono*-alkylated **9** was formed, but formation of ~10 % dimerised pyrphyrin could be observed by UPLC-MS (Figure 13). The *mono*-alkylated species was easily removed by silica column purification, but the formed dimer showed high interaction with the silica and sticked, respectively smeared on the column.

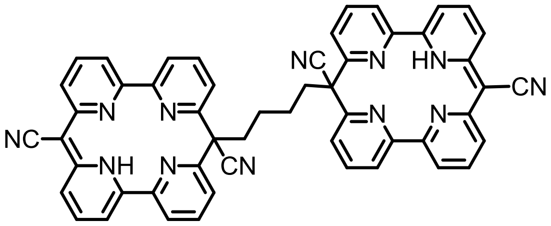

10

***Figure 13**: Observed pyrphyrin dimer (**10**)*

Single crystals of **4**, **6**, **7**, **8** and **9** could be obtained by vapour diffusion.[80] The calculated B97D/Def2-TZVPP (DMF) structure of *mono*-pentyl-pyrphyrin (pyr-pent, **6**, Figure 14a) and the X-ray structure of **6** (Figure 14b) showed strongly reduced planarity as compared to the almost complete planarity of pyrphyrin (**2**, Figure 12).[40] Ligand **6** has a planar 2-pyridyl-2(1*H*)-pyridylideneacetonitrile moiety and a non-planar pentyl di(2-pyridyl)acetonitrile moiety. The cyano-groups are still aligned in an anti-parallel orientation while the orientation of the pentyl group is almost perpendicular to the plane formed by the four nitrogen atoms, a rather uncommon orientation. The assignment of the N3-H proton position in the X-ray structure is supported by additional electron-density next to the N3 atom as well as longer C–N bond lengths for the less aromatic N3–C12 (1.365(3) Å) and N3–C16 (1.377(2) Å) bonds compared with the fully aromatic pyridine on the pentyl di(2-pyridyl)acetonitrile moiety (1.329(3)–1.345(2) Å).

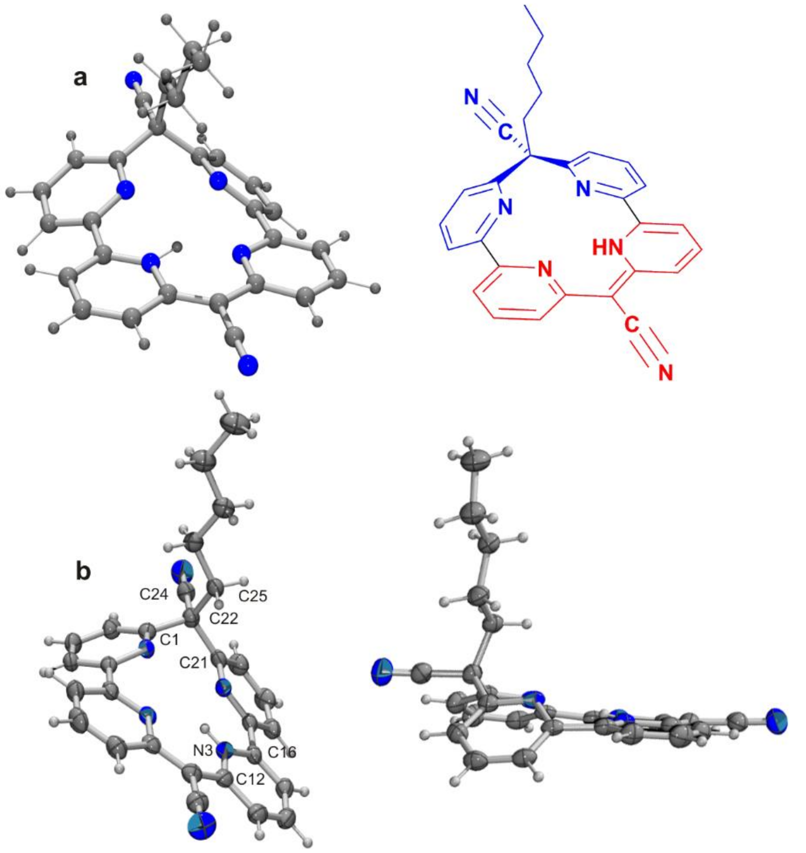

Figure 14 a: B97D/Def2-TZVPP (DMF) calculated structure of **3** (left) and schematic representation of the planar (red) and non-planar (blue) moiety within the macrocycle **6** (right). b: Top and side views ORTEP[2] of **6**. Thermal ellipsoids are at the 50 % probability level. Grey large: carbon, Grey/white small: hydrogen, Blue: nitrogen

The crystal structure of the other mono-derivatised pyrphyrin ligands (**7**, **8** and **9**) displayed very similar geometry. The CN bonds are aligned in anti-parallel orientation and the alkyl residue is in near perpendicular orientation relative to the pyrphyrin plane.

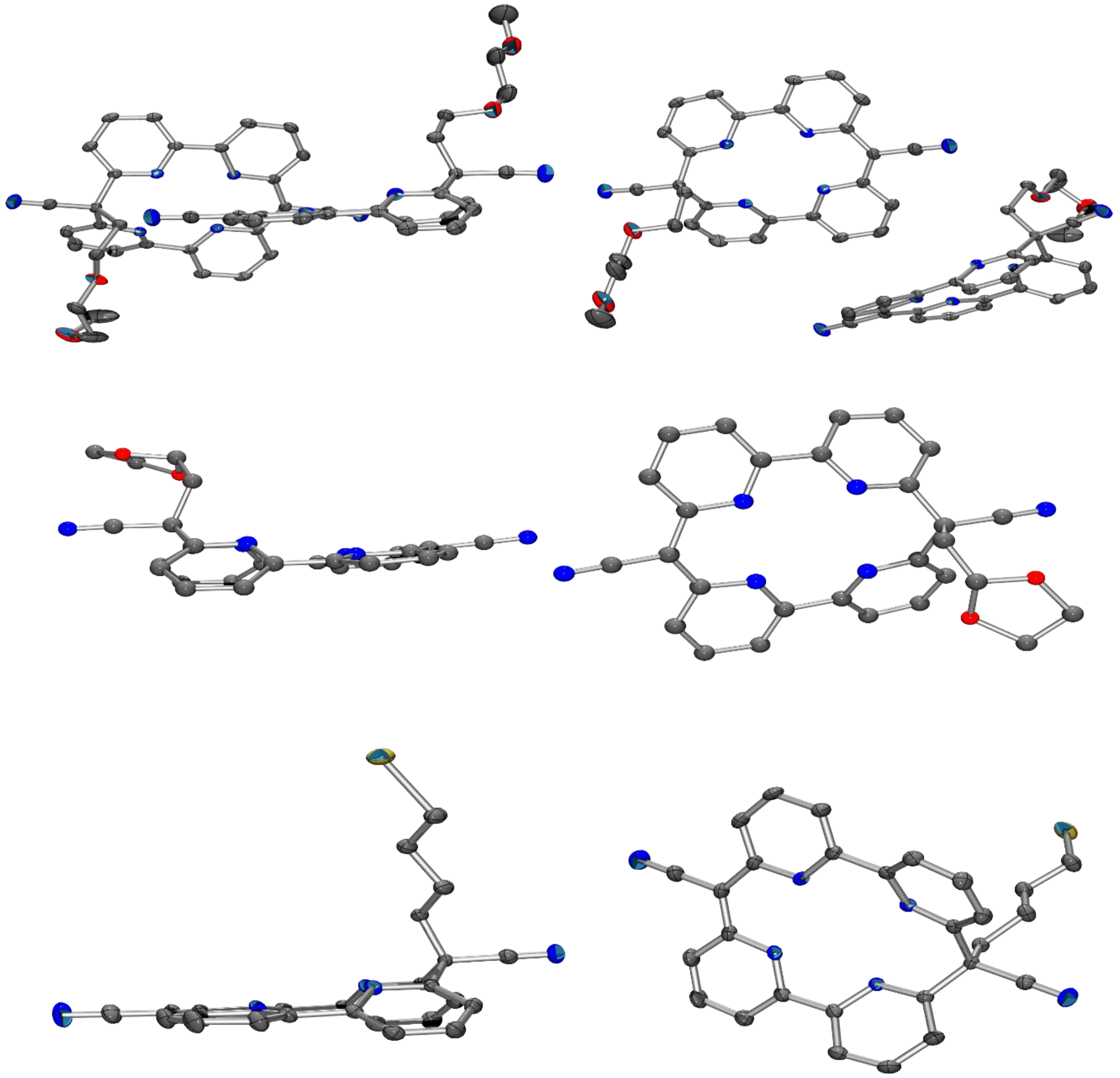

*Figure 15: Side (left) and top (right) views ORTEP[2] of **7** (top), **8** (middle) and **9** (bottom). Thermal ellipsoids are at the 50 % probability level. Hydrogen atoms and co-crystallised solvents are omitted for clarity. Grey: carbon, Blue: nitrogen, Red: oxygen, Yellow: iodine*

Introduction of a second alkyl moiety lead to a considerable change in geometry. The *trans*-pyr-bu$_2$ ligand was crystallised by Ogawa et al.[68] and showed strongly twisted pyridine units within the bipyridine moiety. The structure for *cis*-pyr-bu$_2$ was crystallised by Evelyne Joliat in our group and its structure was determined by X-ray diffraction and calculation (B97D/Def2-TZVPP (DMF), Figure 16).[40] In both cases, a book shaped conformation was observed which shows less twisting of the pyridine subunits within the bipyridine. According to calculations, the *cis*-pyr-bu$_2$ structure should be more stable than the *trans*-pyr-bu$_2$ by 6.7 kcal/mol, which is in agreement to the prioritised formation of *cis*-pyr-bu$_2$ in all syntheses.[40] In both cases the CN bond is still linearly oriented. Di-alkylation of pyrphyrin leads to almost colourless products due to the reduced conjugation of the system.

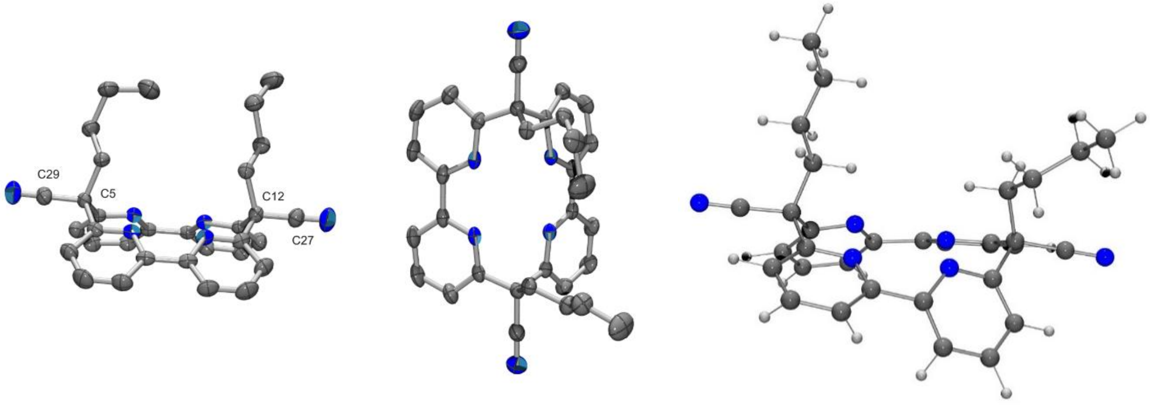

***Figure 16**: left and middle: ORTEP[2] of cis-pyr-bu$_2$ (**4**), side and top view. Ellipsoids are drawn on the 50 % probability level. Only one out of two molecules in the asymmetric unit is displayed, hydrogen atoms are omitted for clarity. right: B97D/Def2-TZVPP (DMF) calculated structure of cis-pyr-bu$_2$, **4**.[40] The structures were obtained by E. Joliat in our group.[3] Grey: carbon, Blue nitrogen, White: hydrogen*

Further pyrphyrin derivatives

Derivatives of pyrphyrin were investigated to tune the electronics, solubilities as well as to enable the immobilisation of pyrphyrin based ligand frameworks. Cleavage by hydrolysis or reduction of the nitriles was one of the approaches. As stated in chapter 2.1.1, pyrphyrin **2** is soluble in strong acids (H_2SO_4, TFA) where it remained stable at room temperature. At higher temperatures, CN hydrolysis and subsequent CO_2 loss was observed by UPLC-MS (Scheme 5, right). The isolation of a pyrphyrin salt with removed nitriles was later achieved in our group by Evelyne Joliat.[3] Pyrphyrin was dissolved in TFA and heated to 122 °C under nitrogen. After complete conversion, TFA was removed in vacuum and the obtained salt was dissolved in nitrogen saturated H_2O and precipitated by NH_4PF_6 to obtain an air stable dark solid.[3] Cleaving the CN groups generated two highly reactive methylene groups which reacted in presence of oxygen or non-inert organic solvents and gave rise to product mixtures. This reaction could only be suppressed by trapping the product as conjugated salt as shown by E. Joliat.[3] Initial trials to reduce the nitriles by hydrogenation with Pd/C did not yield any product (Scheme 5, left).

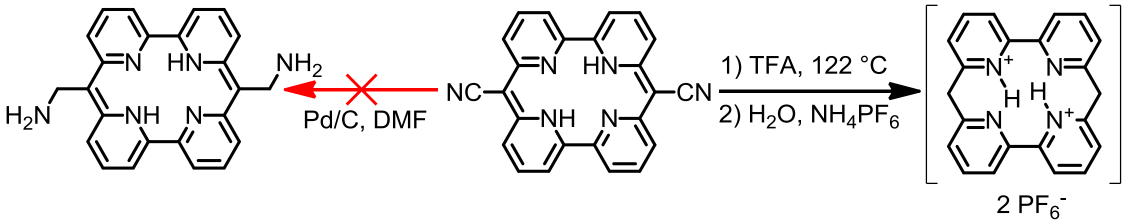

***Scheme 5**: Hydrogenation (left) and CN cleavage (right) of pyrphyrin by the optimised isolation method of E. Joliat[3] in our group.*

Scheme 6 shows the general representation for an altered pyrphyrin based ligand backbone. The bipyridine moieties could be derivatised in the 4,4’ position or the bridging R_2CCN could be exchanged by a R_2CO (E. Joliat[3]) using ethyl chloroformate as coupling reagent where R_2 represents the connections to the macrocycle.

Nitration of 6,6'-dibromo-2,2'-bipyridine (**1**) in the 4,4’-position was achieved in a three step synthesis with an overall yield of 18 % (Scheme 6).[81,82] Conversion of **1** to 6,6'-dibromo-[2,2'-bipyridine] 1,1'-dioxide (**11**) was achieved by dissolution of **1** in TFA and subsequent addition of H_2O_2 (50 % in water) until an equilibria of *mono*-N-oxidised and *di*-N-oxidised species was formed (approximately 5 to 10 % *mono*-N-oxidised product). Repeated portion wise addition of H_2O_2 was needed due to thermal decomposition of H_2O_2. H_2O_2 (30% in water) could be used for the synthesis, but showed lower conversion. Most likely due to the slightly higher pH from the larger amount of water. Trituration of the crude product in *t*-butanol and hexane was sufficient to obtain pure **11**.

For the nitration of **11**, oleum (20 % SO_3 in conc. H_2SO_4) and foaming HNO_3 (100 %) were used in a 1:1 mixture to achieve full conversion to 6,6'-dibromo-4,4'-dinitro-[2,2'-bipyridine] 1,1'-dioxide (**12**) at 90 °C. Using diluted HNO_3 (65 % in water) gave only partial conversion (90 %) to **12** and the *mono*-nitrated product was observed as side product (10 %).[81,82]

Deoxygenation of **12** was more difficult (4h, 100 °C, nitrobenzene) than 2,6-dibromo-4-R-pyridine-1-oxides (R = OMe), which are generally deoxygenated in 30 min at 70 °C in chloroform (70 %, Scheme 7).[81]

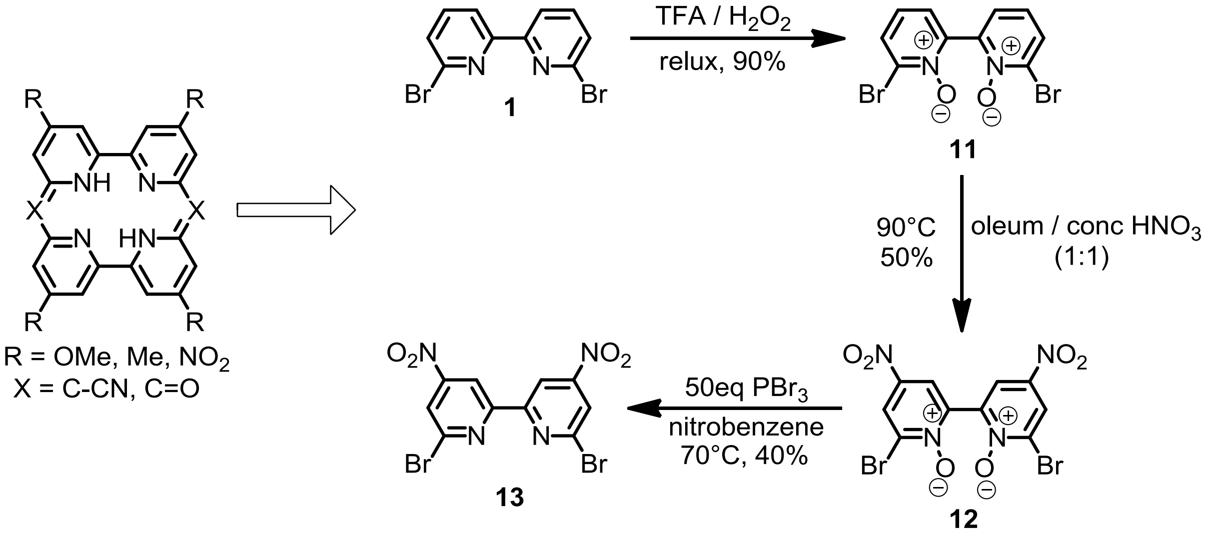

Scheme 6: *Synthesis of 6,6'-dibromo-4,4'-dinitro-2,2'-bipyridine (**13**)*

The homo cross-coupling for the synthesis of 6,6'-dibromo-4,4'-dinitro-2,2'-bipyridine (**13**) was performed prior to functionalisation at the 4,4’-positions, because **1** was available in large amounts from the synthesis of pyrphyrin based macrocycles. In general, the cross-coupling reaction is the lowest yielding step (Scheme 7). Thus, performing this reaction step early on should increase the overall yield. However, very harsh reaction conditions were required for the N-oxidation and 4,4’-nitration of the di-pyridyl species. More gentle conditions gave mainly the mono-oxygenated and mono-nitrated products. 6,6'-Dibromo-4,4'-dimethoxy-2,2'-bipyridine (**14**) was synthesised by Cyril Bachmann in our group (Scheme 7).[83] The synthesis was performed by N-oxidation of 2,6-dibromopyridine followed by nitration, methoxylation, deoxygenation and cross-coupling with an overall yield of 20 %. The N-oxidation, nitration and deoxygenation of **14** were performed under similar albeit milder reaction conditions than for **13**. Prior deoxygenation of the pyridine-N-oxide, the nitro group was methoxylated by NaOMe.[81] The cross-coupling was achieved by lithiation of 2,6-dibromo-4-methoxypyridine with n-BuLi (-90 °C) and $SOCl_2$ as coupling reagent.[84,85]

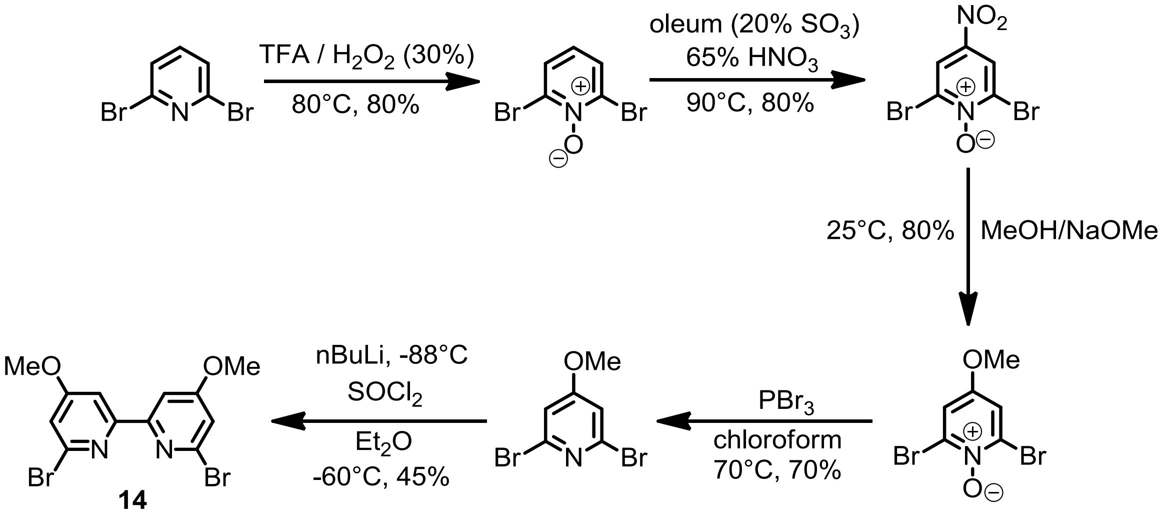

***Scheme 7**: Synthesis of 6,6'-dibromo-4,4'-dimethoxy-2,2'-bipyridine (**14**) performed by Cyril Bachmann in our group.*[83]

The decreased reactivity of 6,6'-dibromo-2,2'-bipyridine compared to 2,6-dibromopyridine does prohibit a higher overall yield for **13** than for **14**, where the cross coupling was performed as the last step. Other cross-coupling reactions might be more difficult and could be circumvented by the pathway of Scheme 6.

Scheme 8 shows the general pathways of the ligand framework derivatisation with either 6,6'-dibromo-2,2'-bipyridine (**1**), 6,6'-dibromo-4,4'-dinitro-2,2'-bipyridine (**13**), 6,6'-Dibromo-4,4'-dimethoxy-2,2'-bipyridine (**14**) or 6,6'-Dibromo-4,4'-dimethyl-2,2'-bipyridine (**15**) as starting material. Pathway A was adapted from literature as an alternative pathway for the pyrphyrin synthesis.[86] The pyrphyrin standard synthesis according to Ogawa et al. was investigated as shown in pathway B.[87] Pathway C was performed by Evelyne Joliat and Cyril Bachmann according to an adopted procedure from the synthesis of bis(2-pyridyl)ketone[88] previously elaborated for the coupling of two 6-bromo-2,2'-bipyridine.[83]

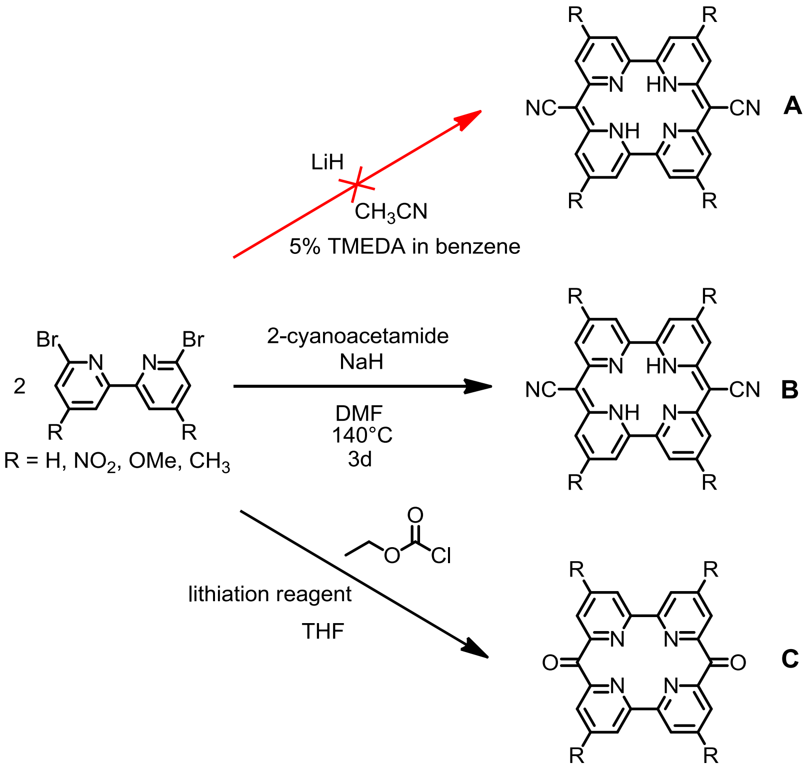

***Scheme 8**: Different synthesis pathways for alternative ligand frameworks. Pathway C was performed by E. Joliat and Cyril Bachmann.*[3]

Coupling of 6,6'-Dibromo-4,4'-dimethyl-2,2'-bipyridine (**15**) along pathway C lead in most cases to partial formation of the desired macrocycle. Reaction conditions are crucial for obtaining the desired product in reasonable yields. Lithiation with n-BuLi in THF below -90 °C lead to quantitative conversion as shown by Peter Müller in our group. Decomposition of the starting material was observed by lithiation above -90 °C. Slow addition of the n-BuLi solution and the ethyl chloroformate was crucial to keep the local temperature below -90 °C. The coupling of 6,6'-dibromo-2,2'-bipyridine (**1**) with ethyl chloroformate was also possible under similar conditions as shown by E. Joliat.[3] Both of this compounds are white solids in comparison to the very intense colouration of the pyrphyrin analogues.

Lithiation of **13** lead to cleaved nitro groups after workup while the bromine remained intact, thus indicating a higher reactivity of an aromatic C-H compared to the bromides. In fact, treatment of **13** with *t*-BuLi followed by quenching with MeOH lead to the formation of 6,6'-dibromo-dimethoxy-2,2'-bipyridine according to UPLC-MS. Hence, using *n*-BuLi, *t*-BuLi and LDA as lithiation and ethyl chloroformate as coupling reagent for the macrocyclic ring formation with **13** (pathway C) gave no desired product.

Initial tests along pathway B with 6,6'-Dibromo-4,4'-dimethyl-2,2'-bipyridine (**15**) showed partial conversion to the desired product in the lower percentage region accompanied by the formation of a wide variety of side products. Synthesis and isolation of the desired product was not feasible under this conditions. Noteworthy was the increased solubility of the tetramethyl pyrphyrin compared to **2**, since **2** could not be detected by UPLC-MS and the tetramethylated pyrphyrin showed a midrange retention time (2.2 min, 5 min method). Even though large amounts (100 mg to 1 g) were used for screening and a dark product mixture could be isolated in both cases, no conversion to the desired product was observed when **13** or **14** were used as starting material for the synthesis along pathway B. Conversion to the desired product might still have occurred, but detection by UPLC-MS was not possible due to the solubility or masking by side products.

In all cases, pathway A showed no desired product formation and the formation of colourless polymeric compounds was observed.

Asymmetric macrocycle synthesis by 6,6'-dibromo-2,2'-bipyridine and 3,3'-dibromo-1,1'-biphenyl gave pyrphyrin **2** and not the desired product **16** (Scheme 9), likely due to a higher reactivity of **1** under the reaction conditions.

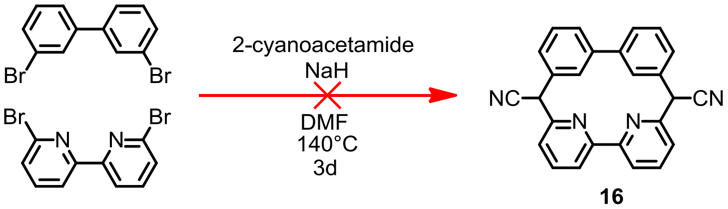

1

16

Scheme 9**: Asymmetric synthesis of **16

2.1.2 *Aza*- and *thia*-bridged macrocycles

*2,9-Dichloro-1,10-phenanthroline (**19**)*

2,9-Dichloro-1,10-phenanthroline (**19**) was synthesised according to Guo et al. and was used as starting material for the preparation of macrocyclic phenanthroline based ligands.[89,90] Compound **19** was synthesised and isolated in gram quantities over three steps as shown in Scheme 10.[89]

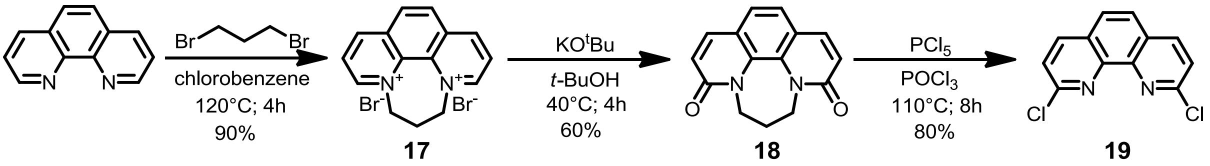

***Scheme 10**: Synthesis of 2,9-dichloro-1,10-phenanthroline (**19**)*[89]

In a first step, anhydrous phenanthroline was N,N-annelated to activate the 2,9 positions for the subsequent oxidation. Anhydrous phenanthroline in chlorobenzene at 120 °C was treated with 1,3-dibromopropane to afford pure 6,7-dihydro-5H-[1,4]diazepino[1,2,3,4-lmn][1,10]phenanthroline-4,8-diium bromide (**17**) as white solid (90 % yield). Anhydrous phenanthroline yielded cleaner conversions than phenanthroline monohydrate used in literature.[89] The reaction could be scaled up to 100 g without any problems and no further purification was needed for the following steps.

Compound **17** was oxidised by air under strong basic conditions (KO^{t}Bu in *t*-BuOH) at 40 °C in 60 % yield. Pure oxygen did not increase the yield nor decrease the reaction time. Higher concentrations of **17** gave similar yields at lower conversion rates. The crude 6,7-dihydro-3H-[1,4]diazepino[1,2,3,4-lmn][1,10]phenanthroline-3,9(5H)-dione (**18**) was isolated as white solid by filtration and extraction (CH_3Cl/water). It could be used directly for the subsequent synthesis of 2,9-dichloro-1,10-phenanthroline (**19**). Removal of excess *t*-BuOH at reduced pressure prior to hot filtration gave the best yields. Exchanging chloroform by dichloromethane resulted in lower purities of the isolated products. Highlighting the often neglected physiochemical difference of CH_2Cl_2 and $CHCl_3$ arising from the different dipole moments.

In a last step, compound **18** was chlorinated by PCl_5 in $POCl_3$ at 110 °C to obtain **19** in 80 % yield. Excess $POCl_3$ was removed under reduced pressure at 40 °C. Distillation at high temperature often lead to significantly reduced yields. The resulting white solid was deprotonated (pH 8) with an ammonia (25 %) solution and the brown solid was isolated by filtration. Even though the purity of the isolated crude product was approximately 95 %, further purification for the macrocyclic ring closure reaction proved to be crucial. Small amounts of trichloro-phenanthroline could be present which could not be separated from dichloro-phenanthroline once corresponding macrocycles were formed. A column chromatography (silica gel, CH_2Cl_2) was sufficient to obtain pure **19**.

*Thia-, aza- and carbon-bridged phenphyrin (**21, 22, 23**)*

Preparation of the *aza*-bridged phenanthroline (**22**) has been reported by Ogawa et al. by cyclisation of 2,9-dichloro-1,10-phenanthroline (**19**) and 2,9-diamino-1,10-phenanthroline with a yield of 84 %.[91,92] The thermal dimerisation procedure has been reported to give very low yields and many side products.[91] The improved synthesis of thia-bridged phenphyrin (**21**) and *aza*-bridged phenphyrin (**22**) was adopted from Wang et al. where **21** and **22** were synthesised in a one pot synthesis starting from the previously prepared compound **19** (Scheme 11).[70,90]

2,9-Dichloro-1,10-phenanthroline (**19**) was heated under a continuous H_2S or NH_3 stream to obtain **21** respectively **22** as an orange yellow salt. The crude products were dissolved in aqueous HCl and precipitated by adjusting the pH to 14 with NaOH to obtain the neutral ligands. Alternatively, washing the crude product with ether and MeOH was enough to obtain **21** and **22** as pure HCl salts, but the yield was generally considerably lower due to the products solubility in polar solvents when protonated. Precipitation of the neutral ligand also lead to a more defined structure and washing with water lead to complete removal of any formed salt by-products. Synthesis of **21** was considerably faster than the synthesis of **22**, even though lower temperature were used for **21**. A kugelrohr oven was used for this synthesis and amounts above 200 mg often lead to incomplete conversion for **22**. Most likely due to the reduced surface area available for reaction. While the corresponding salts of **21** and **22** showed partial solubility in polar solvents such as water and methanol, the neutral ligands exhibited low solubility in organic solvents.

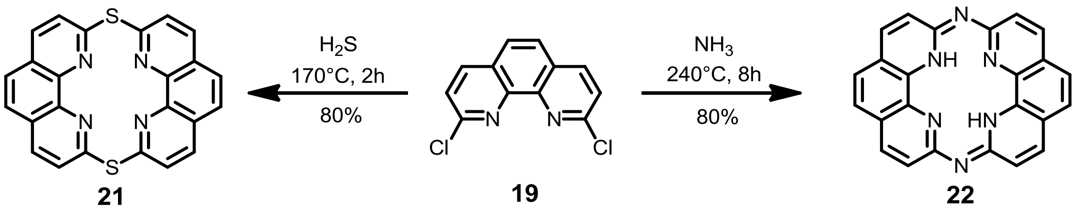

Scheme 11**: Synthesis of aza- and thia-bridged phenphyrins **21** and **22

The thermal reaction of neocuproine and **19** in an autoclave at 260 °C according to literature[91] gave an insoluble black solid that could not be properly identified. Starting material could be removed by acetone. Washing with $CHCl_3$ gave a slightly less impure more reddish product mixture. No formation of **23** was detected. Direct complexation of crude **23** with $ZnCl_2$ yielded miniscule conversion (~1 %) to **40** according to UPLC-MS. Isolation of the product was not possible due to large amounts of side products. (Scheme **12**).

Lithiation of neocuproine with LDA at -78 °C followed by addition of **19** in dry THF showed partial formation of the mono-bridged product, but upon addition of $ZnCl_2$ no desired complexation was observed.

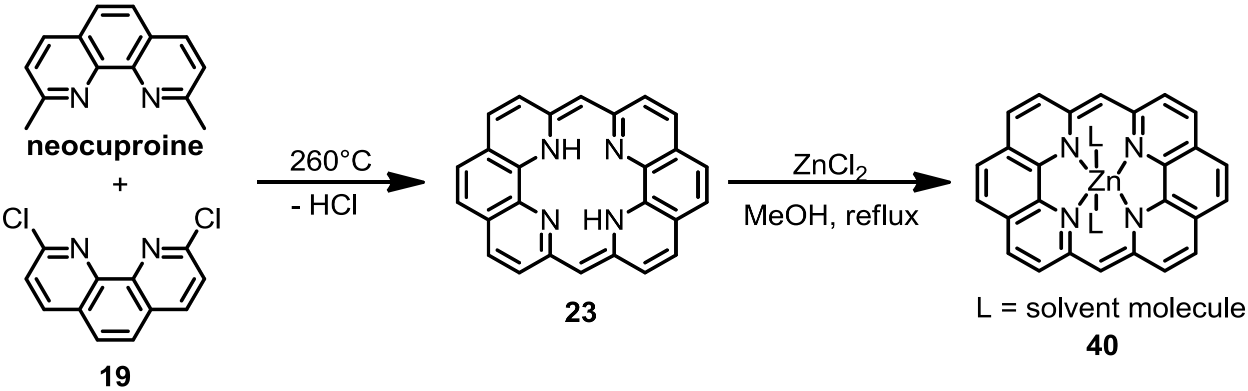

19 **23** **40**

Scheme 12 *Synthesis of carbon-bridged phenphyrin and its Zn complex*

*Aza-bridged pyrphyrin (**24**)*

Synthesis of *aza*-bridged pyrphyrin (**24**) was first reported by Ogawa et al. in a Zn templated ring closure reaction starting from 6,6'-dichloro-2,2'-bipyridine.[69] A 70 % yield of the corresponding zinc complex was reported, but isolation of the ligand was only possible under harsh acidic conditions (conc. H_2SO_4 and gaseous HCl, 50 % yield). In a newer procedure reported in literature, **24** was directly prepared by thermal reaction of 6,6'-dibromo-2,2'-bipyridine with NH_3.[71]

Compound **24** was synthesised in a 20 mL autoclave with 600 mg of **1** and a final NH_3 pressure of approximately 15 bar (280 °C, 2 d) to isolate **24** in 40 % yield as neutral ligand (Scheme 13). Compound **1** was not directly inserted into the metallic autoclave since the formation of complexes was observed in trial runs due to partial corrosion of the autoclave by NH_3. Hence a Teflon vessel was made with a removable lid containing a small opening in the middle for pressure equilibration. A lid was needed, because **1** slowly sublimed under the reaction conditions.

The reaction conditions were crucial to reduce side product formation (Scheme 13). NH_3 liquefies at around 8 bar at room temperature, thus exact pressure settings were difficult to achieve. Either a direct connection to the pressure bottle for the 8 bar of NH_3 or a reduction valve with an output of 2.0 bar were used. Depending on the applied NH_3 pressure, the autoclave was cooled down to 0°C (10 s) respectively -50°C (30 s) to obtain a reproducible amount of liquid NH_3 within the autoclave. If the NH_3 pressure was too high, a considerable amount of 6,6'-diamino-2,2'-bipyridine formed from excess NH_3 and the reaction stopped at the diamine intermediate. It is noteworthy that 6,6'-diamino-2,2'-bipyridine would be useable for the thermal formation of **24** by reaction with an equimolar amount of **1** according to literature.[71] If the NH_3 pressure or temperature was too low or the reaction time too short, partial conversion was observed. Higher temperatures alone did not favour formation of 6,6'-diamino-2,2'-bipyridine over macrocycle **24**. As long as the concentration of NH_3 was in the sweet spot, full heating could be applied to the autoclave. Manual reduction of the NH_3 pressure by occasionally opening the needle valve of the autoclave while the pressure was rising with increasing temperature did often proactively prohibit the formation of 6,6'-diamino-2,2'-bipyridine. Under ideal conditions quantitative conversion of **1** to **24** was observed by UPLC-MS. Investigations with different setups strongly suggested that a delayed and gradual heating was important for complete conversion. Fast heating lead mainly to formation of 6,6'-diamino-2,2'-bipyridine and 6'-bromo-[2,2'-bipyridin]-6-amine, most likely due to the faster sublimation rate of **1** and thus the larger reaction surface area of **1** with ammonia.

Isolation of the product was performed similar to reported procedure for *aza*-phenphyrin (**22**). The green salt was washed with 1 M HCl and filtered to remove major side-products. Compound **24** is partially soluble in 1 M HCl which lead to loses in this purification step. The black solid residue was then dissolved in concentrated HCl and **24** was precipitated as neutral ligand by pH titration with NaOH (pH 10). The yellow brown solid was highly insoluble in most organic solvents similar to the phenanthroline analogue, but high purity could be observed by NMR in d-TFA. The solubility of the crude **24** varied, most likely due to the formation of a mixture of the *mono*-hydrochloride and the *di*-hydrochloride salts. The 2*HCl salt might show lower solubility in conc. HCl and is better soluble in diluted acids. This was supported by the temporary strongly increased solubility of **24** in diluted acids after pre-treatment with concentrated HCl. Therefore, the dissolution was often performed by alternating conc. HCl and water wash until no further dissolution of the filter cake could be observed. With this procedure, any insoluble residues were removed from the product.

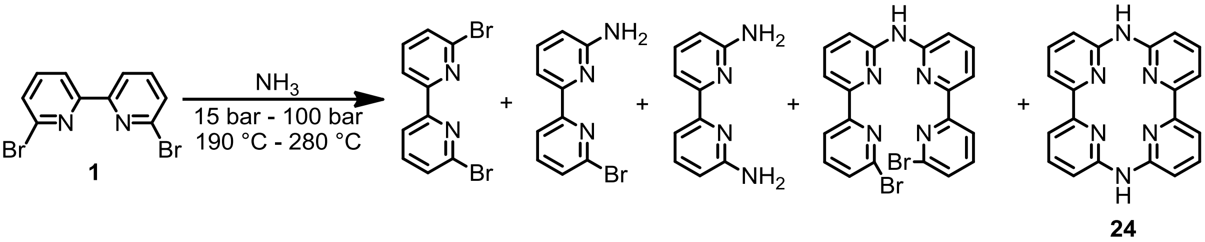

***Scheme 13**: Synthesis of aza-pyrphyrin (**24**)*

*Alkylation of aza-pyrphyrin (Me$_2$aza-pyrphyrin, **25**)*

Ogawa et al. reported the possibility of alkylation of the bridging nitrogen atoms under basic conditions.[69] Indeed, alkylation of **24** was achieved in good yields (80 %) by deprotonation of **24** with an excess (5 eq) of NaH (dry, 95 %) in dry DMF followed by addition of MeI. Deprotonation lead to a fast change in colour and a dark yellow to orange solution was obtained indicating an increase in conjugation due to the deprotonation of the N-H moieties. *Me$_2$aza*-pyrphyrin was readily accessible at room temperature in 1.5 h and showed quantitative conversion. Purification by removal of DMF under reduced pressure and extraction with DCM and water gave pure **25** as a saffron solid. No product was observed in the water phase due to the low solubility of **25**.

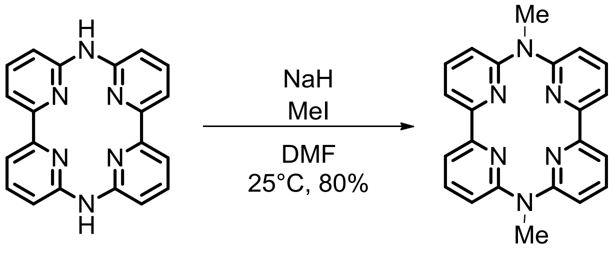

24 **25**

*Scheme 14: Synthesis of Me$_2$aza-pyrphyrin (**25**)*

Alkylation in a similar manner with sterically more demanding reagents showed no or only marginal conversion to the desired products under this reaction conditions.

2.1.3 Tetrapyridyl macrocycle (29)

The larger macrocyclic ligand framework (**29**) reported in literature, consisting of four pyridine subunits bridged by sp$_3$ carbons was synthesised to obtain a more flexible ligand for complexation.[86] MeCN was treated with LiH in dry benzene containing 5 % TMEDA to afford lithioacetonitrile which upon reaction with 6,6'-(1,3-dioxolane-2,2-diyl)bis(2-bromopyridine) (**27**) gave the tetrapyridine macrocycle **28** in 50 % yield. Compound **28** was either hydrolysed by HCl under retention of the dioxolane protective groups or oxidised by *m*-CPBA to form the diacetale **29**.[93] (Scheme 16)

2,6-dibromopyridine was mono-lithiated by an equimolar amount of *n*-BuLi at -78 °C in dry ether followed by the dropwise addition of diethyl carbonate to obtain **26** in 50 % yield after workup (Scheme 15).[94] The keto group of compound **26** was protected by acid catalysed reaction to form the corresponding dioxolane **27** (Scheme 15).[93] The ketone needed to be protected against basic reaction conditions for the synthesis of **28**.[93] The H_2O formed in the reaction was removed by a water separator to push the equilibrium towards the protected product **27**, according to the Le Chatelier principle.

Crude **27** was crystallised in CHCl3/ethanol to obtain pure product as white solid. Conversion of **26** to **27** could only be partially observed by UPLC-MS, since the acidic conditions reverse the protection and an equilibria of **26** and **27** is obtained.

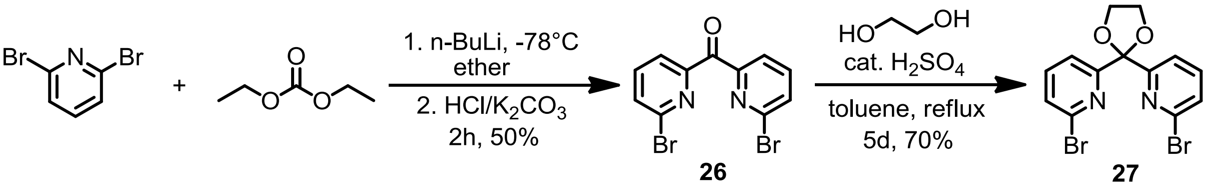

Scheme 15*: Synthesis of 6,6'-(1,3-dioxolane-2,2-diyl)bis(2-bromopyridine) (****27****)*

Compound **27, 28** and **29** were synthesised according to Newkome et al. (Scheme 16).[86] Lithioacetonitrile was prepared at 10 °C due to the melting point of benzene being 5.5 °C. Reaction with **27** was only observed at higher temperatures where a colour change from grey to orange occured. It is likely that macro-cyclisation was templated by Li+. The nitrile of ligand **28** could be cleaved under strongly acidic conditions and oxidised to its ketone form by SeO2. However, cleaner conversion was observed by oxidation over mCPBA. Interestingly, the dioxolane stayed intact and only a single product signal was observed in UPLC-MS, in contrast to the equilibria of protected **27** and the ketone **26**. The protection group seems to be substantially more robust to acidic conditions due to the steric hindrance in the macrocycle, thereby preventing elimination.

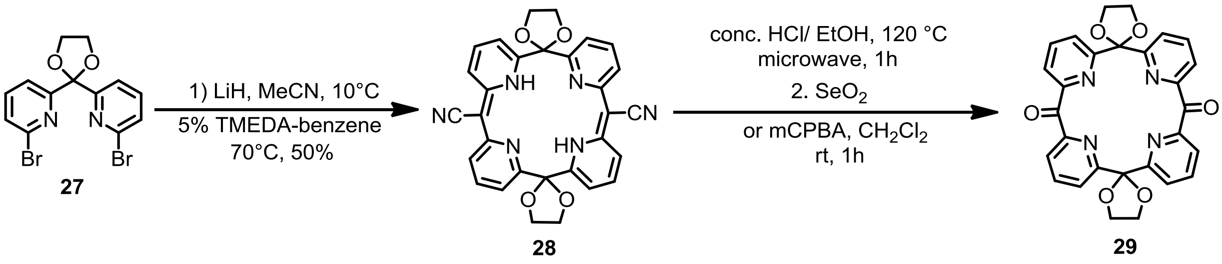

Scheme 16: Synthesis of sp3 carbon-bridged tetrapyridine ligand (**29**)

2.2 Syntheses of macrocyclic complexes

2.2.1 Metallopyrphyrin based complexes

*Metallopyrphyrin complex [$Co^{II}(OH_2)_2(pyr)$] (**41**)*

Complex **41** ([$Co^{II}(OH_2)_2(pyr)$]) could be synthesised by deprotonation of pyrphyrin with KO^{t}Bu or NaH in dry pyridine followed by addition of dry $Co^{II}(ac)_2$ (Scheme 17). Complex **41** was triturated in water at reflux for 12 h to exchange the axial pyridine ligands by water and obtain **41** as black solid in 60 % yield.

Filtration of deprotonated pyrphyrin under nitrogen atmosphere prior to addition of the metal salt was crucial to obtain defined **41**. The wine red pyrphyrin dissolves upon deprotonation in pyridine (sonicated at 70 °C for 2 h) to obtain an intense, luminous red solution. Filtration of the deprotonated pyrphyrin solution removed any insoluble side products and neutral pyrphyrin from the reaction mixture. The red solution turned instantly to black upon addition of dry $Co^{II}(ac)_2$ which implied a fast reaction. Dry $Co^{II}(ac)_2$ was prepared by thermal drying of commercially available $Co^{II}(ac)_2 \cdot 4\ H_2O$ at reduced pressure (120 °C, 1 mbar, 1 d, colour change from pale pink to red). Due to the low solubility of **41**, product formation could not be followed by in situ methods. Instead, the reaction was stirred at 100 °C for 4 h to ensure complete conversion. Pyridine was removed at reduced pressure and the black solid triturated in water at reflux to finally obtain the aqua complex **41** as black solid. Elemental analysis and IR supported the proposed composition. Thermogravimetric analysis (TGA) showed a mass reduction equal to the loss of the axial water ligands between 190 and 300 °C. Above 300 °C sublimation and decomposition was observed by TGA. Complex **41** was insoluble in almost all organic solvents. Compound **41** was readily soluble in pyridine and dark green 1 mM stock solutions could be prepared. Only marginal solubility in hot DMF or DMSO was found. Solubility in pyridine is most likely due to coordination of pyridine to the axial positions thereby reducing potential π- π stacking of **41**. While dissolution of **41** in pyridine gave a dark green solution, a red solution was obtained by dissolution in DMF or DMSO. Various crystallisation attempts were unsuccessful, no single crystals suitable for X-ray diffraction analysis could be obtained.

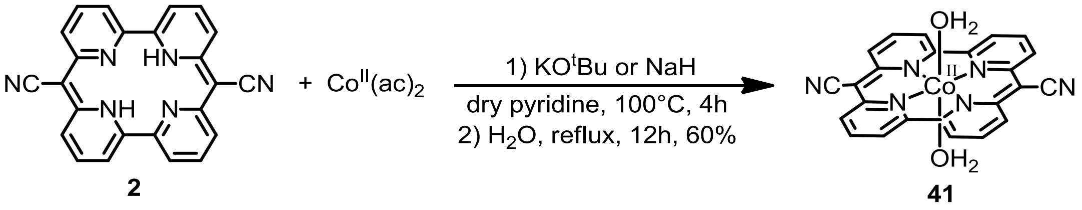

***Scheme 17**: Synthesis of underivatised [$Co^{II}(OH_2)_2(pyr)$] (**41**)*

Complexations of underivatised pyrphyrin with Zn, Mn, Ni, Co or Fe dihalides were performed according to literature (Scheme 18).[72,95] The purities of the resulting blackish solids were difficult to assess due to their low solubilities, indicating formation of neutral metal complexes with π-π stacking similar to porphyrins.[96] The intense IR band of the nitrile bonds did not show a significant shift and could therefore not be used to distinguish the products or the starting material from each other. The clear and strong CN band near the typical absorption band for the CN band of pyrphyrin highly suggested the absence of protonated CCN bands. Otherwise, one would expect a considerable lower absorption and a shift of the CN band to higher wave numbers. The oxidation of the obtained metal complexes and the exchange of the coordinating halogenides by less coordinating counter ions increased their solubility, but the low solubility of the complexes could only be partially improved. Derivatisation of the pyrphyrin backbone was therefore performed to increase the solubility of the resulting metal complexes.[95]

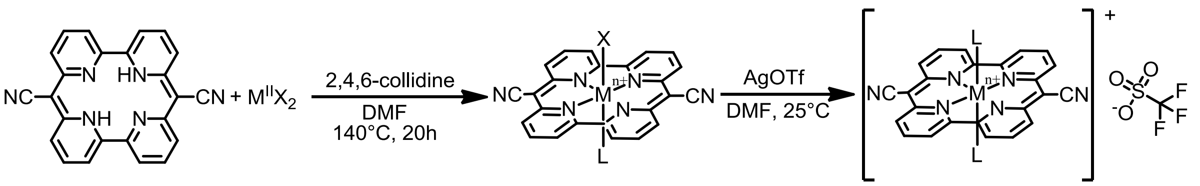

Scheme 18: *General synthesis of metallopyrphyrins where X = Cl, Br or L and L = solvent ligand*

Mono-alkylated metallopyrphyrin complexes

Complexation of *mono*-alkylated pyrphyrin with various 3d-metal salts could be achieved by deprotonation of the ligand with aqueous NaOH in MeOH, DMF or pyridine followed by reflux in presence of the metal source (Scheme 19).[40]

Fe, Co, Ni, Cu and Zn complexes could be obtained and isolated if their corresponding $M^{II}X_2$ salts were used as reagent. All reactions were generally performed under nitrogen atmosphere to specifically target the pure formation of the metallopyrphyrins in the oxidation state +2. Deprotonation of *mono*-alkylated pyrphyrin was necessary to obtain the metal complexes, otherwise the reaction did not reach complete conversion. In most cases, the reaction was stirred at reflux for approximately two days, since the conversion rate to the desired product was slow. Complexation of the red ligands gave rise to very dark red to dark green complexes.

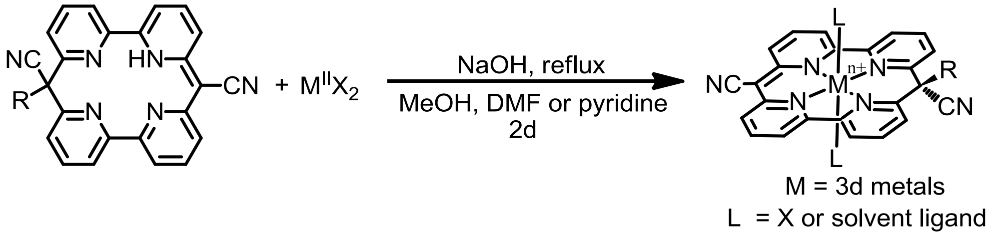

***Scheme 19**: General scheme for the synthesis of mono-alkylated pyrphyrin complexes*

The solubilities of the *mono*-alkylated complexes was mainly determined by the choice of the counter-ions. Hence, complexes [$\mathrm{Co^{II}Br(MeOH)(pyr\text{-}bu)}$] (**44**) and [$\mathrm{Co^{II}Br(MeOH)(pyr\text{-}MePEG)}$] (**42**) showed low solubility in water while complexes [$\mathrm{Co^{II}(THF)(pyr\text{-}bu)}$][$\mathrm{ClO_4}$] (**45**) and [$\mathrm{Co^{II}(H_2O)_2(pyr\text{-}MePEG)}$][$\mathrm{ClO_4}$] (**43**) were readily soluble in water (Figure 17). The complexes **45** and **43** were isolated by lyophilisation and therefore also considerably less dense than **44** and **42**. The increased surface area enhanced the dissolution rate. While **44** and **42** showed a very low solubility in water, stirring at 40 °C overnight or sonication for 1 h at 50 °C gave access to 1 mM aqueous stock solutions. This slow dissolution was attributed to slow exchange of axial bromide with water and the possible π-π stacking of the complexes.

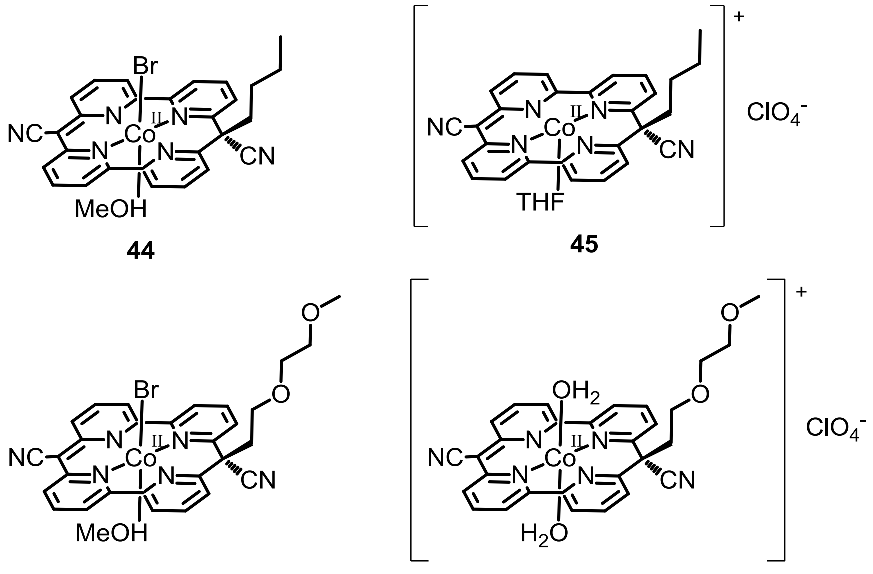
44 **45** **42** **43**

Figure 17**: Drawings of mono-alkyl metallopyrphyrins **42** - **45

$\mathrm{Co^{II}}$ (55 % yield, **45**), $\mathrm{Ni^{II}}$ (85 % yield, **46**), $\mathrm{Cu^{II}}$ (75 % yield, **47**) and $\mathrm{Fe^{II}}$ (85 % yield, **48**) *mono*-butyl-metallopyrphyrin perchlorates were synthesised (Scheme 20) and their physicochemical properties were compared (chapter 2.3). The complexation method showed high robustness for the synthesis of different 3d-metal complexes. The axial sites of the complexes were highly dependent on workup, such as choice of wash solvent. This is supported by the crystal structures of several complexes shown in chapter 2.3.1.

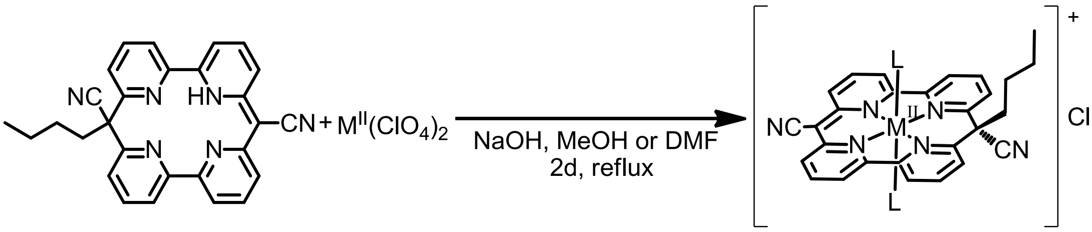

3

M = Co^{II} **45**, Ni^{II} **46**, Cu^{II} **47**, Fe^{II} **48**
L = solvent ligands or vacant site

***Scheme 20**: General synthesis for mono-butyl-pyrphyrin complexes **45**, **46**, **47** and **48**.*

Complex $[Zn^{II}(py)(pyr\text{-}MePEG)][TfO]$ (**49**) could be synthesised according to (Scheme 21) by using pyridine as solvent and $ZnCl_2$ as metal source. The halogenide was precipitated by addition of AgOTf under formation of the corresponding triflate complex. Generally, the precipitation of halogenides by AgOTf was often circumvented by directly using less coordinating metal salts, because remaining silver traces could have undesired influences in catalysis.

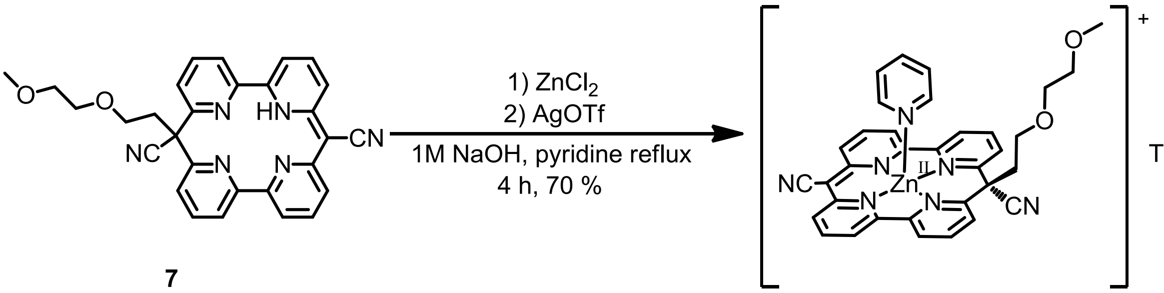

7

49

Scheme 21**: Synthesis of Zn mono-PEG-pyrphyrin **49

No product formation was observed with 4d and 5d metals under similar reaction conditions. The ligand framework might be too small to accommodate late transition metals.

Di-alkylated cobaltopyrphyrin complexes[3,40]

Complexation of the *di*-alkylated pyrphyrin ligand systems was performed by Evelyne Joliat in our group.[3] C*is*- (**4**) or *trans*-pyr-bu2 (**5**) were dissolved in EtOH or CH_3CN followed by addition of $Co^{II}Br_2$ or $Co^{II}(ClO_4)_2$ and were stirred for 2 h to 1 d at reflux. Dark red solids were obtained in 65 to 70 % yield (Scheme 22).[40] All complexes are well soluble in most solvents, including water. [$Co^{II}Br_2$(*cis*-pyr-bu2)] (**50**) and [$Co^{II}(OH_2)_2$(*cis*-pyr-bu2)][ClO_4]2 (**51**) showed higher solubilities than the corresponding [$Co^{II}Br_2$(*trans*-pyr-bu2)] (**52**) and [$Co^{II}(OH_2)_2$(*trans*-pyr-bu2)][ClO_4]2 (**53**) complexes. Probably, due to the stronger dipole moment of **50** and **51**.[40] No base was needed for complexation of **50** to **53** compared to pyrphyrin complexes or the mono-alkylated pyrphyrin complexes **41** to **49**. This further supports the anionic nature of pyrphyrin and *mono*-alkylated pyrphyrins. Induced by deprotonation at the bridging carbons and formation of a planar 2-pyridyl-2(1*H*)-pyridylideneacetonitrile moiety as discussed earlier.

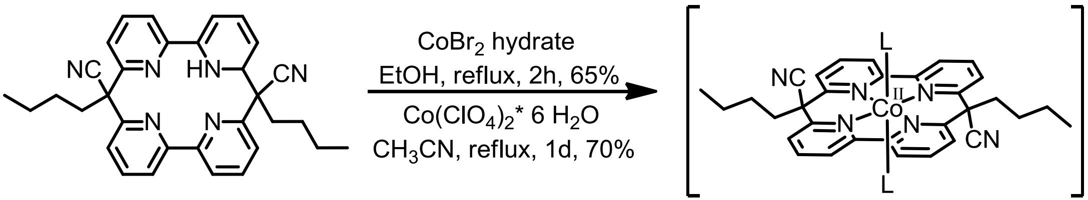

4, **5**

L = Br-, H_2O, ClO_4-

50 - 53

Scheme 22: *Synthesis of [$Co^{II}Br_2$(cis-pyr-bu2)] (**50**), [$Co^{II}(OH_2)_2$(cis-pyr-bu2)][ClO_4]2 (**51**), [$Co^{II}Br_2$(trans-pyr-bu2)] (**52**) and [$Co^{II}(OH_2)_2$(trans-pyr-bu2)][ClO_4]2 (**53**). Synthesised by E. Joliat in our group.*[3,40]

Complexes with other ligands

Ligand **28** (Figure 18) did not coordinate to 3d metals and larger metals such as Mo and Ru under usual complexation conditions. Apart from the larger space in ligand **28** compared to pyrphyrin derivatives, **28** exhibited a stronger twist in the pyridine orientation as seen in the reported crystal structure.[86] This might explain the unsuccessful complexation approaches, because the pre-orientation in pyrphyrin highly favours complexation.

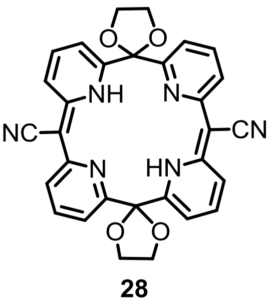

28

Figure 18: *Structure of tertapyridine macrocycle **28***

2.2.2 *Aza*- and *thia*-bridged macrocyclic complexes

Aza-bridged cobalt pyrphyrin complexes

Synthesis of [Co^{II}(ac)$_2$(*aza*-pyr)] (**55**) and [Co^{II}(ac)$_2$(*Me$_2$aza*-pyr)] (**56**) was performed by dissolution of *aza*-pyrphyrin (**8**) or *Me$_2$aza*-pyrphyrin (**9**) in hot MeOH followed by addition of Co^{II}(ac)$_2$ • 4 H_2O (Scheme 23).

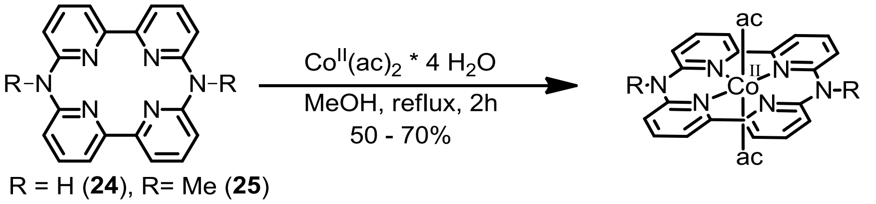

R = H (**24**), R= Me (**25**)

R = H (**55**), R= Me (**56**)

Scheme 23: *General synthesis of cobalt complexes from aza-pyrphyrin systems*

The orange to yellow suspension turned almost immediately into a dark brown suspension upon addition of the metal salt. HPLC-MS showed complete conversion to the desired product after 2 h stirring at reflux. Thus, showing a considerably faster reaction than for the carbon bridged pyrphyrin analogues. The weak colouration of the ligands **24** and **25** supported the hypothesis that they are present in their neutral form, containing protonated or methylated bridging nitrogen atoms respectively (Scheme 24). This further explains why no base was needed for complexation. Solubilities of **24** and **25** could be enhanced by addition of acid, but the complexation rate was reduced. Pure **55** and **56** could be obtained with substoichiometric amounts of Co^{II}(ac)$_2$ • 4 H_2O. Remaining starting material was then removed by dissolution of the crude brown solid in water, followed by filtration. With an excess of Co^{II}(ac)$_2$ • 4 H_2O, pure product could be isolated by purification over C_{18} silica. Addition of water and removal of methanol by reduced pressure followed by lyophilisation gave dark brown solids in 50 to 70 % yield. The proposed structure of Scheme 23 was supported by HR-ESI, where free acetate or coordinated acetate could be detected for **55** and **56**. Typical absorption bands for acetate were observed in the IR spectra.

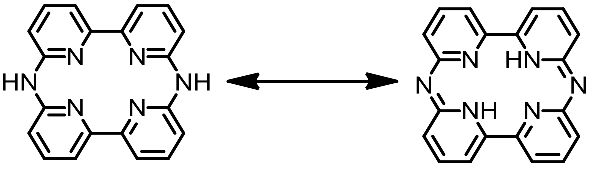

24 neutral form **24 conjugated form**

Scheme 24: *Tautomerisation of the neutral protonated form (left) and the deprotonated conjugated form (right) of aza-pyrphyrin (**24**)*

Aza- and thia-bridged metallophenphyrin complexes

Pure [$Co^{II}(TfO)_2$(*aza*-phyr)] (**57**, synthesised by Christian Bünzli in our group[76]) and [$Ni^{II}(ClO_4)_2$(*aza*-phyr)] (**58**) were obtained in 70 % yield by refluxing *aza*-phenphyrin (**22**, *aza*-phyr) and dry $Co^{II}[OTf]_2$ or $Ni^{II}(ClO_4)_2$ hexahydrate in MeCN for 2d (Scheme 25). Complexation with $Co^{II}Cl_2$ gave a complex with low solubility indicating similar solubility behaviour than pyrphyrin complexes (chapter 2.2.1). The $Co^{II}[OTf]_2$ was generated in situ by treating $Co^{II}[CO_3]$ with an equimolar amount of trifluoromethanesulfonic acid in CH_3CN at reflux. Dry $Co^{II}[OTf]_2$ was not essential, but arised from the treatment of $Co^{II}CO_3$ with TfOH followed by drying under reduced pressure. The structure of **57** was verified by elemental anaylsis and X-ray crystallography. Elemental analysis of complex **58** suggests a square planar configuration. This indicates that the ligand framework is non innocent and could act as neutral or anionic ligand.

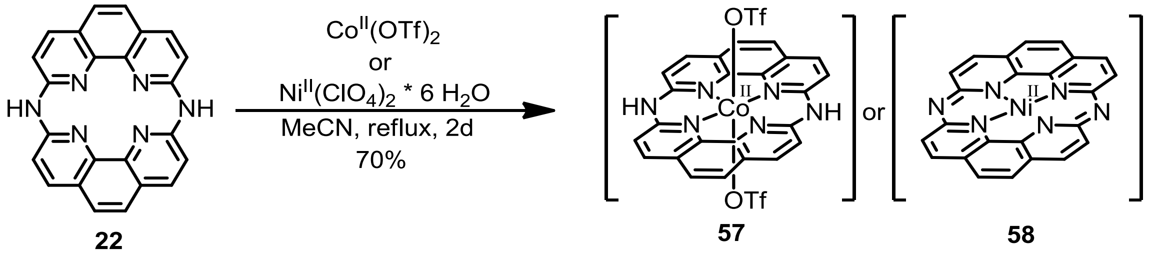

***Scheme 25**: Synthesis of [$Co^{II}(TfO)_2$(aza-phyr)] (**57**) and [$Ni^{II}(ClO_4)_2$(aza-phyr)] (**58**)*

Synthesis of the *thia*-bridged analogues was not successful (Scheme 26). Although complexation could be observed, the formed macrocycles were labile under normal atmosphere and the C-S-C bond was cleaved obtaining an open structured complex as seen in Figure 30.

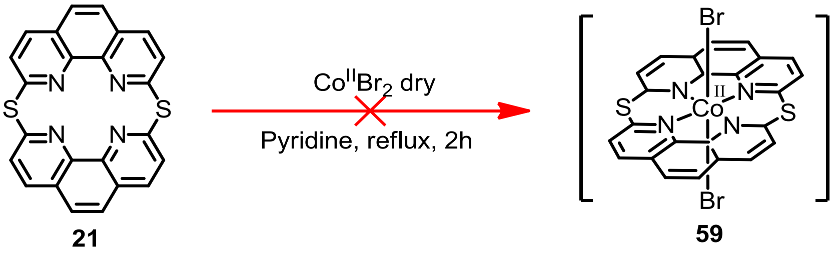

***Scheme 26**: Synthesis of [$Co^{II}Br_2$(thia-phyr)] (**59**)*

2.3 Physicochemical properties of metallocomplexes

2.3.1 Crystal structures

Comparison of cobaltopyrphyrin based complexes

X-ray crystallography of the Co^{II} complexes [Co^{II}Br(MeOH)(pyr-bu)] (**44**), [$Co^{II}Br_2$(*cis*-pyr-bu_2)] (**50**) and [$Co^{II}Br_2$(*trans*-pyr-bu_2)] (**52**) revealed Jahn-Teller distorted octahedral geometry in all cases (Figure 19). Complexes **50** and **52** were crystallised by E. Joliat in our group.[3,40] The bromides or MeOH in the case of **44** occupy the axial positions while the four pyridine moieties are in the equatorial plane. The coordinated bromides are very weakly bound showing unusually long Co-Br bonds, in-line with the proposed Jahn-Teller distortion along the axial direction. Bond lengths of 2.82 Å (Co1-Br1, **44**), 2.68 Å (Co1-Br1, **50**), 2.84 Å (Co1-Br2, **50**) and 2.77 Å (Co1-Br1, **52**) are observed. Since **52** is centrosymmetric, the Co1-Br1 bond length is equal to the Co1-Br2 bond length. The combined van der Waals radii of bromide and cobalt is 2.9 Å[97] and thus only slightly larger than the reported bond lengths for **44**, **50** and **52**. While the free ligands showed twisted or book-shaped bipyridine conformation (Figure 14 and Figure 16), especially for the *di*-alkylated pyrphyrins, upon coordination with Co^{II} near co-planarity is observed. The butyl chains in **44**, **50** and **52** are almost perpendicular to the pyrphyrin plane similar to the uncomplexed *mono*-butyl-pyrphyrin (pyr-bu, **3**), *cis*- and *trans*-dibutyl-pyrphyrin (*cis*-pyr-bu_2, **4** and *trans*-pyr-bu_2, **5**). The antiparallel nature of the nitrile moiety is slightly broken upon complexation due to strain induced by planarisation of the bipyridine backbone. Diastereomere formation where the nitrile group is pointing out of the pyrphyrin plane was not observed. Hence the nitriles allow partial electronic interaction with the pyrphyrin backbone which are in line with calculations.[40] This is also supported by the bond lengths of C22-C25 (**44**, **50**) and C11-C12 (**52**) which are in between 1.57 Å and 1.58 Å, thus significantly longer than a common single bond between two sp^3 hybridized carbon atoms (1.53 Å)[98]. The elongated carbon bonds of C22-C25 (**44**, **50**) and C11-C22 (**52**) are most likely caused by the high π-electron density at C22 and C11 causing a negative hyper conjugation by pushing electron density into the σ^* orbital which was also supported by calculations.[40]

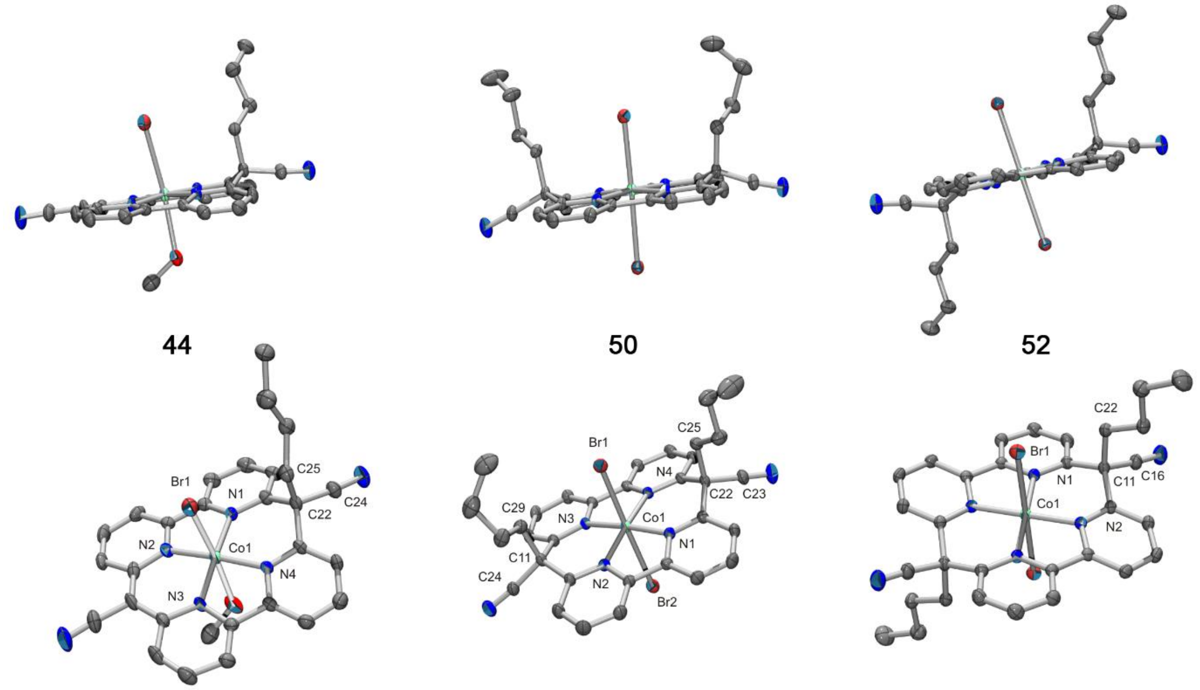

44 **50** **52**

***Figure 19**: ORTEP representation of **44**, **50** and **52** with selected labels. Thermal ellipsoids are at the 50 % probability level, hydrogen atoms are omitted for clarity. Selected bond lengths [Å]: **44**: Co1–Br1 2.8231(10), Co1–N1 1.925(4), Co1–N2 1.904(4), Co1–N3 1.897(4), Co1–N4 1.922(4), C22–C24 1.478(8), C22–C25 1.569(7); **50**: Co1–Br1 2.6791(4), Co1–Br2 2.8386(4), Co1–N1 1.9220(14), Co1–N2 1.9290(14), Co1–N3 1.9219(14), Co1–N4 1.9278(14), C22–C23 1.483(3), C22–C25 1.572(3), C11–C24 1.485(2), C11–C29 1.567(2); **52**: Co1–Br1 2.7741(2), Co1–N1 1.9250(13), Co1–N2 1.9248(13), C11–C16 1.484(2), C11–C12 1.577(2).[40] Grey: carbon, Blue: nitrogen, Red: bromine, Turquoise: cobalt*

A very interesting structure was observed for a derivative of $[Co^{II}(H_2O)_2(pyr\text{-}MePEG)][ClO_4]$ (**42**). Suitable single crystals for X-ray diffraction analysis could be obtained by slow vapour diffusion for $[Co_2^{II/III}O_2(py)_2(pyr\text{-}MePEG)_2][ClO_4]_2$ (**42a**) over one month (Figure 20). Formation of an oxygen or peroxo bridged dimer was observed for **42a** in contrast to the monomers for **44**, **50** and **52**. In most other cases, the structural flexibility of the PEG backbone prevented the formation of single crystals suitable for X-ray diffraction analysis. The pyrphyrin backbone and the nitriles showed almost identical behaviour as for **44**. The alkyl chain is almost perpendicular to the pyrphyrin plane with a bond length of 1.57 Å (C22-C25) which is in-line with the elongated bond lengths for C22-C25 (**42**, **50**) and C11-C12 (**52**) ranging from 1.57 Å to 1.58 Å respectively. In contrast to **44**, the alkyl chain in **42a** bends around the axial pyridine ligand. The O7-O7[1] bond length of **42a** (1.30 Å) is considerable longer than the double bond of oxygen (1.21 Å[99]) and shorter than the reported 1.49(1) Å[100] for the O-O bond length in hydrogen peroxide. A literature search for similar Co-O-O-Co bonds showed approximately 85 hits with a histogram of most O-O bonds between 1.4 and 1.5 Å, typical for a peroxide bond. Thus 1.30 Å measured for the O-O bond of **42a** is not in the range of a traditional cobalt peroxo complex. Very similar bond lengths (1.33 Å[101] and 1.30 Å[102]) were found in literature, and were both assigned to a superoxide bridge. The possibility to measure an NMR spectra and the symmetrical crystal structure did not support the formation of a superoxide. Maybe only the diamagnetic part of the structure is visible in the NMR and the crystal structure could be half occupied by Co^{II}/Co^{III}, thus showing the higher symmetry. The Co1-O7 bond length is 1.87 Å for **42a** and thus shorter than the reported 1.91 Å[101] and 1.92 Å[102] for the superoxide complexes. Formation of Co^{III} was not observed for other cobalt based pyrphyrin complexes even under oxidative conditions, such as oxygen or nitrosyl. Insufficient amounts of single crystals for **42a** were obtained and the crystal structure did not represent the batch material, otherwise a Raman IR could have given further corroboration to a superoxide.

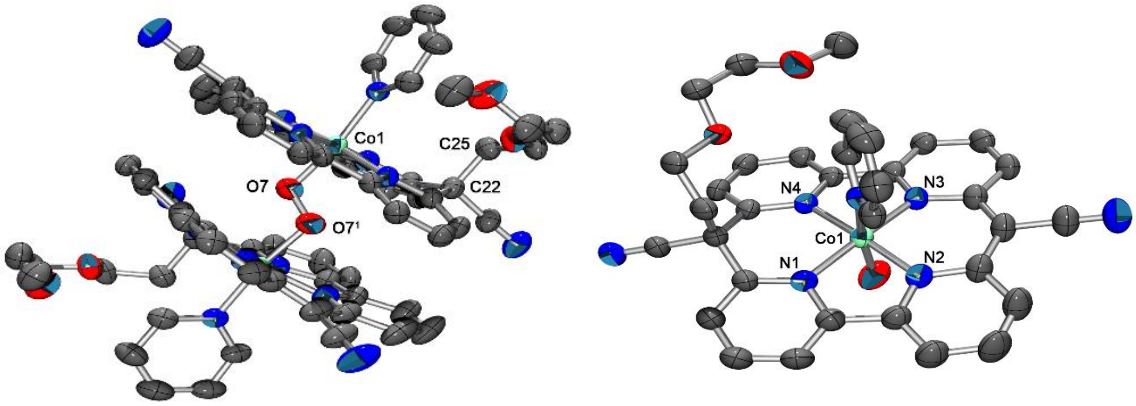

***Figure 20**: Side (left) and top (right) views ORTEP[2] of **42a**. Fragment growth to show two molecules in the side view to highlight the peroxo bridging. Thermal ellipsoids are at the 50 % probability level. Hydrogen atoms and ClO_4 counter ion are omitted for clarity. Selected bond lengths [Å]: **42a**: C22-C25 1.574(5), Co1-O7 1.873(3), O7-$O7^{1}$ 1.303(5); Grey: carbon, Blue: nitrogen, Red: oxygen, Turquoise: cobalt*

Crystals suitable for a rough X-ray analysis could be obtained for $[Co^{III}(py)_2(pyr\text{-}MePEG)][triflate]_2$ (**42b**), a further derivative of **42** that showed a Jahn-Teller distorted octahedral geometry, similar to **44**, **50** and **52** (Figure 21). Two complexes with four triflates as counterions were observed while a residual electron density might belong to an additional 0.33 HOTf as neutral co-crystallised molecules. Thus, a clear Co^{III} is observed in-line with the higher oxidation states of the cobalt atom in **42a**. One of the molecules in the asymmetric unit shows distinct planarity in the pyrphyrin plane as observed for all other metallopyrphyrin complexes. The other molecule shows a slightly twisted pyrphyrin backbone due to the near allocation of triflate anions to the molecule.

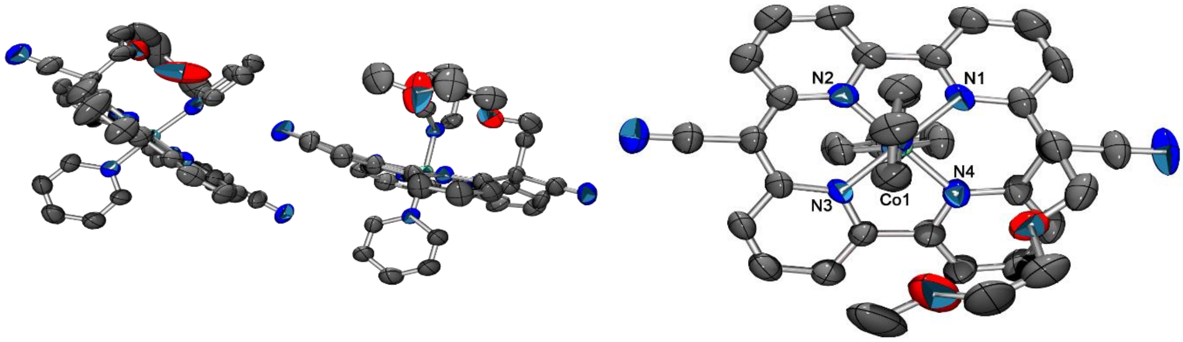

***Figure 21**: Side (left) and top (right) views ORTEP^{2} of **42b**. Thermal ellipsoids are at the 50 % probability level. Hydrogen atoms, triflate anions and co-crystallised protonated triflate are omitted for clarity. For clarity only one of the two molecules of the asymmetric unit is shown in the top view. Grey: carbon, Blue: nitrogen, Red: oxygen, Turquoise: cobalt*

Comparison of the distances of the cobalt and nitrogen bonds showed no significant difference between the $\mathrm{Co^{III}}$ and the $\mathrm{Co^{II}}$ complexes. One would assume a shorter bond length for the coordination of a $\mathrm{Co^{III}}$ to the nitrogen atoms due to the smaller ionic radius compared to a $\mathrm{Co^{II}}$ ion. However, the difference of only one electron seems to be too small to show a measureable difference. An interesting trend could be elucidated by looking at the different Co-N bond lengths. The Co1-N2 and Co1-N3 bond lengths of the planar 2-pyridyl-2(1*H*)-pyridylideneacetonitrile moiety of **42a**, **42b**$^{\mathbf{1}}$ and **44** are shorter than the corresponding Co1-N1 and Co1-N4 bond lengths of the non-planar butyl di(2-pyridyl)acetonitrile moiety. On the other hand, complex **50** and **52** show similar Co-N bond lengths. This supports the proposed anionic character of the *mono*-alkylated pyrphyrin for **42a/b** and **44** compared to the neutral character of *di*-alkylated pyrphyrin complexes **50** and **52**. The shorter bond lengths of cobalt to the planar 2-pyridyl-2(1*H*)-pyridylideneacetonitrile moiety suggests a local anionic character and thus a slight pull of the cobalt atom out of the pyrphyrin centre. Complex **42b**$^{\mathbf{2}}$ does show three short Co-N bond lengths and only one longer Co-N bond length. This discrepancy might arise from the interaction with the nearby triflate anions and the stronger twisted framework. This anionic character accompanied by a slight decentring of the metal atom could be observed for all mono-alkylated pyrphyrin complexes.

bond (Å)	**42a** (Co$^{II/III}$)	**44** (Co^{II})	**50** (Co^{II})	**52** (Co^{II})	**42b^{1}** (Co^{III})	**42b^{2}** (Co^{III})
N1-Co1	1.932(3)	1.925(4)	1.9220(14)	1.9250(13)	1.929(7)	1.928(6)
N2-Co1	1.902(3)	1.904(4)	1.9290(14)	1.9248(13)	1.902(7)	1.898(5)
N3-Co1	1.901(3)	1.897(4)	1.9219(14)		1.898(6)	1.891(6)
N4-Co1	1.925(3)	1.922(4)	1.9278(14)		1.919(5)	1.900(6)

***Table 2**: Distances of the pyridinic N1-Co1, N2-Co1, N3-Co1 and N4-Co1 bonds of the pyrphyrin plane for the complexes **42a**, **44**, **50**, **52** and **42b**. Only N1-Co1 and N2-Co1 bond lengths are shown for **52**, because of the high symmetry. Due to the presence of two molecules of **42b** in the asymmetric unit **42b^{1}** and **42b^{2}** are given.*

Other metal centres for pyrphyrin based complexes

Suitable crystals for X-ray diffraction analysis were obtained for [Cu^{II}(dioxane)*(*pyr-bu)][ClO$_4$] (**47a**), [Cu^{II}*(*pyr-bu)][ClO$_4$] (**47b**), [Ni^{II}*(*pyr-bu)][ClO$_4$] (**46**) and [Zn^{II}(py)(pyr-bu)][OTf] (**49**).

[Cu^{II}(dioxane)*(pyr-bu*)][ClO$_4$] (**47a**) does form a dioxane bridged dimer (Figure 22). The dioxane originated from the crystallisation process of **47**. Single crystals of [Cu^{II}*(pyr-bu*)][ClO$_4$] (**47b**) suitable for X-ray diffraction could be obtained by vapour diffusion of **47** in absence of dioxane (Figure 23).

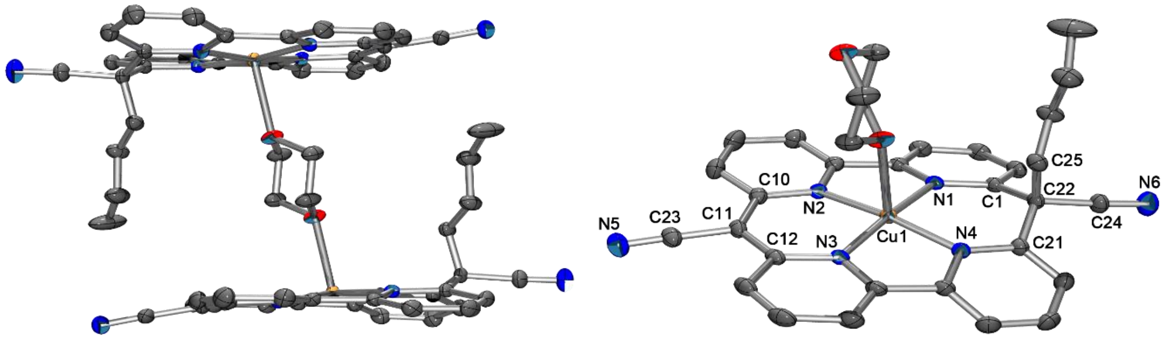

***Figure 22** Side (left) and top (right) views ORTEP^{2} of **47a**. Fragment growth to show two molecules in the side view to highlight the dioxane bridging. Thermal ellipsoids are at the 50 % probability level. Hydrogen atoms, ClO$_4^-$ counter ion and co-crystallised solvent molecules are omitted for clarity. Grey: carbon, Blue: nitrogen, Red: oxygen, Yellow: cupper*

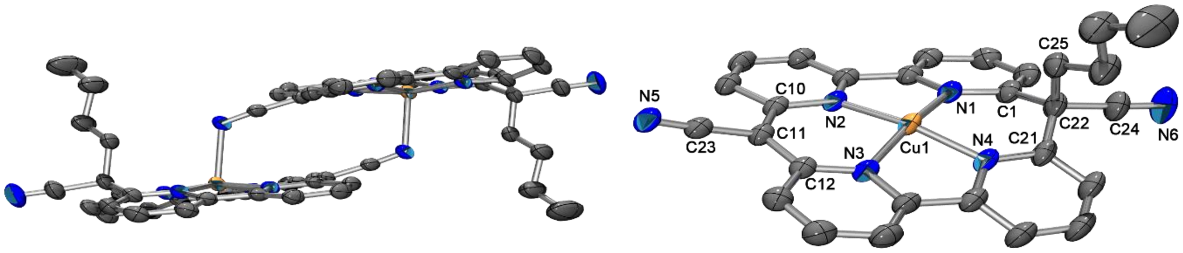

***Figure 23**: Side (left) and top (right) views ORTEP^{2} of **47b**. Fragment growth to show two molecules in the side view to highlight the Cu1-N5 bridging. Thermal ellipsoids are at the 50 % probability level. Hydrogen atoms and ClO$_4^-$ counter ion are omitted for clarity. Grey: carbon, Blue: nitrogen, Yellow: cupper*

While for all Co complexes a distorted octahedral geometry was observed, a Jahn-Teller distorted square pyramidal configuration was observed for **47a** and **47b**. Complex **47b** does from a dimer by coordination of the Cu1 atom with the N5^1 atom of a second **47b** molecule. 2.40 Å were measured for the Cu1-N5^1 distance, thus indicating a weak bond formation between the two atoms. The nitrile bond is slightly pushed out of plane by coordination to Cu1. Seen by the increased distances of C11 (0.32 Å), C23 (0.66 Å) and N5 (1.02 Å) of **47b** to the bipyridine plane (C5-C6-C16-C17) compared to **47a** (0.20 Å (C11), 0.53 Å (C23), 0.83 Å (N5)). Additionally, while complex **47a** has a dihedral angle of 178.1(2) Å for C11-C23-N5, **47b** is with 175.9(2) Å slightly deformed due to the coordination of N5^1 to Cu1. Complexes **47a** (C22-C25, 1.56 Å) and **47b** (C22-C25, 1.56 Å) show similar elongation of the C22-C25 bond compared to the corresponding Co complexes (1.57 Å to 1.58 Å). A bond length of 2.57 Å for the Cu1-O1 bond is relatively long, but in-line with Cu1-O1 distances of a neutral oxygen atom in similar fivefold coordinated Cu-complexes as shown in the histogram of the CSD database (Figure 24).[103]

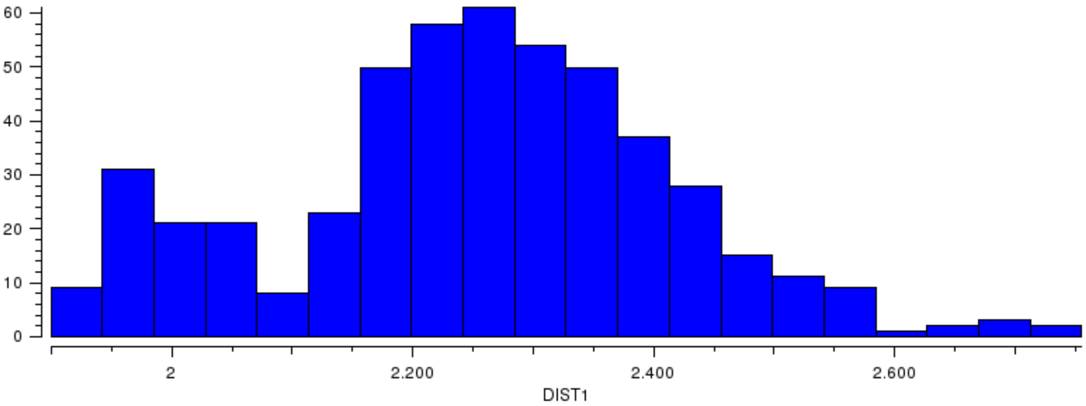

Figure 24: *Histogram of common Cu-O bond lengths of fivefold coordinated Cu complexes having four nitrogens and a neutral oxygen atom in the coordination sphere.*[103]

[Ni^{II}(pyr-bu)][ClO$_4$] (**46**) and [Cu^{II}(pyr-bu)][ClO$_4$] (**47b**) crystallised in the monoclinic space group 15 and showed very similar geometries. Both complexes formed a dimer over a N5^1-Cu1 or N5^1-Ni1 attraction, but the bond length is considerably shorter for **47b** (2.40 Å) than for complex **46** (3.17 Å). Due to this very weak interaction of the nitrile group with the nickel atom of another molecule only a small out of plane bending of the nitrile group was observed. 0.19 Å (C11), 0.33 Å (C23) and 0.47 Å (N5) distances to the C5-C6-C16-C17 plane were measured, thus showing even lower deformation than for **47a**. The measured distance for N5^1-Ni1 is too long for a bond formation and needs to be contemplated as an affinity rather than a bond. The elongated bond of C22-C25 (1.57 Å) fits well into the already observed range of the other complexes (1.56 Å to 1.58 Å).

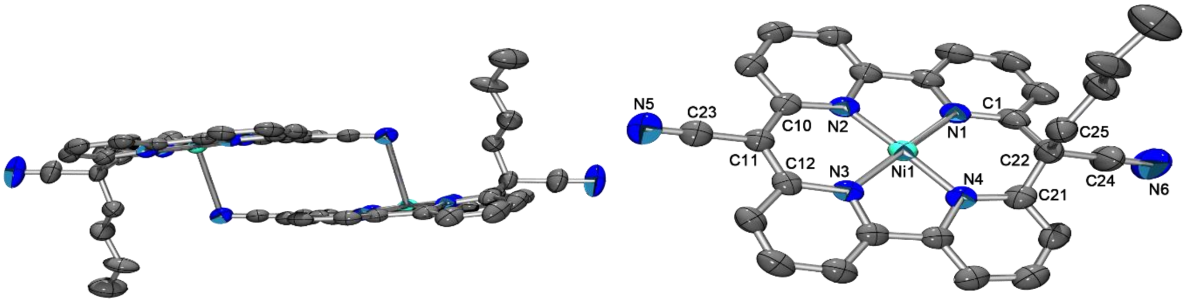

***Figure 25**: Side (left) and top (right) views ORTEP[2] of **46**. Fragment growth to show two molecules in the side view to highlight the Ni1-N5 bridging. Thermal ellipsoids are at the 50 % probability level. Hydrogen atoms and ClO_4 counter ion are omitted for clarity. Grey: carbon, Blue: nitrogen, Light Blue: nickel*

Crystal structure of [Zn^{II}(py)(pyr-MePEG)][OTf] (**49**) shows a strongly disordered square pyramidal geometry. Compared to the other crystal structures where the metal centre is in-line with the pyrphyrin plane, Zn1 is considerably shifted out of the pyrphyrin plane. The Zn1 atom sits 0.82 Å on top of the pyrphyrin plane (C5-C6-C16-C17) which by itself remains mostly planar. As seen for **42a/b** a bending of the MePEG residue around the axial pyridine ligand could be observed. Axial position of pyridine is considerably angled (N1-Zn1-N7, 107.6(1) °; N2-Zn1-N7, 102.4(1) °; N3-Zn1-N7, 105.1(1) °; N4-Zn1-N7, 110.7(1) °) due to the proximities of the PEG residue, the triflate anion and a co-crystallised pyridine. The Zn1 atom stays centred between the N1, N2, N3 and N4 atom of the pyrphyrin framework according to the measured distances of N1-Zn1 (2.08 Å), N2-Zn1 (2.02 Å), N3-Zn1 (2.02 Å) and N4-Zn1 (2.08 Å)).

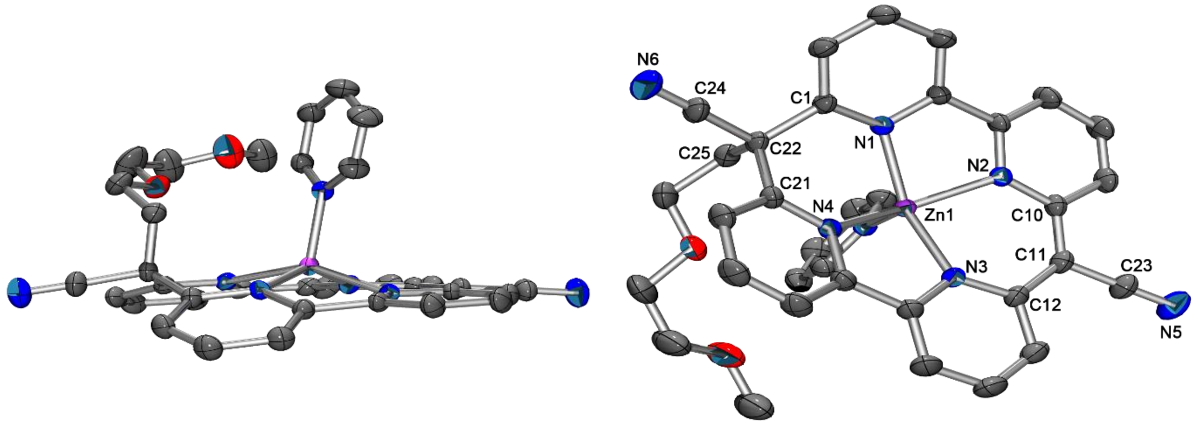

***Figure 26**: Side (left) and top (right) views ORTEP[2] of **49**. Thermal ellipsoids are at the 50 % probability level. Hydrogen atoms, triflate counter ion and co-crystallised solvent molecules are omitted for clarity. Grey: carbon, Blue: nitrogen, Red: oxygen, Violet: zinc*

No crystal structure could be obtained for [Co^{II}(H_2O)$_2$(pyr)] (**42**), but [Mn^{III}(H_2O)$_2$(pyr)][OTf] (**50**) was reported in literature and could be reproduced (Figure

27).[72,95] The Mn^{III} centre is completely in-line with the pyrphyrin plane and the nitrile group is exactly co-planar to the pyrphyrin plane which results from the higher symmetry of the orthorhombic structure of **50** compared to the derivatised pyrphyrin complexes. The two axial coordinated oxygen atoms refer to water ligands. All Co1-N bonds are equidistant.

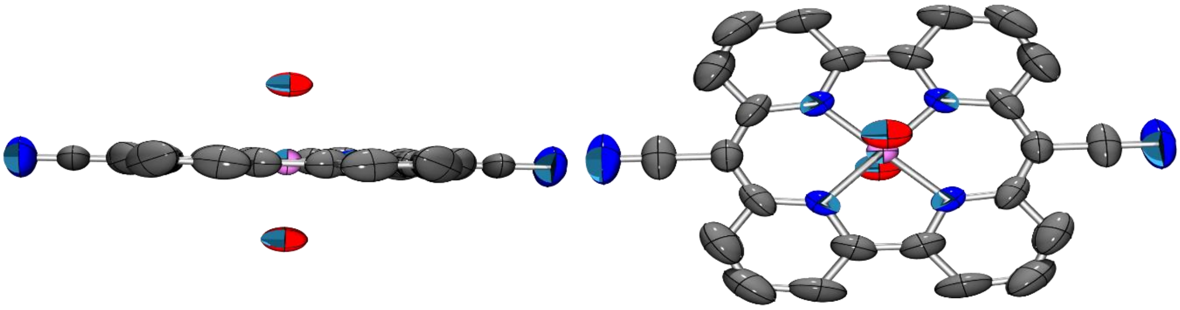

***Figure 27**: Side (left) and top (right) views ORTEP[2] of $[Mn^{III}(H_2O)_2(pyr)][OTf]$ (**50**). Thermal ellipsoids are at the 50 % probability level. Hydrogen atoms and triflate counter ion are omitted for clarity. Grey: carbon, Blue: nitrogen, Red: oxygen, Magenta: manganese*

Aza and thia-bridged cobaltophenphyrin complexes

A planar phenphyrin framework was observed for $[Co^{II}(OTf)_2$(*aza*-phyr)] (**57**) by X-ray diffraction of single crystals (Figure 28, by Christian Bünzli in our group).[76] The single crystal structure is in agreement with literature.[75] Distances of 1.87 Å (Co1-N1) and 1.87 Å (Co1-N2) were measured. The phenphyrin acts as neutral ligand forming a Co^{II} complex with two triflate counter-ions as axial ligands. Residual electron density of the hydrogen atoms can be observed directly by X-ray diffraction, supporting the hypothesis of *aza*-pyrphyrin being a neutral ligand framework.

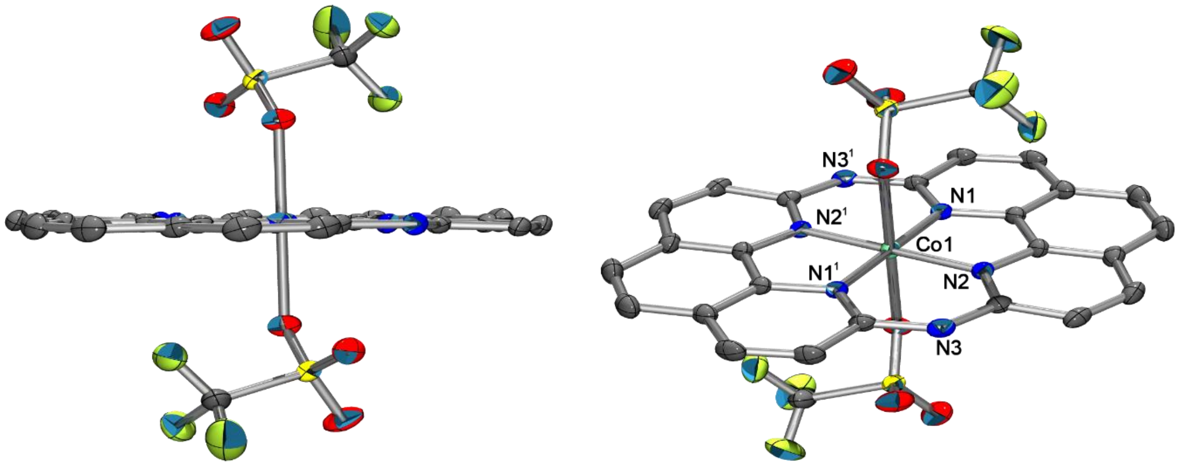

***Figure 28**: Side (left) and top (right) views ORTEP[2] of **57**. Thermal ellipsoids are at the 50 % probability level. Hydrogen atoms are omitted for clarity. Grey: carbon, Blue: nitrogen, Red: oxygen, Turquoise: cobalt, Yellow: sulphur, Vivid Green: Fluor[76]*

A Hydrogen bond formation (N3-H, 1.94 Å; N3-H-$O2^1$, 2.79 Å) could be observed between the hydrogen located at N3 and the oxygen atom of an axial triflate ligand belonging to another identical complex. As shown in Figure 29, complex **57** forms linear chains when the asymmetric unit was extended which corresponds with the formation of brown plate like crystals. 2.79 Å for a N-H-O hydrogen bridge can be considered as a mid to weak interaction.

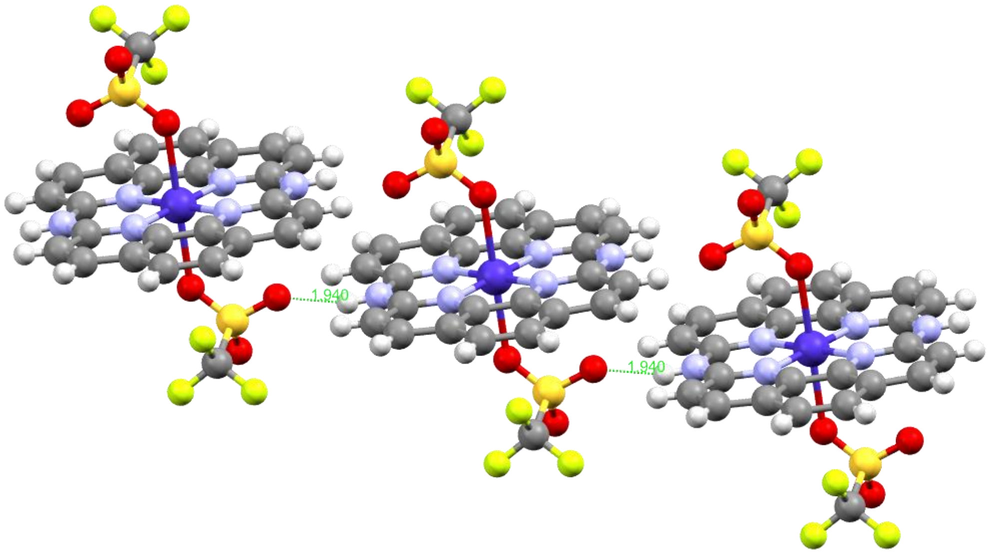

*Figure 29: Mercury[104,105] plot of the chain formation of **57** by formation of hydrogen bridges between the hydrogen atoms located at N3 and the oxygen of a neighbouring triflate anion. Grey: carbon, Light Blue: nitrogen, Red: oxygen, Violet: cobalt, Yellow: sulphur, Vivid Green: Fluor*

Formation of cobalt complexes with thia-bridged phenphyrin lead to ring opening of **21** under normal atmosphere. Suitable single crystals for X-ray diffraction of [Co^{II}(open-

thia-phyr)2] (**59**) showed the formation of a Co^{II} complex where two phenanthroline moieties of two **21** ligands coordinated with the metal centre under ring opening of the macrocycle **21** (Figure 30). Interestingly, no coordination of a second Co^{II} was observed. Complex **59** shows a clear instability of the formed complexes based on *thia*-bridged systems.

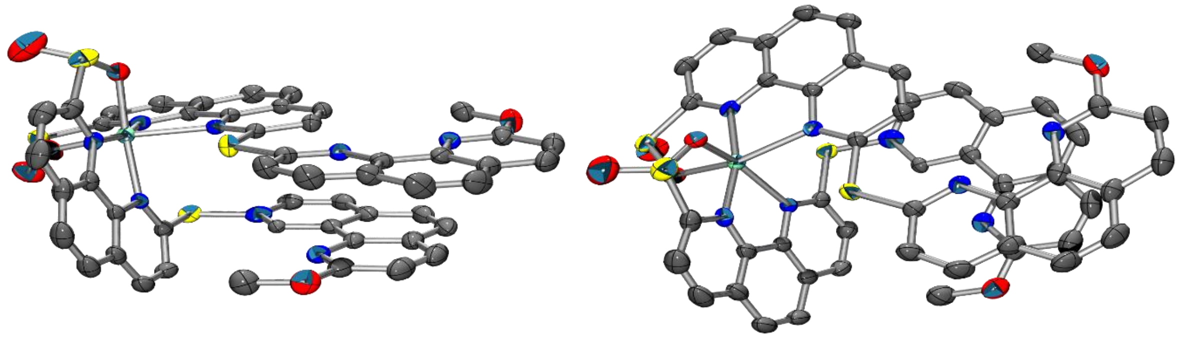

***Figure 30**: Side (left) and top (right) views ORTEP[2] of **59**. Thermal ellipsoids are at the 50 % probability level. Hydrogen atoms, triflate counter ion and co-crystallised solvent molecules are omitted for clarity. Grey: carbon, Blue: nitrogen, Red: oxygen, Turquoise: cobalt, Yellow: sulphur*

2.3.2 Spectroscopy

Aqueous UV/Vis spectroscopy comparison

The different *mono*-alkylated cobaltopyrphyrin complexes [Co^{II}(H$_2$O)$_2$(pyr-MePEG)][ClO$_4$] (**43**), [Co^{II}Br(MeOH)(pyr-bu)] (**44**) and [Co^{II}(THF)(pyr-bu)][ClO$_4$] (**45**) showed very similar UV/Vis absorption spectra as seen in Figure 31, thus indicating exchange of the axial ligands by water in all cases. Three UV/Vis absorption bands with maxima of 294 nm, 381 nm and 478 nm could be observed as well as a steady absorption increase for wave lengths below 275 nm, because of the absorption of the bipyridine backbone. The three absorption bands were specific for the mono-alkyl macrocycle and gave rise to the red aqueous solutions of the complexes. Extinction coefficients of 5’200 M^{-1} cm^{-1} (478 nm), 13’000 M^{-1} cm^{-1} (381 nm) and 22’600 M^{-1} cm^{-1} (294 nm) were observed for **43**, while **44** and **45** showed slightly lower absorption strength with 3’600 M^{-1} cm^{-1} (478 nm), 9’000 M^{-1} cm^{-1} (381 nm) and 18’700 M^{-1} cm^{-1} (294 nm) respectively. In all cases 1 mM stock solutions of the complexes in water could be obtained. The dissolution rate for **44** (overnight stirring or 1h sonicated at 50 °C) was drastically lower than for **43** and **45** (several minutes sonication at RT), due to slow bromide replacement by water.

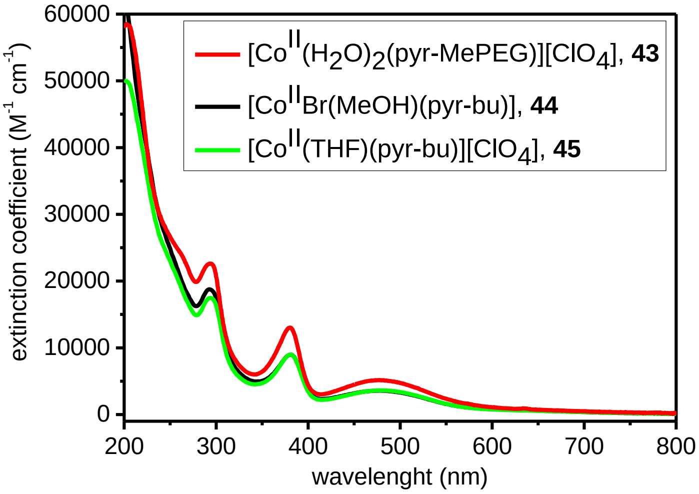

Figure 31*: UV/Vis spectra of [Co^{II}(H$_2$O)$_2$(pyr-MePEG)][ClO$_4$] (**43**), [Co^{II}Br(MeOH)(pyr-bu)] (**44**) and [Co^{II}(THF)(pyr-bu)][ClO$_4$] (**45**) in water.*

Mono-alkylated cobaltopyrphyrin complexes show a band at 381 nm which is absent in the double alkylated complexes [Co^{II}Br$_2$(*cis*-pyr-bu$_2$)] (**50**) and [Co^{II}Br$_2$(*trans*-pyr-bu$_2$)] (**52**) from E. Joliat[3] (Figure 32), thus the band was assigned to the 2-pyridiyl-2(1H)-pyridylideneacetonitrile unit present in **43**, **44** and **45**. The weak shoulder at ~650 nm was assigned to a cobalt based transition since this absorption is absent in the free ligand. This is in agreement with calculations for the similar Zn^{II} complex of ligand **3**.[106] The UV/Vis spectra of complexes **50** and **52** in water are similar as shown in Figure 32. An increased absorption characteristic of the 2,2’-bipyridine at 299 nm compared to **44** indicated weaker conjugation of the planar 2,2’-bipyridine moieties as already observed in the free ligands.[68] The weak absorptions at 450 nm (~2500 M^{-1} cm^{-1}) are absent in the free ligands due to their bent structure.[3] Based on calculations, these transitions were assigned to cobalt-based transitions.[40] It was verified that the axial ligands of *mono*- and *di*-alkylated cobaltopyrphyrins are in fact exchanged by aqua ligands upon dissolution of the complexes in water. No change in the UV/Vis absorption spectra was visible when the perchlorate analogues [Co^{II}(THF)(pyr-bu)][ClO$_4$] (**45**), [Co^{II}(OH$_2$)$_2$(*cis*-pyr-bu$_2$)][ClO$_4$]$_2$ (**51**) and [Co^{II}(OH$_2$)$_2$(*trans*-pyr-bu$_2$)][ClO$_4$]$_2$ (**53**) were compared to [Co^{II}Br(MeOH)(pyr-bu)] (**44**), [Co^{II}Br$_2$(*cis*-pyr-bu$_2$)] (**50**) and [Co^{II}Br$_2$(*trans*-pyr-bu$_2$)] (**52**) respectively. Addition of up to 14 equivalent KBr to the perchlorate complexes did not change the UV/Vis spectra, but addition of saturated KBr solution lead to precipitation of the bromide complex from the perchlorate analogue as shown by E. Joliat in our group.[40]

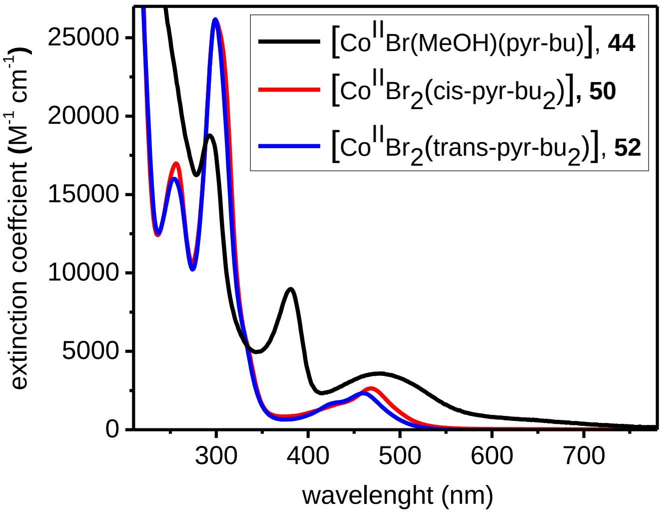

Figure 32*: UV/Vis of [Co^{II}Br(MeOH)(pyr-bu)] (**44**), [Co^{II}Br$_2$(*cis*-pyr-bu$_2$)] (**50**) and [Co^{II}Br$_2$(*trans*-pyr-bu$_2$)] (**52**) in water. UV/Vis of **50** and **52** was measured by E. Joliat in our group.[3,40]*

Diluted aqueous solutions of **44** and **50** were stable under irradiation for over 20 days. However, aqueous solutions of **52** were even unstable in the dark and under argon.[40] This was attributed to a bond break between the bridging carbon and the alkyl chain (C11-C22, Figure 19). This hypothesis was strongly supported by the emerging of a band at 380 nm in the UV/Vis spectrum, which is indicative for the formation of a 2-pyridyl-2(1H)-pyridylideneacetonitrile moiety. ESI-MS confirmed the loss of a butyl chain. No decomposition of **50** was observed, likely due to a smaller ring strain for the *cis*-*di*-butylpyrphyrin (**4**) as compared to the *trans*-*di*-butylpyrphyrin (**5**).[40,68] This highlights the strong stability of the macrocyclic ligand framework even under light irradiation, which is not self-evident due to the intrinsic light absorptions of this systems.[5]

The influence of the metal centre on the UV/Vis spectra of complexes with *mono*-butylpyrphyrin (**3**) or *mono*-methyl-polyethylene-glycolpyrphyrin (**7**) as ligand are shown in Figure 33. All complexes should be present in the aqueous form, meaning their axial ligands are exchanged by water. Complex [Co^{II}(THF)(pyr-bu)][ClO$_4$] (**45**), [Ni^{II}(pyr-bu)][ClO$_4$] (**46**) and [Cu^{II}(MeOH)(pyr-bu)][ClO$_4$] (**47**) were synthesised under the same conditions while a slightly different synthesis was used for [Zn^{II}(py)(pyr-MePEG)][OTf] (**49**). All complexes show the characteristic bands between 400 - 600 nm and 330 – 400 nm for *mono*-alkylated pyrphyrins. The metal centre has a strong influence on the position of the absorptions maxima as well as on the ratio between the different bands. A smaller difference of the absorption maximum of the 2-pyridyl-2(1H)-pyridylideneacetonitrile moiety at around 375 nm was observed for the different complexes. The nickel complex **46** has an additional band with an absorptions maximum at 335 nm which seems absent in the other complexes. A defined absorption maximum can be seen for the nickel (**46**) and zinc (**49**) complex at 256 nm. The tailing in the UV/Vis spectra of **45** and **47** at approximately 250 nm supports the presence of this transition in complex **45** and **47**. This correlates with the UV/Vis spectra for **50** and **52** which both show a clear band with an absorption maxima at 256 nm. The zinc complex **49** shows formation of a five coordinate square-pyramid, as evidenced in the crystal structure (Figure 20). The zinc is considerably pulled out of the pyrphyrin plane and thus one would assume a larger difference in the UV/Vis spectra compared to **45**, **46** and **47** where the metal centres are in-plane with the pyrphyrin framework. This is indeed the case as seen in Figure 33. Complex **49** shows a stronger absorption below 300 nm which might be attributed to the higher bipyridine character of **49** due to the decentred zinc atom, thus reducing the electron delocalisation. Complex **49** and the zinc complex of underivatised pyrphyrin exhibited low fluorescence when irradiated with ultraviolet light.

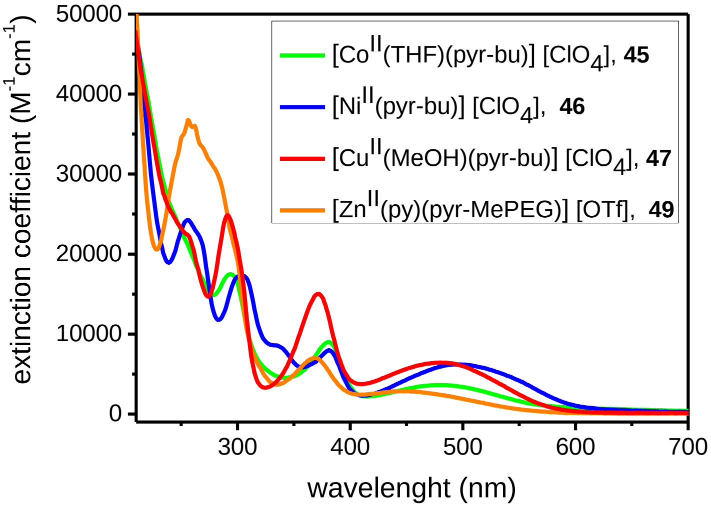

***Figure 33**: UV/Vis spectra of [Co^{II}(THF)(pyr-bu)][ClO$_4$] (**45**), [Ni^{II}(pyr-bu)][ClO$_4$] (**46**), [Cu^{II}(MeOH)(pyr-bu)][ClO$_4$] (**47**) and [Zn^{II}(py)(pyr-MePEG)][OTf] (**49**)*

The *aza*-bridged cobalt complexes **55** and **56** have a complex UV/Vis spectra with various absorption maxima (Figure 34). A yellow colour was observed upon dissolution in water. Thus, it is not surprising that the characteristic band between 400 and 600 nm of carbon bridged mono-alkylated pyrphyrin is missing. Instead, a structured absorption between 338 and 435 nm was observed which is similar to the absorption in **45** attributed to the absorption of the 2-pyridyl-2(1H)-pyridylideneacetonitrile moiety. It is unlikely that the complexes **55** and **56** are deprotonated at the N-H under this conditions (see chapter 2.3.3). The absorption band is most likely formed by planarisation of the ligand frameworks of *aza*-pyrphyrin (**24**) and *Me$_2$aza*-pyrphyrin (**25**) upon complexation which increases conjugation over the cobalt metal centres. Ligands **55** and **56** could not be measured in water or organic liquids, due to solubility issues. Dissolution was only possible in acidified water.

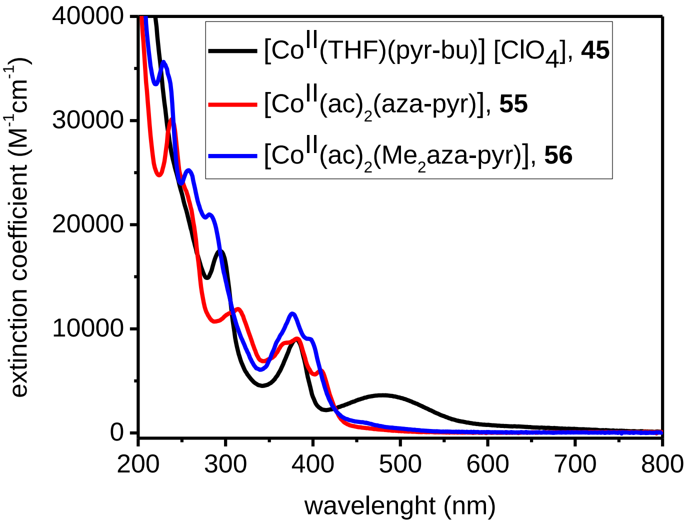

***Figure 34**: UV/Vis of **45**, **55** and **56** in water*

Aza-phenphyrin complexes **57** (Co) and **58** (Ni) are not water soluble and need to be dissolved in acidified water or organic solvents such as DMF. They can therefore not be directly compared to the other complexes.

IR spectroscopy of nitrile containing complexes

All IR measurements were performed in solid state with a Golden Gate FT-IR. Highly characteristic and intense CN valence vibration modes at 2181(5) cm^{-1} and 2182(5) cm^{-1} were observed for the macrocycles **2** (pyrphyrin) and **3** (*mono*-butylpyrphyrin) respectively (Table 3). Literature predicts weak absorption bands between 2260 and 2200 cm^{-1} for nitriles while exhibiting increased absorptions for stronger conjugated systems, accompanied by a shift to lower wavenumbers.[79] Thus, bands are at the low edge for a CN stretch frequency. Together with the unusual intense absorption, this highlights the formation of the conjugated pyrphyrin (Scheme 2).

Comparison of the different IR stretching frequencies for nitriles of the complexes gave further insight into their electronic configuration. Bands below 2200 cm^{-1} belong to the conjugated 2-pyridyl-2(1H)-pyridylideneacetonitrile moiety, whereas absorptions above 2200 cm^{-1} indicate an interrupted conjugation at the α-carbon of the nitrile due to alkylation. Nitrile stretching frequencies of the nitriles next to the interrupted conjugation do not appear in *mono*-alkylated pyrphyrins due to an overlap with the far stronger absorption of the conjugated 2-pyridyl-2(1H)-pyridylideneacetonitrile unit. Weak bands are found for **50** and **52** at 2241(5) (calc. 2249) and 2244(5) (calc. 2252) cm^{-1} respectively.[40] Table 3 shows that the nitrile bands shift to lower energies upon complexation by cobalt, giving strong bands from 2169 to 2176 cm^{-1}. This is in line with calculations as well as with the proposed conjugation increase upon complexation.[40]

Choosing different metals for complexation leads to detectable differences in the nitrile vibration modes. Nitrile bands of the nickel complex **46** (2191(5) cm^{-1}) and the iron complex **48** (2184(5) cm^{-1}) exhibit a shift to higher energies as compared to the cobalt complexes while the band for zinc complex **49** (2164(5) cm^{-1}) is shifted to lower energies. The band for cupper complex **47** is in a similar range as the corresponding cobalt complexes. The increase in the stretching frequency of complex **46**, compared to the free ligands **2** and **3**, indicates a reduction of the electron donation upon complexation. A possible interpretation is that the formation of a square planar 16 electron complex (Figure 25) might reduce the internal electron pushing onto the nitrile bond supported by the very low interaction of the cyanide with other nickel atoms. On the other hand, complex **49** has the lowest measured stretch frequency for the nitrile bond which is not supported simply by structural interpretation of Figure 26. Complex **49** shows by far the lowest planarity of all complexes and the zinc atom sits on top of the pyrphyrin plane which should in theory reduce the ability of electron delocalisation due to a smaller overlap of the orbitals. However, the Zn^{II} complex is in theory a 20 electron complex and might therefore push the electrons more into the direction of the CN bond and thus leading to weakening of the nitrile bond.

	2	**3**	**41**	**43**	**44**	**45**	**46**	**47**	**48**	**49**
CN band (cm^{-1})	2181(5)	2182(5)	2169(5)	2171(5)	2171(5)	2176(5)	2191(5)	2176(5)	2184(5)	2164(5)

Table 3: *CN valence vibration modes for pyrphyrin (**2**) and mono-butylpyrphyrin (**3**) as well as complexes [Co^{II}(OH$_2$)$_2$(pyr)] (**41**), [Co^{II}(H$_2$O)$_2$(pyr-MePEG)][ClO$_4$] (**43**), [Co^{II}Br(MeOH)(pyr-bu)] (**44**), [Co^{II}(THF)(pyr-bu)][ClO$_4$] (**45**), [Ni^{II}(pyr-bu)][ClO$_4$] (**46**), [Cu^{II}(MeOH)(pyr-bu)][ClO$_4$] (**47**) and [Fe^{II}(H$_2$O)$_2$(pyr-bu)][ClO$_4$] (**48**) and [Zn^{II}(py)(pyr-MePEG)][OTf] (**49**) by Golden Gate FT-IR. (blue = ligands, green = cobalt complexes)*

Magnetic properties (SQUID, EPR)

The synthesis of paramagnetic Co^{II} complexes opened to the question about their spin state. Therefore, SQUID magnetometry of [Co^{II}(OH$_2$)$_2$(pyr)] (**41**), [Co^{II}Br(MeOH)(pyr-bu)] (**44**), [Co^{II}Br$_2$(*cis*-pyr-bu$_2$)] (**50**) and [Co^{II}Br$_2$(*trans*-pyr-bu$_2$)] (**52**) was performed. Such d^7 system show often high spin states. Figure 35 displays the recorded magnetic data, which generally obeys the Curie-Weiss law.

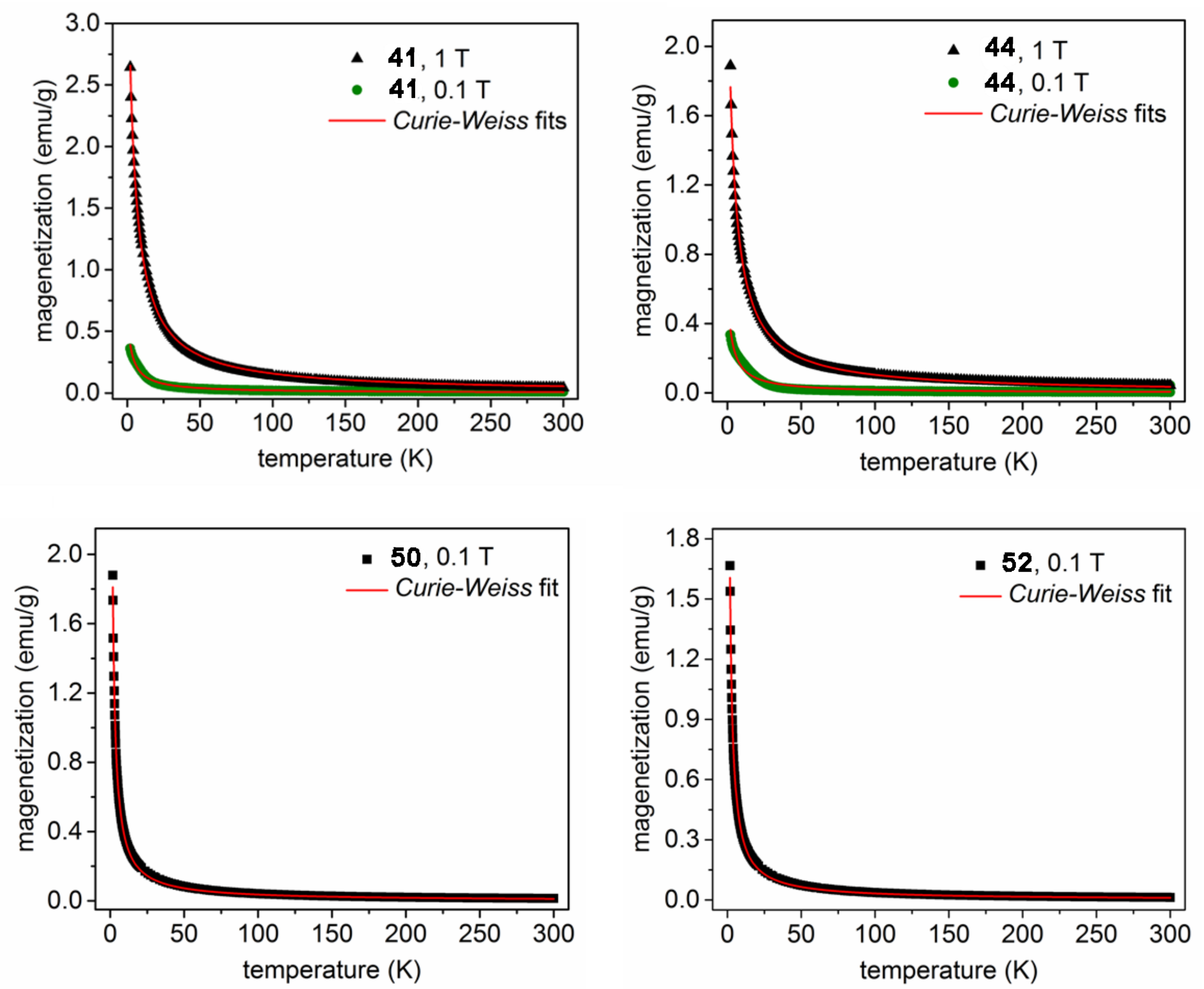

***Figure 35**: SQUID magnetometry for* [$Co^{II}(OH_2)_2$(pyr)] (**41**), [Co^{II}Br(MeOH)(pyr-bu)] (**44**), [$Co^{II}Br_2$(*cis*-pyr-bu_2)] (**50**) and [$Co^{II}Br_2$(*trans*-pyr-bu_2)] (**52**) *over a temperature range of 300 K at magnetic fields of 0.1 and 1.0 T and corresponding Curie-Weiss fit.*

The effective magnetic moments of complex **50** (4.61 μ_B/Co) and **52** (4.42 μ_B/Co) are in good agreement with the values of other d^7 high spin Co^{II} complexes reported in literature (Table 4).[107-110] Thus, **50** and **52** are high spin Co^{II} d^7 complexes. On the other hand, complex **41** and **44** do not precisely follow the Curie-Weiss law at 0.1 T and at low temperature. Complex **41** showed a considerably lower μ_{eff} of 1.85 μ_B/Co while complex **44** was somewhere in between with a μ_{eff} of 3.52 μ_B/Co. The low μ_{eff} of complex **41** corresponds to the formation of a low-spin Co^{II} complex, in good agreement with other low-spin Co^{II} complexes.[111,112] The high Curie temperatures of -3.93 K (**42**) and -3.48 K (**33**) as well as the deviation from the Curie-Weiss behaviour at low temperatures supports the presence of non-trivial electron-electron interactions. This indicates that complex **41** and **44** both exhibit non-negligible antiferromagnetic interactions between the magnetic centres. Most likely due to π-π stacking which leads to shielding of the external magnetic field. Complex **44** is special in regard of the in-between value. This makes perfectly sense when one considers the increasing conjugation, anionic character of the ligands and the π-π stacking from **50** and **52** to **44** and finally to **41**, which should give rise to a stronger shielding. One could also assume an interaction by coordination of the nitrile residue with another Co^{II} metal centre as indicated in the crystal structure of **46** (Figure 25) and **47b** (Figure 23) instead of π-π stacking, but support for this theory could not be obtained from the crystal structures.[108,109] Furthermore, it is surprising that the low- and intermediate-spin compound **41** and **44** could by no means be oxidised to the corresponding Co^{III} complexes.

Compound	Θ (K)	μ_{eff} (μ_B)
41	-3.93	1.85
44	-3.48	3.52
50	-0.25	4.61
52	-0.28	4.42

***Table 4**: Summary of the magnetic properties of complexes [$Co^{II}(OH_2)_2$(pyr)] (**41**), [Co^{II}Br(MeOH)(pyr-bu)] (**44**), [$Co^{II}Br_2$(*cis*-pyr-bu_2)] (**50**) and [$Co^{II}Br_2$(*trans*-pyr-bu_2)] (**52**). Curie-temperatures Θ in Kelvin and magnetic moments μ_{eff} per cobalt centre.*

EPR (Figure 36) of complexes **41** and **44** support the conclusions of the SQUID results by showing a typical low spin Co^{II} complex for **41**. EPR of the pure solids lead to loss of the fine-coupling due to the reduced lifetime of the spin states by strong spin-spin interactions which originated from the proximity of the molecules. In the solid state spectra, both complexes look similar but the high spin complex **44** tends to show broader signals. This is in-line with expectations, since the lifetime of the spin states is lower in low spin complexes and one would assume sharper signals for **41** regarding the lower μ_{eff}.

To observe the hyper-fine couplings, the experiments were performed in a diluted state. Complex **41** and **44** were dissolved in a mixture of 3,5-lutidine and pyridine (2:1) to obtain a dark red solution for **41** and a dark green solution for **44**. By observation of similar complexes one can assume that all axial ligands are exchanged by pyridine after dissolution. The solutions were frozen in liquid nitrogen. Addition of 3,5-lutidine was important due to the formation of a glass upon freezing which would not happen in pure pyridine. The hyperfine-coupling of complex **44** shows a ^{57}Co octet (^{57}Co: I = 7/2) with relative large coupling constants as well as partial quintet split-up of the components. Likely, only two of the four inner nitrogen atoms (^{14}N: I = 1) are showing couplings to the cobalt atom which would support the presence of two different Co-N bond types as seen by the slightly different bond lengths in the crystal structure (Table 2). If the cobalt couples with all inner nitrogen atoms, a nonet split-up would be expected explaining the higher signal split in **41**. This suggests that mainly the nitrogen atoms of the 2-pyridyl-2(1H)-pyridylideneacetonitrile moiety are coupling with Co, thus giving a low spin value for complex **41**. Complex **44** has one such moiety and in the high spin complexes **50** and **52** no such groups are present. Supported by the crystal structures in Table 2, showing increased Co-N bond lengths for **50** and **52** compared to the Co-N bond lengths belonging to the 2-pyridyl-2(1H)-pyridylideneacetonitrile moiety. Complex **44** shows a relatively similar spectra in solid or glass. The positive and negative signal components of complex **44** at 2900 G and 3300 G are approximately in the same range which would indicate small structural changes upon dissolution. Thus, the change in Co-Br bond length might be of low significance for the geometric configuration. The Co-Br bond length is with 2.8231(10) Å very long and its influence is most likely small. On the other hand, complex **41** shows a change of the downfield component from 2900 G in solid to 3350 G in glass which is surprising as one would expect only marginal structural changes from exchanging the aqua ligands by pyridine. Possibly, the different spin density in solid and liquid might be the origin of this phenomenon. The higher spin density in solid might have a bigger impact on the low spin complex **41** compared to complex **44** which already exhibits a considerable higher spin density and is less influenced by the additional intermolecular interactions in solid. It could also be that the exchange of the axial ligands by pyridine changes the electronics stronger than assumed.[113]

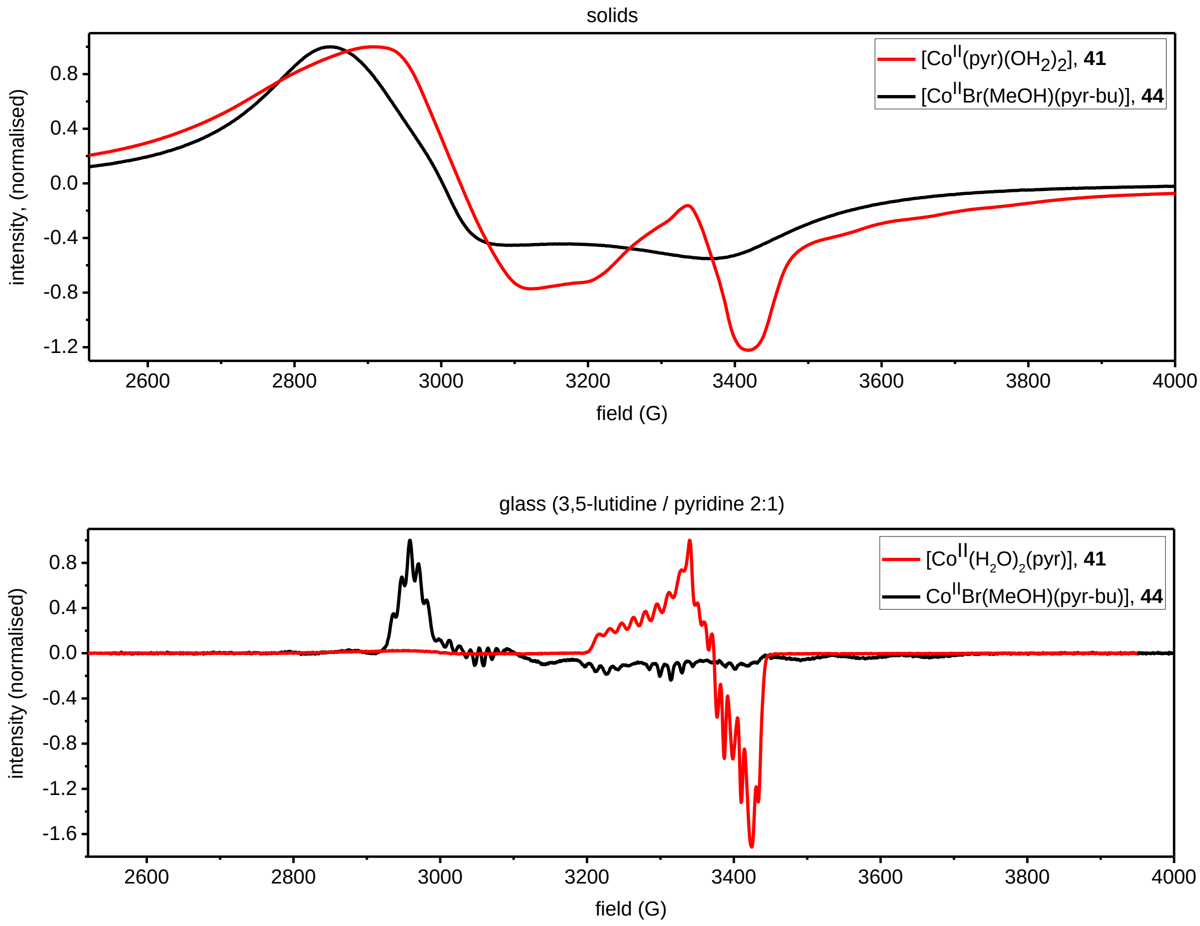

***Figure 36**: EPR spectra of complex [Co^{II}(OH_2)$_2$(pyr)] (**41**) and [Co^{II}Br(MeOH)(pyr-bu)] (**44**) measured as solid (top) and in a glass of a frozen 2:1 mixture of 3,5-lutidine/pyridine (bottom).*

*NMR Spectroscopy of **42b** and **46***

Complexes [Co^{III}(py)$_2$(pyr-MePEG)][triflate]$_2$ (**42b**) and [Ni^{II}(pyr-bu)][ClO$_4$] (**46**) are diamagnetic and could be analysed by NMR spectroscopy.

^{1}H NMR, ^{1}H COSY, ^{13}C NMR, ^{13}C DEPT and C-H spectra and correlations of **42** in d$_6$-dmso gave a highly complex signal distribution. The possibility to measure sharp signals for complex **42b** clearly confirmed the formation of a Co^{III} species. Signals could be attributed to the product and pyridine could be identified as axial ligand. Additional signals are present which might arise from a partial ligand exchange in d$_6$-dmso. Thus, further support was obtained for the crystal structure **42a** and **42b** (Figure 20) showing formation of Co^{III} complexes.

^{1}H NMR, ^{13}C NMR, 1D NOE and C,H-correlation of complex **46** in d-CH$_3$CN were performed and all peaks could be assigned to the proposed structure (Figure 37). Crystal structure of complex **46** shows formation of a square planar Ni^{II} complex (Figure 25). Elemental analysis (C, H, N) also supported the co-crystallisation of ½ THF and ½ MeOH per molecule. This is further supported by the presence of a strongly disordered electron density attributed to a partial occupancy of THF which was treated by SQUEEZE. The 1H NMR spectrum does not support this hypothesis since no significant undefined signals could be observed. A big solvent signal of CH$_3$CN could be observed at ~1.95 ppm as well as traces of water (~2.12 ppm) and acetone (2.15 ppm).[114] Satellite signals were also observed for acetonitrile. An expected deshielding is observed for all signals upon complexation of ligand **3** which is especially pronounced for the bipyridine signals.

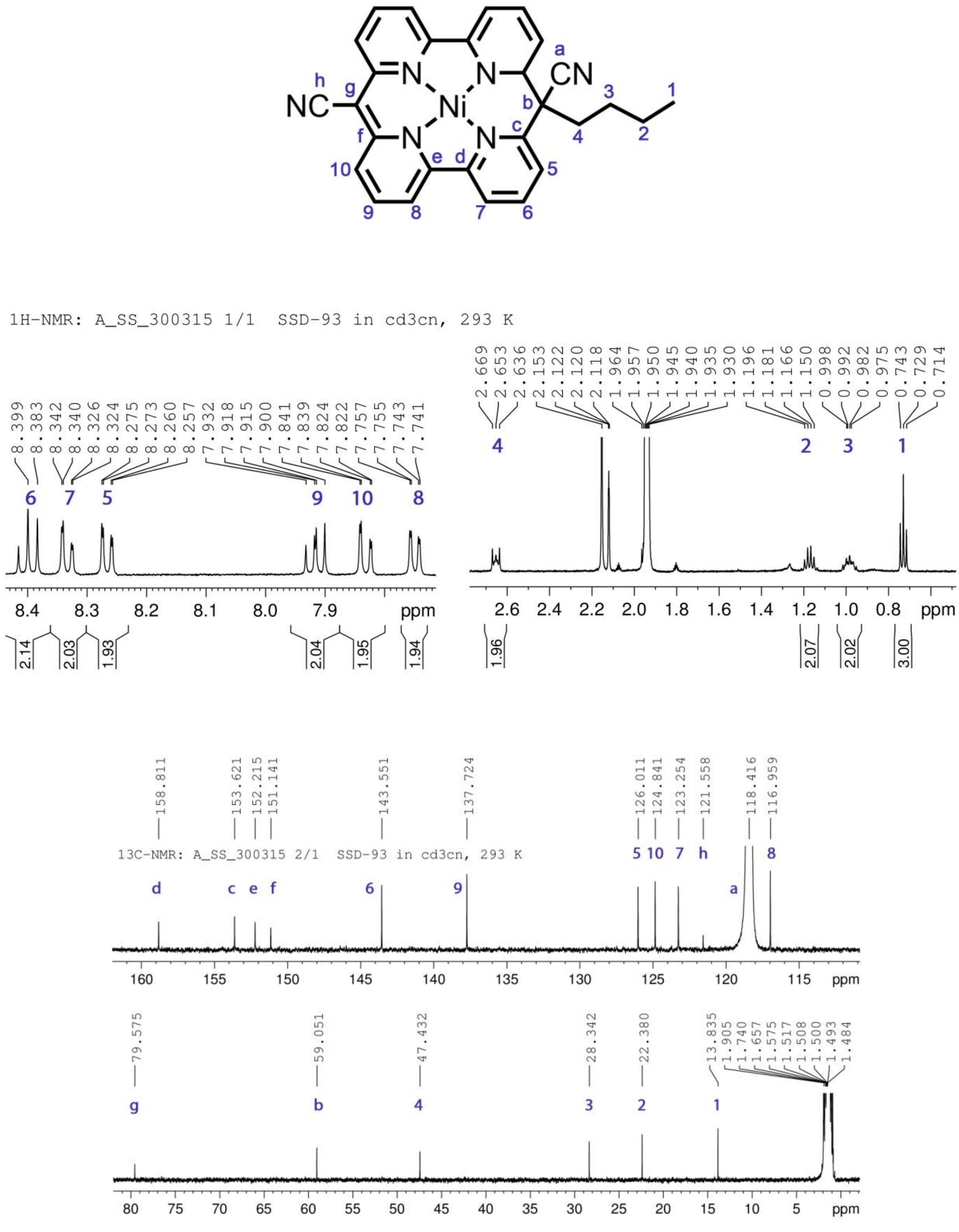

Figure 37: *^{1}H and ^{13}C NMR (middle and bottom) of [Ni^{II}(pyr-bu)][ClO$_4$] (**46**) in CH$_3$CN along with the corresponding assignment (top).*

2.3.3 UV/Vis titration of *aza*-bridged cobalt pyrphyrin complexes (55, 56)

The pK_a values of the complexes [$Co^{II}(ac)_2$(*aza*-pyr)] (**55**) and [$Co^{II}(ac)_2$(*Me_2aza*-pyr)] (**56**) were determined by UV/Vis spectroscopy at different pH values (pH 2-12). Global fitting of the absorption change at suitable wavelengths for each individual pK_a value or a multiple pK_a value fit were performed. This measurements were performed in 40 mM Britton Robinson Buffer (BRB) to imitate the conditions of the electrochemical benchmarking (see chapter 2.5.2) and to allow for a relatively linear pH increase from pH 2 to 12 upon addition of a NaOH solution.[115] pH titration of complex **55** showed absorption changes over the full pH range (Figure 38). The deprotonation processes of **55** could almost completely be reversed by titration with acid. This is surprising, because other poly-pyridyl cobalt catalysts often showed formation of cobalt oxide and concomitant decomplexation.

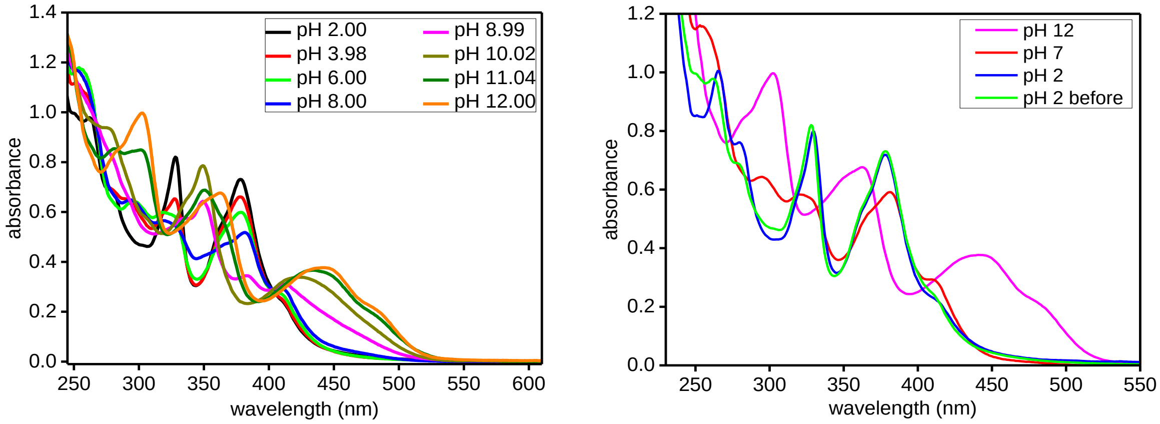

Figure 38: *UV/Vis spectra of the pH dependent titration (left) and the corresponding back titration (right) of a 50 µM solution of [$Co^{II}(ac)_2$(aza-pyr)] (**55**) in 40 mM BRB solution where "pH 2 before" refers to the initial UV/Vis spectrum.*

Two clear pK_a values at 8.70(2) and 10.74(3) could be identified for **55** with at least another pK_a value between pH 2 and 6 (Figure 39). A closer look at the UV/Vis change between pH 2 and 6 shows the formation of a brief isosbestic point and the possible presence of two pK_a values (3.0(1), 4.60(5)). The change of the absorption is distributed over a very broad pH range which supports the assignment of two pK_a values. Thus, up to four pK_a values were observed for complex **55**. It is possible that further pK_a's are present, but do not show a change in absorption and can therefore not be identified with UV/Vis spectroscopy. Purely potentiometric methods are needed to verify the exact pK_a values and more importantly, the number of protons associated with each pK_a. (Figure 39)

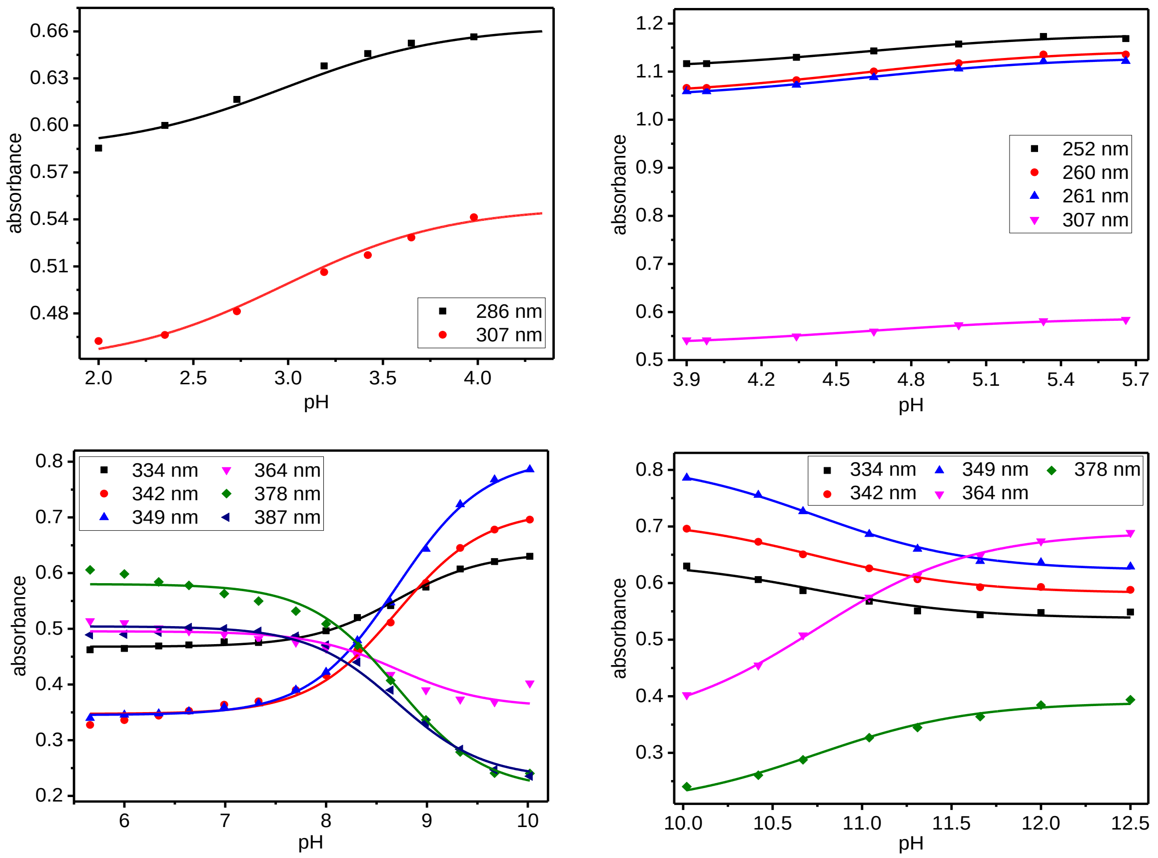

Figure 39: Global fits of pH dependent UV/Vis titration curves for [Co^{II}(ac)$_2$(aza-pyr)] (**55**) at selected wavelengths.

The N-methylated complex **56** showed almost no UV/Vis absorption change upon titration (Figure 40). This is surprising given the large changes in the corresponding non-methylated complex **55** (Figure 38). The titration is partially reversible, however some specific tailing bands (395 nm and 455 nm) are considerably less pronounced after retritration.

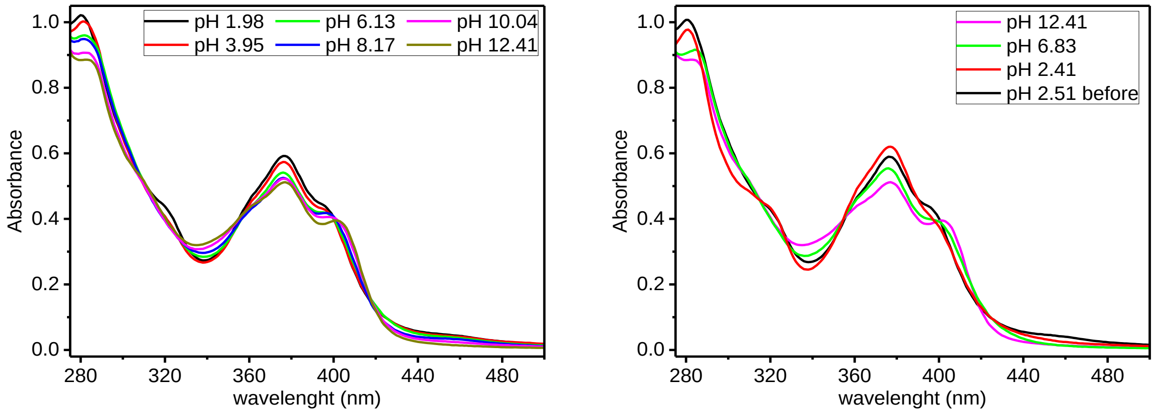

***Figure 40**: UV/Vis spectra of the pH dependent titration (left) and the corresponding back titration (right) of a 50 µM solution of [Co^{II}(ac)$_2$(Me$_2$aza-pyr)] (**56**) in 40 mM BRB solution where "pH 2.51 before" refers to the initial UV/Vis spectrum.*

Despite the low absorption change, two pK$_a$ values for **56** at 4.6(1) and 10.2(2) can be assigned (Figure 41). Three pK$_a$ values could be reasonably global fitted over the complete pH range (2.5(1), 5.1(1) and 9.9(1)) (Figure 41). The error on the pK$_a$ value is considerably larger than indicated by the mathematical error as seen in the discrepancy between the isolated global fitting and the global fitting across the total pH range. This uncertainty mainly arises from the low absorption change. Thus, complex **56** has at least two pK$_a$ values at 4.5(5) and 10.2(5) with the possibility of a third pK$_a$ value at 2.5(5) and additional UV/Vis silent pK$_a$s.

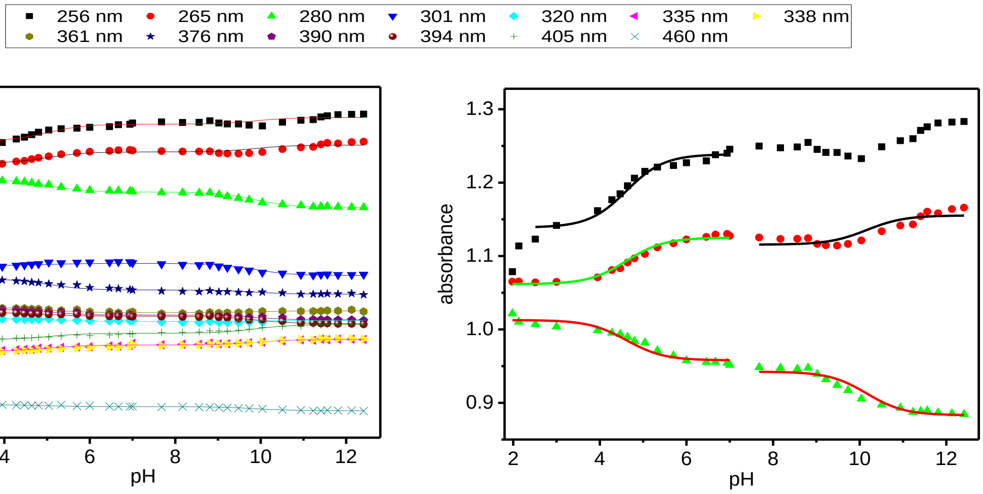

***Figure 41**: Global fits of pH dependent UV/Vis titration curves for [Co^{II}(ac)$_2$(Me$_2$aza-pyr)] (**56**) at selected wavelengths.*

Table 5 shows an overview of the pK$_a$ values for complex **55** and **56** as well as reference complexes **80** and **81**. For interpretation, all complexes are thought to have exchanged their non pyridinic ligands by water in solution as observed in the UV/Vis spectra and in the ^{81}Br NMR spectrum for complex **80**.[83] It is hypothesised that **80** and **81** show an irreversible deprotonation of water and formation of a hydroxo cobalt complex.[83] The pK$_a$ values at 9.46(3) and 9.8(1) are therefore assigned to the formation of the hydroxo species. Complex **80** and **81** showed no UV/Vis change between pH 2.0 and the pK$_a$^{4} value. No additional pK$_a$ values were expected, since deprotonation of the ligand framework is not possible at higher pH. Deprotonation at the tertiary alcohol of the ligands would be possible, but corresponding pK$_a$ values of simple alcohols or even phenols show pK$_a$ values of ~30 or ~20 respectively.[116,117] Complexation might considerably reduce the pK$_a$ values, but certainly not below the pK$_a$ value of the Co^{III}-OH formation. It is reasonable to assume that the pK$_a$^{4} or pK$_a$^{3} values of **55** (8.70(2), 10.74(3)) and **56** (10.2(6)) also belong to the deprotonation of an axial water molecule (Figure 42).

	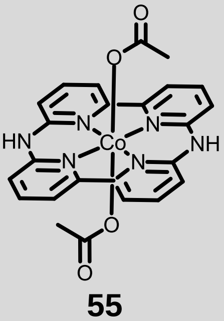 **55**	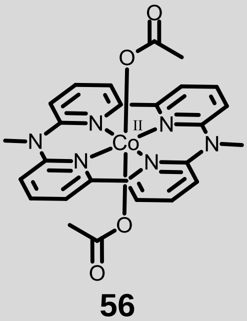 **56**	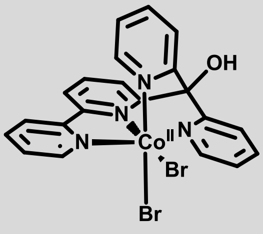 **80**	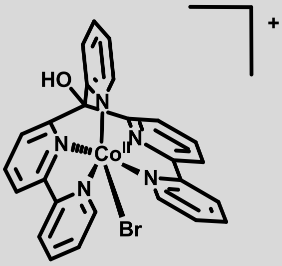 **82**
pK_a^1	3.0(1)	2.5(6)	-	-
pK_a^2	4.60(5)	4.5(6)	-	-
pK_a^3	8.70(2)	-	-	-
pK_a^4	10.74(3)	10.2(6)	9.46(3)	9.8(1)

Table 5: *pK_a values of complexes* ***55***, ***56***, ***80*** *and* ***82***

The *aza*-bridges in the ligand framework of **55** and **56** are two potentially easily available centres for protonation and deprotonation as evident from the additional pK_a values. Deprotonation of neutral R_2N-H bonds display high pK_a values. Deprotonation of neutral R_2N-H bonds is considerably facilitated when conjugation of the system is increased. While pyrrolidine has a pK_a of 44, a continuously decreasing pK_a value for pyrrole (pK_a 23), indol (pK_a 21.0) and carbazole (pK_a 19.90) was reported.[118] The two neutral R_2N-H in complex **55** are potentially far easier deprotonated due to the complexation with cobalt and a stronger conjugated system than in e.g. carbazole. In complex **55**, a pK_a at 8.70(2) could be identified which is absent in complex **56**. Given that the methylation of the nitrogen atom eliminates this deprotonation, the pK_a at 8.70(2) was assigned to a deprotonation of a neutral R_2N-H moiety (Figure 42). This would leave two unassigned pK_a values for complex **55** and **56** with significantly indifferent values at ~2.75 and ~4.5. Deprotonation of protonated secondary amines ($R_2NH_2^+$) is generally an easy process, following the same trends as the corresponding deprotonation of the neutral secondary amines. The pK_a value of the conjugated acid of aniline for instance is 3.8 while the conjugated acid of indole already has a pK_a value of -3.6.[119,120] Although the first pK_a value of ~2.75 seems rather high for the first deprotonation of the conjugated acid it would make chemical sense, since they seem present in both complexes and there are no other reasonable deprotonations of the ligand system. The deprotonation of the second $R_2N^+H_2$ moiety is in both cases slightly more difficult shown by their pK_a^2 value. The two closely followed pK_a^1 and pK_a^2 value support the proposed mechanism, since one would not assume a substantially different pK_a value for this similar deprotonations.

Figure 42 shows the complete proposed deprotonation mechanism of complex **55** with the first two deprotonations of the conjugated acids, followed by the deprotonation at the secondary amine and finally the deprotonation of an axial water molecule. Complex

56 follows the same assignment, however, the deprotonation of the amine is not possible and therefore this pK_a value is missing in comparison to complex **55**.

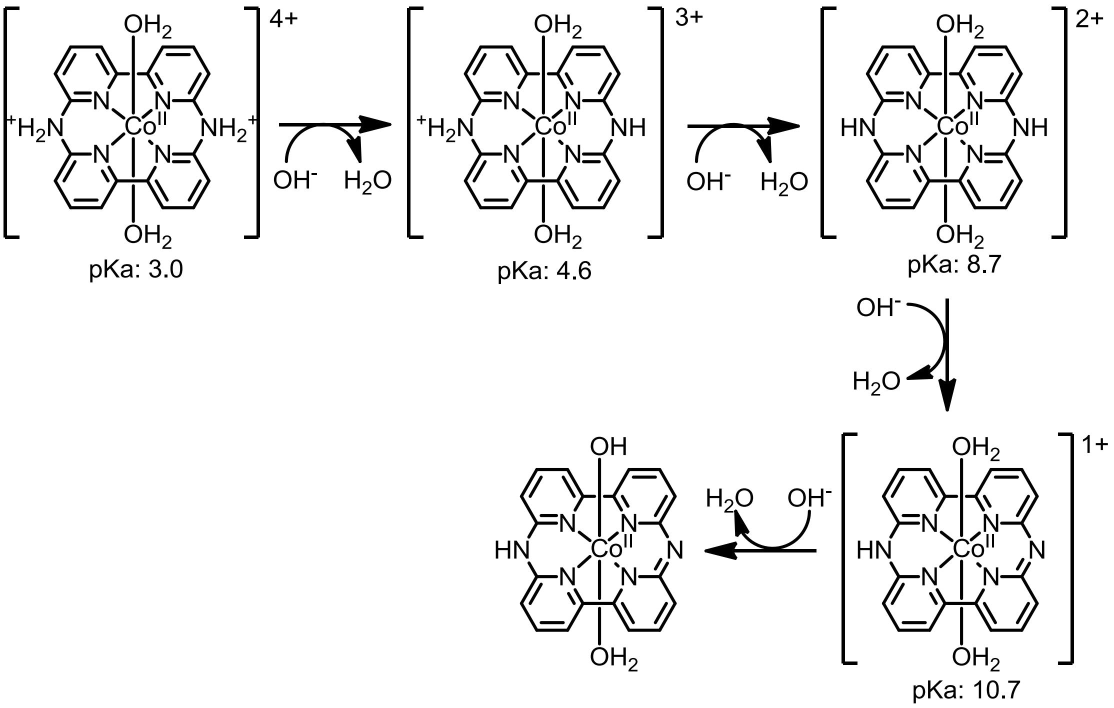

***Figure 42**: Proposed deprotonation mechanism of complex [Co^{II}(ac)$_2$(aza-pyr)] (**55**).*

2.3.4 Electrochemistry

Electrochemistry of cobaltopyrphyrin complexes in DMF

Differential pulse (DP) and cyclic voltammetry (CV) scans of the *mono*-alkylated cobaltopyrphyrin complexes **43**, **44** and **45** in DMF showed a variety of almost identical reductive transitions (Figure 43). In all cases four one electron reductions at very similar potentials are observed (Table 6). While the first two reductive transitions are reversible, irreversible transitions are observed below -2 V vs ferrocene. At mild oxidative conditions (-0.26 V for **44**, 0.19 V for **45** vs ferrocene) a transition was observed which was absent in the CV of the ligand **3** and thus attributed to a M^{III}/M^{II} transition. Though chemically reasonable, this would imply a relatively easy access to the oxidised Co^{III} complexes. Nevertheless, chemical oxidation of the Co^{II} complexes was still surprisingly difficult (chapter 2.3.1). The reduction at approximately -1.12 V vs ferrocene is absent in the ligand system **3**, thus assigned to a reduction of the M^{II} to a M^{I} centre. The reduction at approximately -1.8 V was assigned to a ligand based reduction, since the ligand framework **3** has an irreversible transition with an E_{pa} of –1.91 V. Reductions at even higher applied voltage are most likely mainly ligand framework based. As expected, one could not see a significant difference between the electrochemistry of **43** and **45** since the alkyl chain does not contain any easily reducible centres and should only marginally change the electronics on the ligand framework. The perchlorate containing complexes **43** and **45** show small transitions between the first and second one electron transition which are absent in case of complex **44**. This transitions might arise from small interaction of perchlorate with the cobalt centre, while in the case of **44** the axial bromide forms a better defined Co^{I} species.

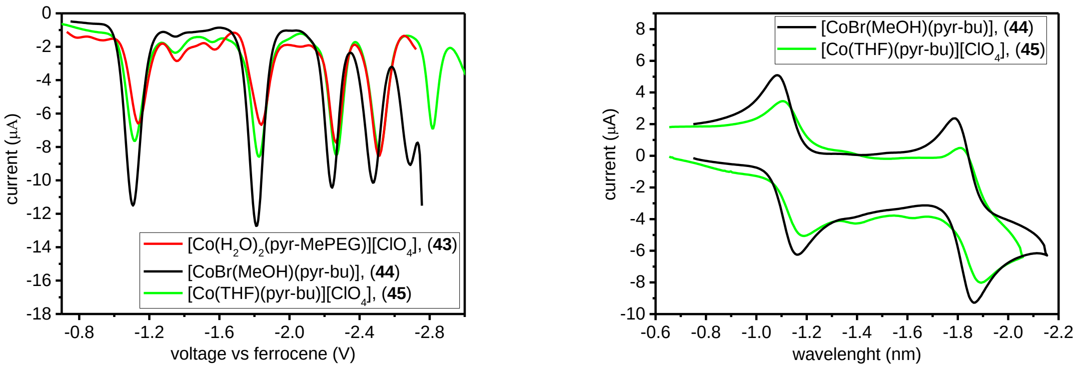

***Figure 43**: DP and reversible CV scans of $[Co^{II}(H_2O)_2(pyr\text{-}MePEG)][ClO_4]$ (**43**), $[Co^{II}Br(MeOH)(pyr\text{-}bu)]$ (**44**) and $[Co^{II}(THF)(pyr\text{-}bu)][ClO_4]$ (**45**). Conditions: 1 mM complex, 0.1M $TBAPF_6$ in DMF, WE = GCE, CE = Pt, RE = Ag/AgCl, referenced by measuring ferrocene (500 mV vs SHE).*[121]

Addition of TFA to a DMF solution of **44** gave a current enhancement in the region of the second reduction potential by formation of a catalytic wave (Figure 44). If **44** would be applied as WRC, most likely hydrogen would be formed on the second reduction potential and not on the first. This would imply that even though the Co^{II} of complex **44** is reduced at -1.12 V to its Co^{I} state, no hydrogen is formed until the ligand framework is reduced at -1.82 V.

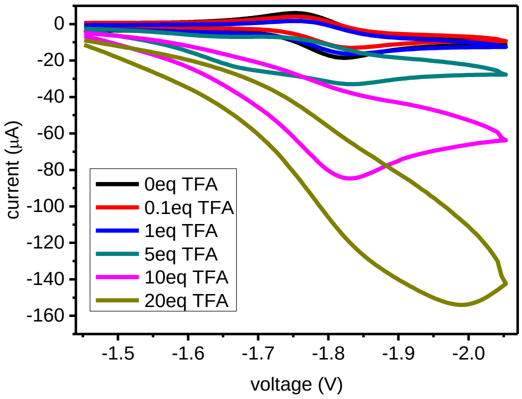

Figure 44: *CV scans of [Co^{II}Br(MeOH)(pyr-bu)] (**44**) with increasing TFA concentration in DMF (1mM) and 0.1 M [$^{n}Bu_4N$][PF_6] as electrolyte in V vs. ferrocene (500 mV vs SHE, WE: GC, CE: Pt, RE: Ag/AgCl).*[121]

While cyclic voltammetry of the *mono*-alkylated complexes showed two reversible reductions up to -2 V vs $Fc^{0/+}$, di-alkylated complexes (measure by E. Joliat[3,40]) showed three or more transitions within this reduction window (Table 6). The Co^{I} species for the di-alkylated complexes are only slightly easier accessible (100 – 150 mV). The ligand based reduction is considerably easier accessible for the di-alkylated complexes (~500 mV). This could arise from ligand **3** acting as ionic ligand compared to the neutral ligands **4** and **5** which indeed follow the same trend. The increased conjugation leads to a higher planarisation and a raised electron delocalisation, thus stabilising and increasing the electron density on the ligand framework which finally leads to higher reduction potentials of ligand framework based reductions. [$Co^{II}Br_2$(*trans*-pyr-bu_2)] was partially instable in solution where the cleavage of a butyl chain was observed. This might explain the various irreversible reductions up to -2 V. However, the reductions at -1.29 V for **4** and –1.30 V for **5** seem to be identical and are reversible in both cases which would suggest the butyl chain is still attached at this potential.

One reversible oxidative wave was observed at -0.26, -0.14 and -0.11 V vs. $Fc^{0/+}$ for **44**, **50** and **52** respectively, which is in agreement with the electron donating properties of the bromide ligands. Supporting the hypothesis that the bromide ligands while exchanged by water in aqueous solutions remain loosely bound in DMF. The $Co^{II/I}$ potentials show a slight anodic shift (~60 mV) from the perchlorates (**51** and **53**) to the corresponding bromides (**50** and **52**). The first ligand based reductions displayed little sensitivity to the axial ligands. Admittedly, one would expect the same for **44** and **45** which do not show this behaviour and even show a small cathodic shift from the bromide (**44**) to the perchlorate (**45**). The higher electron density on the cobalt centre due to the anionic nature of ligand **3** might reduce the influence of the axial ligand supported by the presence of at least one shorter Co-Br bond in the crystal structure of **50** and **52** (Figure 19). It is noteworthy that the potential of the reduced PS $[Ru(bpy)_3]^{2+}$ is sufficiently negative to reduce Co^{II} to Co^{I} for all complexes. It is also sufficient for the first ligand centred reductions in the case of the di-alkylated complexes. This is important for their application as water reduction catalysts which will be thoroughly described in chapter 2.4.

Compound	$E_M^{III/II}$	$E_M^{II/I}$	E_{L/L^-}	$E_{L^-/L^{2-}}$
43				
3 + 1eq. TFA			-1.91^a	
44	-0.26	-1.12	-1.82	
45	0.19^a	-1.15	-1.85	
4 + 1eq. TFA			-1.29^a	
50	-0.14	-0.97	-1.33	-1.76
51	–^{b}	-0.91	-1.32	-1.74
5 + 1eq. TFA			-1.30^a	
52	-0.11	-1.01	-1.33	–^{c}
53	–^{b}	-0.95	-1.32	–^{c}
$[Ru(bpy)_3]^{2+}$	0.81	-	-1.74	-1.91

***Table 6**: Electrochemical data of the protonated ligand **3** - **5**, the corresponding cobalt complexes as well as $[Ru(bpy)_3]^{2+}$ (all 1 mM) in DMF and 0.1 M* $TBAPF_6$ *as electrolyte in V vs. $Fc^{0/+}$ (GC WE, Pt CE, Ag/AgCl RE). ^{a} irreversible wave, E_{pa} or E_{pc}, respectively; ^{b} >0.75 V vs $Fc^{0/+}$; ^{c} several, irreversible peaks.*

*Spectroelectrochemistry of [Co^{II}Br(MeOH)(pyr-bu)] (**44**)*

The combination of electrochemical reduction and simultaneous UV/Vis absorption spectroscopy (spectroelectrochemistry) is a powerful tool for studying compounds in their reduced form. Complex [Co^{II}Br(MeOH)(pyr-bu)] (**44**) was analysed by spectroelectrochemistry to get further insight into the individual transitions. Figure 45 shows the UV/Vis spectra of compound **44** before reduction and after the reversible first and second reduction as shown in Figure 43. The difference between the reference in blue and the starting conditions in black are due to the method. To achieve a fast bulk electrolysis a high contact surface to the electrode was essential, thus a fine platin mesh was used in a 0.1 cm UV/Vis cuvette. The Pt grid was subtracted from the UV/Vis spectra. This lead to lower UV/Vis absorption due to less light being detected by the instrument. Thus, the extinction coefficients are lower than in reality where one would have to compensate for the Pt wire grid. It is however unclear why a fine structure with two absorption maxima at approximately 478 nm and 576 nm was observed. This might be a measurement artefact due to the small difference in absorption.

Most importantly, it is clearly apparent that the UV/Vis absorption spectra is only marginally affected by the first reduction. On the other hand, after the second reduction a considerably changed UV/Vis absorption spectra was observed, showing absorption change in the visible region. Based on the previous insight from electrochemistry, the first reduction was assigned to a $Co^{II/I}$ transition while the second reduction was interpreted as ligand based. Given that the UV/Vis of the complex and the UV/Vis of the ligand framework both show a similar UV/Vis spectra one would assume that the biggest contributor to the spectra is indeed the ligand and not the metal. At least in solution where the axial ligands are a solvent molecule and a very weakly bound bromide. The mostly unchanged UV/Vis after the first reduction corresponds well with this hypothesis. The metal centred transition of $Co^{II/I}$ corresponds to the exchange of the Br anion with a DMF solvent molecule which should not have a major impact on the UV/Vis spectrum.

The second reduction shows a relatively strong UV/Vis absorption spectra change which fits well to the hypothesis of a ligand based reduction. After the first reduction a Co^{I} species is formed which results in an overall neutral complex. Thus, further reduction of the system changes the UV/Vis absorption considerably because of charge redistribution. An increase in absorption indicates a planarisation of the complex upon reduction. Hence, a structural adaptation to the underivatised pyrphyrin complexes by further elongation of the alkylchain bond. It is however unclear where the reduction occurs, as no easily available centres for reduction are identified. Possibly, the additional charge is delocalised over the ligand. An additional strong evidence that the second reduction is ligand-based is the left-shift shift of the 395 nm band (381 nm in water) to 351 nm, which was assigned to the 2-pyridyl-2(1H)-pyridylideneacetonitrile moiety. The strong influence of the reduction on this transition strongly supports a ligand based transition considering even different metal centres showed a lower impact on the relative position of this transition (Figure 33).

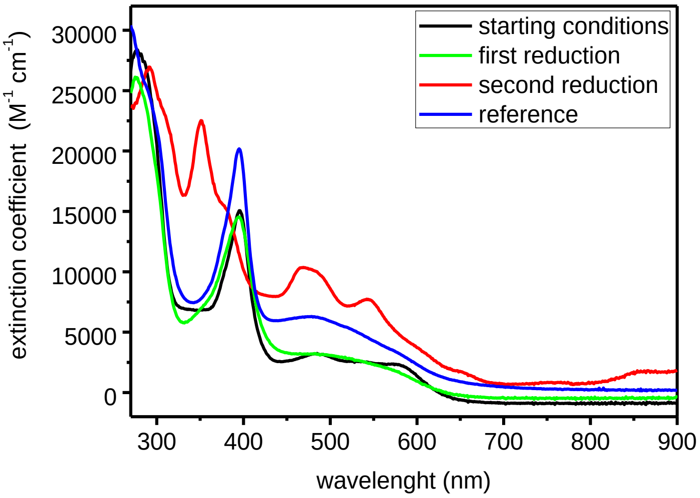

***Figure 45**: UV/Vis spectra of complex [Co^{II}Br(MeOH)(pyr-bu)] (**44**, 0.5 mM in DMF) at different potentials representing the UV/Vis spectra of the individual reduced species. Conditions: 0.1M TBAPF$_6$ in DMF, WE = Pt, CE = Pt, RE = Ag/AgCl, referenced by measuring ferrocene (500 mV vs SHE).*[121]

The two reversible transitions in **44** were probed for bulk reversibility. For this purpose, interval measurements were performed where the UV/Vis absorption spectra change at selected wavelengths was monitored. A starting condition voltage (-0.54 V) was applied until the UV/Vis spectrum did not change anymore, followed by a voltage of -1.74 V (second reduction, E_{L/L^-}) until no further UV/Vis absorption spectra change was detected. This process was repeated several times to show the bulk and long-term reversibility of both transitions. Figure 46 shows the high reversibility of the transitions by almost complete retention of the UV/Vis absorption spectra upon application of -0.54 V even after several intervals. This corroborates the reversibility of the first ligand based reduction and confirms the chemical stability of this doubly reduced form.

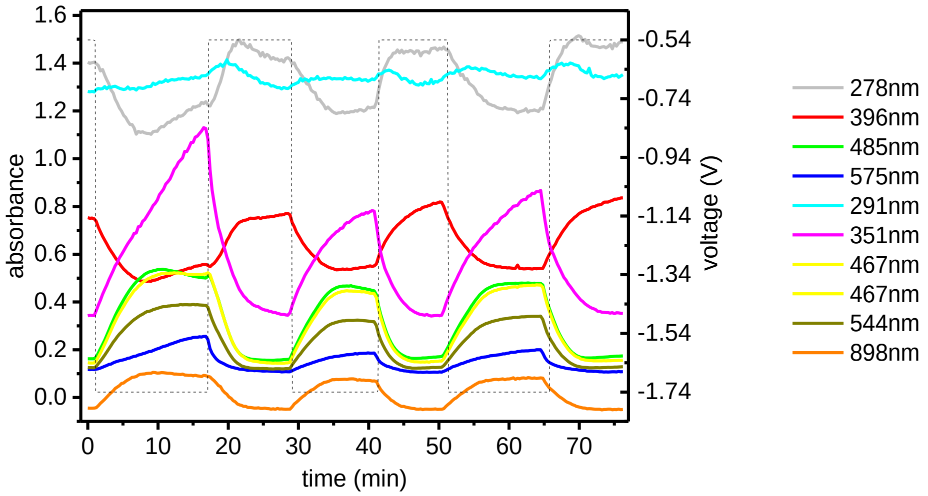

Figure 46: *UV/Vis spectra of reversibility measurements for complex [Co^{II}Br(MeOH)(pyr-bu)] (**44**) by interval application of -0.54 V and -1.74 V vs ferrocene in DMF (500 mV vs SHE). Conditions: 0.5 mM complex, 0.1M TBAPF$_6$ in DMF, WE = GC, CE = Pt, RE = Ag/AgCl, referenced by measuring ferrocene.*[121]

Comparison of different metallopyrphyrin complexes in DMF

Differential pulse (DP, Figure 47) and cyclic voltammetry (CV, Figure 48) scans of *mono*-butylpyrphyrin complexes in DMF with different metal centres **45** ([Co^{II}(H$_2$O)$_2$(pyr-bu)][ClO$_4^-$]), **46** ([Ni^{II}(pyr-bu)][ClO$_4^-$]) and **47** ([Cu^{II}(pyr-bu)][ClO$_4^-$]) showed in all cases two reversible reductions followed by various irreversible transitions. The assignment of the first two reductions was already discussed (Table 6).

A significant shift of the reduction potential is observed for the different metal centres (Figure 47) whereas similar Co^{II} catalysts showed near unchanged potentials as seen in Figure 43. In all cases perchlorate was used as anion and should thus not affect the spectra, even though it has already been shown that the influence of the chosen anion is not so important under reductive conditions. Figure 47 also shows the DP of the ligand **3** as reference, where the first ligand based reduction is irreversible and in the range of the second reductions of the metal complexes.

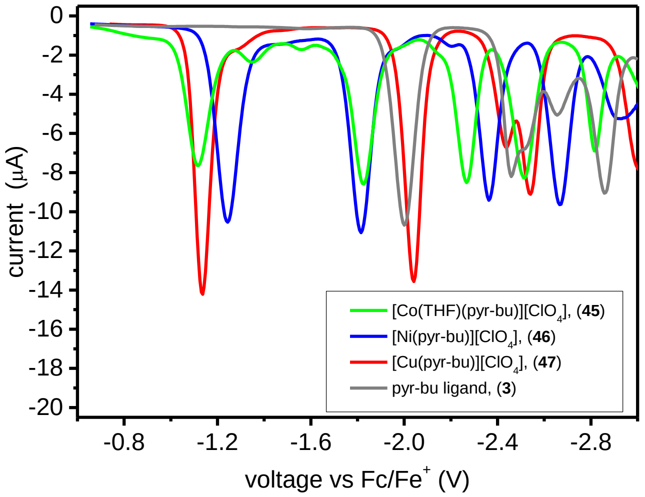

Figure 47*: DP scans of [Co^{II}(THF)(pyr-bu)][ClO$_4$]), (****45****), [Ni^{II}(pyr-bu)][ClO$_4$] (****46****), ([Cu^{II}(pyr-bu)][ClO$_4$] (****47****) and ligand* ***3****. Conditions: 1 mM complex, 0.1M TBAPF$_6$ in DMF, WE = GC, CE = Pt, RE = Ag/AgCl, referenced vs ferrocene (500 mV vs SHE).*[121]

Figure 48 shows two reversible reductions with their subsequent potential shifts based on the metal centre followed by the numerical values in Table 7. The choice of the metal has an influence on the potential of the ligand based, second reduction. Superficial interpretation of the reduction potential can be based on the 18 electron rule. Complex **46** was shown to form a square planar complex. **46** is a 16 electron complex compared to the 17 electron complexes **45** and **47**. Reduction of the 16 e$^-$ complex **46** is more difficult than the reduction of the 17 e$^-$ complexes **45** and **47**. The resulting Ni^I 17 e$^-$ complex is easiest to reduce a second time probably because a 18 e$^-$ complex is obtained. The 16 e$^-$ Co^I complex is easily reduced a second time and is considerably easier to reduce a third time to obtain an 18 e$^-$ species. Accordingly, reduction of the Cu^I complex is far more difficult. This resulted in an absolute shift as well as a relative difference of the first to the second reduction for complex **45** (0.7 V), **46** (0.57 V) and **47** (0.90 V).

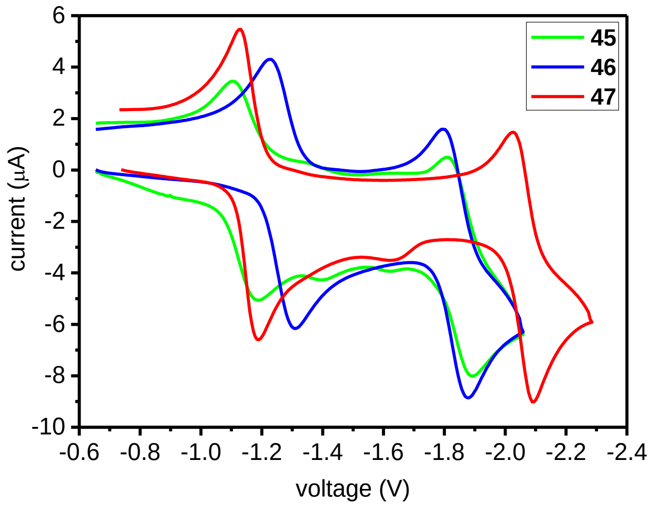

***Figure 48**: CV scans of the first two reversible reductions of **45** ($[Co^{II}(THF)(pyr\text{-}bu)][ClO_4]$), **46** ($[Ni^{II}(pyr\text{-}bu)][ClO_4]$) and **47** ($[Cu^{II}(pyr\text{-}bu)][ClO_4^-]$). Conditions: 1 mM complex, 0.1M $TBAPF_6$ in DMF, WE = GC, CE = Pt, RE = Ag/AgCl, referenced vs ferrocene (500 mV vs SHE).[121]*

Compound	$E_M^{II/I}$	E_{L/L^-}	Δ
45	-1.15	-1.85	0.70
46	-1.27	-1.84	0.57
47	-1.16	-2.06	0.90

***Table 7**: Electrochemical data of cobalt complexes **45**, **46** and **47** (all 1 mM) in DMF and 0.1 M $TBAPF_6$ as electrolyte in V vs. $Fc^{0/+}$. WE = GC, CE = Pt, RE = Ag/AgCl, referenced vs ferrocene (500 mV vs SHE).[121]*

2.4 Photocatalysis

Homogenous aqueous photocatalysis was performed for [Co^{II}(H$_2$O)$_2$(pyr-MePEG)][ClO$_4$] (**43**), [Co^{II}Br(MeOH)(pyr-bu)] (**44**), [Ni^{II}*(*pyr-bu)][ClO$_4^-$] (**46**), [Co^{II}Br$_2$(*cis*-pyr-bu$_2$)] (**50**, E. Joliat[3,40]), [Co^{II}Br$_2$(*trans*-pyr-bu$_2$)] (**52**, E. Joliat[3,40]), [Co^{II}(ac)$_2$(*aza*-pyr)] (**55**), [Co^{II}(ac)$_2$(*Me$_2$aza*-pyr)] (**56**), [Co^{II}(OTf)$_2$(*aza*-phyr)] (**57**, C. Bünzli[76]) and [Ni^{II}(OTf)$_2$(*aza*-phyr)] (**58**). Additionally, complex [Co^{II}(OH$_2$)$_2$(pyr)] (**41**) was investigated as heterogeneous catalyst due it’s insolubility in water. All cobalt catalysts showed good catalytic performance and could be recycled, making pyridine based macrocyclic cobalt complexes competing catalysts for future applications. The nickel complexes did not show significant hydrogen formation and are catalytically inactive. In this subchapter, the pyrphyrin based catalysts **43**, **44**, **46**, **50** and **52** will be discussed, followed by the heterogeneous catalysis of **41**. Then, photocatalysis of the *aza*-bridged complexes **55**, **56** and **57** is discussed. Catalysis of **43** and **44** in ascorbate is shown first, with a discussion of the drawbacks of this system. The switch to the new system containing a TCEP/ascorbate mixture is highlighted when first applied for catalyst **44**.

An illustration of the experimental setup is shown in Figure 49. An argon stream (matrix gas) was presaturated by passing through water (blue). The presaturated argon stream was then passed through the catalytic solution (yellow). The catalytic solution was irradiated by a water cooled LED at 390 nm or 453 nm with a photon flux of *0.30 ± 0.02* μEs^{-1}. The gas was then dried over molecular sieve, passed through an over pressure valve (OPV) and analysed by GC/TCD in 5 min intervals. The response time of the setup is approximately 15 min depending on the headspace volume. Integration of the measured rate profile gives the total amount of produced hydrogen. Calibration is performed by measurement of known amounts of gas in matrix, and referenced by electrochemical gas production for H$_2$.[40]

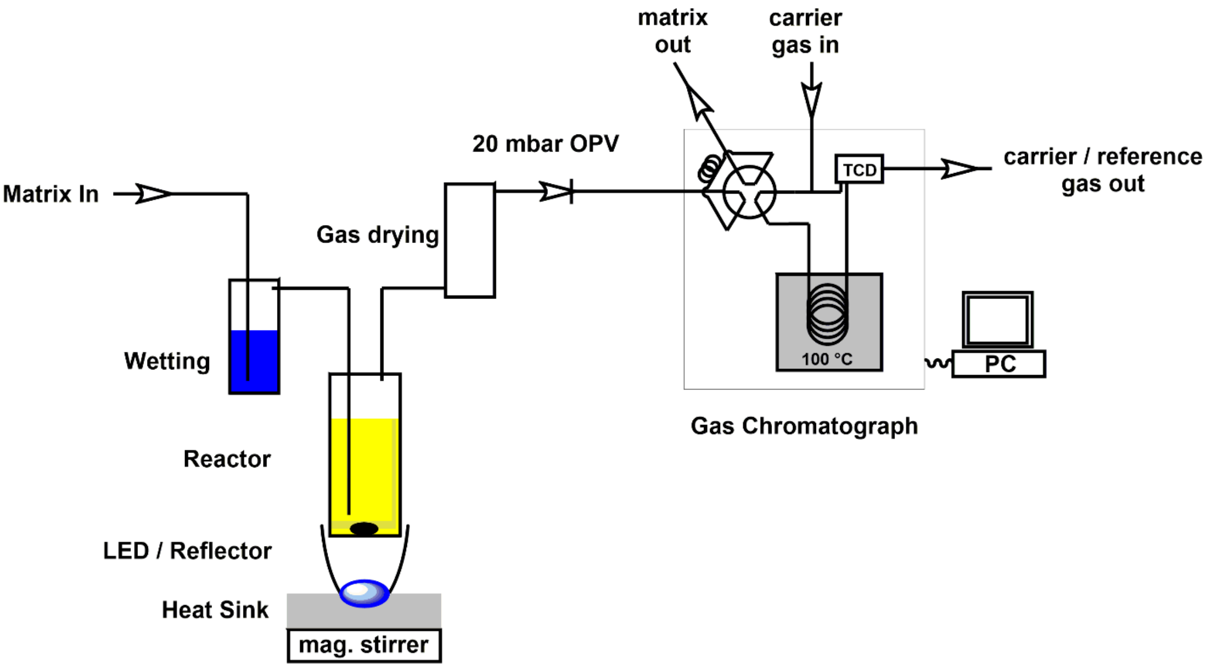

***Figure 49**: Illustration of the measurement setup for photocatalytic water splitting.*[40]

2.4.1 Photocatalysis with pyrphyrin based WRCs

*Photocatalysis of [$Co^{II}(H_2O)_2$(pyr-MePEG)][ClO_4] (**43**) and [Co^{II}Br(MeOH)(pyr-bu)] (**44**) with ascorbate*

A catalytic study of complex [$Co^{II}(H_2O)_2$(pyr-MePEG)][ClO_4] (**43**) and [Co^{II}Br(MeOH)(pyr-bu)] (**44**) with 1 M H_2Asc/NaHAsc buffer (pH 4) as sacrificial electron donor (SED) and 0.5 mM [Re(bipy)$(CO)_3$(py)][TfO] as photosensitiser (PS) in water gave 6’000(200) and 5’200(100) TON_{Co} respectively at 1 µM WRC loading. Thus, they are among the best catalysts reported so far (Figure 50).[20] Complex **43** showed at all concentrations slightly higher $TONs_{Co}$. Higher catalyst loadings of **43** lead to a higher H_2 formation rate up to 5 µM, whereafter catalysis became slower. The intrinsic light absorption of complex **43** (13’000 M^{-1} cm^{-1} at 385 nm) could lead to a reduced availability of photons for the photosensitiser (3’625(26) M^{-1} cm^{-1} at 343 nm,) and lead thus to slower H_2 evolution. However, the decline in H_2 formation rate at higher WRC concentrations is not observed for catalyst **44**. Complex **44** shows very similar behaviour than other poly-pyridyl catalysts, showing a fast increase in the H_2 formation rate, followed by a steep decline until H_2 formation ceased.[20,59] The different behaviours of complex **43** and **44** at higher concentrations is surprising considering their almost identical physicochemical properties (chapter 2.3). At 20 µM **43**, a delayed, reproducible maximal H_2 evolution (4.5 to 5 h delay) was observed. At higher WRC concentrations the system seems photon flux limited in both cases, since the maximal hydrogen formation rate is either flattening (**44**) or even sinking (**43**). At lower concentrations the catalysis could be limited by the catalyst concentration. This is supported by the increasing $TONs_{Co}$ at lower catalyst loading. We note that concentrations below 0.5 µM are not feasible. A blank measurement with ascorbate in absence of WRC showed formation of 9 µmol hydrogen while at 0.1 µmol WRC loading 12(2) µmol or 10(1) µmol were formed in presence of **43** and **44** respectively. Thus, making the background most likely the main contributor of the H_2 measurement.

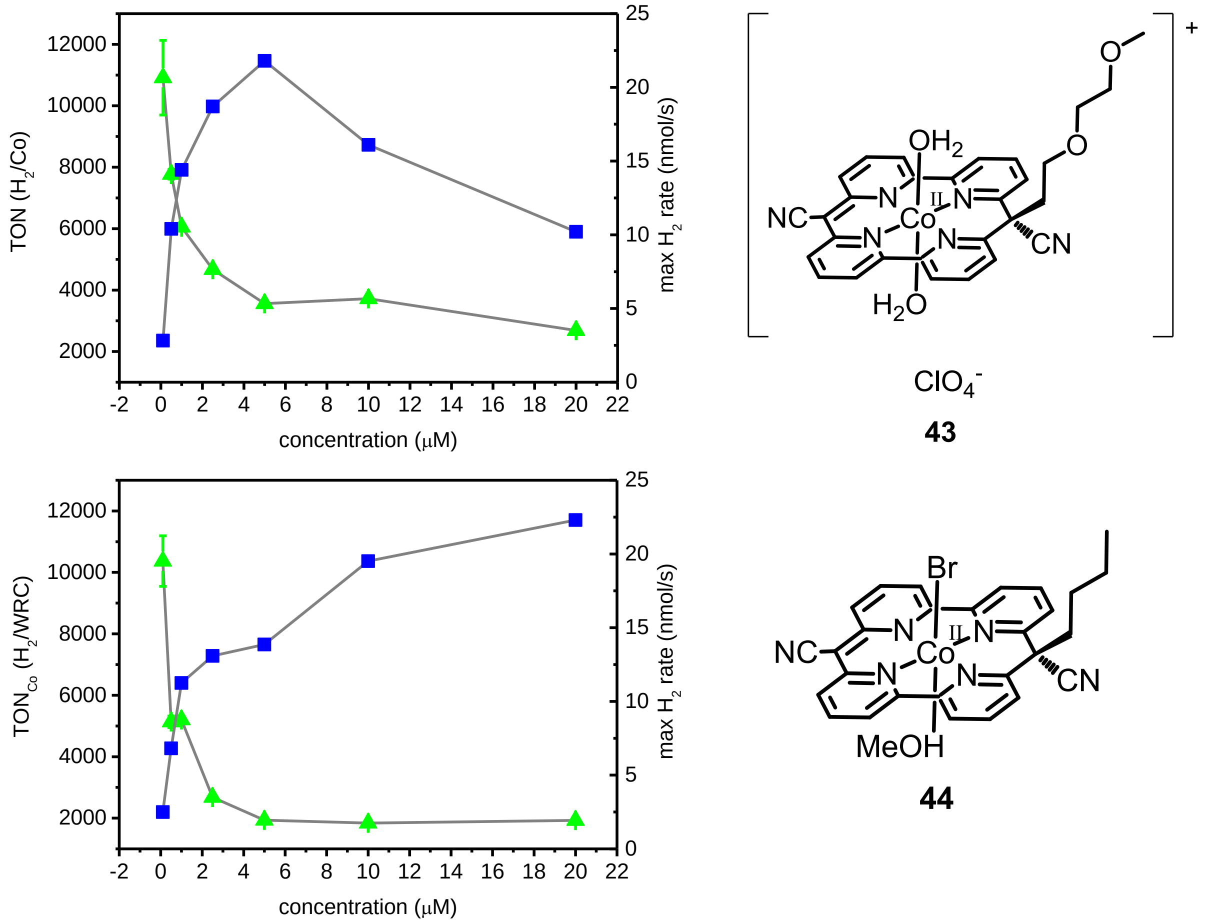

Figure 50: *TON$_{Co}$ (H$_2$/Co, green) and hydrogen evolution rate (nmol/s, blue) obtained in a catalytic concentration study of* ***43*** *(top, mean value of several measurements) and* ***44*** *(bottom). Conditions 0.5 M ascorbic acid, 0.5 M sodium ascorbate, 0.5 mM [Re(bipy)(CO)$_3$(py)][TfO] and 390 nm LED, photon flux of 0.30 ± 0.02 µEs^{-1} at pH = 4.03 – 4.11 in water (V$_{tot}$ = 10 mL). Right: graphical representation of* ***43*** *(top right) and* ***44*** *(bottom right).*

Figure 51 shows the H_2 formation rate course for catalysis with **43** at different loadings in water with a 1 M H_2Asc/NaHAsc buffer (pH = 4.03 - 4.11) as sacrificial electron donor and 0.5 mM [Re(bipy)(CO)$_3$(py)][TfO] as photosensitiser. The H_2 evolution rate at 20 µM is considerably different. The H_2 formation rate at lower WRC concentrations is in line with other poly-pyridyl catalysts and complex **44**, where a fast increase is followed by a rapid decline in performance.[20,59] This shows that the WRC is not able to drive the catalysis at ideal conditions for a prolonged time. Finding the system limitations for the catalysis is crucial to improve performance.

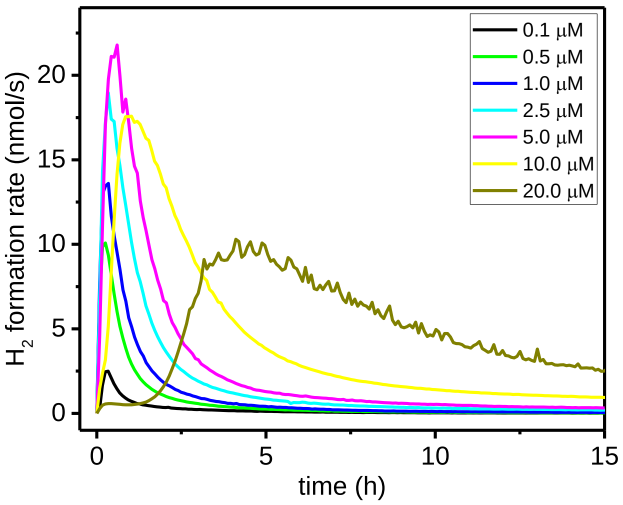

Figure 51: *H_2 production rate (nmol/s) obtained for **43** at different catalyst loadings with 0.5 M ascorbic acid, 0.5M sodium ascorbate, 0.5 mM [Re(bipy)(CO)$_3$(py)][TfO] and 390 nm LED, photon flux of 0.30 ± 0.02 µEs^{-1} at pH 4.03 – 4.11 in water (V_{tot} = 10 mL).*

Even at higher catalyst (10 µM) loadings, only approximately 8 % of the ascorbic acid is consumed, thus the amount of ascorbic acid is not the limiting factor. Cessation of the hydrogen formation could be explained by degradation of the PS (detectable by HPLC) as well as accumulation of dehydroascorbic acid (DHA). The H_2Asc/NaHAsc buffer in the acidic pH range is a typical SED where ascorbate is oxidised to DHA.[122] This leads to a drawback, since the electron back transfer by reaction of the reduced photosensitiser (PS^-) with DHA leads to inhibition of the catalytic cycle.[33] This PS limitation is illustrated by recycling the catalytic solution (Figure 52). Therefore, once the H_2 formation ceased, an equal amount of PS (0.5 mM) was added to restart H_2 formation and the TON_{Co} of a 20 µM solution of **43** could be improved from 2’400 to a total of 3’500 $TONs_{Co}$ which corresponds to a relative increase of 50 %. A second recycling of the catalytic solution only lead to formation of an additional 200 $TONs_{Co}$ for a total of 3’700 TON_{Co}. The non-proportional increase of the TON_{Co} is most likely due to the increasing accumulation of DHA and the steadily increasing probability of short cutting the catalytic cycle. This is supported by the decrease in the maximal H_2 formation rate from 6.5 to 3.8 to 1.0 nmol/s H_2. Hence, the reaction is most likely limited by an increasing DHA concentration, leading to a reduction of the maximal H_2 formation rate and a higher probability of PS^- to be quenched by a DHA molecule rather than the WRC. Furthermore, the stability of the PS is a further limiting point.

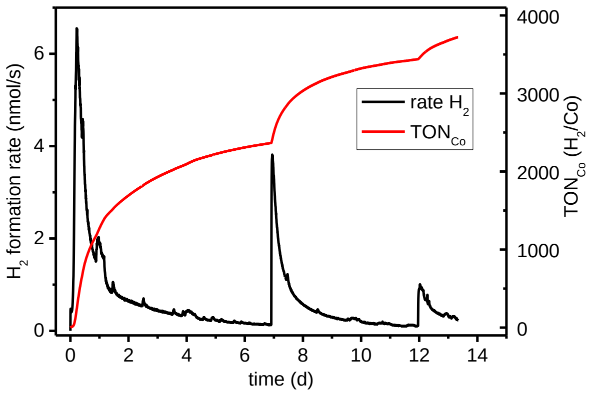

***Figure 52**: H_2 evolution rate (left) and the TON_{Re} (H/Re) and TON_{Co} (H_2/Co) (right) at 20 µM **43**, 0.5 M ascorbic acid, 0.5M sodium ascorbate, 0.5 mM $[Re(bipy)(CO)_3(py)][TfO]$ and 390 nm LED, photon flux of 0.30 ± 0.02 μEs^{-1} at pH 4.03 – 4.11 in water and addition of an equal amount of PS added after 166 h and 287 h (V_{tot} = 10 mL).*

*Photocatalysis of $[Co^{II}Br(MeOH)(pyr\text{-}bu)]$ (**44**), $[Ni^{II}(pyr\text{-}bu)][ClO_4^-]$ (**45**), $[Co^{II}Br_2(\text{cis-}pyr\text{-}bu_2)]$ (**50**), $[Co^{II}Br_2(\text{trans-}pyr\text{-}bu_2)]$ (**52**) with TCEP*

An irreversible SED would prevent the electron back transfer of the DHA/AscOH pair. This can be achieved by recycling DHA with an additional irreversible SED (Figure 53).[55] The DHA/AscOH pair does then transform into an electron relay. Tris(2-carboxyethyl) phosphine hydrochloride (TCEP) reduces DHA to ascorbate over a wide pH range.[123,124] The resulting TCEPO does not undergo electron back transfer reaction as DHA. TCEPO can be quantified by ^{31}P NMR and compared to the formed amount of H_2 detected by GC. Figure 53 shows the cycle of the improved catalytic system (developed by C. Bachmann in our group[83]) where TCEP continuously regenerates DHA. All TCEP needs to be oxidised before the accumulation of DHA leads to the inhibition of the catalytic cycle, thus a considerable more robust system for photocatalytic water splitting was obtained.[55]

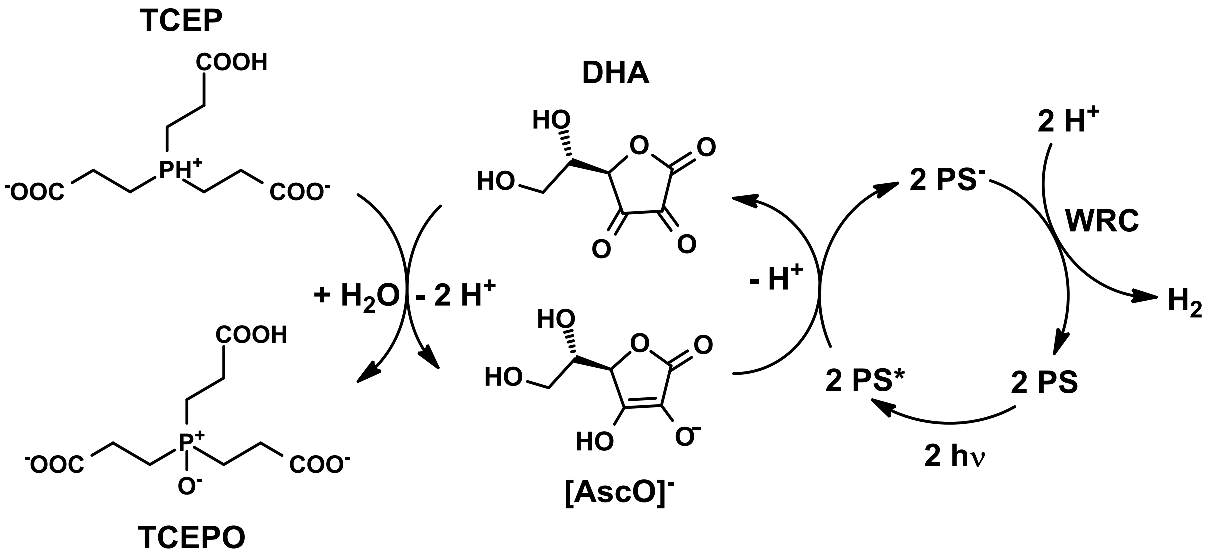

Figure 53: Ascorbate coupled photocatalysis with TCEP as SED. All three carboxylic acid moieties are deprotonated at pH 5 and two at pH 4 according to the reported pK$_a$ values of TCEP.[125] This system was developed and investigated by C. Bachmann in our group.[55,83]

Homogenous photocatalysis with [Co^{II}Br(MeOH)(pyr-bu)] (**44**), [Ni^{II}(pyr-bu)][ClO$_4^-$] (**45**), [Co^{II}Br$_2$(*cis*-pyr-bu$_2$)] (**50**)[3], [Co^{II}Br$_2$(*trans*-pyr-bu$_2$)] (**52**)[3] and the perchlorate complexes **45**, **51**[3] and **53**[3] as WRCs gave very high TONs$_{Co}$ of up to 22’000 H$_2$/Co. Photocatalysis of **50** to **53** was performed by E. Joliat in our group.[3] Catalysis was performed at various WRC concentrations in aqueous solution (10 mL), with H$_2$Asc/NaHAsc buffer (pH 5, 0.1 M) as SED and 0.5 mM [Ru(bpy)$_3$]Cl$_2$ as photosensitiser (453 nm LED, 0.30(2) µEs^{-1}). 0.1 M TCEP was added to recycle the DHA. Table 8 shows the summary of the results.

In all cases, H$_2$ formation started immediately after turning the light on. The H$_2$ rate was similar for all catalysts and increased sharply at the start until a maximum was reached after ~1 h for the 1 µM solutions (Figure 54). After the maximum a steady decline was observed until H$_2$ formation stopped at ~70 h.

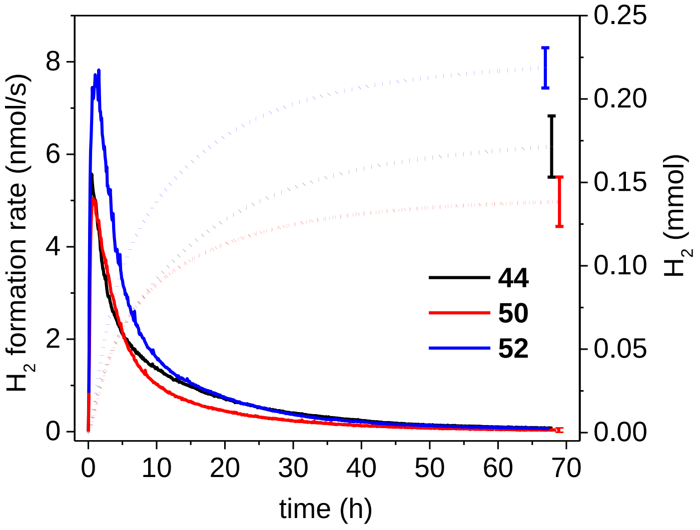

***Figure 54**: Hydrogen evolution rate (nmol/s, drawn line) and total formed hydrogen (mmol, dotted line) for 1 µM solutions of* **44**, **50** and **52** with 0.5 mM *[Ru(bpy)$_3$]Cl$_2$ as PS, 0.1 M TCEP as recycling agent, 0.1 M AscO$^-$/AscOH buffer (pH 5) as SED at 453 nm LED, photon flux of 0.30 ± 0.02 µEs^{-1}.*[40]

The overall performance is probably not limited by the stability of the cobalt catalysts since the TON$_{Co}$ increased when the WRC concentration was lowered. This is further supported by the possibility to restart the catalysis by addition of more (0.1 M) TCEP and 0.5 mM [Ru(bpy)$_3$]Cl$_2$. A reaction solution of 5 µM **44** could be restarted after the hydrogen formation ceased to form an additional 0.80(6) mmol H_2 showing no catalytic deactivation whatsoever. The maximal turnover frequency (TOF$_{max}$, H_2/WRC/h) increased with descending WRC concentration within the investigated region. This implies that the H_2 formation rate is light limited, even at 1 µM WRC and 500 µM PS. We conclude that this catalysts performs extremely well, showing high TON$_{Co}$, moderate TOF$_{max}$ and compare well with a previously reported pentadentate polypyridyl based Co^{II} complex (TOF$_{max}$ 5'900(400); TON$_{Co}$ 33'000(2000)).[55] Complete degradation of the PS was observed after reaction at all concentrations. Complete oxidation of the TCEP was observed at concentrations ≥5 µM WRC with concomittant cease of H_2 formation. Comparable TON$_{Co}$ and TOF$_{max}$ were obtained for the bromide and perchlorate analogues of the catalysts since the axial ligands are exchanged by water in aqueous media. Formation of nanoparticles is unlikely, since mercury poisoning measurements for **45** and **52** at 5 µM catalyst loading showed the same H_2 evolution course and lead to almost identical TON$_{Co}$ and TOF$_{max}$. Blank measurements confirmed that no H_2 was formed in absence of PS and only a marginal amount of H_2 was formed when no WRC (3.5(2) µmol) or 5 µmol CoBr$_2$ (5.9(3) µmol) was added.

The chemical oxidation of TCEP to TCEPO coincided with the amount of H_2 determined by GC. Generally, lower catalyst concentrations showed better conformity while at higher concentrations slightly larger deviations were observed. Complex **44**

([Co^{II}Br(MeOH)(pyr-bu)]) showed in most cases the largest discrepancy between GC and ^{31}P NMR. It is unclear why such a deviation was observed. Excess TCEP after the reaction was sometimes partially oxidised by oxygen before and while measuring the ^{31}P NMR. For instance, all TCEP was oxidised for concentrations ≥ 5 µM of **44** which lead to the ceasing of hydrogen evolution, but still only 70 % of the chemically oxidised TCEP contributed to the formation of hydrogen as implied by GC.

Photocatalysis with 5 µM [Ni^{II}(pyr-bu)][ClO$_4^-$] (**45**) gave 250(10) TON$_{Ni}$ for a total of 12(1) µmol H_2 (Figure 55), thus showing only slightly increased hydrogen formation than seen for blank measurements. 4(2) µmol H_2 was formed in absence of any WRC and 6(3) µmol H_2 was obtained when 5 µmol $CoBr_2$ was used as WRC (Table 8). Hence, complex **45** is a very bad WRC at best.

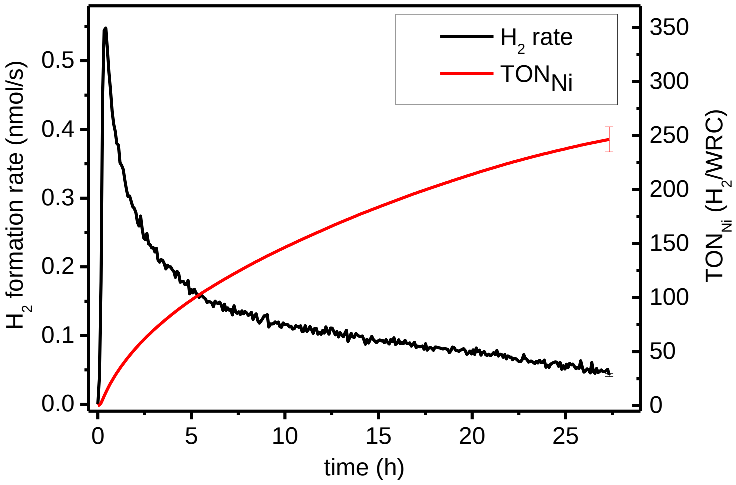

Figure 55**: Hydrogen evolution rate (nmol/s, black) and TON$_{Ni}$ (H_2/WRC, red) for 5 µM **45 with 0.5 mM *[Ru(bpy)$_3$]Cl_2 as PS, 0.1 M TCEP as recycling agent, 0.1 M H_2Asc/NaHAsc buffer (pH 5) as SED at 453 nm LED, photon flux of 0.30 ± 0.02 µEs^{-1}.*

***Table 8**: Summarised results of the photocatalytic experiments. Conditions: Total volume 10 mL H_2O, PS: 500 µM $[Ru(bpy)_3]Cl_2$, WRC: Co-complexes **44**, **45** and **50-53** at various concentrations (1, 2, 5 or 10 µM), 0.1 M TCEP, 0.1 M NaHasc, pH 5, 453 nm LED, photon flux of 0.30 ± 0.02 µE/s. Highlighted in blue: Blanks. Highlighted in grey: Bromo-complexes **44**, **50** and **52**. Highlighted in white: perchlorato-complexes **45**, **51** and **53**.*[40]

Co-WRC	conc.WRC (µM)	total H_2 [a] (µmol)	Max. rate [a] (nmol/s)	Reaction time [b] (h)	TON_{Co} [a] (H_2/Co)	Max. TOF_{Co} [a] (H_2/Co/h)
-[c]	0	0	0	0	-	-
-[d]	0	3.5 ± 2	0.21 ± 0.03	22	-	-
$CoBr_2$	5	5.9 ± 2.5	0.71 ± 0.04	18	120 ± 50	51 ± 3
50[e]	5	0	0	0	0	0
44	1	170 ± 20	5.6 ± 0.4	47	17‘200 ± 1800	2000 ± 140
44	2	340 ± 40	6.4 ± 0.4	84	17‘000 ± 1700	1150 ± 80
44	5	710 ± 60	8.3 ± 0.5	107	14‘200 ± 1100	590 ± 40
44	10	800 ± 70	7.8 ± 0.5	91	8’000 ± 700	280 ± 20
45	5	730 ± 40	7.1 ± 0.3	114	14‘600 ± 700	510 ± 30
45[f]	5	770 ± 40	7.8 ± 0.3	90	15‘500 ± 700	560 ± 30
50	1	140 ± 20	5.1 ± 0.2	24	13‘800 ± 1500	1820 ± 80
50	2	130 ± 20	4.7 ± 0.2	37	6’600 ± 770	840 ± 40
50	5	260 ± 40	6.4 ± 0.6	49	5’200 ± 640	460 ± 50
50	10	420 ± 40	4.9 ± 0.2	96	4’200 ± 360	180 ± 10
51	5	330 ± 30	5.5 ± 0.3	71	6’500 ± 610	390 ± 20
52	1	220 ± 20	7.8 ± 0.4	41	21‘900 ± 1200	2800 ± 130
52	2	370 ± 30	8.4 ± 0.4	80	18‘300 ± 1100	1500 ± 80
52	5	530 ± 30	6.1 ± 0.2	109	10‘700 ± 500	440 ± 20
52[f]	5	480 ± 30	6.6 ± 0.2	145	9’600 ± 500	470 ± 20
52	10	650 ± 70	5.9 ± 0.5	111	6’700 ± 630	210 ± 20
53	5	490 ± 30	6.6 ± 0.3	88	9’700 ± 450	480 ± 20

[a] Measured by GC.

[b] Time required to form 95 % of totally measured H_2 (GC).

[c] 0.1 M NaHasc and 0.1 M TCEP; no WRC, no PS.

[d] 500 µM $[Ru(bpy)_3]Cl_2$, 0.1 M NaHasc and 0.1 M TCEP; no WRC; according to publication of *C. Bachmann et al.*[15]

[e] 0.1 M NaHasc and 0.1 M TCEP; no PS.

[f] Hg poisoning experiment: Hg was added at the end of the preparation of the catalytic solution (**45**, 455 mg; **52**, 477 mg).

*Photocatalysis of [$Co^{II}(OH_2)_2$(pyr)] (**41**)*

Photocatalytic water splitting in a homogenous solution with complex **41** was not possible due to the insolubility of the complex in water. However, **41** showed hydrogen evolution as a heterogeneous catalyst.

1 mM stock solution of **41** was thought to precipitate as fine solid after mixing with water. This was not visible by eye or dynamic light scattering (DLS). 3’200(300) TON_{Co} and 0.16(2) mmol H_2 were obtained with a 5 µM catalyst solution (Figure 56). The maximal H_2 evolution rate was always below 2 nmol/s. This is rather low compared to homogenous catalysts such as **44**, **50** and **52** where rates of 6-8 nmol/s hydrogen were obtained (Table 8). This supports the hypothesis of precipitation of **41**, resulting in a heterogeneous catalysis. One would assume a considerable slower H_2 formation rate for heterogeneous catalysis due to the considerable smaller surface of **41** as solid. A blank experiment with $CoBr_2$ as catalyst under otherwise equal conditions showed only formation of 6(3) µmol H_2 which confirmed that complex **41** is catalytic active. In comparison with homogenous catalysts a slower decline in the hydrogen formation rate was observed. The PS was decomposed after the reaction and all TCEP was oxidised. The H_2 evolution can be restarted by addition of fresh PS (500 µM) and TCEP (0.1 M) after H_2 evolution ceased. An additional 2’100(300) TON_{Co} (0.11(2) mmol H_2) was obtained which corresponds to 66 % of the initial formed hydrogen. This shows that in the first instance the catalytic performance is not limited by the catalyst.

Since two holes are needed to oxidise TCEP to TCEPO, a 5 µM solution of catalyst should be able to give 20’000 TON_{Co} before the 0.1 M TCEP is completely oxidised. Thus, it is surprising why complete oxidation of the TCEP was observed after catalysis. Only 16 % (5 µM **41**) of the TCEP oxidation lead to hydrogen formation. The remaining 84 % of the TCEP was oxidised without formation of hydrogen. It is unclear what was reduced instead of protons. Reduction of the PS, WRC and pyridine could be possible. Although, this would only cover a small percentage of this 84 %, because of the low concentration of these molecules.

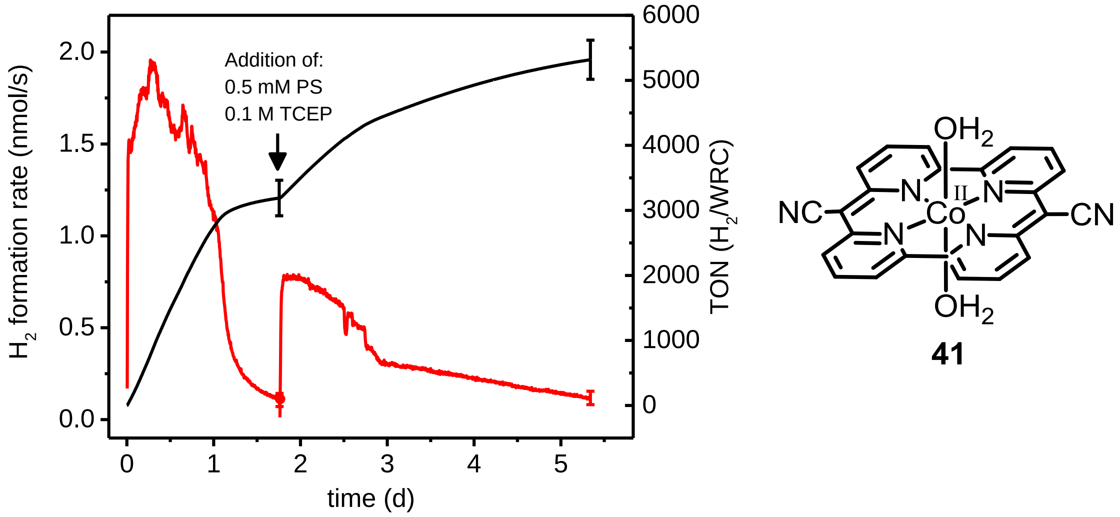

***Figure 56**: Left: Hydrogen evolution experiments for solutions of 5 µM catalysts **41**, 500 µM $[Ru(bpy)_3]Cl_2$, 0.1 M TCEP, 0.1 M NaHasc, pH 5, 453 nm LED, photon flux of 0.30 ± 0.02 μEs^{-1} , V_{tot} = 10 mL. Addition of fresh 0.5 mM PS and 0.1 M TCEP after 1 d 18 h. Red line: hydrogen evolution rate; black line: the amount of generated hydrogen. Right: ChemDraw representation of complex **41**.*

The H_2 determined by GC for the pyridine containing solution of **41** was compared to the chemical oxidation of TCEP by ^{31}P NMR. In contrast to the moderate deviations for other poly-pyridyl catalysts, a distinct discrepancy of the two values was observed. In some cases up to 90 % of the TCEP was oxidised without H_2 formation according to GC. The H_2 measured by GC corresponded very well with the faradaic yield of the in-line electrolysis of acidified water with a Pt electrode, thus the measurement system is very accurate. As previously highlighted, sometimes relatively fast oxidation of excess TCEP with air could be observed before and while the ^{31}P NMR was performed. This could certainly amount to a moderate difference, but nowhere near to the observed extent. Main difference to the other measured catalysts was the application of the catalyst **41** (1 mM in pyridine) as well as its heterogeneity. Even if all of the added pyridine (50 µL, 620 nmol), the existing PS (0.5 mM, 5µmol) and WRC (5 µM, 50 nmol) would be reduced, it would only amass to a tiny fraction (0.6 %) of the formed TCEPO (0.1 M, 1 mmol). According to the amount of other reagents present in the catalytic solution the only reasonable assumption would be a reduction of ascorbate by TCEP. The most likely scenario is a reduction of ascorbate to the γ-lactone of the D-gluconic acid by reducing a second ketone to the corresponding alcohol group (Scheme 27). $[Co^{II}(OH_2)_2(pyr)]$ (**41**) showed the biggest difference between measured hydrogen (GC) and oxidised TCEP (NMR) followed by complexes **44** ($[Co^{II}Br(MeOH)(pyr\text{-}bu)]$), $[Co^{II}Br_2($*cis*-pyr-bu$_2)]$ (**50**) and $[Co^{II}Br_2($*trans*-pyr-bu$_2)]$ (**52**). This might indicate that the reduction of ascorbate is catalysed by the WRC and low spin Co^{II} complexes might be better suited for the job.

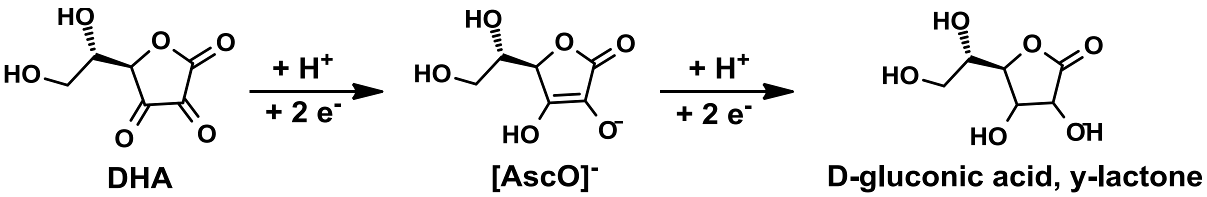

Scheme 27: *Proposed reduction of DHA to ascorbate and proposed reduction to D-gluconic acid at pH 5 under photocatalytic conditions.*

Incremental measurements of a 5 µM solution of **41** (from 1 mM pyridine stock solution) showed a steady and relatively linear increase of the total H_2 formed until a plateau was reached after ~23 h (Figure 57, Table 9). The relative correlation between the TCEP oxidation (NMR) and the hydrogen formation rate (GC) increased until it flattened out at approximately 20 % (Table 9). The discrepancy is large from the first measurement point after 3 h where only 10 % of the oxidised TCEP correlated to the formation of hydrogen. The ratio between the two measurements is not stable but seems to stay around 15 to 20 % after 5 h reaction time.

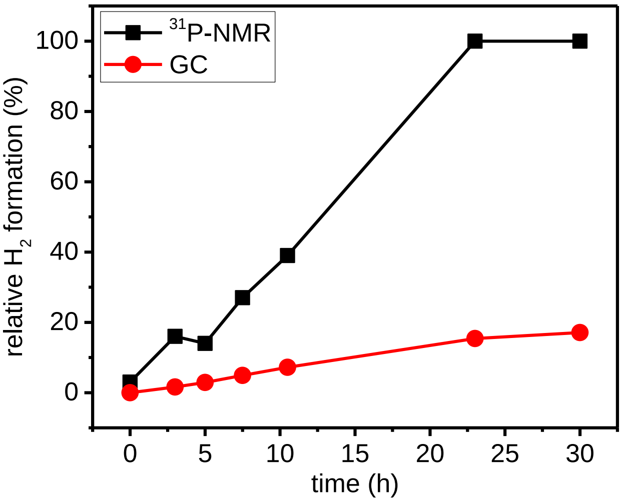

Figure 57: *TCEP oxidation measured by ^{31}P NMR given in % of the formed TCEPO and the corresponding GC measurements showing the % value for the theoretically formed TCEPO if all formed hydrogen was formed by oxidation of TCEP. 5 µM **41** (1 mM in pyridine), 500 µM $[Ru(bpy)_3]Cl_2$, 0.1 M TCEP, 0.1 M NaHasc in water (pH 5), 453 nm LED, photon flux of 0.30 ± 0.02 µEs^{-1}, V_{tot} = 11 mL*

	Start	3 h	5 h	7.5 h	10.5 h	23 h	30 h
^{31}P NMR	3 %	16 %	14 %	27 %	39 %	100 %	100 %
GC	0 %	1.6 %	2.9 %	4.9 %	7.2 %	15.4 %	17.1 %
GC/NMR	-	10 %	21 %	18 %	18 %	15 %	17 %

Table 9: *TCEP oxidation measured by ^{31}P NMR given in % of the formed TCEPO and the corresponding GC measurements showing the % value for the theoretically formed TCEPO if all formed hydrogen was formed by oxidation of TCEP. 5 µM **41** (1 mM in pyridine), 500 µM $[Ru(bpy)_3]Cl_2$, 0.1 M TCEP, 0.1 M NaHasc in water (pH 5), 453 nm LED, photon flux of 0.30 ± 0.02 µEs^{-1}, V_{tot} = 11 mL*

Further insight was obtained by catalytic experiments in which **41** was directly subjected as solid catalyst without pyridine. Complex **41** showed slow but robust H_2 evolution, which could be restarted several times with only marginal impact on the performance as seen in Figure 58. Restarting of the H_2 evolution was achieved by addition of fresh PS and TCEP after the H_2 formation ceased, since all TCEP was oxidised and the PS decomposed according to NMR and HPLC. With this method it was possible to obtain 443(16) TON_{Co}, 400(14) TON_{Co}, 368(13) TON_{Co}, 674(24) TON_{Co} in four consecutive runs with the same reaction mixture. A total of over 3.0 mmol H_2 formed without indication of slowing. Even the fourth catalysis yielded 76 % of the initial TON_{Co} relative to the added TCEP and PS. Complex **41** is a very fine black powder. Addition of **41** gave visible heterogeneous mixtures. Strong stirring was needed, since **41** is very hydrophobic and would otherwise float at the water surface. The Teflon coated stirring bar accumulated some of the catalyst over time. Main drawback of the catalysis is the slow H_2 evolution rate relative to the high catalyst loading due to the low accessibility of the catalyst in the water phase. The H_2 formation rate declines due to the light absorption of decomposition products. The solution turned darker after each catalytic run. It is noteworthy, that this is robust and stable catalyst under the catalytic conditions. Figure 58 shows a considerably slower ceasing of the hydrogen formation rate than for similar homogenous catalysts. After complete oxidation of TCEP a sharp decline in the hydrogen formation rate is observed. At this point, DHA accumulates and short cuts the catalysis which leads to termination of the hydrogen formation.

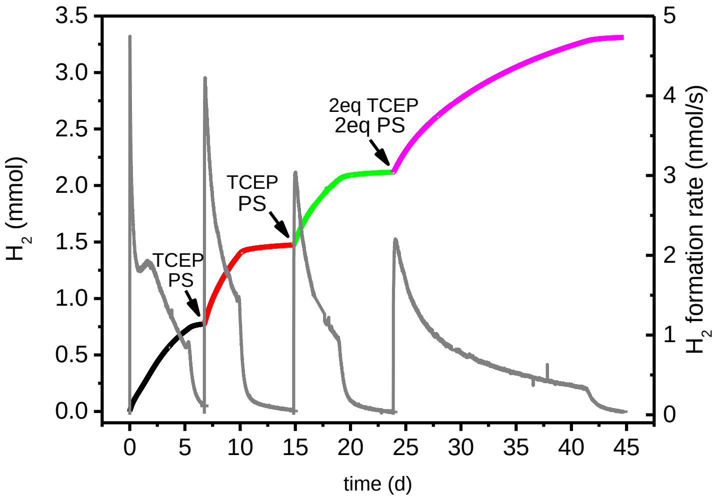

Figure 58: *Hydrogen evolution experiments for 175 µM* ***41****, 500 µM* $[Ru(bpy)_3]Cl_2$*, 0.1 M TCEP, 0.1 M NaHasc in water (pH 5), 453 nm LED, photon flux of 0.30 ± 0.02* μEs^{-1}*,* V_{tot} *= 10 mL. Red line: hydrogen evolution rate; black line: the amount of generated hydrogen. Fresh 0.1 M TCEP and 0.5 mM* $[Ru(bipy)_3]Cl_2$ *was added after each run. For the 4th run 0.2 M TCEP and 1 mM* $[Ru(bipy)_3]Cl_2$ *was added.*

2.4.2 Homogenous photocatalysis with *aza*-bridged macrocyclic complexes

Homogenous photocatalysis with [Co^{II}(ac)$_2$(*aza*-pyr)] (**55**), [Co^{II}(ac)$_2$(*Me$_2$aza*-pyr)] (**56**) and [Co^{II}(TfO)$_2$(*aza*-phyr)] (**57**) as WRC gives up to 11’000 TON$_{Co}$ (Table 10). Complex [Ni^{II}(ClO$_4$)$_2$(*aza*-phyr)] (**58**) is catalytic inactive.

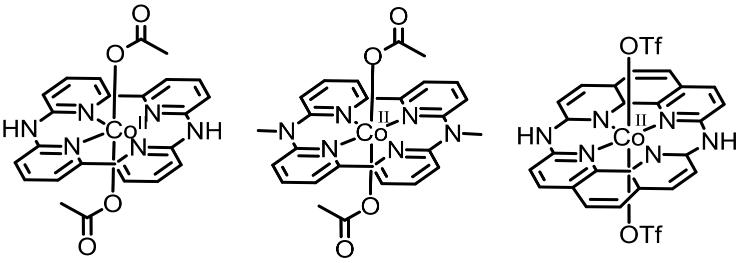

55 **56** **57**

Figure 59: *Structure of complex **55**, **56** and **57**.*

Complexes **55** to **57** showed a similar maximal H$_2$ formation rate of about 2 nmol/s which does not increase with increasing WRC concentration. This implies that the system is not WRC limited in this region. The H$_2$ rate increased steadily for [Co^{II}(ac)$_2$(*aza*-pyr)] (**55**) and [Co^{II}(TfO)$_2$(*aza*-phyr)] (**57**) until a maximum is reached. Afterwards a steep decline of the H$_2$ production was observed similar to other cobalt pyrphyrin complexes (Figure 60). Complex **55** shows a slower increase and decrease around the H$_2$ formation maximum. In contrast, complex [Co^{II}(ac)$_2$(*Me$_2$aza*-pyr)] (**56**) had a clear delay in H$_2$ formation of ∼15 h, followed by a relatively slow increase and decrease of the hydrogen formation rate (Figure 60). A reduction of the WRC to form the catalytic active species would happen within seconds (300 nmol/s photons, 50 nmol WRC at 5 μM, 10 mL). Thus, it does not explain the observed delay. The inactivity or different mechanism could arise from the missing hydrogen atom at the bridging nitrogen.

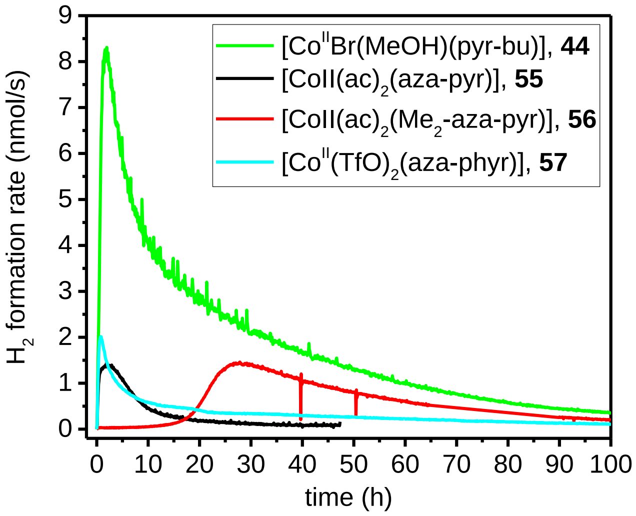

Figure 60: *Hydrogen evolution rate (nmol/s) for 5 µM solutions of* ***44*** *and* ***55*** *to* ***57*** *with 0.5 mM* $[Ru(bpy)_3]Cl_2$ *as PS, 0.1 M TCEP as recycling agent, 0.1 M* H_2Asc*/NaHAsc buffer (pH 5) as SED at 453 nm LED, photon flux of 0.30 ± 0.02* μEs^{-1}.

Less H_2 at a much lower rate was formed in comparison to the carbon bridged macrocyclic cobalt complexes, especially at elevated WRC concentrations (Figure 54). The TCEP oxidation was always higher than the formed H_2 but in-line with the observed differences for the alkylated pyrphyrin complexes. Complex **56** did show slightly lower turnover numbers at 1 µM (5000(300) TON_{Co}) than at 2 µM (7000(400) TON_{Co}) and similar TON_{Co} at 5 µM (4600(300) TON_{Co}). This implies a WRC limited mechanism for **56** at low concentrations. Complex **55** could easily be recycled by addition of fresh TCEP (0.2M) and PS (1 mM) after the reaction ceased. This gave an additional 7'600 TON_{Co}, showing sustainable catalytic activity. Recycling of **56** gave 35 % of the initially formed hydrogen. Changing from pH 5 to pH 4 did not lead to different results for **56** and **57**.

Aza-bridged macrocycles are synthetically easier accessible, but show slower H_2 formation rates compared to their carbon bridged analogues. Recycling of **55**, **56** and **57** did clearly show that the TON_{Co} are not limited by the WRCs, but by PS degradation.

Co-WRC	conc. WRC [a] (µM)	Total H_2 [a] (µmol)	Max. rate [a] (nmol/s)	Reaction time [b] (h)	TON_{Co} [a] (H_2/Co)	Max. TOF_{Co} [a] (H_2/Co/h)
55	1	36 ± 4	2.0 ± 0.1	23	3‘600 ± 450	740 ± 30
55[c]	1	76 ± 2	1.1 ± 0.1	115	7‘600 ± 1400	400 ± 20
55	5	56 ± 7	1.4 ± 0.1	39	1‘100 ± 150	100 ± 10
56	1	50 ± 3	1.7 ± 0.2	51	5000 ± 300	630 ± 30
56	2	140 ± 8	1.8 ± 0.1	92	7000 ± 400	320 ± 20
56	5	230 ± 20	1.4 ± 0.1	166	4600 ± 300	100 ± 10
57	1	110 ± 10	2.5 ± 0.1	50	11‘200 ± 1300	900 ± 50
57	5	130 ± 30	2.0 ± 0.1	125	2700 ± 600	150 ± 10
57	10	100 ± 20	2.2 ± 0.2	62	1000 ± 200	80 ±10

*Table 10: Summarised results of photocatalytic experiments with **55**, **56** and **57** as WRC at 1, 2 and 5 µM. Conditions: Total volume 10 mL H_2O, PS: 500 µM $[Ru(bpy)_3]Cl_2$, 0.1 M TCEP, 0.1 M NaHasc, pH 5, 453 nm LED, photon flux of 0.30 ± 0.02 µE/s. Highlighted in light blue: experiments with **55**. Highlighted in dark blue: experiments with **56**. Highlighted in green: experiments with **57**.[76] [a] Measured by GC. [b] Time required to form 95 % of totally measured H_2 (GC). [c] Restarting of catalysis by addition of 1 mM $[Ru(bpy)_3]Cl_2$ and 0.2 M TCEP after the reaction ceased.*

2.5 Catalytic benchmarking

WRCs are characterised by their stability (TON), catalytic activity or rates (TOF) and their overpotentials relative to the thermodynamic limit. The different setups used in photocatalytic water splitting by different groups makes the comparisons of catalysts difficult. Thus, predictions on how to improve upon known catalysts is difficult. Benchmarking of WRCs under identical conditions will give further insight regarding their performance and limitations. Additional methods, like electrochemistry are suitable for obtaining thermodynamic and mechanistic insights. An electrochemical setup simplifies the process since electrons are directly provided and no PS or SED are needed. Savéant, Artero and Dempsey et al. proposed schemes to benchmark WRCs in organic solvents, for example by assessing catalytic tafelplots.[126-129] In 2015 Artero and co-workers eluded trends for the relationship between the nature of the ligand backbone and the photocatalytic WRC stability of well-known poly-pyridyl cobalt complexes.[28] As such, it was shown that poly-pyridyl based complexes gave higher TONs_{Co} than $[\text{Co(bpy)}_3]^{2+}$. Purely pyridine based complexes showed lower stability than catalysts containing bipy subunits. Tetradentate poly-pyridyl complexes with a cis-open site performed better than their trans-counterparts. It was evident that even small changes of the conditions (SED, PS, pH, concentrations, ratios, light source) have strong influences on the parameters (TON, TOF, overpotential).[28]

A deeper insight in the mechanisms of poly-pyridyl complexes in aqueous media is required for predicting better performing WRCs. Apart from the achieved TONs and TOFs, the catalytic onset potential (COP) is assumed to be one of the more important parameters for sustainable molecular water splitting. The COP of poly-pyridyl complexes is high, especially compared those of cobaloxime complexes.[48,128,130,131] The lower overpotentials of poly-pyridyl complexes might result in more efficient WRCs. In this chapter we compare various poly-pyridyl cobalt WRCs for photocatalytic water splitting (Figure 61) by means of electrochemistry and their photocatalytic performance under the conditions described in chapter 2.4. Additionally, some selected examples of direct in-line GC measurements by electrolysis are given. This work was a result of a collaboration with Cyril Bachmann in our group, who synthesised catalysts **80**-**88** and performed the photocatalytic measurements of said catalysts.[83]

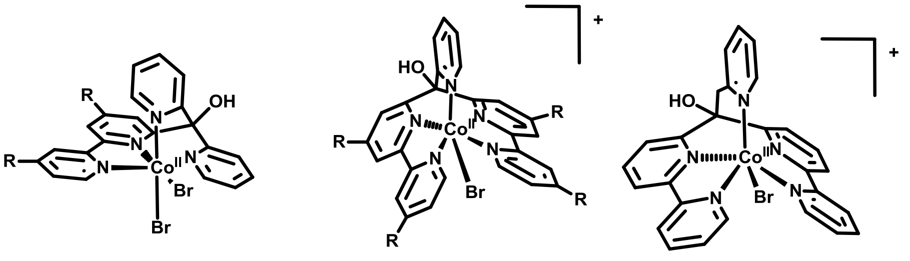

80; [CoBr(L1a)]Br (R = H)
81; [CoBr(L1b)]Br (R = OMe)

82; [CoBr(L2a)]Br (R = H)
83; [CoBr(L2b)]Br (R = OMe)

84; [CoBr(C-appy)]Br

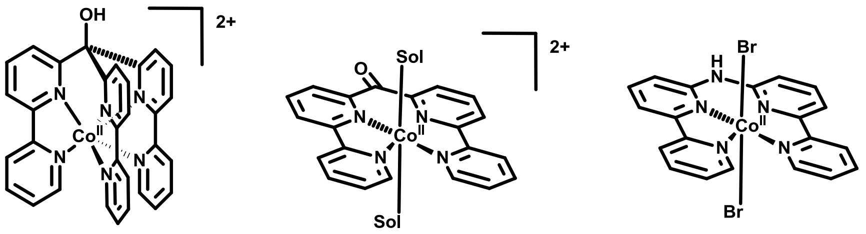

85; [Co(hpy)]Br$_2$

86; [Co(bpy$_2$CO)(Sol)$_2$]OTf$_2$

87; [CoBr$_2$(bpy$_2$NH)]

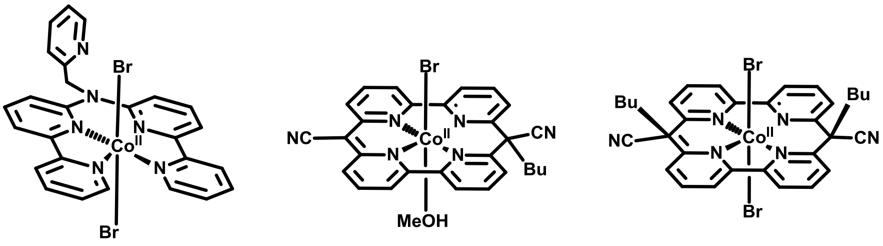

88; [CoBr$_2$(N-appy)]

44; [CoBr(pyr-bu)(MeOH)]

50; [CoBr$_2$(*cis*-pyr-bu$_2$)]

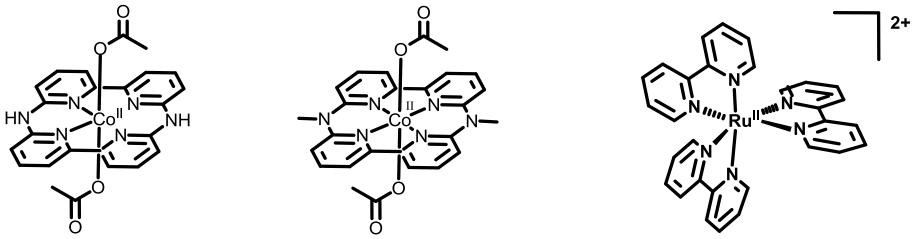

55; [Co(ac$_2$)$_2$(*aza*-pyr)]

56; [Co(ac$_2$)$_2$(*Me$_2$aza*-pyr)]

RuPS; [Ru(bpy)$_3$]Cl$_2$

Figure 61: Structures of the complexes in this chapter and the Re and Ru based photosensitisers. [20,40,49,55]

2.5.1 Comparison of the WRCs in photocatalytic proton reduction

All cobalt complexes of the benchmarking study were studied for their activity as WRCs under the conditions described in chapter 2.4. Complexes **80** to **88** were measured by Cyril Bachmann in our group.[83] Complex **50** was measured by Evelyne Joliat in our group.[3] Complex **57** was measured by Christian Bünzli in our group.[76] Table 11 gives the summary of the reactions with the catalysts shown in Figure 61. More in depth results for the already discussed complexes [Co^{II}Br(MeOH)(pyr-bu)] (**44**), [Co^{II}Br$_2$(*cis*-pyr-bu$_2$)] (**50**), [Co^{II}(ac$_2$)$_2$(*aza*-pyr)] (**55**), [Co^{II}(ac)$_2$(*Me$_2$aza*-pyr)] (**56**) and [Co^{II}(TfO)$_2$(*aza*-phyr)] (**57**) are found in chapter 2.4. Figure 62 shows a graphical overview of the TONs$_{Co}$ and maximum H_2 formation rate of all investigated catalysts for a faster reference.

For most complexes, two main domains were observed in the WRC concentration study, which is in agreement with the results of other poly-pyridyl cobalt complexes reported in literature.[20,40,49,55,132,133] Maximal H_2 formation rate for most complexes at WRC concentrations below 5 µM is limited by the activity of the WRCs and the electron transfer from the PS to the WRC. At low WRC concentrations the reduced PS$^-$ is quenched relatively slow due to the low probability of a WRC molecule meeting a PS$^-$. The reduced PS$^-$ undergoes degradation due to the instability of PS$^-$ in water and leads to a ceasing of the hydrogen production.[134] Hence, when going to lower WRC concentrations a steep decline in the maximal hydrogen formation rate and the total formed amount of hydrogen is observed for most catalysts. Nevertheless, the highest TONs and TOFs are obtained at very low WRC concentrations, because the WRCs are less severely limited by the measurement system than at higher WRC concentrations. The obtained results should be on the lower end and performance could possibly drastically improve if the system could be driven under exclusively WRC limited conditions. This hypothesis is highly supported by the possibility to restart the catalysis by addition of fresh TCEP and PS after the hydrogen formation ceased (2.4). At higher WRC concentrations (≥20 µM for non-macrocyclic catalysts) the main limitation for the obtained TONs and total produced hydrogen was the availability of the SED. Often a sharp decline of the hydrogen formation rate can be observed at high WRC concentrations, because all TCEP is oxidised to TCEPO by recycling of the DHA and providing fresh ascorbate to drive the catalytic cycle. This is attributed to accumulation of DHA which will shortcut the catalytic cycle as discussed in chapter 2.4. A levelling off of the maximal hydrogen formation rate is observed at high WRC concentration, indicating a photonflux limited region. At high concentrations (≥ 5 µM), TONs are limited by the consumption of the SED for fast catalysts (~20 nmol/s H_2), respectively PS decomposition for slower catalysts. Small changes in the reaction setup (pH, PS or SED) can have a huge impact on the catalytic performance of the WRCs, thus interpretation have to be considered with great care.

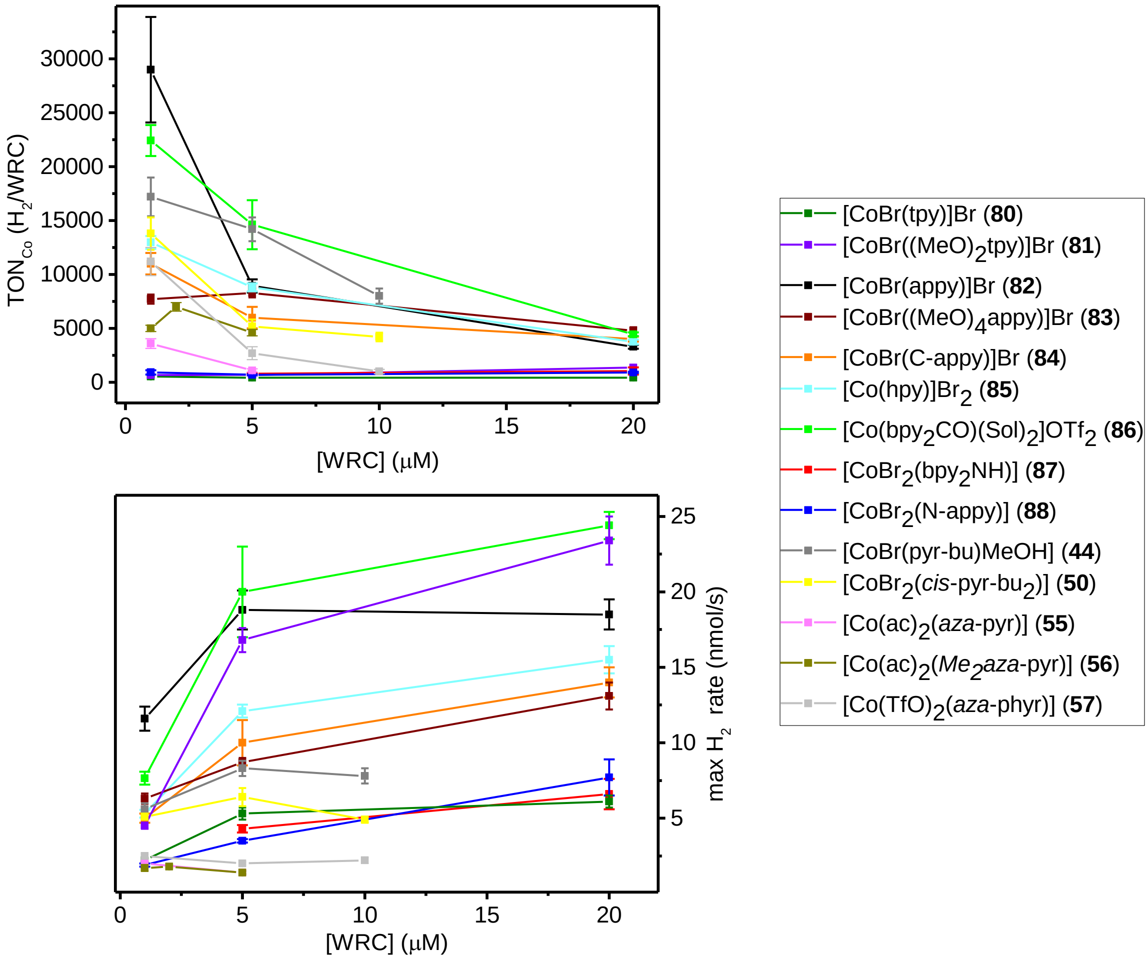

***Figure 62**: WRC concentration dependent TON in cobalt (top graph) and maximal hydrogen evolution rates (bottom graph) of photocatalysis in 10 mL water with 0.1 M TCEP, 0.1 M NaAscO (pH 5), 0.5 mM $[Ru(bpy)_3]Cl_2$ (RuPS) and 1, 5, 10 or 20 µM of different cobalt poly-pyridyl complexes (450 nm LED, 0.3 µE/s).*

At pH 5 [CoBr(tpy)]Br (**80**) showed a very low performance (Figure 62), because the low maximal H_2 formation rate competes with the PS decomposition as discussed in the previous paragraph. However, **80** showed greatly improved performance at pH 4 (5’000 TON_{Co}, 1 µM) when using ascorbate as buffer and SED with $[Re(bipy)(CO)_3(py)][TfO]$ as PS.[20] Similar catalysts were investigated by Castellano et al. and showed great catalytic performance with TON_{Co} between 4’000 and 5’000 at pH 4 highlighting the importance of the measuring conditions.[133] The similar complex $[CoBr((MeO)_2tpy)]Br$ (**81**) exhibits a two to five times higher maximal hydrogen formation rate at pH 5 compared to complex **80** leading to overall higher TONs. This effect is also represented in the electrochemical data of **81** showing a mechanistic change from pH 4 to pH 5 which is also present in complex **80**, but roughly shifted by one pH unit into the acidic region. The higher electron density on the cobalt centre in complex **81** induced by the electron pushing OMe substituents lead to an increase of the first reduction potential as discussed in chapter 2.5.2 as well as a shift of the pKa value by one. Thus, effectively favouring proton reduction with **81** at pH 5 which leads to the higher H_2 formation rates. Photocatalysis of a 5 μM solutions at pH 4 showed with 20 nmol/s for **80** and 30 nmol/s for **81** similar rates, but the higher stability of **81** lead to TON_{Co} of 6’000 vs the 2’000 TON_{Co}[20] obtained with complex **80**. This observation emphasises the importance of the electronics of the WRC, as rather small changes on the ligand backbone can have a strong influence on the overall performance in catalysis.Lower rates were observed for the five coordinated complex [CoBr((MeO)$_4$appy)]Br (**83**) compared to the non methoxylated analogue [CoBr(appy)]Br (**82**). Nevertheless, a similar amount of hydrogen was formed at 5 μM and 20 μM. Only at 1 μM a strong difference was observed, where the faster complex **82** achieved 29’000(5000) TONs compared to 7’700(400) TONs for **83**. This supports the hypothesis that at low concentrations the maximal rate of the WRC is often limiting the overall TONs obtained, because hydrogen formation is in competition with the PS degradation. Measurement of a 5 μM solution at pH 4 showed a strong rate increase for **83** (23 nmol/s) compared to **82** (15 nmol/s), thus leading to higher TONs (2’500 vs 1’200 H_2/Co). This result could also be observed by electrochemistry, because a significantly lower COP was observed by increased acidified solutions of **83** compared to **82** while they showed an almost identical COP at pH 5 (Table 12). The results highlight that even slight changes in the pH value can have a huge impact on the catalytic performance, thus concentration studies alone are not sufficient to characterise the activities of WRCs. In general, stronger trigonal prismatic distorted complexes seemed to show higher activities (TOF) and performance (TON). In-line with complex [CoBr(C-appy)]Br (**84**) showing a lower performance than **82**. However, [Co(hpy)]Br$_2$ (**85**) showed very similar performance to **84** where one would expect a better performance than even for **82**. [Co(hpy)]Br$_2$ (**85**) is hexa-coordinated and in comparison to the other catalysts there is no easily available site for proton reduction. Thus, a reorganisation has to occur prior to the formation of the active catalyst. A different mechanism for hydrogen production compared to **83** and **84** makes comparison between these catalysts difficult.

The amine bridged complexes [Co(ac)$_2$(*aza*-pyr)] (**55**), [Co(ac)$_2$(*Me$_2$aza*-pyr)] (**56**), [Co^{II}(TfO)$_2$(*aza*-phyr)] (**57**), [Co(bpy$_2$NH)Br$_2$] (**87**) and [CoBr$_2$(N-appy)] (**88**) showed all very low maximal hydrogen formation rates (1.4-4.3 nmol/s at 5 μM WRC) leading also to lower TONs (~1’000 TON_{Co}, 5 μM) compared to the carbon bridged analogues (Table 10, Table 11). Complex **56** and **57** deviated from the other catalysts by giving rise to 4’600(300) TON_{Co} (1.4(0.1) nmol/s H_2) and 2’700(200) TON_{Co} (2.0(1) nmol/s H_2) at 5 μM despite their low maximal hydrogen formation rate. Performance drastically increased at lower WRC concentrations for the macrocyclic complexes showing moderate to good H_2 formation at very low rates (1 μM, ~2 nmol/s). This highlights that the rate alone is not sufficient to predict the performance of a given catalyst. Even though complex **87** and **88** form a planar tetradentate ligand framework similar to the planar macrocyclic complexes, there is an obvious difference in performance at low concentrations. Direct comparison between catalysts seems therefore only possible in very similar catalysts with similar electronics, thus producing hydrogen over the same mechanism.

While a decomposition of the PS was indeed the limiting factor for the catalysis of **55**, **56** and **57**, degradation seems to occur at a considerable slower rate than for many non-macrocyclic complexes. Still, complexes **55**, **56** and **57** showed generally worse TONs, TOFs and maximal hydrogen formation rates than the carbon bridged macrocyclic complexes [Co^{II}Br(MeOH)(pyr-bu)] (**44**), [$Co^{II}Br_2$(*cis*-pyr-bu_2)] (**50**) and [$Co^{II}Br_2$(*trans*-pyr-bu_2)] (**52**). This is in-line with expectations, since the hydrogen formation rate for the *aza*-complexes is considerably lower than for their carbon analogues. It also clearly shows that the exchange of the bridging carbon atom by a nitrogen atom drastically reduces the maximal hydrogen formation rate, suggesting an interaction with the OH or H at the bridging carbon respectively. Electrochemical data showed that the COP for all *aza*-bridged complexes is more than sufficient to efficiently produce hydrogen and is not the reason for the lower performance (*Table 12*). The lower planar distortion of the complexes might be the reason for the lower performance, which would be consistent with the observation of Castellano et al., showing that trans-open coordination sites give lower TONs than cis-open structures.[28,133] Macrocyclic complexes **44**, **50** and **52**, **55**, **56** and **57** (Table 8 and Table 11) represent an exception, where moderate to high $TONs_{Co}$ and stable WRCs were observed with exclusively trans-open configuration. The macrocyclic ligand framework most likely increases the stability of the complexes, especially in the case of **44** where the ligand can act as anionic framework.

[Co(bpy_2CO)$(Sol)_2$]OTf_2 (**86**) deviated from the trends of the other planar complexes and performed extremely well giving similar or even higher TONs than [CoBr(appy)]Br (**82**). A crystal structure of **86** could be obtained from a protic solution where the formation of a dimer was observed making a different mechanism for hydrogen formation possible and thus impede direct comparison to other non-macrocyclic complexes.

In summary, any poly-pyridyl cobalt complex will probably show at least some catalytic activity as WRC for photocatalytic water splitting. Comparison of the different catalysts under the same conditions allows a systematic insight in the structure-activity relationship, which are often overlaid by different aspects. While concentration studies as well as pH dependency studies are fundamental to avoid misleading interpretation, they are not sufficient on their on to predict catalytic performance. Additional methods like electrochemistry are needed to obtain further insight and to be able to design better suited catalysts.

WRC	[WRC] (µM)	Maximal rate^a (nmol H$_2$/s)	TON$_{Co}$ ^{b} (H$_2$/Co)	Max. TOF$_{Co}$^{b} (h^{-1})	Total H$_2$ ^{b} (µmol)
[Co^{II}Br(MeOH)(pyr-bu)] (**44**)	10	7.8 ± 0.5	8000 ± 700	280 ± 20	800 ± 70
	5	8.3 ± 0.5	14‘200 ± 1100	590 ± 40	710 ± 60
	1	5.6 ± 0.4	17‘200 ± 1800	2000 ± 140	170 ± 20
[Co^{II}Br$_2$(*cis*-pyr-bu$_2$)] (**50**)	10	4.9 ± 0.2	4200 ± 360	180 ± 10	420 ± 40
	5	6.4 ± 0.6	5200 ± 640	460 ± 50	260 ± 40
	1	5.1 ± 0.2	13‘800 ± 1500	1820 ± 80	140 ± 20
[Co^{II}(ac)$_2$(*aza*-pyr)] (**55**)	5	1.4 ± 0.1	1‘100 ± 150	100 ± 10	56 ± 7
	1	2.0 ± 0.1	3‘600 ± 450	740 ± 30	36 ± 4
[Co(ac)$_2$(Me$_2$aza-pyr)] (**56**)	5	1.4 ± 0.1	4600 ± 300	100 ± 10	230 ± 20
	2	1.8 ± 0.1	7000 ± 400	320 ± 20	140 ± 8
	1	1.7 ± 0.2	5000 ± 300	630 ± 30	50 ± 3
[Co^{II}(TfO)$_2$(*aza*-phyr)] (**57**)	10	2.2 ± 0.2	1000 ± 200	80 ± 10	100 ± 20
	5	2.0 ± 0.1	2700 ± 600	150 ± 10	130 ± 30
	1	2.5 ± 0.1	11200 ± 1300	900 ± 50	110 ± 10
[CoBr(tpy)]Br (**80**)	20	6.1 ± 0.4	423 ± 29	110 ± 7	85 ± 6
	5	5.3 ± 0.4	438 ± 33	382 ± 29	22 ± 2
	1	2.2 ± 0.15	530 ± 54	792 ± 54	5.3 ± 0.5
[CoBr(DMTPy)Br (**81**)	20	23.4 ± 1.6	1360 ± 93	420 ± 29	272 ± 19
	5	16.8 ± 0.8	687 ± 38	1210 ± 58	34 ± 2
	1	4.5 ± 0.2	660 ± 50	1620 ± 72	6.6 ± 0.5
[CoBr(appy)]Br (**82**)	20	18.5 ± 1.0	3290 ± 160	330 ± 18	660 ± 30
	5	18.8 ± 1.30	8900 ± 600	1350 ± 90	450 ± 30
	1	11.6 ± 0.8	29000 ± 4900	4170 ± 50	240 ± 16
[CoBr(TMaPPy)]Br (**83**)	20	13 ± 1	4780 ± 320	236 ± 16	956 ± 65
	5	8.7 ± 0.3	8280 ± 400	626 ± 22	414 ± 20
	1	6.3 ± 0.34	7710 ± 420	2270 ± 120	77 ± 4
[Co(C-appy)]Br (**84**)	20	14.0 ± 1.0	4010 ± 22	520 ± 18	800 ± 50
	5	10.0 ± 1.5	6000 ± 1000	720 ± 108	300 ± 50
	1	5.0 ± 0.3	11000 ± 1000	1800 ± 108	110 ± 10
[Co(hpy)]Br$_2$ (**85**)	20	15.5 ± 0.9	3750 ± 330	280 ± 16	750 ± 45
	5	12.1 ± 0.4	8810 ± 380	870 ± 30	440 ± 19
	1	5.3 ± 0.3	12970 ± 590	1900 ± 90	130 ± 6
[Co(bpy$_2$CO)]OTf$_2$ (**86**)	20	24.4 ± 1.0	4450 ± 160	440 ± 16	890 ± 33
	5	20.0 ± 3	14600 ± 2280	1440 ± 220	730 ± 110
	1	7.6 ± 0.5	22400 ± 1030	2750 ± 150	224 ± 14
[Co(bpy$_2$NH)Br$_2$] (**87**)	20	6.6 ± 1.0	1050 ± 320	119 ± 18	210 ± 60
	5	4.3 ± 0.25	790 ± 30	310 ± 18	39 ± 2
	1	-	-	-	-
[CoBr$_2$(N-appy)] (**88**)	20	7.7 ± 1.2	915 ± 70	140 ± 20	180 ± 30
	5	3.5 ± 0.12	695 ± 53	252 ± 9	35 ± 3
	1	1.9 ± 0.1	914 ± 192	684 ± 36	9.2 ± 1.8
[Co(H$_2$O)$_6$)Br$_2$	20	0.8 ± 0.2	50 ± 35	14 ± 4	10 ± 5
	5	0.7± 0.05	110 ± 40	50 ± 5	5 ± 2
	0	0.2 ± 0.05	-	-	4 ± 2.5

***Table 11**: Summarised results of photocatalytic reactions with different WRCs in 10 mL water with 0.1 M TCEP, 0.1 M NaAscO, 0.5 mM [Ru(bpy)$_3$]Cl$_2$ (RuPS) at pH 5, 450 nm LED, 0.3 µE/s and different WRC concentrations.*
^{a} Measured by GC, ^{b}According to total H$_2$ measured by GC

2.5.2 Electrochemistry at various pH values

Electrochemistry is suited for the investigation of thermodynamic and kinetic parameters of molecular WRCs.[47,126,128,135] It is known from literature that water reduction at the cobalt centre can occur over different reduction/protonation steps (Figure 63).[28,46,136] All protonations and reductions are represented by cobalt centred processes, however this is often a terminology since the redox processes can also be ligand based. The polarisation of the Co-H bond might vary, but is represented in Figure 63 by a hydride.

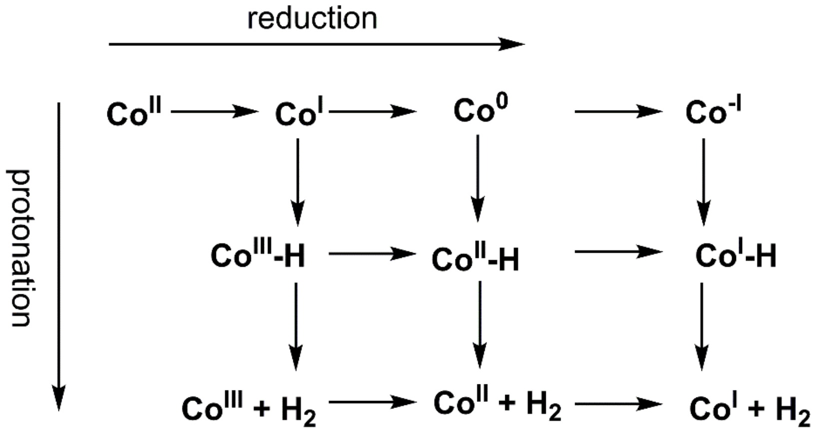

***Figure 63**: Schematic representation of possible electron and proton transfer steps upon (electro)chemical reduction of a Co^{II} WRC in the presence of protons. Horizontal arrows represent reduction and vertical arrows protonation steps.*

Molecular chemistry can be strongly influenced by the choice of the solvent. As such, electrochemistry in water of the WRCs gives the best insight into the mechanistic of the process, given that sustainable proton reduction is best performed in water. Solubility of poly-pyridyl catalysts is in almost all cases more than sufficient to allow electrochemical investigations even under buffered aqueous conditions.[28] It was shown by Ott et al. that measuring of WRCs in a Britton Robinson buffer solution (BRB, H_3PO_4:AcOH:$B(OH)_3$) across a broad pH range could give valuable insight the properties of the WRCs.[115] Figure 61 shows the broad variety of investigated WRCs for the electrochemical and photocatalytic trials. Complexes **80** to **88** were synthesised by Cyril Bachmann in our group.[83] In contrast to electrochemistry in organic solvents, irreversibility of all transitions was observed. This was to some degree expected, since at the catalytic active reduction a reversible reduction would not be feasible. Meaning that only the cathodic reduction potential (E_{pc}) of the transition can be identified complicating interpretation. The E_{pc} does not exactly correspond to the reduction potential of the transition which is defined as the mean value of the E_{pc} and the anodic reduction potential (E_{pa}) for reversible transitions. Nevertheless, reasonable assumptions can be based upon the obtained results and detailed analysis of the electrochemical responses allowed the correlation of the E_{pc}s and the pH as shown for [CoBr(tpy)]Br (**80**, Figure 64) giving rise to a Pourbaix diagram based on the peak currents.[83,137]

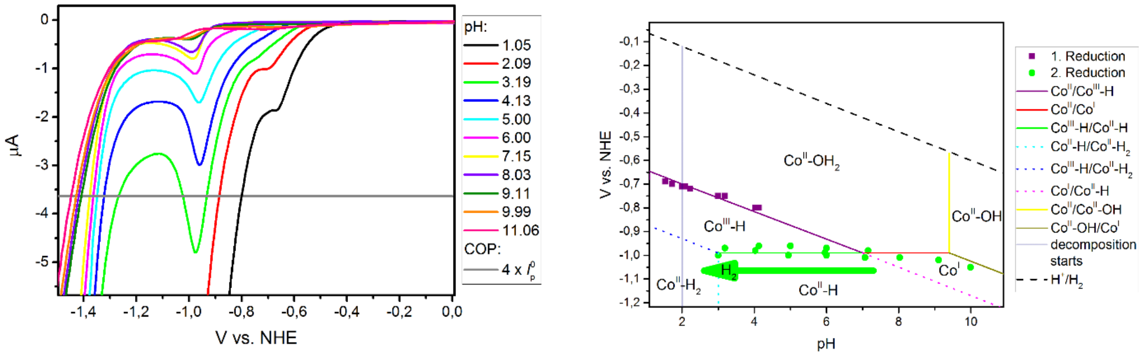

***Figure 64**: Voltage current response for the E_{pc} of [CoBr(tpy)]Br (**1a**) as a function of pH (left graph), Pourbaix diagram (right graph, based on peak potentials) of **1a** (1 mM in 0.1 M NaOTf and 40 mM BRB (each 40 mM H_3PO_4, CH_3COOH and $B(OH)_3$) referenced to NHE with $MVCl_2$. CE: Pt, RE: AgCl in 3 M KCl, WE: HMDE), 100mV/s.*[83]

Two irreversible reductions from 0 V to -1 V vs NHE can be observed. Even though the first reduction is partially superimposed on the second transition hampering the E_{pc} identification of the first transition, a clear pH dependency was observed (42 mV/pH). The first reduction reduction is assigned to a Co^{II} to Co^{III}-H transition involving one electron and one proton supported by the slope and the absence of catalysis due to the low current intensity (purple, Figure 64, right). The second reduction is pH independent and assigned to the transition of a Co^{III}-H to a Co^{II}-H (green, Figure 64, right). The second reduction reduces in intensity with increasing pH suggesting a Co^{II} to Co^{I} reduction above pH 7 up to the pK_a value of the Co^{II}-OH$_2$/Co^{II}-OH couple at pH 9.3 estimated by UV/Vis titration (yellow, Figure 64, right). The Co^{II}-OH is hardly soluble and might even form dimers according to UPLC-MS, causing a drop of the current response above pH 8. Below pH 2 partial reversible decomplexation (40 % decomplexation at pH 1) of **80** was observed by UPLC-MS. The purple line crosses the green line approximately at pH 7 which would mean that Co^{I} has a pK_a value of ~7. The pK_a value of Co^{II}-H is 3 or lower, since no pH dependency was observed down to pH 3.0. A current increase from pH 7 downwards was observed for the first and second transition. Thus, the current increase for the second reduction is attributed to an increased availability of Co^{II}-H$_2$ by protonation of Co^{II}-H. Co^{II}-H$_2$ irreversibly decomposes to Co^{II} and H_2 closing the catalytic cycle. This predicts a highly active WRC in the acidic region with an overpotential ≥ 800 mV. Clearly, at higher pHs (> 4 pH), the rate of catalysis drops to insignificant values, in-line with photocatalytical experiments (chapter 2.5.1).

To be able to compare the various measured WRCs the onset potential for the catalysis (COP) was defined by four times the peak current of a defined one electron reduction (4 x i^0p) which should ensure a good basis for comparison. Multiple electron transitions are very unlikely at this current values, but still low enough to ensure small deviation from the effective value. 1 mM concentrations of all catalysts were examined in a 40 mM BRB over a pH range from 2-11 with a hanging mercury drop electrode (HDME). A 0.85 mM solution of methyl viologen dichloride ($[MV]Cl_2$, -0.44 V vs NHE)[138] was measured, because the first reduction (MV^{+2}/MV^{+1}) is reversible and was used as reference for the onset potential of a one electron reduction (i^0p) as well as reference to the standard hydrogen electrode (NHE).[139]

Each catalysts exhibited one or two pre-catalytic reductions as already seen for other poly-pyridyl catalysts which is illustrated by the first reduction of **80** in Figure 64.[28,40,140] The first reduction (E_{pc1}) was assigned to a Co^{II}/Co^{I} transition or a Co^{II}/Co^{II}-H transition if there is a proton coupled electron transfer (PCET, chapter 2.3). If there is a second non catalytic reduction (E_{pc2}) present it is generally attributed to a Co^{I}/Co^{0}, Co^{I}/Co^{II}-H or Co^{III}-H/Co^{II}-H based transition. Most pre-catalytic reductions are pH independent which suggests that the reduced species cannot be protonated or only at a very slow rate. Decreasing pH values often lead to an overlap of the pre-catalytic reductions by a catalytic wave, obscuring their reduction potentials. All complexes showed a strong current increase at strong cathodic potentials which was assigned to the catalytic proton reduction. All reductions at pH 5 are shown in Table 12, since photocatalytic proton reduction was also performed at pH 5 with all WRCs. Naturally, the COP is pH dependent and shifts to a more cathodic potential with increasing pH obtaining a slope often close to -59 mV per pH unit and thus implies a PCET in the rate determining step (rds) of the catalytic hydrogen evolution. The pentadentate poly-pyridyl complex [CoBr(appy)]Br (**82**) and [CoBr(C-appy)]Br (**84**) deviate from this general trend implying a two electron reduction at the rate determining step with a slope of 35(1) mV or 23(1) mV respectively (Table 12). This leads to a decrease of the overpotential at lower pH values. Blank experiments were performed to exclude any background effects of the electrolyte in the BRB solution or of $[Co(H_2O)_6]Br_2$ as catalyst. Proton reduction at the HDME occurs at significant lower potentials for the blank measurements than for most investigated catalysts. Though, some complexes show a very similar or even more cathodic COP in a certain pH range (**80** pH > 3-4; **81** pH 4-5, **84** pH ≥ 4) thus making evaluation under this specific conditions impossible. Additionally, the reduction potential of the used PS in photocatalysis ($[Ru(bpy)_3]Cl_2$, RuPS) is shown in Table 12, because a more positive or too close reduction potential of the PS^- compared to the COP of the WRCs will reduce the proton reduction rate or even stop catalysis altogether. $[Ru(bpy)_3]Cl_2$ shows a constant reduction potential of -1.21 V in the catalytic relevant region of pH 3 to pH 7. This is enough driving force for most WRCs as seen in Table 12. However, pH ranges are observed where the COP of the WRC is stronger cathodic than for the PS, severely limiting hydrogen formation in photocatalysis.

Table 12: Summarised results of the electrochemical examinations of complexes from Figure 61 at 1 mM in 40 mM BRB (each 40 mM H_3PO_4, CH_3COOH and $B(OH)_3$) referenced to NHE with $MVCl_2$. CE: Pt, RE: AgCl in 3 M KCl, WE: HMDE. The catalytic onset potential (COP) was defined as the 4 fold electron flow of the one electron reduction determined for 1 mM MV^{2+}.

WRC	E_{pc1} in V[a]	E_{pc2} in V[a]	COP in V at pH 5[a] (mV / pH unit)
[CoBr(tpy)]Br (**80**)[b]	-0.97 (pH 7-9)[c]	-	-1.35[d]
[CoBr((MeO)$_2$tpy)]Br (**81**)	-1.15 (pH 6-8)	-	-1.49[d]
[CoBr(appy)]Br (**82**)[e]	-0.68 (pH 5-9)[f]	-0.97 (pH 4-9)[g]	-1.07 (-35 ± 1)
[CoBr((MeO)$_4$appy)]Br (**83**)	-0.96 (pH 6-9)[h]	-	-1.08 (-58 ± 6, pH 4-10)
[Co(C-appy)]Br (**84**)[b]	-0.78 (pH 2-6)	-	-1.23 (-23 ± 1)[i]
[Co(hpy)]Br$_2$ (**85**)[j]	-0.53 (pH 2-8)[k]	-	-1.02 (-51 ± 3)
[Co(bpy$_2$CO)]OTf$_2$ (**86**)[b]	-[l]	-[l]	-1.01 (-65 ± 2)
[Co(bpy$_2$NH)Br$_2$] (**87**)[b]	-0.50 (pH 2-9)	-0.55 (pH 2-9)	-1.14 (-53 ± 3)[m]
[CoBr$_2$(N-appy)] (**88**)[b]	-0.53 (pH 4-9)[n]	-0.58 (pH 4-10)[o]	-1.15 (-69 ± 3)[p]
[CoBr(MeOH)(pyr-bu)] (**44**)	[q]		-1.15 (-39 ± 2)
[CoBr$_2$(*cis*-pyr-bu$_2$)] (**50**)	-0.36 (pH 2-9)	-0.59 (pH 2–11)	-1.11 (-58 ± 1)
[Co(ac$_2$)$_2$(*aza*-pyr)] (**55**)	-0.17 (pH 3-6)	-	-1.02 (-78 ± 4)
[Co(ac$_2$)$_2$(*Me$_2$aza*-pyr)] (**56**)	-0.27 (pH2-11)	-0.58 (pH 2-6)	-1.11 (-42 ± 2, pH 3-7; pH 8-11: almost constant)
[Ru(bpy)$_3$]Cl$_2$ (**RuPS**)	-1.21 (pH 3-7)	-	constant
[Co(H$_2$O)$_6$]Br$_2$	-1.1 (pH 5) -1.12 (pH 6) -1.16 (pH 7)	-	-1.36 (-66.9 ± 0.1)
None (plain HMDE)[a]	-	-	-1.25 (pH 2-7: -62 ± 1; pH 7-12: constant)

[a] The standard error was estimated to be ± 0.01 V; [b] Electrolyte: 0.1 M NaOTf; [c] below pH 3 E_{pc1} is obscured by the catalytic wave and above pH 9 it decreases with 50 mV/pH; most probably due to deprotonation of coordinated H_2O; [d] At pH 5 the COP is more cathodic than the proton reduction at the HMDE; [e] Electrolyte: 0.5 M NaOTf; [f] pH 2: E_{pc1} is -0.70 V and above pH 9 E_{pc1} decreases with 60 mV/pH; most probably due to deprotonation of coordinated H_2O; [g] below pH 4 E_{pc2} is obscured by the catalytic wave and above pH 9 the potential increases with 35 mV/pH; [h] below pH 6 E_{pc1} is obscure by the catalytic wave; [i] below pH 5 the COP is too close to the background from HMDE; [j] Electrolyte: 0.1 M KNO_3; [k] above pH 8 the complex precipitated under these conditions; [l] the CV of this structure was very complex; [m] above pH 10 the COP is too close to the background from HMDE; [n] below pH 4 and above pH 9 E_{PC1} becomes more cathodic; [o] below pH 4 E_{pc2} becomes more cathodic; [p] above pH 9 the COP is too close to the background from HMDE; [q] the CV of this structure exhibited several partially pH dependent reductions between -0.2 - -0.8 V.

The increasing onset potential for proton reduction of [CoBr(tpy)]Br (**80**) from pH 3-4 (Figure 65) is in good agreement with the lower hydrogen formation rates and TONs at pH 5 compared to the better performance of **80** at pH 4.[43,49]
Derivatisation of the bipy subunits by two or four methoxy substituents in complexes [CoBr(tpy)]Br (**80**) or [CoBr(appy)]Br (**82**) to give [CoBr($(MeO)_2$tpy)]Br (**81**) and [CoBr($(MeO)_4$appy)]Br (**83**) respectively had a significant effect on the electrochemical properties. The methoxy substituents are electron donating and increase the E_{PC1} of **80** (-0.68 V) and **82** (-0.96 V) compared to **81** (-0.97 V) and **83** (-1.15 V) (Table 12). There is no direct correlations of the hydrogen formation rate to the measured COP. While **83** showed indeed a lower hydrogen evolution rate and performed considerably worse at low concentrations than [CoBr(appy)]Br (**82**), [CoBr($(MeO)_2$tpy)]Br (**81**) showed a higher rate and generally higher TONs than [CoBr(tpy)]Br (**80**). This was due to an increased pKa of the reduced complex of **81**, thus allowing catalysis at higher pH values (Table 11). The higher pKa of the reduced species of **83** compared to **82** by introduction of the electron donating groups lead to lower overpotentials in acidic conditions. This could indicate a change of the pKa value for Co^I and or Co^I-H. However, since the slope of **83** is with -58 mV/pH considerably higher than the - 35 mV/pH for **82** at pHs at ≥5 a lower COP is observed for **82**.

The non-macrocyclic complexes [CoBr(appy)]Br (**82**), [CoBr(C-appy)]Br (**84**) and $[Co(hpy)]Br_2$ (**85**) support the hypothesis that a high distortion of an octahedral configuration towards a trigonal prismatic coordination will lead to lower reduction potentials (E_{PC1}, Table 12).[49] Octahedral $[Co^{II}(bpy)_3]^{2+}$ is reduced at -0.9 V vs NHE,[141] whereas the reduction potential of [CoBr(C-appy)]Br (**84**) is at -0.78 V, thus 100 mV more cathodic than for [CoBr(appy)]Br (**82**).[49] Trigonal prismatic $[Co(hpy)]Br_2$ (**85**) exhibited the lowest E_{pc1} of these compounds (Table 12). The value of -0.53 V for **85** is in good agreement with the one reported in acetonitrile (-1.18 V *vs*. Fc/Fc$^+$;[142] which corresponds to -0.54 V *vs*. NHE)[143,144]. The E_{pc1} of [CoBr(tpy)]Br (**80**) is several 100 mV more cathodic (-0.97 V) compared to **82**, **84** and **85**, which is attributed to the only marginally distorted octahedral structure.[20] Distortion towards a prismatic structure also generally leads to a higher catalytic performance.[49] Indeed, the COPs of **82**, **84** and **85** in Figure 65 follow this trend, being the lowest for $[Co(hpy)]Br_2$ (**85**, -1.02 V) with the strongest distorted octahedral structure followed by the slightly less distorted [CoBr(appy)]Br (**82**, -1.07 V) and being the highest for [CoBr(C-appy)]Br (**84**, -1.23 V). The drastically lower COP of the less distorted [CoBr(tpy)]Br (**80**) compared to [CoBr(appy)]Br (**82**) below pH 4 contradicts this hypothesis. However, a structural reorganisation of the WRC is expected upon protonation or reduction which might lead to a different mechanism for **80** below pH 4 invalidating direct comparison between the catalysts in this measurement region. It is therefore noteworthy that lower overpotentials for hydrogen evolution by distortion is only observable when comparing very similar complexes. The structural effect is otherwise dominated by stronger effects. A lower overpotential does also not necessarily lead to higher catalytic performance. Similarly, a higher hydrogen formation rate does not necessarily lead to higher TON_{Co} (Table 11).

[Co(bpy$_2$CO)]OTf$_2$ (**86**) might form dimers as observed by single crystal X-ray diffraction, thus invalidating direct comparison with other catalysts. The electrochemical behaviour is very complex and four partially pH dependent pre-catalytic peaks were observed. However, **86** was one of the catalysts with the most positive COP and also showed very high catalytic activity (Table 11, Figure 65).

Even though a hanging mercury dropping electrode was used for the pH dependent CV measurements (shows the highest overpotential of any traditional working electrodes under this measurement conditions), a considerable background (hydrogen formation at mercury electrode) was observed at all pH values. From all measured catalysts, only [CoBr(tpy)]Br (**80**, pH 4-7), [CoBr((MeO)$_2$tpy)]Br (**81**, pH 5-12), [CoBr(C-appy)]Br (**84**, 2-4), [CoBr$_2$(cis-pyr-bu$_2$)] (**50**, pH 10-11), [Co(bpy$_2$NH)Br$_2$] (**87**, pH 11) and [CoBr$_2$(N-appy)] (**88**, pH 10-11) showed a higher COP than the blank mercury electrode at certain pH regions. Thus, they are excluded from analysis in this regions (Figure 65 and Figure 67). In most cases the WRCs exhibit a lower overpotential for proton reduction compared to the background signal, thus showing catalytic activity as electrocatalysts. Nevertheless, it is evident that one of the major drawbacks of poly-pyridyl catalysts is their high overpotential compared to the thermodynamic proton reduction potential (Figure 65). Even the lowest COPs are 600-800 mV more negative than the thermodynamic proton reduction potential. In comparison, the catalyst [CoBr$_2$((DO)(DOH)pn)] (**89**)[128], a derivative of the well-known cobaloximes, shows with an overpotential of only 300-400 mV the typical low reduction potential for this class of WRCs (Figure 65). This results are in good agreement with data found for this and similar complexes in organic solvents.[48,128,130] It needs to be noted that Artero et al. showed that at the proposed COP of **89** no hydrogen formation was observed. Hydrogen production was only detected below -0.75 V vs NHE attributed to the formation of nanoparticles. This again supports the conclusion that thorough and careful investigations are needed to obtain further insights into the behaviour of the catalysts.[145] It also needs to be noted that a WRC in electrocatalysis might react considerably different than a WRC in photocatalysis.

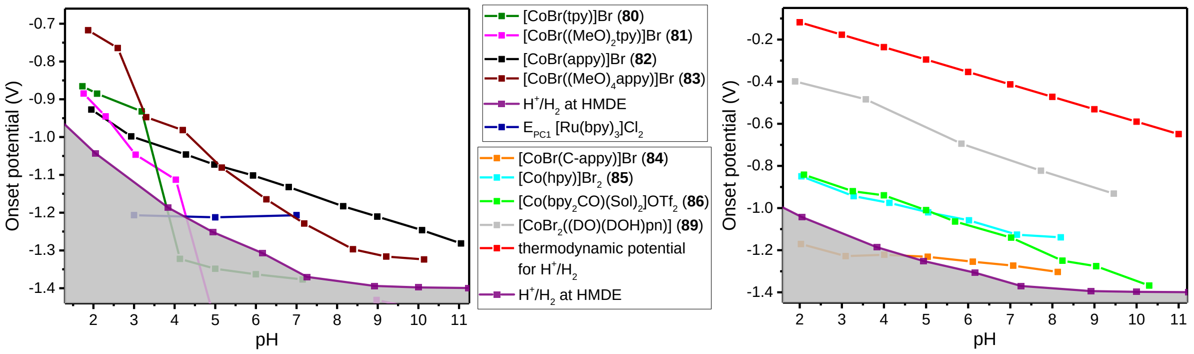

***Figure 65**: Catalytic onset potentials (COP) of complex **80** – **86** and **89** along with the blank measurement (HMDE, purple), E_{PC1} of $[Ru(bpy)_3]Cl_2$ (RuPS, dark blue) and the (calculated) thermodynamic H^+/H_2 potential (red) as a function of pH in 40 mM BRB and electrolyte (*Table 12*). The pH was adjusted with 10-20 µL additions of 5 M aqueous NaOH per pH unit. The grey area represents the region where proton reduction at the HMDE occurs. Potentials were referenced to the NHE with MV^{2+} (1 mM) and the onset potential was defined as the four fold electron flow of the one electron reduction ($MV^{2+} \rightarrow MV^{+}$).*

The non-macrocyclic N-bridged complexes $[Co(bpy_2NH)Br_2]$ (**87**) and $[CoBr_2(N\text{-appy})]$ (**88**) showed two pre-catalytic reductions (E_{pc1} and E_{pc2}) with a small peak separation between -0.5 and -0.6 V (Table 12). The low reduction potentials might be a consequence of the sp^2 character of the bridging N-atom. The extended conjugation might stabilise the reduced complexes leading to less cathodic reduction potentials. Similarly, all macrocyclic complexes showed pre-catalytic reductions at rather positive potentials. Supported by the strong stabilisation of the reduced species by the delocalisation of the electron along the extended π-system of the ligand framework.

The COP values of $[Co^{II}(ac_2)_2(\textit{aza}\text{-pyr})]$ (**55**) and $[Co^{II}(ac_2)_2(Me_2\textit{aza}\text{-pyr})]$ (**56**) are quite positive for poly-pyridyl complexes (Figure 67). Surprisingly, **55** shows one of the lowest onset potentials of all poly-pyridyl catalysts. Methylation on the nitrogen atom lead to a dramatically more positive COP below pH 7. While a more or less steady decline in COP with a slope of -78 mV/pH was observed for $[Co^{II}(ac_2)_2(\textit{aza}\text{-pyr})]$ (**55**), $[Co^{II}(ac_2)_2(\textit{Me}_2\textit{aza}\text{-pyr})]$ (**56**) showed a considerable flatter slope with -42 mV/pH between pH 3 to pH 7 and only small COP changes from pH 8 to pH 11 (-1.21 V to -1.22 V). This implies a mechanistic change of the hydrogen evolution with increasing pH for catalysis with **56**. An almost pH independent reduction peak at -1.256 V to -1.226 V was observed (Figure 66). The small changes of 7 mV/pH was thought to be the result of a peak broadening at higher pH values. However, the current decrease at -1.25 V with increasing pH value suggests a catalytic deactivation of this reduction.

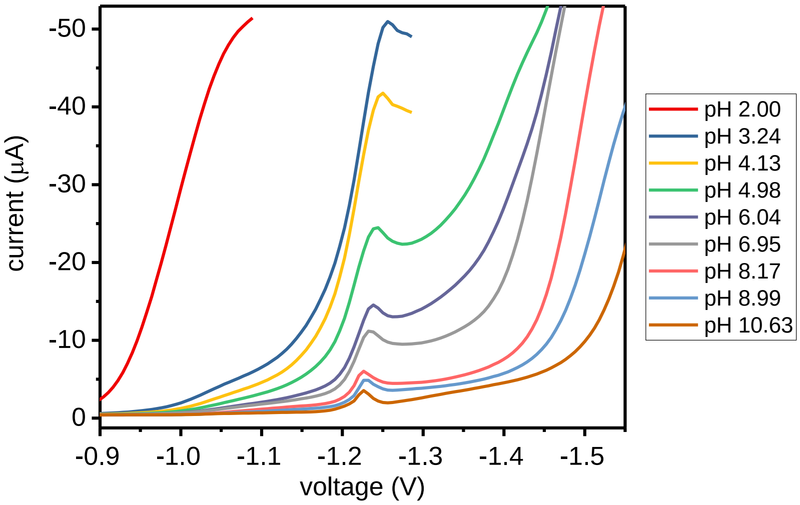

Figure 66: *Electrochemical examinations of complex [Co^{II}(ac$_2$)$_2$(Me$_2$aza-pyr)] (**56**) at 1 mM in 40 mM BRB (each 40 mM H_3PO_4, CH_3COOH and $B(OH)_3$) referenced to NHE with MVCl$_2$. CE: Pt, RE: AgCl in 3 M KCl, WE: HMDE. The catalytic onset potential (COP) was defined as the 4 fold electron flow of the one electron reduction determined for 1 mM MV^{2+}.*

Reduction of the bridging secondary amine in [Co^{II}(ac$_2$)$_2$(*aza*-pyr)] (**55**) to the corresponding imine (Figure 42) might be the reason for the more positive COP (Figure 67), which is not accessible in [Co^{II}(ac$_2$)$_2$(*Me$_2$aza*-pyr)] (**56**). Even though **56** showed one of the lowest COP (-1.02 V at pH 5) of all investigated poly-pyridyl based cobalt catalysts, one of the lowest maximal hydrogen formation rate (1.4 nmol/s H_2, 5 µM WRC, pH 5) was observed in photocatalysis. Actually, all *aza*-bridged complexes showed very low hydrogen formation rates. While this resulted in low hydrogen formation for [Co(bpy$_2$NH)Br$_2$] (**87**) and [CoBr$_2$(N-appy)] (**88**) arguably good TON$_{Co}$ were observed for [Co^{II}(ac$_2$)$_2$(*aza*-pyr)] (**55**) and [Co^{II}(ac$_2$)$_2$(*Me$_2$aza*-pyr)] (**56**). Though, **55** and **56** exhibited even lower maximal hydrogen formation rates than **87** and **88** (Table 12). This shows again that indebt electrochemical investigations combined with varied photocatalysis experiments are needed to estimate the efficiency of a WRC as simple comparison of the COP does not correspond with the maximal hydrogen formation rates. Additionally, higher maximal hydrogen formation rates do not necessarily lead to higher TON$_{Co}$ as discussed in chapter 2.5.1. However, inclusion of a bridging nitrogen atom seems to heavily reduce the maximal obtainable hydrogen formation rate leading to slower catalysts.

No additional trends could be elucidated for the macrocyclic complexes and complexes **87** and **88** (Figure 67). Their electrochemistry is often very complex and hampers interpretation. All macrocyclic and *aza*-bridged complexes showed considerably lower rates than good performing open-cycle poly-pyridyl complexes.

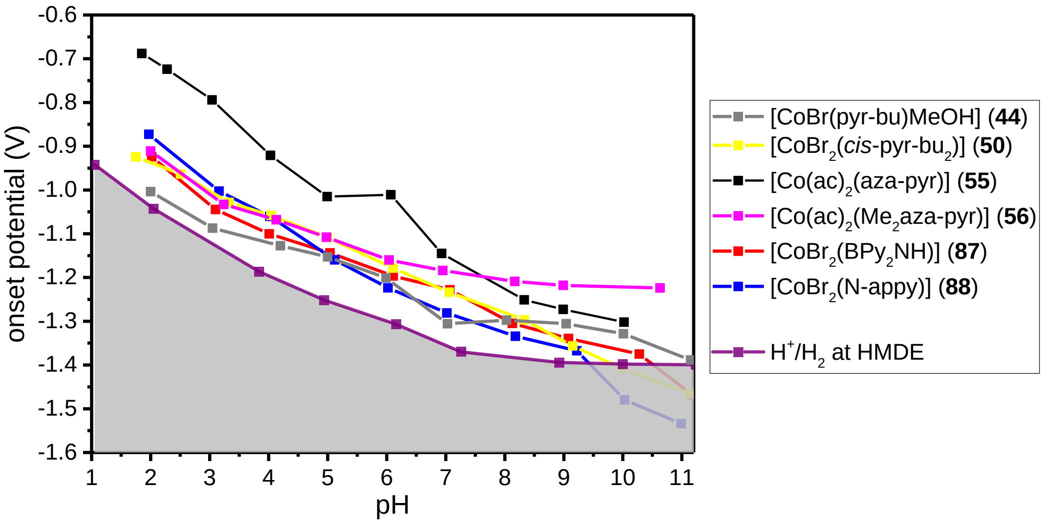

***Figure 67**: Catalytic onset potentials (COP) of complex **44**, **50**, **55**, **56**, **87** and **88** along with the blank measurement (HMDE, purple) as a function of pH in 40 mM BRB and electrolyte (*Table 12*). The pH was adjusted with 10-20 µL additions of 5 M aqueous NaOH per pH unit. The grey area represents the region where proton reduction at the HMDE occurs. Potentials were referenced to the NHE with MV^{2+} (1 mM) and the onset potential was defined as the four fold electron flow of the one electron reduction (MV^{2+} → MV^{+}).*

2.5.3 In-line GC electrocatalysis

Setup development

It was shown in literature that at the proposed COP of [$CoBr_2$((DO)(DOH)pn)] (**89**) of no hydrogen formation was observed[145]. Thus, further analytical measurements were needed to verify the electrochemical onset potential for proton reduction for the investigated WRCs by direct measurement of the formed hydrogen. Therefore we exchanged the reactor vial in Figure 49 by a three vial setup which allowed continuous in-line detection of the formed hydrogen by electrolysis. Figure 68 shows the most recent setup for in-line GC electrocatalysis which is the result of optimisations based on several preceding devices. In the following some aspects of the device design are explained and highlighted.

A three chamber setup separated by NS5 glass frits gave the best results. The counter electrode (CE), working electrode (WE) and reference electrode (RE) were separated from each other. The CE and RE (both in buffered electrolyte solution without analyte) were in direct contact over the NS5 frit with the catalytic solution (yellow, Figure 68, buffered electrolyte solution with catalyst). NS5 frits did show a very slow mixing of the solutions from the different chambers while still ensuring a sufficient ion flow from WE to RE (Compared to the relatively fast equilibration of the solvent chambers when NS4 frits were used). Theoretically, the RE electrode could be positioned nearer to the WE, especially when using a secondary reference electrode as shown in Figure 68. This could be achieved by an additional inlet at the WE chamber. A better current response would be expected in such cases, since the resistance between RE and WE would be reduced due to the missing NS5 glass frit and the shorter distance. However, for our intended purposes it would not lead to any benefits. The distance between WE and RE inhibits CV measurements, because the E_{PC} and E_{PA} positions are highly dependent on the distance between WE and RE. A broadening with increasing distance seemingly leading to irreversible transitions was observed. Therefore the potential offset of the reference electrode was always premeasured in a 797VA Computrace electrochemical analyser. Additional inlets at the chamber with the working electrode would allow to keep the pH constant over the reaction course by continuous titration. However, the pH change up to the COP is miniscule and can be neglected.

Pressure equilibration between the different compartments was achieved by a glass tubing connection above the liquid surface and was crucial for the setup. In absence of an internal pressure equilibration, even very slight pressure differences lead to a pressure equilibration by continuously forcing the solution from the higher pressure chambers over the frit to the lower pressure chambers. As noted, mixing of the analyte containing solution with the electrolyte solutions should be reduced to a minimum. The argon carrier gas was directly inserted into the solutions by tubing similar to the normal photocatalytic measurement method. However, the inlet was split by a T-fitting ensuring separate bubbling through the solution at the CE and WE, thus increasing the response of the system and leading to less hydrogen evolution fluctuation. Similarly, both outlets were combined by a T-fitting to insert the gas flow into the GC after drying over molecular sieve. It was important to use T-fittings with an adequate dead volume, since a too small dead volume lead to different pressures between the two tubing's which lead to one-sided bubbling. Similarly, the inlet tubing should show a higher resistance than the outlet tubing otherwise parallel bubbling through the solutions is often hampered. This was achieved by using smaller inner diameters for the inlet tubing compared to the outlet tubing. After this improvements, it remains to be tested if the pressure equilibration over the glass tubing is still needed.

As CE a coiled up platinum wire with a larger surface than the WE was used while a commercial available secondary Ag/AgCl (3 mol/l KCl) was used as RE. Since the investigated complexes exhibit high COPs according to our electrochemical investigations, a WE with a very high onset potential in water was crucial. Mercury was therefore WE of choice for this measurements. Initially, a plastic coated wire and later on a teflon coated Pt wire was used to ensure that the conductibility of the connection wire was only given when the wire was in direct contact with the mercury and not the catalytic solution. The penetration of the mercury surface lead to relatively large deformation of the surface, because of the high surface tension of mercury. Ensuring a total absence of small direct contacts with the connection wire was difficult. Thus, a cell was designed where a tungsten wire is melted into the glass to ensure wiring to the potentiostat from below the mercury surface which lead to the design shown in Figure 68. It was possible to add a magnetic stirring bar which would sit on top the mercury layer and stir the solution continuously. Nevertheless, all linear sweep voltammetry (LSV) measurements were performed in absence of a magnetic stirrer due to the high background fluctuations at low currents when stirring.

The in-line GC measurements normally showed a delay of the LSV (~15 min) compared to the in-line detection of hydrogen by GC. This arised from the resting time of the carrier gas (H_2 saturation of the catalytic solution, distance to the GC column and interaction of H_2 with the mol sieve) and the time resolution of the GC measurements (one measurement every 5 min). Electrolysis with Pt wire as WE and CE at 0.1 M H_2SO_4 showed near to 100 % faradaic yield.

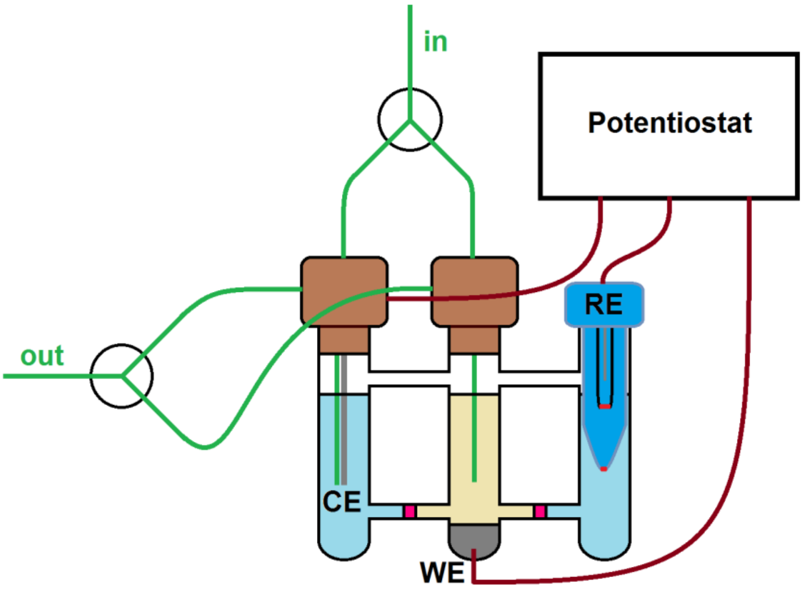

Figure 68: Illustration of the measurement setup for in-line GC electrolysis. The three glass vial setup replaces the catalytic solution vessel *in Figure 49*. Green: tubing of the argon gas flow. Brown: wiring of the electrodes to the potentiostat. Magenta: NS5 glass frits. Red: frits. Yellow: catalytic solution. CE (grey): counter electrode, curled Pt wire. WE (dark grey): working electrode, liquid mercury in contact with a tungsten wire. RE (dark blue): secondary reference electrode, Ag/AgCl (3mol/l KCl).

*LSV of [CoBr$_2$((DO)(DOH)pn)] (**89**) and [Co(tpy)Br]Br (**80**)*

Linear sweep voltammetry (LSV) and in-line GC measurements of [CoBr$_2$((DO)(DOH)pn)] (**89**) showed that the main hydrogen production occurred below -0.8 V, thus verifying the results of Artero et al. and ensuring the feasibility of the developed measurement setup.[145] In contrast to literature, small amounts of hydrogen were observed at the first reduction from -0.3 V to -0.5 V vs NHE, thus implying low catalytic activity at the first reduction. It needs to be noted that the current by LSV should lead to a considerable higher hydrogen formation and the faradaic yield remained in the single digit percentage region. Thus, a considerable amount of the measured current showed reduction without formation of hydrogen which was at least partially attributed to the reduction of the catalyst to form nanoparticles which act as the active catalyst below -0.8 V.[145] Hence, the proposed onset potentials reported in Figure 65 are most likely not the real COPs which could mean that the main advantage of cobaloximes compared to poly-pyridyl catalysts (lower COP) is in fact lost. However, the small amounts of hydrogen detected in our system could also imply that the first reduction is indeed catalytically active, but the reduced **89** decomposes fast under the measurement conditions forming more stable nanoparticles that exhibit a higher COP. The fast decomposition could explain the low performance of **89** as WRC in water.

The faradaic yield over the complete measurement region is relatively high with 85 to 90 % including the first reduction which showed almost no hydrogen formation.

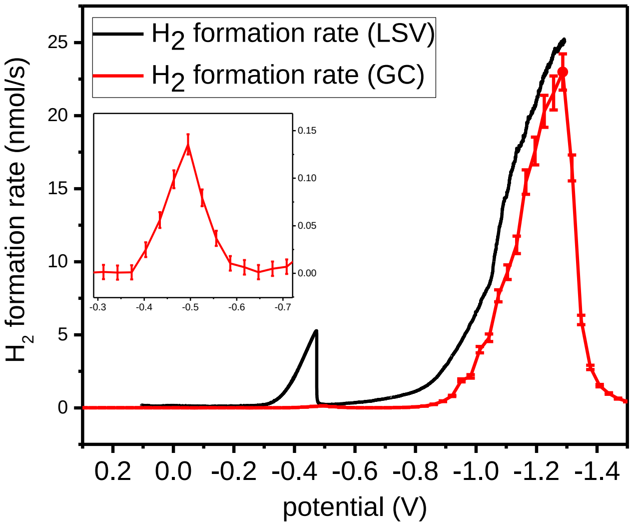

***Figure 69**: Linear sweep voltammetry (LSV) curves for in-line GC electrolysis of [$CoBr_2$((DO)(DOH)pn)] (**89**) and the corresponding in-line GC measurements (GC). Potentials were referenced to the NHE with MV^{2+}. (1 mM WRC, 40 mM BRB, 0.1 M NaOTf, pH 2, 0.1 mV/s, WE: Hg, CE: Pt, RE: Ag/AgCl 3 M)*

LSV and in-line GC measurements of [Co(tpy)Br]Br (**80**) at different pHs showed clear hydrogen formation at similar potentials compared to the COP proposed by CV in BRB (Figure 65). At low and moderate hydrogen formation rates in LSV and GC measurements the sharp current drop of the COP between pH 3.2 to pH 4.2 observed for the CV in BRB (Figure 64) is shifted to higher pH values (pH 7, Figure 70). However, at high hydrogen formation rate a clear current drop can be observed from pH 2 to pH 4 (Figure 71). The different structure of the hydrogen evolution rate courses leads to somewhat different results depending on the definition of the onset potential. Thus, at higher hydrogen formation rates different effects are observed than at lower hydrogen formation rates (Figure 70 vs Figure 71). Considering that hydrogen can be detected reliably at very low rates, comparison of lower rates as shown in Figure 70 is more reasonable than at the higher rates shown in Figure 71 to define a onset potential. Nevertheless, one needs to be aware of these effects which are equally relevant for the definition of the COP (in our case 4*i^0p) in the BRB CV. Quantitative faradaic yields were observed within the uncertainty of the measurements in all cases. Blank measurements under identical measurement conditions in absence of WRC were performed at all pH values (pH 7 shown in Figure 71) and always showed a significant higher onset potential than in presence of a WRC. Considering the relatively high COP of the investigated poly-pyridyl catalysts, often relatively small differences (100-200 mV) of the onset potentials were observed between the catalytic solutions and the blank mercury measurements. Additionally, it was shown by repeated blank measurements that the baseline did deviate to some extent. It is therefore recommended to measure a baseline for each individual measurement followed by exchange of the electrolyte with identically prepared electrolyte and addition of WRC containing electrolyte solution into the WE chamber. This ensures the highest possible reproducibility.

It was favourable to degas all solutions prior adding them into the measurement cell, because the catalyst could be reduced by mercury. Similarly, application of a small negative current at low pH inhibited this process and does not interfere with the detection of the onset potential.

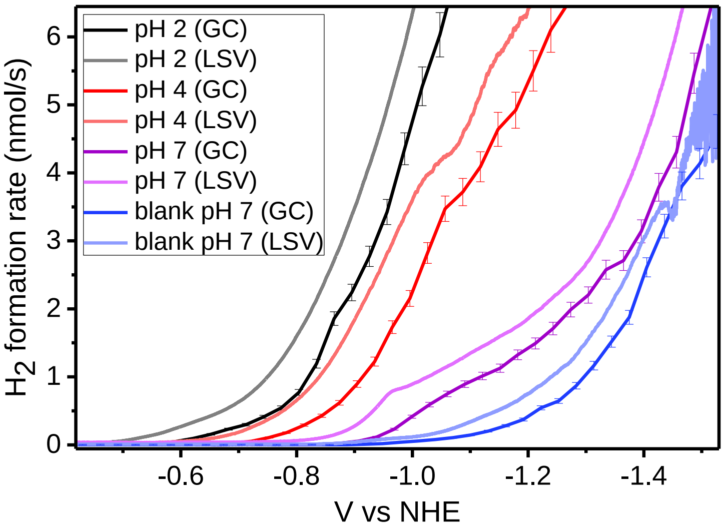

***Figure 70**: Zoomed in linear sweep voltammetry (LSV) curves for in-line GC electrolysis of [Co(tpy)Br]Br (**80**) and the corresponding in-line GC measurements (GC) at pH 2, 4 and 7 as well as the blank measurement at pH 7 under identical conditions in absence of WRC. Potentials were referenced to the NHE with MV^{2+}. (1 mM WRC, 40 mM BRB, 0.1 M NaOTf, 0.1 mV/s, WE: Hg, CE: Pt, RE: Ag/AgCl (3 M KCl))*

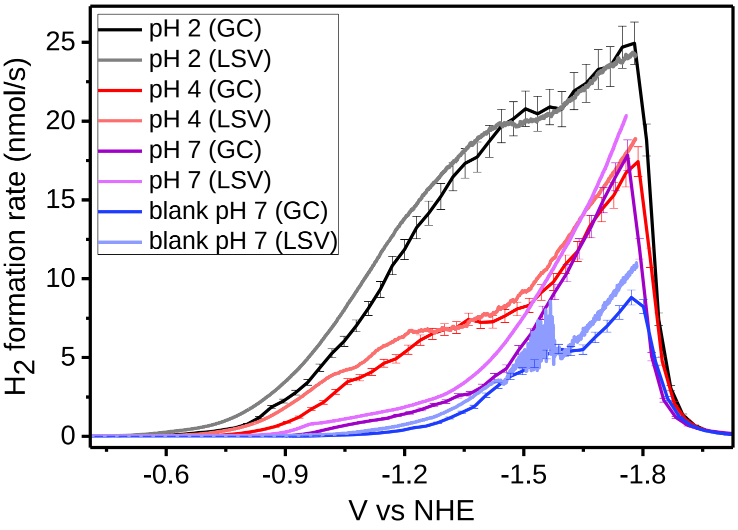

***Figure 71**: Zoomed out linear sweep voltammetry (LSV) curves for in-line GC electrolysis of [Co(tpy)Br]Br (**80**) and the corresponding in-line GC measurements (GC) at pH 2, 4 and 7 as well as the blank measurement at pH 7 under identical conditions in absence of WRC. Potentials were referenced to the NHE with MV^{2+}. (1 mM WRC, 40 mM BRB, 0.1 M NaOTf, 0.1 mV/s, WE: Hg, CE: Pt, RE: Ag/AgCl (3 M KCl))*

3. Conclusion and Outlook

All cobalt complexes with poly-pyridyl or phenanthroline based macrocycles showed good to very good catalytic performance as WRCs in homogenous photocatalysis ([$Co^{II}(OH_2)_2$(pyr)]) (**41**), ([$Co^{II}(H_2O)_2$(pyr-MePEG)][ClO_4] (**43**), [Co^{II}Br(MeOH)(pyr-bu)] (**44**), [$Co^{II}Br_2$(*cis*-pyr-bu$_2$)] (**50**)[3], [$Co^{II}Br_2$(*trans*-pyr-bu$_2$)] (**52**)[3], [Co^{II}(ac)$_2$(*aza*-pyr)] (**55**), [Co^{II}(ac)$_2$(*Me$_2$aza*-pyr)] (**56**) and [Co^{II}(TfO)$_2$(*aza*-phyr)] (**57**[76]). The pyrphyrin complexes showed particularly good performance and TONs higher than 20’000 H_2/Co could be obtained. This contrasts reported cobalt porphyrin complexes, which are not very efficient WRCs. We conclude that pyridyl subunits are important for improving WRC performance.

With these ligands and complexes, solubilities are often an issue. Exchanging the axial ligands by less coordinating counter-ions such as perchlorate did influence solubilities for non-alkylated and mono-alkylated pyrphyrin complexes while di-alkylated pyrphyrin complexes showed reasonable solubilities in water even with halides as axial ligands. Solubilities in slightly acidic water are in all cases good enough for homogenous catalysis. The axial ligands did not show an influence on the catalytic performance, therefore the structurally better defined halide complexes were preferred. Performance of the *aza*-bridged complexes **55**, **56** and **57** reached up to 11’000 TON_{Co}, considerably less than their carbon-bridged analogues. This was mainly due to the low maximal H_2 rates which were generally in the range of 2.5 nmol/s (5 µM), compared to the 6-9 nmol/s (5 µM) for carbon-bridged complexes. Catalytic studies showed that all complexes remained catalytically active, even after H_2 formation ceased. Therefore, catalysis is not in first priority limited by the WRCs stabilities. Nickel complexes such as [Ni^{II}(pyr-bu)][ClO_4^-] (**46**) and [$Ni^{II}(ClO_4)_2$(*aza*-phyr)] (**58**) did not show catalytic activity. This coincides with our investigations with nickel based poly-pyridyl catalysts where no catalytic activities were found as well. The anionic nature of the mono- and non-alkylated complexes leads to stronger metal to ligand interactions and thus to more robust catalysts. Even though the solubilities of macrocyclic systems are often lower than for acyclic cobalt poly-pyridyl catalysts, mercury poising experiments excluded formation of nanoparticles throughout.

The nice performance of macrocyclic complexes makes further research with such systems highly attractive. Functionalisation of the ligand backbone or at the bridge allows widespread tuning of electronics of the ligand and the complex. The ketone bridged cobalt complex (Scheme 1) is the result of such a backbone change. Preliminary results show very high catalytic activity being in agreement with the previous statement. Immobilisation of the catalysts allows for better assessing of the stabilities by recycling experiments. The catalytic performance might then be driven to the point where the WRCs become limiting by decomposition, giving an indication of the maximal performance of such WRCs. Immobilisation might be achieved by covalent binding on a surface or by non-covalent interactions. Functionalisation at the bridging atom (carbon or nitrogen) by alkylation might allow for such a system. Phosphate groups might be introduced along the same strategy for a more covalent binding on oxide surfaces. Alternatively, the anchor group might be introduced at the pyridyls, because keeping sp^2 hybridisation at the bridging functions leads to better stability and performance, as partly shown in this study.

Macrocyclic poly-pyridyl complexes showed only low performance as PS. $[Zn^{II}(py)(pyr\text{-}bu)][OTf]$ (**49**) showed low fluorescence and so did the zinc complex of underivatised pyrphyrin. The fluorescence is low and the absorption bands of the complexes are generally more blue shifted compared to similar porphyrins, disfavouring pyrphyrin based PS. Increased absorption by derivatisation of the ligand backbone to obtain better performing PSs is probably the best way to go in the future.

Benchmarking the catalysts and comparison with cobaloximes and acyclic poly-pyridyl complexes is difficult even under identical conditions. We conclude that trends can only be defined when comparing structurally (and mechanistically) similar catalysts. Within similar catalysts, higher TON_{Co} are generally achieved for those with a higher maximal H_2 formation rate. Similarly, higher overpotentials in similar catalysts lead to lower H_2 formation rates. pH values play an important role and can lead to diverging behaviour. Cobalt poly-pyridyl complexes show generally higher maximal H_2 formation rate (up to 20 nmol/s, 5 μM) than macrocyclic poly-pyridyl complexes (up to 9 nmol/s, 5 μM), but are more long-term stable and produce ultimately more H_2. Different mechanisms might work for different classes of catalysts. Exchanging the bridging carbon atom with a nitrogen reduces H_2 formation rates and lowers catalytic performance. The good performance of $[Co^{II}(TfO)_2($*aza*-phyr$)]$ (**57**) and $[Co^{II}(ac)_2($*Me₂aza*-pyr$)]$ (**56**), especially at low concentrations are the “exception to the rule” since these higher conjugated system lead to better results. This supports the hypothesis that the bridging atom is essential for the catalytic behaviour; $[Co^{II}(ac)_2(Me_2aza\text{-}pyr)][ac]_2$ (**56**) clearly outperforms $[Co^{II}(ac)_2(aza\text{-}pyr)]$ (**55**).

According to electrochemistry, all catalysts are reduced at least once before entering catalysis. An in depth understanding how the catalytic active species looks like and how H_2 is formed is the base for development of better WRCs. $[CoBr_2((DO)(DOH)pn)]$ (**89**) showed a low overpotential regarding H_2 evolution which is typical for cobaloximes like catalysts. A closer look at this system showed that meaningful electrochemical H_2

evolution is observed later than the CV implied. Thus, data has to be evaluated carefully and brought in clear context to what they are compared to. Further spectroelectrochemical experiments such as performed for [Co^{II}Br(MeOH)(pyr-bu)] (**42**) or the performed in-line GC measurements are especially promising. Instead of a linear sweep voltammetry, it would be very interesting to see how the WRCs perform at a continuous fixed voltage at the onset potential. The very specific IR bands of pyrphyrin and mono-alkylated pyrphyrin are also very promising candidates for spectroelectrochemical investigation by combining IR spectroscopy with electrochemistry since cleavage of an alkylchain upon reduction would lead to formation of a visible CN stretch frequency. Thus, the proposed loss of a butyl chain of [Co^{II}Br$_2$(*trans*-pyr-bu$_2$)] (**40**) upon irradiation could be verified.

Poly-pyridyl macrocycles based cobalt complexes thus show very promising catalytic activity and are suitable candidates for immobilised WRCs in future devices.

4. Experimental Part

4.1 Syntheses

4.1.1 General

A standard nitrogen/vacuum line was used for all dry or air free reactions. Glassware was either dried in a drying oven at 130 °C overnight or by a hot air gun and applied vacuum. Water was doubly distilled before use. Ice was produced in-house from deionised water by a micro-cube ICE from Kibernetik. Distilled technical grade solvents were used for extractions and column chromatography. Dry EtO_2 and THF were dried over Na/benzophenone. Deuterated solvents ($CDCl_3$, d_6-dmso, d_6-acetone, d_7-dmf, *d*-TFA, D_2O) were purchased from Armar. Column chromatography was performed either using aluminium oxide 90 neutral (neutral alumina) or silica gel 60 (silica), chromafix C_{18} ec columns were obtained from Macherey-Nagel. TLC was run either on POLYGRAM-plates of aluminium oxide neutral F_{254} from Macherey-Nagel or on aluminium-plates of silica gel F_{254} from Merck.

All chemicals were of reagent grade and used without further purification. Phosphorus(V) oxychloride (99 %), phosphorus(V) chloride (99 %), n-heptane (99 %), 1,10-phenanthroline (99 %), chlorobenzene (99 %), ^tBuOH (99 %), cobalt(II) carbonate (99.5 %), trifluormethanesulphonic acid (99 %) and TFA (99.5 %) were purchased from abcr. Anhydrous DMF (99.8 %, extra dry) was purchased from Acros. Sodium hydroxide pellets (purum) and K_2CO_3 (purum) were purchased from ERNE surface. 2,6-dibromopyridine (purum) and 6,6'-dibromo-4,4'-dimethyl-2,2'-bipyridine was purchased from I^2CNS. Anhydrous $MgSO_4$ (puriss), HCl (32 %), H_2SO_4 (95 – 97 %) and acetic acid (glacial, puriss) were purchased from Merck. n-Butyllithium solution (2.5 M or 1.6 M in hexane), sodium hydride (60 % dispersion in mineral oil, or dry (95 %)), α-cyanoacetamide (99 %), 1-iodobutane (99 %), 1-bromopentane (98 %), 1-bromo-2-(2-methoxyethoxy)ethane (90 %), 2-(bromomethyl)-1,3-dioxolane (96 %), KO^tBu (98 %), 1,4-diiodobutane (99 %), iodomethane (puriss), 1,10-phenanthroline (99 %), 1,3-dibromopropane (99 %), phosphorus tribromide (99 %), diethyl ether (puriss, dried over molecular sieve), H_2O_2 (50 % wt), nitrobenzene (puriss), diethylcarbonate (99 %), ethylene glycol (99 %), LiH (95 %), benzene (99.9 %), anhydrous pyridine (99.8 %), cobalt(II) acetate tetrahydrate (98 %), cobalt(II) bromide hydrate, NaOH solution (1.0 N), dioxane (puriss), $ZnCl_2$ (98 %), pyridine (puriss), silver trifluoromethanesulfonate (98 %), (+)-sodium-L-ascorbate (puriss), (+)-ascorbic acid (puriss), fuming HNO_3 (100 %), fuming H_2SO_4 (20 -30 % free SO_3), ortho-phosphoric acid (85 %), boric acid (99.99 %), cobalt(II) perchlorate hexahydrate, nickel(II) perchlorate hexahydrate, iron(II) perchlorate hexahydrate, cupper(II) perchlorate hexahydrate and dioxane (puriss) were purchased from Sigma Aldrich (Merck).

Acetone (puriss), dichloromethane (puriss), methanol (puriss), hexane (puriss), pentane (puriss), chloroform (puriss), toluene (puriss), ethanol (puriss), diethylether (puriss), isopropylether (puriss), THF (puriss), DMF (puriss) and CH_3CN (puriss) were purchased from either Sigma Aldrich (Merck), Merck or CDH. N_2, O_2, NH_3 () and H_2S were purchased from PanGas. Tris(2-carboxyethyl) phosphine hydrochloride (purum) was purchased from Apollo Scientific. $NaHCO_3$ (purum) was purchased from Honeywell. Na_2CO_3 was purchased from Romil.

The syntheses of $[Ru(bpy)_3]Cl_2 \cdot 5\ H_2O$[41] , $[Re(bipy)(CO)_3(py)][TfO]$[42], *cis*-pyr-bu$_2$ (**4**)[40], *trans*-pyr-bu$_2$ (**5**)[40], [Co^{II}Br$_2$(*cis*-pyr-bu$_2$)] (**50**)[3], [Co^{II}Br$_2$(*trans*-pyr-bu$_2$)] (**52**)[3], [CoBr(tpy)]Br (**80**)[20] and complexes **81** to **88**[83] have been described in literature.

4.1.2 Ligand Syntheses

*6,6'-Dibromo-2,2'-bipyridine (**1**)*

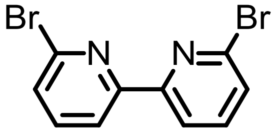

The synthesis was adapted from literature.[77] 2,6-dibromopyridine (90 g, 0.38 mol) and dry Et_2O (550 mL) were transferred into a 2 L three necked round bottom flask. The flask was equipped with a low temperature thermometer, a mechanical stirrer and a pressure equilibrated 250 mL dropping funnel containing n - BuLi (2.5 M in hexane; 152 mL, 0.38 mol) solution. The solution was cooled down to -70 to -80 °C by partially inserting into a liquid nitrogen bath and a white suspension was obtained. The n-BuLi solution was added dropwise over 24 min while keeping the temperature below -70 °C. The dropping funnel was washed with dry Et_2O (10 mL) and afterwards $POCl_3$ (8.9 mL, 0.093 mol) in dry Et_2O (250 mL) was added dropwise to the reaction mixture within 1 h. The reaction was kept below -60 °C. After stirring for an additional 20 min at -60 to -50 °C the cooling bath was removed and the reaction allowed to warm up to 0 °C (1 h 30 min). The suspension turned more and more sluggish. H_2O (500 mL) was added at 0 °C and the organic phase was evaporated at reduced pressure. The H_2O phase was extracted three times with 800 mL dichloromethane and the organic phases were washed once with 500 mL water. The combined organic phases were dried over $MgSO_4$ and filtrated. The slightly yellowish solution was concentrated until crystallisation started. Addition of an equal amount of heptane and cooling to 4 °C in the fridge yielded the desired product **1** (23.6 g, 76 mmol, yield: 40 %) in high purity after filtration. **HPLC**: 20.61 min (23 min method); **^{1}H NMR** ($CDCl_3$, 300 MHz) δ (ppm): 8.35 (d, 2 H), 7.63 (t, 2 H), 7.48 (d, 2 H).

*(6E,17E)-23,24,25,26-Tetraazapentacyclo[17.3.1.1^{2,6}.1^{8,12}.1^{13,17}]hexacosa-1(23),2,4,6,8(25),9,11,13,15,17,19,21-dodecaene-7,18-dicarbonitrile (**2, pyr, pyrphyrin**)*

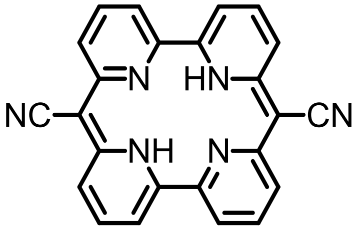

The Synthesis was adapted from literature.[68,87] NaH (23.5 g, 60 % in mineral oil, 0.59 mol) and dry DMF (400 mL) were transferred into a 2 L three necked round bottom flask. The flask was equipped with a magnetic stirring bar, a thermometer and a 250 mL pressure controlled dropping funnel containing α-cyanoacetamide (25.2 g, 0.30 mol) dissolved in dry DMF (100 mL). The suspension was cooled down to 3 °C and the α-acetamide was added dropwise over one hour while keeping the temperature below 5 °C. After the H_2 formation ceased (15 min), **1** (23.5 g, 0.075 mol) was added portion wise under a light nitrogen counter flow. The ice bath and thermometer were removed; the dropping funnel exchanged with a cooling condenser and the colourless suspension was heated to 120 °C (oil bath temperature). The suspension turned dark violet red within the first hour at 120°C and formed an agglomerate which distributed evenly after some hours. After 2.5 d the reaction was cooled down to ambient temperature after which 150 mL water was added. After filtration and washing with water (500 mL), acetone (500 mL) and dichloromethane (500 mL) the pure dark violet red pyrphyrin ligand **2** (2.24 g, 15 % yield) was obtained. **FT-IR** (KBr) (cm^{-1}): 3047, 2185, 1627, 1592, 1527, 1438, 1194, 1182, 985, 972, 864, 844, 777, 722, 648, 629, 517; **Anal. calcd.** for $C_{24}H_{14}N_6$ (%): C, 74.60; H, 3.65; N, 21.75 ; Found: C, 74.42; H, 3.67; N, 21.37.

*(7E)-18-Butyl-23,24,25,26-tetraazapentacyclo[17.3.1.1^{2,6}.1^{8,12}.1^{13,17}]hexacosa-1(23),2(26),3,5,7,9,11,13(24),14,16,19,21-dodecaene-7,18-dicarbonitrile (**3, pyr-bu**)*

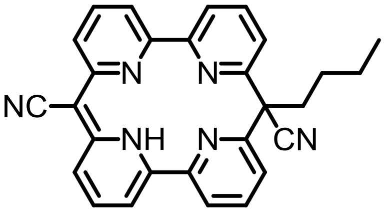

The synthesis was adapted from literature.[68] NaH (0.36 g, 14.4 mmol), pyrphyrin (0.30 g, 0.78 mmol) and dry DMF (40 mL) were added into a 100 mL one necked schlenk flask. The flask was equipped with a magnetic stirring bar and a cooling condenser. The dark violet red suspension was stirred for 2 h at 60 °C while turning into a brighter reddish suspension. 1-butyl-iodide (3 mL, 24.5 mmol) was added dropwise via a syringe at 30 °C. After 3 h at 120 °C, the dark red solution was added into 200 mL water to precipitate a dark red oily and sticky solid which was centrifuged, decanted and washed twice with water. The washed solid was transferred with MeOH into a 50 mL one necked round bottom flask, concentrated and dried at high vacuum overnight (0.5 g, dark red solid). After purification over silica column (8:2; CH_2Cl_2: hexane) **3** was obtained as a glittering red solid (0.1 g, 28 % yield). **HPLC**: 21.9 min (23 min method); **^{1}H NMR** ($CDCl_3$, 300 MHz): δ (ppm) = 7.87-7.35 (m, 2 H), 7.77-7.69 (m, 2 H), 7.68-7.56 (m, 2 H), 7.68-7.44 (m, 4

H), 7.7.15-7.02 (m, 2 H), 2.80-2.45 (m, 2 H), 1.25-1.00 (m, 4 H), 0.8-0.55 (m, 3 H); **ESI-MS**: m/z = 465.1 $[M + Na]^+$ **FT-IR** (KBr) (cm^{-1}): 2933, 2182, 1623, 1576, 1549, 1516, 1463, 1430, 1378, 1335, 1178, 988, 797, 747, 629

*(7E)-18-Pentyl-23,24,25,26-tetraazapentacyclo[17.3.1.1^{2,6}.1^{8,12}.1^{13,17}]hexacosa-1(23),2(26),3,5,7,9,11,13(24),14,16,19,21-dodecaene-7,18-dicarbonitrile (**6, pyr-pent**)*

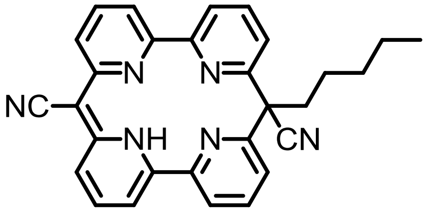

The synthesis was adapted from literature.[68] NaH (0.12 g, 4.9 mmol), pyrphyrin (0.1 g, 0.26 mmol) and dry DMF (10 mL) were added into a 25mL one necked schlenk flask. The flask was equipped with a magnetic stirring bar and a cooling condenser. The dark violet red suspension was stirred for 1.5 h at 60 °C while turning into a brighter reddish suspension. 1-pentyl-bromide (1.4 g, 9.1 mmol) was added dropwise via a syringe at 30 °C. After 27 h at 110 °C the now dark red solution was poured into 200 mL water to precipitate a dark red solid which was filtrated and washed with water. The washed solid was dried by evacuation at high vacuum to afford a dark red solid (0.1 g). After purification over silica column (4:6; CH_2Cl_2:hexane) **6** was obtained as a dark red solid (32 mg, 32 % yield). **HPLC**: 22.43 min (23 min method); **FT-IR** (KBr) (cm^{-1}): 2955, 2926, 2856, 2182, 1624, 1579, 1551, 1516, 1464, 1431, 1178, 988, 796, 786, 748, 629

*(7E)-18-[2-(2-Methoxyethoxy)ethyl]-23,24,25,26-tetraazapentacyclo[17.3.1.1^{2,6}.1^{8,12}.1^{13,17}]hexacosa-1(23),2(26),3,5,7,9,11,13(24),14,16,19,21-dodecaene-7,18-dicarbonitrile (**7, pyr-MePEG**)*

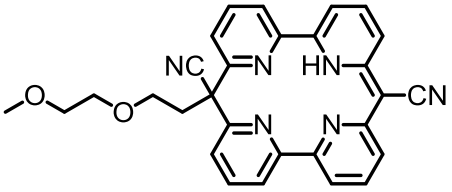

The synthesis was adapted from literature.[68] NaH (0.40 g, 16 mmol), pyrphyrin (0.20 g, 0.52 mmol) and dry DMF (20 mL) were added into a 50 mL one necked schlenk flask. The flask was equipped with a magnetic stirring bar and a cooling condenser. The dark violet red suspension was stirred at 50 °C for 2.5 h to afford a brighter reddish suspension. 1-bromo-2-(2-methoxyethoxy)-ethane (2.84 g, 15.5 mmol) was added dropwise via a syringe at 50 °C. The temperature was raised to 120 °C and the reaction kept under these conditions for 27 h. The now dark red solution was poured into 200 mL water to precipitate a bright red sticky solid which was centrifuged, decanted and washed twice with water. The washed solid was transferred with MeOH and CH_2Cl_2 into a 50 mL one necked round bottom flask. Evaporation of the solvent and drying by evacuation at high vacuum overnight yielded a bright red crude product (0.33 g). After purification over silica column (6:4; EtOAc:hexane) **7** (0.13 g, 0.27 mmol, 51 % yield) was obtained as glittering red solid. **HPLC**: 19.8 min (23 min method); **ESI-MS**: m/z = 487.0 $(M - H)^-$, 489.1 $(M + H)^+$, 511.2 $(M + Na)^+$; **^{1}H NMR** (C_6D_6, 300 MHz): δ (ppm) = 7.88-7.82 (d, 2 H), 7.67-7.60 (d, 2H), 6.95-6.90 (t, 2 H), 6.86-6.75 (m, 4H), 6.38-6.32 (d, 2 H), 3.43-3.35 (t, 2 H), 3.14-3.11 (m, 4 H), 3.11-3.04 (t, 2 H), 3.01-2.98 (s, 3 H); **Anal. calcd.** for $C_{29}H_{24}N_6O_2$ (%): C, 71.30; H, 4.95; N, 17.20 %; Found: C, 70.68; H, 5.01; N, 16.75.

*(7E)-18-(1,3-Dioxolan-2-ylmethyl)-23,24,25,26-tetraazapentacyclo[17.3.1.12, 6.18,12.113,17]hexacosa-1(23),2(26),3,5,7,9,11,13(24),14,16,19,21-dodecaene-7,18-dicarbonitrile (**8**)*

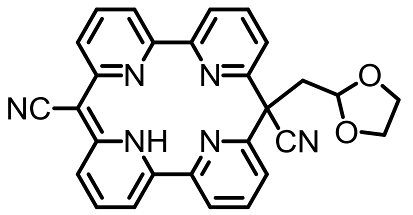

The synthesis was adapted from literature.[68] NaH (10 mg, 2.5 mmol), pyrphyrin (39 mg, 0.10 mmol) and dry DMF (10 mL) were added into a 25 mL one necked schlenk flask. The flask was equipped with a magnetic stirring bar and a cooling condenser. The dark violet red suspension was stirred at 60 °C for 2 h to afford a brighter reddish suspension. 2-(bromomethyl)-1,3-dioxolane (1.34 g, 8 mmol) was added dropwise via a syringe at 60 °C. The temperature was raised to 120 °C and the reaction was kept under these conditions for 20 h. The now dark red solution was poured into 100 mL water to precipitate a bright red sticky solid which was centrifuged, decanted and washed twice with water. The washed solid was transferred with MeOH and CH_2Cl_2 into a 25 mL one necked round bottom flask. Evaporation of the solvent and drying by evacuation at high vacuum overnight yielded a bright red crude product (52 mg). After purification over silica column (6:4; EtOAc:hexane) **8** (13 mg, 0.03 mmol, 28 % yield) was obtained as glittering red solid. **HPLC**: 19.6 min (23 min methode); **ESI-MS**: m/z = 473.4 $(M + H)^+$.

*(7E)-18-(4-Iodobutyl)-23,24,25,26-tetraazapentacyclo[17.3.1.12,6.18, 12.113,17]hexacosa-1(23),2(26),3,5,7,9,11,13(24),14,16,19,21-dodecaene-7,18-dicarbonitrile (**9**)*

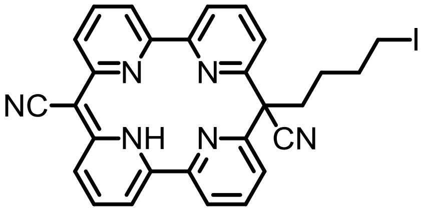

The synthesis was adapted from literature.[68] Compound **2** (50 mg, 0.13 mmol) and KO^{t}Bu (15 mg, 0.13 mmol) were added into a 25 mL one necked round bottom schlenk equipped with a magnetic stirring bar and a septum. Dry DMF (10 mL) was added via syringe under nitrogen atmosphere. The resulting dark red suspension was heated to 70 °C and sonicated for 1 h 30 min to obtain a dark red solution. 1,4-Diiodobutane (20.5 µL, 0.16 mmol) was added via Eppendorf pipette under a nitrogen counter flow and the reaction mixture was heated to 120 °C. The solution turned dark violet within 5 min. After 18 h the heating was suspended and the suspension was poured onto 150 mL H_2O. The red precipitate was isolated by centrifugation and filtration as well as rinsing with an excess of water. The dark red sticky solid was dried at reduced pressure to obtain 59 mg crude product. After purification over silica column (100:0 to 90:10; CH_2Cl_2: MeOH) **9** was obtained as a dark red solid (11 mg, 15 %). **UPLC-MS**: 3.7 min (5 min method), m/z = 569.1 $(M + H)^+$; **^{1}H NMR** ($CDCl_3$, 500 MHz): δ (ppm) = 15.61 (s, 1 H), 7.92-7.90 (d, J = 7.5 Hz, 2 H), 7.82-7.80 (t, J = 8 Hz, 2 H), 7.68-7.66 (d, J = 8 Hz,2 H), 7.59-7.57 (m, 4 H), 7.15-7.13 (m, 2 H), 3.03-3.00 (t, J = 7 Hz, 2 H), 2.80-2.77 (m, 2 H), 1.75-1.72 (t, J = 7.3 Hz,2 H), 1.41-1.38 (m, 2 H)

*6,6'-Dibromo-[2,2'-bipyridine] 1,1'-dioxide (**11**)*

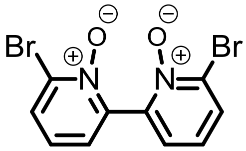

The synthesis was adapted from literature.[81,82] 2,9-Dibromobipyridine (10 g, 32 mmol) was added into a 250 mL two necked round bottom schlenk and dissolved in 100 mL TFA under argon. The colourless solution was heated to 80 °C and H_2O_2 (10 ml,50 % wt,175 mmol) was added dropwise over 30 min. After 1 h 30 min and 20 h an additional 10 mL, respectively 5 mL of H_2O_2 (50 % wt, 175 mmol and 88 mmol) was added until no further conversion could be observed by UPLC-MS. The reaction was stopped and 50 mL t-butanol was added. The solvent was partially removed at reduced pressure to remove the water and the TFA. After the solution was reduced to around 20 mL, 20 mL fresh butanol was added. The solution was again concentrated at reduced pressure to approximately 20 mL and formation of a white precipitate was observed. This cycle was performed two additional times. The final suspension was cooled to 5 °C and left standing overnight. The Suspension was filtered and washed with t-butanol (50 mL) and pentane (100 mL). The obtained white solid was dried to obtain a crude white solid (quantitative). The crude solid was purified by trituration at 75 °C overnight (1 L t-butanol, 200 mL hexane). The heating was suspended and the suspension cooled down to 5 °C. The suspension was filtered and washed with t-butanol and pentane to obtain **11** as white solid (9.8 g, 23 mmol, 90 %). **UPLC-MS**: 3.3 min (5 min method), m/z = 312.90 $(M + H)^+$;**^{1}H NMR** (d_6-dmso, 500 MHz): δ (ppm) = 8.070-8.066 (dd, J = 2.0 Hz, 8.0 Hz, 2 H), 7.69-7.67 (dd, J = 1.8 Hz, 7.8 Hz, 2 H), 7.36-7.32 (t, J = 8.0 Hz, 2 H).

*6,6'-Dibromo-4,4'-dinitro-[2,2'-bipyridine] 1,1'-dioxide (**12**)*

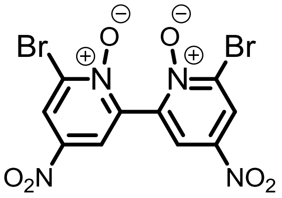

The synthesis was adapted from literature.[81,82] Compound **11** (1 g, 3 mmol) and foaming sulfuric acid (3 mL) were added into a 50 mL one necked round bottom flask and formed immediately a sticky brown suspension. The reaction was heated up to 40°C followed by addition of a 1:1 mixture of foaming sulfuric acid and foaming nitric acid (18 mL). An almost complete brown solution was obtained. The mixture was heated up to 90 °C while at approximately 76 °C a complete solution was obtained. After 3 h 20 min the heating was suspended and the solution was poured onto 125 mL ice in a 250 mL Erlenmeyer. After the ice has melted the Erlenmeyer was filled up with water to the 125 mL mark. A shortly blueish tone turned into a yellow solution with a white precipitate. The suspension was filtrated and the white solid was washed with water (200 mL). The filter cake was dried by high vacuum to afford **12** as white solid (590 mg, 1.4 mmol, 47 %). **UPLC-MS**: 2.0 min (5 min method), m/z = 434.86 (M + H)$^+$; ^{1}**H NMR** (d$_6$-dmso, 500 MHz): δ (ppm) = 8.98-8.95 (d, J = 3.0 Hz, 2 H), 8.69-8.67 (d, J = 3.0 Hz, 2 H).

*6,6'-Dibromo-4,4'-dinitro-2,2'-bipyridine (**13**)*

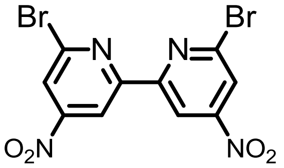

The synthesis was adapted from literature.[81,82] Compound **12** (250 mg, 0.57 mmol) and 50 mL nitrobenzene were added into a 100 mL one necked round bottom flask. PBr$_3$ (2.7 mL) was added and a cooling condenser was attached. The colourless suspension was heated to 70 °C to obtain a yellow solution. After 20 h stirring at 70°C under nitrogen atmosphere the heating was stopped and the suspension (precipitation while cooling) was poured onto 150 mL ice two obtain two colourless phases. The acidic phases were quenched with Na$_2$CO$_3$ to obtain a suspension which was then extracted with dichloromethane (4 x 200 mL). The combined organic solutions were dried over magnesium sulphate and the solvent was removed by reduced pressure. The crude product was recrystallised over CH$_2$Cl$_2$ and ether to afford **13** as white solid (92 mg, 0.23 mmol, 40 %). **UPLC-MS**: 3.3 min (5 min method), m/z = 402.9 (M + H)$^+$;^{1}**H NMR** (d$_6$-dmso, 500 MHz): δ (ppm) = 8.81-8.78 (d, J = 1.8 Hz, 2 H), 8.61-8.59 (d, J = 1.8 Hz, 2 H).

*6,7-Dihydro-5H-[1,4]diazepino[1,2,3,4-lmn][1,10]phenanthroline-4,8-diium bromide (**17**)*

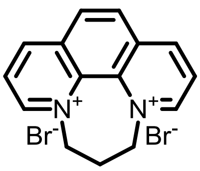

The synthesis was adapted from literature.[89] Anhydrous 1,10-phenanthroline (100 g, 0.55 mol) was added into a three necked 2 L round bottom flask equipped with a 500 mL pressure equilibrated dropping funnel a cooling condenser and a mechanical stirrer. Chlorobenzene (1 L) was added and the mixture was heated to 75 °C under nitrogen. 1,3-dibromopropane (280 mL, 2.5 mol) was added dropwise within 1 h to the colourless solution. The reaction solution was heated to 120 °C after complete addition. The formation of a bright yellow precipitate could be observed during the course of the reaction. After 7 h the suspension was cooled to rt. Filtration and washing of the filter cake with hexane yielded **17** as a yellow powder (210 g, 0.55 mol, 100 %) in high purity. **HPLC**: 3.8 min (5 min method); ^{1}**H NMR** (D$_2$O, 500 MHz): δ (ppm) = 9.73-9.72 (d, J = 5.8 Hz, 2 H), 9.53-9.51 (d, J = 8.5 Hz, 2H), 8.66-8.62 (m,2 H), 8.62-8.59 (m, 2 H), 5.22-5.20 (t, J = 7.0 Hz,2 H), 3.52-3.46 (q, J = 7.0 Hz, 3 H).

*6,7-Dihydro-3H-[1,4]diazepino[1,2,3,4-lmn][1,10]phenanthroline-3,9(5H)-dione (**18**)*

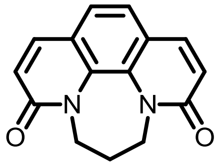

The synthesis was adapted from literature.[89] Compound **17** (100 g, 0.26 mol) and t-BuOH (800 mL) were added into a one necked 2 L round bottom flask and sonicated for 30 min at 45 °C. Over 30 min KO^{t}Bu (120 g, 1.07 mol) was added: The reaction suspension was stirred at 40 °C for 1 d while a continuous flow of oxygen was bubbled trough the vessel. The resulting yellow precipitate was isolated by filtration and suspended in water (800 mL) and extracted with chloroform (2 x 400 mL, 1 x 200 mL). The organic phase was washed with water (2 x 500 mL). The combined organic phase was dried over $MgSO_4$ and evaporated at reduced pressure to afford Compound **18** as yellow brown solid in high purity (45.4 g, 0.18 mol, 69 %). **UPLC-MS**: 1.5 min (5 min method), m/z = 253.1 $(M + H)^+$; **^{1}H NMR** ($CDCl_3$, 500 MHz): δ (ppm) = 7.70-7.68 (d, J = 9.0 Hz, 2 H), 7.34 (s, 2 H), 6.78-6.77 (d, J = 9.5 Hz, 2 H), 4.30 (bs, 4H), 2.45-2.42 (q, J = 6.5 Hz, 2 H).

*2,9-Dichloro-1,10-phenanthroline (**19**)*

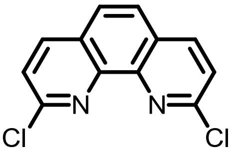

The synthesis was adapted from literature.[89] Compound **18** (15 g, 0.06 mol) was added into a 500 mL three necked round bottom flask equipped with a magnetic stirring bar and a reflux condenser. Freshly distilled and degassed $POCl_3$ (150 mL) and PCl_5 (25 g, 0.12 mol) was added and the reaction was stirred at 110 °C for 16 h under nitrogen atmosphere. The excess $POCl_3$ was removed by distillation at reduced pressure and the residual material was quenched by pouring the mixture over ice (300 mL). The resulting white suspension was then basified with ammonia solution (25 %, pH 8) upon which a brown precipitate was formed. The suspension was filtrated and rigorously washed with ether (300 mL). The brown precipitate was dried and recrystallised from methanol (1 L) to afford compound **19** (14.5 g, 0.06 mol, 100 %) as white solid. **UPLC-MS**: 3.2 min (5 min method), m/z = 249.1 $(M + H)^+$, 519.1 $(M_2 + Na)^+$; **^{1}H NMR** ($CDCl_3$, 200 MHz,): δ (ppm) = 8.21 (d, *J* = 8.5 Hz, 2 H), 7.82 (s, 2 H), 7.65 (d, *J* = 8.4 Hz, 2 H); **Anal. calcd.** for $C_{12}H_6Cl_2N_2$ (%): C, 57.86; H, 2.43; N, 11.25 %; Found: C, 58.23; H, 2.37; N, 11.18.

*2,9-Dibromo-1,10-phenanthroline (**20**)*

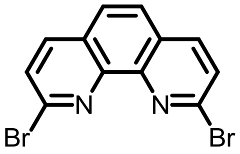

The synthesis was adapted from literature.[89] A 100 mL two neck round bottom flask, equipped with a reflux condenser, was charged with 2,9-dichloro-1,10-phenanthroline (480 mg, 2.0 mmol) and PBr_3 (3 mL, 32 mmol). The resulting suspension was stirred at 170 °C for

9 h. The reaction mixture was quenched by addition of ice and the brown suspension was neutralized with sat. aq. $NaHCO_3$. After filtration and drying of the precipitate, the resulting brown solid was dissolved in DCM:MeOH 50:1 and filtered through a plug of silica. The filtrate was concentrated under reduced pressure and the residue dried under HV to give **20** as a yellow solid (450 mg, 1.3 mmol, 69%). **^{1}H NMR** ($CDCl_3$, 200 MHz): δ (ppm) = 8.09 (d, *J* = 8.4 Hz, 2 H), 7.83 (s, 2 H), 7.79 (d, *J* = 8.4 Hz, 2 H).

*2,13-Dithia-23,26,27,30-tetraazaheptacyclo[12.8.4.43,12.06,29.09,28.017, 25.020,24]triaconta-1(22),3,5,6,8,9,11,14,16,18,20,23,25,27,28,29-hexadecaene (**21, thia-phenphyrin, thia-phyr**)*

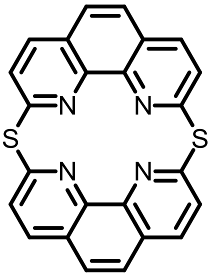

The synthesis was adapted from literature.[70] Compound **19** (200 mg, 0.80 mmol) was added into a 25 mL one necked round bottom flask which was placed in a ball tube oven. The vacuum inlet of the bulb tube oven was exchanged by a septum penetrated by a copper hose to continuously flush the system with H_2S. The exhaust H_2S was quenched by bubbling through an acetic acid bath. The system was thoroughly flushed with H_2S and afterwards slow rotation at 170 °C was applied under a slow but steady stream of H_2S. The white solid starting material turned reacted to a orange brown solid. The reaction was suspended after 2 h and cooled to rt to obtain a brown solid which was washed with CH_2Cl_2 (10 mL) and MeOH (10 mL). The washed product (100 mg, yellow orange solid) was dissolved in H_2O, (10 mL each), sonicated and acidified by addition of TFA. Excess TFA was removed at reduced pressure afford **21** as a yellow solid (147 mg, 0.35 mmol, 87 %). **HPLC**: 3.6 min (5 min method); **^{1}H NMR** (TFA-*d*, 500 MHz): δ (ppm) = 9.00-8.98 (d, J = 8.8 Hz, 4 H), 8.42 (s, 4 H), 8.25-8.23 (d, J = 8.7 Hz, 4 H); **Anal. calcd.** for $C_{24}H_{12}N_4S_2$ + 4/3 TFA (%): C, 53.74; H, 2.31; N, 9.17; Found: C, 53.71; H, 2.31; N, 9.42.

*2,13,23,26,27,30-Hexaazaheptacyclo[12.8.4.43,12.06,29.09,28.017,25.020,24] triaconta-1(22),3,5,6,8,9,11,14,16,18,20,23,25,27,28,29-hexadecaene (**22, azaphenphyrin, aza-phyr**)*

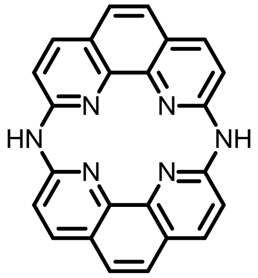

The synthesis was adapted from literature.[70,91] Compound **19** (140 mg, 0.563 mmol) was added into a 25 mL one necked round bottom flask which was placed in a ball tube oven. The vacuum inlet of the bulb tube oven was exchanged by a septum penetrated by a copper hose to continuously flush the system with NH_3. The exhaust NH_3 was quenched by bubbling through an acetic acid bath. The system was thoroughly flushed with NH_3 and afterwards slow rotation at 270 °C was applied under a slow but steady stream of NH_3. The white solid starting material melted and turned into a brown liquid. The reaction was suspended after 8 h and cooled to rt to obtain a brown solid. The crude product was dissolved in H_2O (70 mL), sonicated and acidified by addition of HCl (1.5 mL, 36 %). The obtained orange solution was filtered and basified by addition of NaOH pellets to induce precipitation of **22** as yellow solid. The suspension was decanted and centrifuged as well as washed with H_2O (5 x 20 mL). The yellow solid was dried under reduced pressure to afford 15 as a fluffy yellow powder (91.4 mg, 0.024 mmol, 84 %). **HPLC**: 3.1 min (5 min method); **UPLC-MS**: 2.5 min (5 min method), m/z = 387.3 $(M + H)^+$; **^{1}H NMR** (TFA-*d*, 500 MHz): δ (ppm) = 8.97-8.95 (d, J = 9.0 Hz, 4 H), 8.28 (s, 4 H), 8.16-8.14 (d, J = 9.0 Hz, 4 H).

*7,18,23,24,25,26-Hexaazapentacyclo[17.3.1.12,6.18,12.113,17]hexacosa-1(23),2(26),3,5,8(25),9,11,13(24),14,16,19,21-dodecaene (**24, azapyrphyrin, aza-pyr**)*

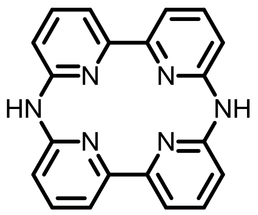

The synthesis was adapted from literature.[71] 6,6'-dibromo-2,2'-bipyridine (0.6 g, 1.9 mmol) was added into a small teflon vessel and closed with a Teflon cap with a small hole in the middle for pressure equilibration. The teflon vessel was inserted into a 20 mL autoclave which was three times evacuated and flushed with nitrogen. The autoclave was then evacuated and flushed with gaseous ammonia three times. The valve was closed after the autoclave had been cooled for 30 s at -50 °C under a 2.0 bar NH_3 pressure. The autoclave was heated to 280 °C (~15 bar) and the reaction was stopped after two days to obtain a pale green solid (0.32 g). The solid transferred into a NS5 frit and was washed with 2 M HCl solution. The black residue was than dissolved in concentrated HCl and basified with 10 M NaOH solution (pH 10) to obtain a yellow brown precipitate. The solubility of the product is often different, showing sometimes good solubility in concentrated HCl and other times almost no solubility. This was attributed to the formation of insoluble salts. Thus, it was often necessary to switch between water and concentrated HCl to dissolve the washed *aza*-pyrphyrin. The purified product was isolated by filtration and washed with water to obtain pure **24** (0.13 g, 0.38 mmol, 40% yield) as red brown to green brown solid after drying. **UPLC-MS**: 1.2 min (5 min method), m/z = 339.1 $(M + H)^+$; **^{1}H NMR** (TFA-*d*, 500 MHz): δ (ppm) = 8.33 (bs, 4 H), 8.18 (bs, 4 H), 7.58 (bs, 4 H).

7,18-Dimethyl-7,18,23,24,25,26-hexaazapentacyclo[17.3.1.12,6.18,12.113,17] hexacosa-1(23),2(26),3,5,8(25),9,11,13(24),14,16,19,21-dodecaene ***(25, N,N-dimethyl-azapyrphyrin, Me2aza-pyr)***

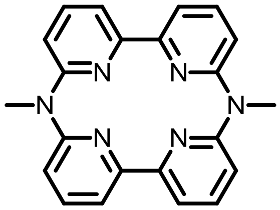

The synthesis was adapted from literature.[71] Dry NaH (21 mg, 0.88 mmol) was added into a 50 ml one necked round bottom schlenk equipped with a magnetic stirrer and a septum. Dry DMF (20 mL) and **24** (57 mg, 0.17 mmol) was added. Almost immediately a red solution was formed that turned within 5 min into a dark yellow solution. The reaction was stirred for 30 min at 25 °C. MeI (250 µl, 4.0 mmol) was added via an Eppendorf pipette. The yellow turbid (NaH) solution turned paler and change the colour towards brown. After 1 h 30 min the septum was exchanged by a glass plug with a teflon seal and the flask was evacuated and heated to 70 °C. After 5 h of drying a white brown solid was obtained. The solid was extracted with water (25 mL) and dichloromethane (2x 50 mL) to remove the NaI. The organic phases were washed with 25 mL water and the combined organic phases dried over sodium sulfate. The organic solvent was evaporated under reduced pressure to obtain 50 mg (81 % yield) **25** as yellow orange solid. **UPLC-MS**: 1.2 min (5 min method), m/z = 367.2 $(M + H)^+$; ^{1}**H NMR** ($CDCl_3$, 500 MHz): δ (ppm) = 8.14-8.11 (t, J = 8.2 Hz, 4 H), 7.74-7.73 (d, J = 7.6 Hz, 4 H), 7.55-7.50 (bm, 4 H), 3.84 (s, 6 H).

Bis(6-bromopyridin-2-yl)methanone ***(26)***

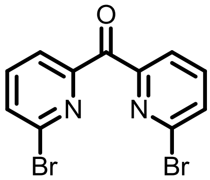

The synthesis was adapted from literature.[94] 2,6-Dibromopyridine (10 g, 42.2 mmol) and dry ether (320 mL) was added into a 750 mL sulfonation flask equipped with a mechanical stirrer and a 50 mL pressure equilibrated dropping funnel under nitrogen. The flask was cooled down to -78 °C under nitrogen atmosphere. n-BuLi (1.6 M, 28.75 mL, 46 mmol) was dropwise added within 20 min to obtain a yellow solution. Diethyl carbonate (2.3 mL in 40 mL ether, 19 mmol) was added dropwise below -60 °C. A brown solution was obtained which was stirred for 2 h at -78 °C. The cooling was suspended and the reaction mixture quenched with 10 % HCl solution (pH 1). The resulting acidic solution was basified by addition of 10 M K_2CO_3 solution (pH 8). The ether was removed by reduce pressure and the water phase extracted with dichloromethane (3 x 150 mL). The combine organic phases were dried by $MgSO_4$. The crude product (7 g) was obtained after filtration and evaporation of the dichloromethane under reduced pressure. The crude product was purified by crystallisation (1:1, hexane:ethylacetate) to afford **26** as white solid in high purity (3.4 g, 9.94 mmol, 47 %). **UPLC-MS**: 2.3 min (5 min method), m/z = 340.9 $(M + H)^+$;^{1}**H NMR** ($CDCl_3$, 300 MHz): δ (ppm) = 8.07-8.03

(dd, J = 1.1 Hz, 7.4 Hz, 2 H), 7.77-7.71 (t, J = 7.6 Hz, 2 H), 7.68-7.65 (dd, J = 1.1 Hz, 7.8 Hz).

*6,6'-(1,3-Dioxolane-2,2-diyl)bis(2-bromopyridine) (**27**)*

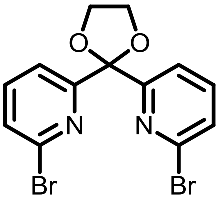

The synthesis was adapted from literature.[93] Compound **26** (2.4 g, 7.0 mmol), sulfuric acid (0.1 mL), toluene (44 mL) and freshly distilled ethylene glycol (3.9 mL, 7.0 mmol) were added into a 100 mL two necked round bottom flask equipped with a thermometer and a water separator. The reaction was stirred under reflux for 2.5 d and then an additional 50 mL toluene and 2 mL ethylene glycol was added. After an additional 2.5 days the heating was suspended and the toluene solution was transferred into a 250 mL one necked round bottom flask and evaporated at reduced pressure to obtain a white solid (2.54 g). The white solid was dissolved in chloroform (60 mL) and crystallised by addition of ethanol (100 mL) and storing at 4 °C overnight. The suspension was filtrated and washed with ethanol to afford compound **27** as pure white crystals (1.76 g, 4.6 mmol, 65 %). **UPLC-MS**: 2.6 min (5 min method), m/z = 384.9 $(M + H)^+$; **ESI-MS**: m/z = 384.9 $(M + H)^+$, 406.9 $(M + Na)^+$, 790.8 $(M_2 + Na)^+$ **^{1}H NMR** ($CDCl_3$, 300 MHz): δ (ppm) = 7.80-7.78 (dd, J = 1.8 Hz, 7.9 Hz, 2 H), 7.58-7.54 (t, J = 7.9 Hz, 2 H), 7.38-7.36 (dd, J = 1.8 Hz, 7.9 Hz).

*Dispiro[1,3-dioxolane-2,2'-[25,26,27,28]tetraazapentacyclo[19.3.1.13,7.19, 13.115,19]octacosa[1(25),3(28),4,6,9(27),10,12,15(26),16,18,21,23]dodecaene-14',2''-[1,3]dioxolane]-8',20'-dicarbonitrile (**28**)*

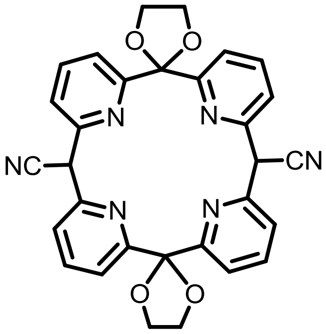

The synthesis was adapted from literature.[86] LiH (213 mg, 27 mmol) was weighed into a 25 ml one necked round bottom schlenk equipped with a magnetic stirring bar and a septum. 10 mL benzene, 67 µL CH_3CN and 4 mL TMEDA were added to form a grey suspension. After no hydrogen formation was visible anymore (10 min), compound **27** (503 mg, 1.3 mmol) was added to the suspension. A nitrogen flushed cooling condenser was added and the grey suspension was heated to reflux and stirred for 3 d. The grey suspension turned slowly orange brown. The heating was suspended and the reaction was quenched with water (30 mL). The two phases were extracted with CH_2Cl_2 (3 x 50 mL) washed with water (30 mL) and the combined organic phases dried over $MgSO_4$. The CH2Cl2 was evaporated at reduced pressure to obtain **28** as crude olive green sticky oil. The crude product was suspended in water (20 mL) and refluxed over night to remove the remaining LiH. A colour change from olive green to orange was observed. The wet solid was filtered and washed with water prior drying at reduced pressure to obtain 23 as pale orange solid in unknown purity (151 mg, 47 %). **UPLC-MS**: 3.2 min (5 min method), m/z = 531.2 (M + H)$^+$.

4.1.3 Synthesis of metal complexes

*[Co^{II}(OH$_2$)$_2$(pyr)] (**41**)*

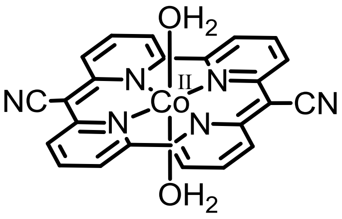

A suspension of pyrphyrin (**2**) (100 mg, 0.26 mmol) in pyridine (60 mL) was treated with KO^{t}Bu (58 mg, 0.52 mmol) and sonicated for 2 h at 70 °C to afford an orange brown solution. The solution was filtered under exclusion of air and Co(acetate)$_2$ tetrahydrate (72 mg, 0.29 mmol) was then added to instantaneously give a black green solution. The mixture was heated to 100 °C and stirred for 2 h, then heating was stopped and the mixture was cooled to 25 °C. 10 mL water was added to quench the reaction. The dark green solution slowly turned dark red. The solvent was removed under reduced pressure to afford a black solid with low solubility. Water (150 mL) was used to suspend (10 min sonicated) the black solid. The suspension was heated to reflux and stirred overnight to purify the product. The suspension was rigorously washed with water to afford **41** as a black solid (111 mg, 0.23 mmol, 89 %). **FT-IR** (ATR) (cm^{-1}): 3079 (w), 2923 (w), 2851 (w), 2169 (m), 1672 (w), 1672 (w), 1600 (m), 1559 (s), 1547 (m), 1466 (s), 1415 (s), 1366 (m), 1307 (m), 1288 (m), 1246 (s), 1220 (m), 1182 (s), 1112 (w), 1066 (w), 1036 (m), 1017 (m), 993 (m), 869 (w), 780 (s), 758 (m), 734 (m); **HR-ESI-MS**: *m/z* (%): 443.0445 (100, [M – 2 H$_2$O]$^+$, calcd for [$C_{24}H_{12}CoN_6$]$^+$: 443.0450), 459.0395 (21, [(M_2 – 2 H$_2$O + O]$^+$, calcd for [$C_{24}H_{12}CoN_6O$]$^+$: 459.0399); **SQUID**: T$_C$ (Θ) ≈ -3.93 K, μ_{eff} ≈ 1.85 μ_B; **Anal. calcd.** for [$C_{24}H_{16}CoN_6O_2$] (%):C 60.13; H 3.36, found: C 60.06; H 3.052.

*[Co^{II}Br(MeOH)(pyr-MePEG)] (**42**)*

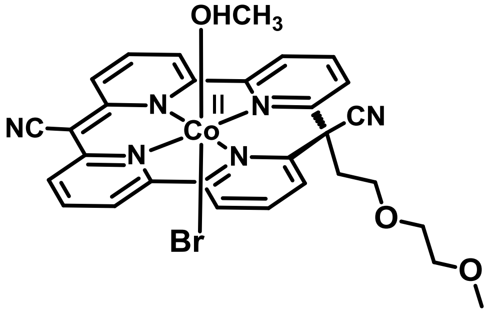

Compound **7** (50 mg, 0.10 mmol), CoBr$_2$ (37 mg, 0.11 mmol), sodium hydroxide solution (1 M, 0.10 mmol) and MeOH (15 mL) were added into a 25 mL one necked schlenk flask equipped with a magnetic stirring bar and a cooling condenser. After three days at reflux (70 °C) the heating and stirring was suspended. The reaction suspension was cooled down to room temperature and filtrated to afford a black solid of **42** (61 mg, 0.07 mmol, 67 %) after washing with small amount of MeOH and water. **HPLC**: 14.3 min, 15.1 min (23 min method).

*$[Co^{II}(H_2O)_2(pyr\text{-}MePEG)][ClO_4]$ (**43**)*

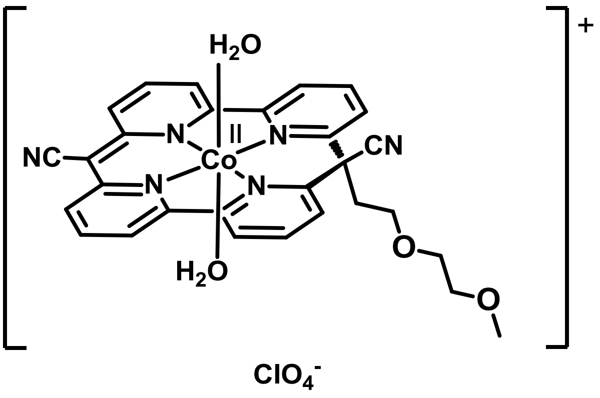

Compound **7** (100 mg, 0.21 mmol), $[Co^{II}(ClO_4)_2]$ hexahydrate (80 mg, 0.22 mmol), sodium hydroxide solution (1 M, 0.21 mL) and MeOH (20 mL) were added into a 50 mL one necked schlenk flask, equipped with a magnetic stirring bar and a cooling condenser. The reaction mixture turns into a dark red solution. After 3 d at reflux (80 °C) the heating and stirring was suspended and diethyl ether (30 mL) was added at room temperature. The dark red solution was put into the freezer for 2.5 d to obtain a very fine crystalline suspension. The suspension was filtered over a celite bed and washed with 6:3 diethyl ether: MeOH. The purified product was obtained by suspending the celite several times in MeOH until the resulting organic solution was only slightly coloured (80 mL). Evacuation of the organic solvent and drying over high vacuum gave **43** as black red crystalline solid (98 mg, yield: 68 %). **HPLC**: 13.1 min, 14.3 min, 15.1 min (23 min method); **FT-IR** (KBr) (cm^{-1}): 2924, 2175, 1604, 1562, 1478, 1456, 1423, 1251, 1088, 1021, 789, 624; **ESI-MS**: m/z = 546.0 (M - 2 H_2O)$^+$; **Anal. calcd.** for $C_{29}H_{27}ClCoN_6O_8$ (%): C, 51.08; H, 3.99; N, 12.32; Found: C, 51.77; H, 3.57; N, 12.27.

*$[Co^{II}Br(MeOH)(pyr\text{-}bu)]$ (**44**)*

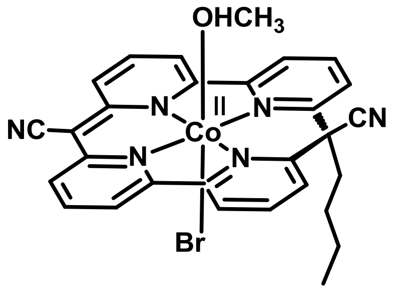

Compound **3** (70 mg, 0.16 mmol), $CoBr_2$ hydrate (57 mg, 0.17 mmol) and MeOH (20 mL) were added into a 50 mL one necked schlenk flask equipped with a magnetic stirring bar and a cooling condenser. Sodium hydroxide solution (1 M in water, 160 µmol, 0.16 mol) was added and the reaction suspension was heated to reflux and turned into a dark whine red suspension. The heating and stirring was suspended after 2 d. 5 mL Et_2O was added and the black solid precipitate was isolated by filtration. The crude product was washed with MeOH/Et_2O (1:1) and water to obtain **44** as black solid after drying under reduced pressure (76 mg, 0.13 mmol, 83 %). Dark red single crystals suitable for X-ray analysis were obtained by vapour diffusion with acetone as solvent and isopropyl ether as antisolvent. **FT-IR** (ATR) (cm^{-1}): 3059 (w), 2953 (w), 2926 (w), 2860 (w), 2323 (w), 2171 (m), 1983 (w), 1603 (s), 1572 (m), 1558 (m), 1542 (w), 1474 (s), 1447 (s), 1419 (s), 1372 (m), 1310 (m), 1287 (m), 1249 (m), 1220 (m), 1181 (m), 1169 (m), 1101 (w), 1014 (m), 985 (m), 939 (w), 905 (w), 782 (s), 746 (m), 727 (w); **UV/Vis** (H_2O) (ε, M^{-1} cm^{-1}): 293 (18770, *sh*), 381 (8980), 472 nm (3676); **HR-ESI-MS**: *m*/*z* (%): 500.1160 (100, [*M*

– Br – $CH_3OH]^+$, calcd for $[C_{28}H_{21}CoN_6]^+$: 500.1154), 1079.1502 (10, [(M_2 – Br – 2 $CH_3OH)_2]^+$, calcd for $[C_{56}H_{42}Co_2N_{12}Br]^+$: 1079.1497); **SQUID**: T_C (Θ) ≈ -3.48 K, $\mu_{eff} \approx 3.52\ \mu_B$; **Anal. calcd.** for $[C_{29}H_{25}BrCoN_6O]$ (%):C 56.88; H 4.11; N 13.72; Found: C 56.73; H 3.97; N 13.65.

*$[Co^{II}(THF)(pyr\text{-}bu)][ClO_4]$ (**45**)*

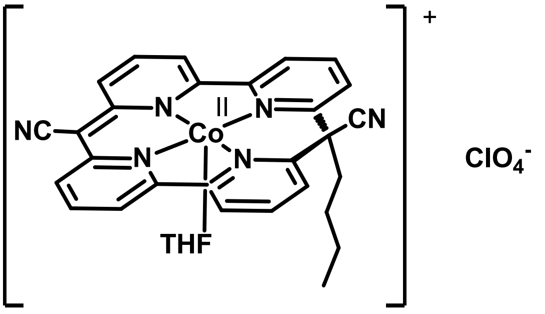

A suspension of **3** (25 mg, 0.056 mmol), $Co^{II}(ClO_4)_2$ hexahydrate (25 mg, 0.068 mmol) and 1 M NaOH (56 µL, 0.056 mmol) in 10 mL MeOH was stirred for 4 d at reflux. Complete conversion to a wine-red solution was observed by HPLC. Heating and stirring was stopped and the solvent was removed under reduced pressure. Then, the crude black product was dissolved in MeOH (7 mL), and THF (10 mL) was added. After removing of the solvent, the resulting black powder was washed with water and filtered to obtain **45** as black red solid (20 mg, 0.030 mmol, 53 %). **FT-IR** (ATR) (cm^{-1}): 3520 (w), 3094 (w), 2953 (m), 2923 (m), 2853 (m), 2176 (m), 1604 (m), 1563 (m), 1543 (w), 1476 (s), 1456 (s), 1421 (s), 1378 (m), 1308 (w), 1252 (m), 1225 (w), 1186 (m), 1080 (s), 1020 (s), 992 (m), 911 (w), 910 (w), 842 (w), 819 (w), 788 (s), 752 (w), 727 (w) cm^{-1}; **UV/Vis** (H_2O) (ε, $M^{-1}\ cm^{-1}$): 294 (17478), 381 (9000), 483 (3623, *sh*); **(+)-HR-ESI-MS**: *m*/*z* (%): 500.1155 (73, [*M* – THF]$^+$, calcd for $[C_{28}H_{21}CoN_6]^+$: 500.1154); **(-)-HR-ESI-MS**: *m*/*z* (%): 98.9489 (100, $[ClO_4]^-$, calcd for $[ClO_4]^-$: 98.9491), 220.8872 (20, $[(ClO_4)_2 + Na]^-$, calcd for $[Cl_2O_8Na]^-$: 220.8873); **Anal. calcd.** for $[C_{32}H_{29}ClCoN_6O_5]$ (%):C 57.19, H 4.35, N 12.51; Found C 57.48, H 4.38, N 12.52.

*$[Ni^{II}(pyr\text{-}bu)][ClO_4]$ (**46**)*

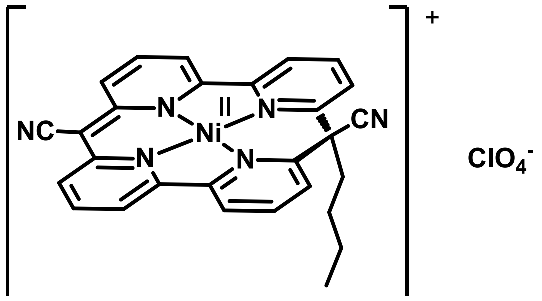

Ligand **3** (25 mg, 0.056 mmol) and $Ni^{II}(ClO_4)_2$ hexahydrate (25 mg, 0.068 mmol) were added into a 25 ml one necked round bottom schlenk. 10 mL dry DMF was added and the reaction suspension was heated to 70 C to obtain almost instantly a dark violet suspension. The reaction was stirred at 70 °C overnight and showed only marginal increased product formation. Thus, the reaction temperature was increased to 120 °C. After 3 d the heating was suspended and the solvent was removed at 15 mbar and 80 °C to obtain a reddish black solid which contained still excess of base and nickel perchlorate. 10 ml MeOH was added to suspend the product and 5 ml water was added to dissolve any remaining NaOH and perchlorate. The suspension was filtrated, washed with water and MeOH and dried at high vacuum to obtain **46** as pitch black solid. The crude black solid was suspended and sonicated in CH_3CN to form an almost complete solution. A large excess of water was added to precipitate the product. Precipitation was increased by reducing of the solvent volume over a continuous nitrogen flow. The suspension was filtrated, washed with water and dried at high vacuum to obtain **46** as pitch black solid (24 mg, 0.040 mmol, 71 %). Dark red single crystalline prisms suitable for X-ray diffraction were obtained by vapour diffusion with CH_3CN as solvent and THF as antisolvent. **FT-IR** (ATR) (cm^{-1}): 3085 (w), 2958 (w), 2924 (w), 2857 (w), 2191 (w), 1612 (m), 1564 (m), 1484 (s), 1456 (m), 1429 (m), 1376 (m), 1261 (m), 1188 (m), 1072 (s), 1016 (s), 806 (m), 787 (s); **(+)-HR-ESI-MS**: *m*/*z* (%): 499.1177 (100, [*M*]$^+$, calcd for $[C_{28}H_{21}N_6Ni]^+$: 499.1176); **(-)-HR-ESI-MS**: *m*/*z* (%): 98.9489 (100, $[ClO_4]^-$, calcd for $[ClO_4]^-$: 98.9491; **Anal. calcd.** for $[C_{28}H_{21}ClN_6NiO_4]$ + ½ THF + ½ MeOH (%):C 56.21, H 4.18, N 12.90; Found C 56.38, H 4.11, N 12.28; **^{1}H NMR** (CD_3CN, 500 MHz): δ (ppm) = 8.42-8.38 (t, J = 7.9 Hz, 2 H), 8.34-8.32 (dd, J = 1.2 Hz, 8.1 Hz, 2 H), 8.28-8.25 (dd, J = 1.2 Hz, 7.7 Hz, 2 H), 7.94-7.89 (t, J = 7.9 Hz, 2 H), 7.85-7.81 (dd, J = 1.2 Hz, 8.7 Hz), 7.76-7.73 (dd, J = 1.2 Hz, 7.3 Hz, 2 H), 2.67-2.63 (m, 2 H), 1.21-1.14 (q, 7.4 Hz), 1.02-0.94 (q, J = 7.8 Hz, 2 H), 0.75-0.70 (t, J = 7.3 Hz); **^{13}C NMR** (CD_3CN, 126 MHz): .δ (ppm) = 158.8, 153.6, 152.2, 151.1, 143.6, 137.7, 126.0, 124.8, 123.3, 121.6, 117.0, 79.6, 59.1, 47.4, 28.3, 22.4, 13.8.

[Cu^{II}(MeOH)(pyr-bu)][ClO$_4$] (47)

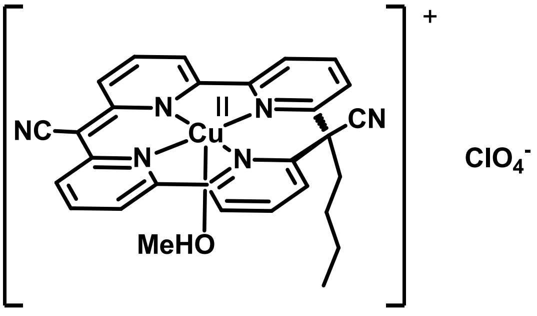

A suspension of **3** (30 mg, 0.078 mmol), Cu^{II}(ClO_4)$_2$ hexahydrate (32 mg, 0.085 mmol) and 1 M NaOH (78 µL, 0.078 mmol) in 10 mL MeOH was stirred for 3 d at reflux. Complete conversion to a wine-red solution was observed by HPLC. Heating and stirring was stopped and the solvent was removed under reduced pressure. Then, the crude black product was suspended and sonicated in water. The suspension was filtrated and the resulting black powder was washed with water and MeOH to obtain pure **47** as black red solid after drying at high vacuum (36 mg, 0.057 mmol, 73 %). Dark red single crystals suitable for X-ray diffraction were obtained by vapour diffusion with CH_3CN as solvent and dioxane or cyclohexane as antisolvent. **FT-IR** (ATR) (cm^{-1}): 3099 (w), 2959 (w), 2872 (w), 2828 (w), 2171 (m), 1599 (m), 1562 (m), 1537 (w), 1471 (s), 1444 (s), 1418 (s), 1395 (s), 1377 (m), 1305 (m), 1247 (m), 1247 (m), 1222 (m), 1181 (m), 1059 (s), 1011 (s), 791 (s); **(+)-HR-ESI-MS**: *m*/*z* (%): 504.11135 (100, [*M - MeOH*]$^+$, calcd for $[C_{28}H_{21}CuN_6]^+$: 504.11182); **(-)-HR-ESI-MS**: *m*/*z* (%): 98.94922 (100, $[ClO_4]^-$, calcd for $[ClO_4]^-$: 98.9491; **Anal.**

calcd. for $[C_{29}H_{25}ClCuN_6O_5]$ (%):C 54.72, H 3.96, N 13.20; Found C 54.99, H 3.88, N 13.19.

*[$Fe^{II}(H_2O)_2$(pyr-bu)][ClO_4] (**48**)*

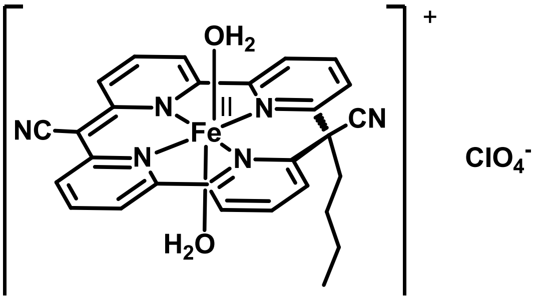

A suspension of **3** (30 mg, 0.078 mmol), $Fe^{II}(ClO_4)_2$ hydrate (31 mg, 0.085 mmol if hexahydrate) and 1 M NaOH (78 µL, 0.078 mmol) in 10 mL MeOH was stirred for 3 d at reflux. Complete conversion to a brown-red solution was observed by HPLC. Heating and stirring was stopped and the solvent was removed under reduced pressure. Then, the crude black product was suspended and sonicated in water. The suspension was filtrated and the resulting black powder was washed with water and MeOH to obtain pure **48** as black brown-red solid after drying at high vacuum (43 mg, 0.068 mmol, 87 %). **UPLC-MS**: 2.9 min (5 min method), m/z = 498.1 (M + H)$^+$; **FT-IR** (ATR) (cm^{-1}): 3084 (w), 2956 (w), 2926 (w), 2857 (w), 2184 (w), 2104 (w), 1665 (w), 1597 (m), 1567 (m), 1470 (m), 1418 (m), 1381 (w), 1249 (w), 1188 (w), 1076 (s), 1017 (m), 795 (m), 766 (m).

*[Zn^{II}(py)(pyr-MePEG)][OTf] (**49**)*

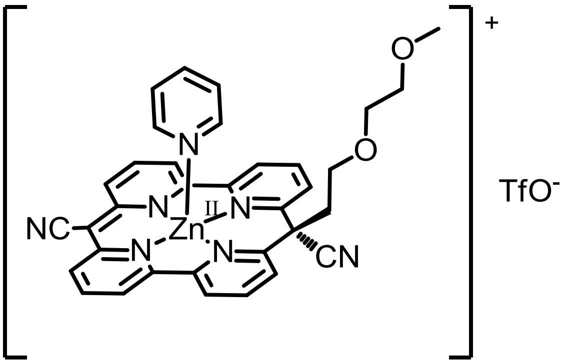

Ligand **7** (30 mg, 0.061 mmol), $ZnCl_2$ (8 mg, 0.058 mmol) and pyridine (20 mL) were added into a 50 mL one necked round bottom flask. The resulting red solution suspension was stirred for 1 d resulting at reflux to obtain a dark red solution showing complete complexation. The heating was stopped and the pyridine was removed at reduced pressure. The crude product was washed with water to remove possible $ZnCl_2$ residues. The crude product was then suspended in water (20 mL) and AgOTf (15 mg, 0.058 mmol) was added to exchange the chloride by triflate. The suspension was heated to 50 °C and stirred for 2 d. The precipitated AgCl was removed by filtration and the water phase was lyophylised giving pure **49** as dark red solid (23 mg, 0.029 mmol, 48 %). Dark red single crystals suitable for X-ray diffraction were obtained by vapor diffusion with pyridine as solvent and THF as antisolvent. **FT-IR** (ATR) (cm^{-1}): 3090 (w), 2922 (w), 2164 (m), 1593 (m), 1551 (m), 1464 (s), 1420 (s), 1387 (m), 1373 (m), 1262 (s), 1154 (s), 1101 (m), 1029 (s), 1013 (s), 798 (s); **(+)-HR-ESI-MS**: *m/z* (%): 551.11688 (100, [*M – pyridine*]$^+$, calcd for $[C_{29}H_{23}CoN_6O_2Zn]^+$: 551.11685); **Anal. calcd.** for $[C_{35}H_{28}F_3N_7O_5SZn]$ + ½ pyridine (%):C 54.88, H 3.90, N 12.8; Found

C 54.62, H 3.90, N 12.87; **^{1}H NMR** (d$_6$-dmso, 500 MHz): δ (ppm) = 8.74-8.70 (d, J = 8.0 Hz, 2 H), 8.58-8.50 (m, 2 H), 8.52-8.40 (t, J = 8.0 Hz, 2 H), 8.38-8.35 (d, J = 8.0 Hz, 2 H), 8.05-7.96 (m, 4 H), 7.81-7.75 (t, J = 7.5 Hz, 1 H), 7.67-7.63 (d, J = 8.0 Hz, 2 H), 7.40-7.35 (m, 2 H), 3.51-3.46 (t, J = 5.5 Hz, 2 H), 3.21-3.17 (m, 2 H), 2.94-2.90 (m, 2 H); **^{13}C NMR** (d$_6$-dmso, 126 MHz): .δ (ppm) = 157.14, 152.34, 151.26, 149.55, 145.14, 143.10, 138.91, 136.09, 124.57, 123.86, 122.75, 121.93, 112.91, 70.83, 69.24, 66.59, 57.94, 52.96.

*[Co^{II}(ac)$_2$(*aza*-pyr)] (**55**)*

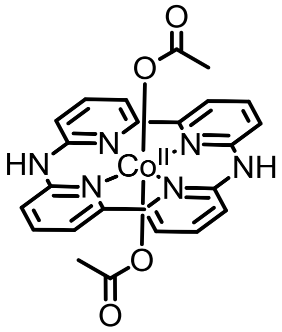

Ligand **24** (30 mg, 0.089 mmol), Co^{II}(ac)2 tetrahydrate (20 mg, 0.080 mmol) and 20 ml MeOH were added into a 50 ml round bottom flask. The reaction mixture was stirred at room temperature and formed immediately a dark brown solution with little precipitate. Almost complete conversion was observed after 23 h with only small traces of starting material still present. The dark solution was filtered over a PTFE syringe filter to obtain a clear dark red brown solution. The MeOH was removed by reduced pressure to afford 53 mg crude red solid. The solid was dissolved in 20 ml H_2O and filtrated by a celuloseacetate syringe filter to get rid of possible impurities. The yellow brownish solution was lyophylised to obtain pure **55** as light brown solid (40 mg, 0.078 mmol, 87 %). **FT-IR** (ATR) (cm^{-1}): 3198 (w), 3084 (w), 1595 (s), 1544 (s), 1470 (s), 1418 (s), 1373 (s), 1333 (m), 1298 (s), 1270 (m), 1257 (m), 1173 (m), 1146 (m) 1042 (m), 1025 (m), 928 (w), 784 (s), 738 (w); **(+)-HR-ESI-MS**: *m*/*z* (%): 396.05227 (75, [*M – 2 ac – H*]$^+$, calcd for [$C_{20}H_{13}CoN_6$]$^+$: 396.05282), 198.53001 (100, [M – 2 ac]$^{2+}$, calcd for [$C_{20}H_{14}CoN_6$]$^{2+}$: 198.53005; **(-)-HR-ESI-MS**: *m*/*z* (%): 513.07249 (100, [M^{III} – 2 H]$^-$, calcd for [$C_{24}H_{18}CoO_4N_6$]$^-$: 513.07270; **Anal. calcd.** for [$C_{24}H_{20}CoN_6O_4$] + 2 CH_3OH (%):C 53.89, H 4.87, N 14.50; Found C 49.02, H 4.30, N 13.57.

*[Co^{II}(ac)$_2$(Me$_2$*aza*-pyr)] (**56**)*

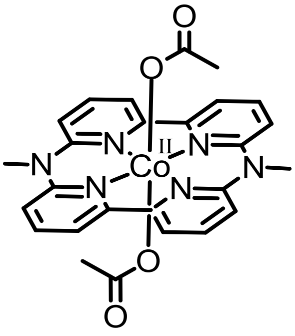

Ligand **25** (30 mg, 0.082 mmol), Co^{II}(ac)$_2$ tetrahydrate (21 mg, 0.084 mmol) and MeOH (100 mL) were added into a 250 mL one necked round bottom flask. The orange suspension was stirred at reflux for 2h resulting while forming an orange solution. The heating was stopped and the methanol was removed at reduced pressure. The crude product was dissolved in water (100 mL) and purified by three sequential chromafix C$_{18}$ columns: activated with MeOH (10 mL), washed with (H_2O) 10 mL, loaded with product solution (7 mL), rinsed with water (5 mL) and washed with MeOH (10 mL). This cycle was repeated until the whole product solution was purified (100 mL). The MeOH/H_2O phase was reduced to approximately 10 mL. The resulting aqueous orange-yellow solution was lyophilised to obtain upon freezing a black solid that gave rise to pure **56** as black solid (25 mg, 0.046 mmol , 56 %). **(+)-HR-ESI-MS**: *m*/*z* (%): 543.11817 (100, [*M*]$^+$, calcd for [$C_{26}H_{24}CoN_6O_4$]$^+$: 543.11855); **Anal. calcd.** for [$C_{26}H_{24}CoN_6O_4$] (%):C 57.46, H 4.45, N 15.46; Found C 49.00, H 4.34, N 13.05.

*[Co^{II}(TfO)$_2$(*aza-*phyr)] (**57**)*

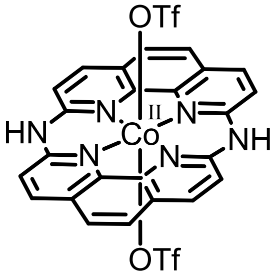

Complex **57** was synthesised by Christian Bünzli in our group.[76] Ligand **22** (28 mg, 0.072 mmol) was added into a 50 mL one necked round bottom schlenk and suspended in CH_3CN (25 mL). Co(OTf)$_2$ (25 mg, 0.069 mmol) was dissolved in CH_3CN (3 mL) and added to the suspension. The reaction was heated to reflux and stirred for 20 h. The heating was stopped and the yellow suspension was reduced to approximately 6 mL at reduced pressure. Precipitation was supported by storage of the reaction vial at 4 °C for 2 h. The suspension was filtrated and washed with H_2O (3 x 3 mL). The yellow solid was dried at high vacuum to obtain **57** as pure curry coloured solid (36 mg, 0.048 mmol, 67 %). Yellow crystals suitable for X-ray diffraction were obtained by vapour diffusion with CH_3CN as solvent and THF as antisolvent. **FT-IR** (ATR) (cm^{-1}): 3278 (w), 3171 (w), 3053 (w), 1636 (w), 1600 (w), 1558 (s), 1470 (s), 1371 (m), 1277 (s), 1227 (s), 1141 (s), 1027 (s), 848 (s), 798 (m), 730 (m); **UV/Vis** (H_2O) (ε, M^{-1} cm^{-1}): 277 (60700); **ESI-MS**: m/z = 444.1 (M - 2 OTf – 1 H)$^+$; **(+)-HR-ESI-MS**: *m*/*z* (%): 444.05255 (50, [*M – 2 OTf – H*]$^+$, calcd for [$C_{24}H_{13}CoN_6$]$^+$: 444.05282), 222.53014 (100, [M – *2 OTf*]$^{2+}$, calcd for [$C_{24}H_{14}CoN_6$]$^{2+}$: 222.53005; **(-)-HR-ESI-MS**: *m*/*z* (%): 148.95261 (100, [*OTf*]$^-$, calcd for [CF_3O_3S]$^-$: 148.95257; **Anal. calcd.** for [$C_{26}H_{14}CoF_6N_6O_6S_2$] (%):C 42.00, H 1.90, N 11.30; Found C 41.94, H 1.73, N 11.92.

*[Ni^{II}(*aza-*phyr)] (**58**)*

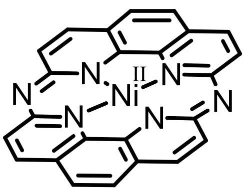

Ligand **22** (25 mg, 0.065 mmol), Ni(ClO$_4$)$_2$ hexa hydrate (26 mg, 0.071 mmol) and 20 mL dry DMF were added into a 50 mL one necked round bottom schlenk. The resulting yellow suspension was heated to 140 °C and stirred for 20 h to obtain an almost complete yellow-brown solution. The heating was suspended and an orange precipitate formed upon cooling. Precipitation was supported by storing the reaction vessel overnight in the fridge. The solid turned greenish upon cooling within one hour and turned complete green overnight. The green suspension was filtrated and washed with THF and DMF to obtain pure **58** as green solid (24 mg, 0.054 mmol, 83 %). **UPLC-MS**: 1.4 min (5 min method), m/z = 443.1 (M – 1 H)$^+$; **FT-IR** (ATR) (cm^{-1}): 3019 (w), 3010 (w), 1668 (w), 1559 (m), 1550 (m), 1447 (s), 1412 (s), 1377 (s), 1323 (m), 1257 (m), 1224 (m), 1201 (m), 1134 (m), 1086 (m), 988 (m), 981 (w), 941 (w), 838 (s), 793 (w), 736 (w); **(+)-HR-ESI-MS**: *m*/*z* (%): 443.05484 (100, [*M* + *H*]$^+$, calcd for [$C_{24}H_{13}N_6Ni$]$^+$: 443.05496), 222.03115 (100, [M + 2 H]$^{2+}$, calcd for [$C_{24}H_{14}N_6Ni$]$^{2+}$: 222.03112;**Anal. calcd.** for [$C_{24}H_{12}N_6Ni$] + H_2O (%):C 62.51, H 3.06, N 18.23; Found C 62.96, H 2.73, N 17.55.

*[$Co^{II}Br_2$(thia-phyr)] (**59**)*

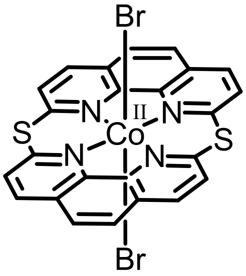

$CoBr_2$ hydrate was dried at high vacuum while heat was applied by a heat gun obtaining dry $CoBr_2$ as green powder. Compound **21** (100 mg, 0.15 mmol), dry $CoBr_2$ (34 mg, 0.15 mmol) and 20 mL dry pyridine was added into a 50 mL one necked round bottom schlenk. Immediately a brown suspension was obtained. The suspension was heated to reflux and stirred for 2 h. The reaction suspension was stirred at ambient temperature overnight. The yellow solution with red-brown precipitate was filtrated and washed with pyridine (30 mL) and Et_2O (10 mL) to obtain **59** after drying by high vacuum as beige solid (85 mg, 0.13 mmol, 89 %). **UPLC-MS**: 1.1 min (5 min method), m/z = 514.0 (M – 2 Br + 1 Cl)$^+$, 549.0 (M – 2 Br + 2 Cl + H) $^+$; **FT-IR** (ATR) (cm^{-1}): 3010 (m), 2009 (w), 1574 (s), 1498 (m), 1468 (s), 1449 (m), 1412 (m), 1351 (m), 1335 (m), 1261 (m), 1134 (s), 1074 (s), 925 (m), 868 (s), 838 (s), 794 (m), 722 (m); **Anal. calcd.** for [$C_{24}H_{12}Br_2CoN_4S_2$] (%):C 45.09, H 1.87, N 8.76; Found C 45.22, H 1.87, N 8.51.

4.2 Analytical Methods

^{1}H and ^{13}C NMR spectra were recorded on a Varian Mercury (200 MHz), a Varian Gemini-2000 (300 MHz) or a Bruker 500 UltraShield (500 MHz). Chemical shifts are reported relative to residual solvent peaks. s = singlet, d = doublet, t = triplet, q = quadruptlet, bs = broad singlet, m = multiplet. **UPLC-MS / ESI-MS:** UPLC separation was performed on an Acquity^{TM} Ultra Performance LC with an Acquity UPLC® BEH C18 column (1.7 µm, 2.1 × 50 mm; 0.3 mL/min flow rate) and a gradient of 0.1 % aqueous formic acid and acetonitrile eluents. The mass spectra were recorded on an Esquire HCT from Bruker (Germany), the injection rate was 3 µL/min, the nebulizer pressure was 10 psi, and the dry gas flow rate was 5 L/min at 350 °C. All solvents were of HPLC/LCMS grade. **HPLC** traces were recorded with a VWR Hitachi Elite LaChrome with a C18-nucleodur or Phenomenex Core Shell column and H_2O/MeOH as eluent (gradient starting with 10% MeOH, 0.1% TFA in H_2O to pure MeOH). **Elemental Analyses** were performed on a Leco CHNS-932 elemental analyzer. **UV/VIS** spectra were measured using a Cary 50 spectrometer with solution samples in 1 cm quartz cells. For air sensitive samples, cells with silicon septa lids were used to keep samples under an inert gas atmosphere during measurements. **Luminescence measurements** were performed on a Perkin-Elmer LS50B fluorescence spectrometer with argon-purged solution samples in 1 cm cells. **Electrochemical measurements:** A Metrohm or 797VA Computrace electrochemical analyzer was used with a standard three-electrode setup of glassy carbon working (ID = 2 mm), Pt auxiliary electrode and Ag/AgCl reference electrode. All potentials were referenced to Fc as an internal standard and are given vs. $Fc^{0/+}$. LSV measurements were performed in a self-designed setup (2.5.3) controlled by a Metrohm autolab potentiostat (PGSTAT302N) operated with the NOVA software. **Spectroelectrochemical analysis** was performed in an optical transparent thin layer electrolysis (OTTLE) cell in the UV/Vis spectrometer described above. The working electrode was a platinum gauze immersed into the OTTLE cell, auxiliary electrode was a platinum wire, and the reference electrode was an Ag/AgCl electrode. To control the potential a Metrohm autolab potentiostat (PGSTAT302N) operated with the software NOVA was used. **Crystallographic data** were collected at 183(2) K on an Oxford Diffraction Xcalibur system with a Ruby detector using Mo K_α radiation (λ = 0.7107 Å) that was graphitemonochromated or an Oxford Diffraction SuperNova dual source system with an Atlas detector using Cu K_α (λ = 1.54184 Å) or Mo K_α radiation (λ = 0.7107 Å). Suitable crystals were covered with oil (Infineum V8512), placed on a nylon loop that is mounted in a CrystalCap Magnetic™ (Hampton Research) and immediately transferred to the diffractometer. The program suite CrysAlis^{Pro} was used for data collection, multi-scan absorption correction and data reduction.[146] The structure was solved with direct methods using SIR97[147] and was refined by full-matrix least-squares methods on F^2 with SHELXL-97.[148] ORTEP representations were created by the program ORTEP-3.[149] **Hydrogen evolution measurements:** Gas chromatograms were recorded using either an automated Bruker GC-450 or GC-456 gas chromatograph with argon as carrier gas and a 3 m x 2 mm packed molecular sieve 13X 80–100 column. The column and reference gas flow (Ar) was set to 20 $mLmin^{-1}$. The oven was operated isothermally at 100 °C. An argon flow of 6 $mLmin^{-1}$ (adjusted with an onboard electronic flow control device and referenced with a F-200CV-002 from Bronkhorst) was passed through the reaction mixture and into the GC, in which 1 mL gas samples were automatically injected at defined time intervals (usually 5 min) using a 6-Port 2-Position Valve from Vicci. The gases were detected using a thermal conductivity detector operated at 150 °C (filament temperature 170 °C; retention time ~1 min for H_2). Calibration was achieved by mixing Ar and H_2 in known ratios with two mass flow controllers (Bronkhorst, F-201CV-200 for Ar and F-200CV-002 for H_2, 0.51% H_2 in Ar (Pangas)). This setup allowed the detection of H_2 down to minimum mole fractions of $2 \cdot 10^{-6}$. At Ar flows of 6$mLmin^{-1}$ through the reaction the detection limit was $H_2/s \geq 1 \cdot 10^{-11}$. **FT-IR** spectra were measured on a Perkin Elmer Spectrum BX II with KBr-pellets or via a golden gate mount.

5. Supporting Information

5.1 Crystallographic Tables

Identification code	*cis*-pyr-bu$_2$ (**4**)	pyr-pent **(6)**	[Co^{II}Br(MeOH)(pyr-bu)] (**44**)
Empirical formula	$C_{32}H_{30}N_6$	$C_{35}H_{36}N_6$	$C_{29}H_{25}BrCoN_6O_{1.13}$
Formula weight	498.62	540.70	614.64
Crystal system	triclinic	monoclinic	monoclinic
Space group	P-1	P21/c	P21/n
a [Å]	8.2048(3)	15.7566(9)	7.5599(7)
b [Å]	14.7409(5)	15.9366(8)	14.9746(15)
c [Å]	22.1721(9)	11.6429(6)	22.551(3)
α [°]	85.744(3)	90	90
β [°]	87.213(3)	93.076(5)	93.612(9)
γ [°]	89.981(3)	90	90
Volume [Å^3]	2671.06(16)	2919.4(3)	2547.9(5)
Z	4	4	4
Density (calculated) [Mg/m^3]	1.240	1.230	1.602
Absorption coefficient [mm^{-1}]	0.589	0.074	2.279
F(000)	1056	1152	1.249
Crystal size [mm^3]	0.28 x 0.18 x 0.04	0.41 x 0.21 x 0.07	0.16 x 0.10 x 0.09
Crystal description	yellow plate	pink plate	black prism
Radiation [nm]	CuKα (λ = 1.54184)	MoKα (λ = 0.71073)	MoKα (λ = 0.71073)
Theta range for data collection [°]	2.00 to 76.57	2.89 to 25.35	2.79 to 25.35
Index ranges	-10<=h<=10, -14<=k<=18, -27<=l<=21	-15<=h<=18, -19<=k<=16, -14<=l<=13	-9<=h<=7, -17<=k<=18, -27<=l<=21
Reflections collected	36749	14701	14184
Independent reflections	11019 [R(int) = 0.0236]	5315 [R(int) = 0.0432]	4661 [R(int) = 0.0662]
Reflections observed	9451	3740	3379
Criterion for observation	>2sigma(I)	>2sigma(I)	>2sigma(I)
Completeness to theta	98.8 % to 74.33°	99.8 % to 25.35°	99.9 % to 25.35°
Absorption correction	Semi-empirical from equiv.	Semi-empirical from equiv.	Semi-empirical from equiv.
Max. and min. transmission	0.9768 and 0.7692	0.9949 and 0.6469	0.8212 and 0.6420
Data / restraints / parameters	11019 / 0 / 689	5315 / 0 / 389	4661 / 0 / 347
Goodness-of-fit on F^2	1.097	1.025	1.057
Final R indices [I>2sigma(I)]	R1 = 0.0780, wR2 = 0.2287	R1 = 0.0551, wR2 = 0.1275	R1 = 0.0652, wR2 = 0.1379
R indices (all data)	R1 = 0.0866, wR2 = 0.2328	R1 = 0.0845, wR2 = 0.1463	R1 = 0.0980, wR2 = 0.1532
Largest diff. peak and hole [e.Å^{-3}]	0.354 and -0.276	0.314 and -0.247	0.924 and -0.622

Identification code	pyr-Ibu (**9**)	pyr-dioxolane (**8**)	$[Co_2^{II/III}O_2(py)_2(pyr\text{-}peg)_2][ClO_4]_2$ (**42a**)	$[Cu^{II}$(dioxane)*(pyr-bu)*$][ClO_4]$ (**47a**)	$[Cu^{II}$*(pyr-bu)*$][ClO_4]$ (**47b**)
Empirical formula	$C_{29}H_{23}Cl_2IN_6$	$C_{29}H_{22}N_6O_{2.29}$	$C_{68}H_{56}Cl_2Co_2N_{14}O_{14}$	$C_{72}H_{74}Cl_2Cu_2N_{12}O_{16}$	$C_{56}H_{42}Cl_2Cu_2N_{12}O_8$
Formula weight	653.33	491.24	1482.02	1561.41	1208.99
Temperature/K	183(1)	183(1)	183(1)	183(1)	183(1)
Crystal system	monoclinic	triclinic	monoclinic	triclinic	monoclinic
Space group	$P2_1/n$	P-1	C2/c	P-1	I2/a
a [Å]	18.0213(7)	8.1484(4)	21.6783(5)	11.6907(3)	12.6730(8)
b [Å]	8.1644(3)	12.4805(5)	14.3656(3)	12.6433(4)	32.9520(10)
c [Å]	20.1201(8)	12.9265(7)	21.1450(6)	12.7379(4)	14.0846(9)
α [°]	90	76.393(4)	90	106.675(3)	90
β [°]	113.448(5)	85.878(4)	110.446(3)	98.853(2)	116.456(8)
γ [°]	90	82.997(4)	90	106.147(2)	90
Volume [$Å^3$]	2715.8(2)	1266.87(11)	6170.2(3)	1675.64(9)	5265.8(6)
Z	4	2	4	1	4
Density (calculated) [Mg/m^3]	1.598	1.288	1.595	1.547	1.525
Absorption coefficient [mm^{-1}]	1.407	0.688	5.712	0.796	0.978
F(000)	1304	513.0	3048	810	2472
Crystal size [mm^3]	0.31 × 0.25 × 0.03	0.09 × 0.06 × 0.04	0.36 × 0.11 × 0.07	0.3 × 0.19 × 0.17	0.31 × 0.15 × 0.11
Radiation [nm]	MoKα (λ = 0.71073)	CuKα (λ = 1.54184)	CuKα (λ = 1.54184)	MoKα (λ = 0.71073)	MoKα (λ = 0.71073)
2Θ range for data collection [°]	4.928 to 61.002	7.0 to 148.9	7.538 to 136.508	5.258 to 61.014	4.37 to 52.744
Index ranges	$-25 \le h \le 15$, $-10 \le k \le 11$, $-24 \le l \le 28$	$-10 \le h \le 9$, $-15 \le k \le 15$, $-15 \le l \le 16$	$-26 \le h \le 26$, $-16 \le k \le 17$, $-25 \le l \le 25$	$-16 \le h \le 16$, $-18 \le k \le 18$, $-18 \le l \le 18$	$-15 \le h \le 15$, $-41 \le k \le 41$, $-16 \le l \le 17$
Reflections collected	18818	21457	46040	37654	26970
Independent reflections	8277 [R_{int} = 0.0288, R_{sigma} = 0.0413]	5053 [R_{int} = 0.0316, R_{sigma} = 0.0250]	5658 [R_{int} = 0.0589, R_{sigma} = 0.0222]	10205 [R_{int} = 0.0353, R_{sigma} = 0.0351]	5387 [R_{int} = 0.0312, R_{sigma} = 0.0227]
Data/restraints/parameters	8277/0/343	5053/60/347	5658/92/489	10205/6/480	5387/60/395
Goodness-of-fit on F^2	1.047	1.036	1.049	1.038	1.036
Final R indexes [I>=2σ (I)]	R_1 = 0.0446, wR_2 = 0.1084	R_1 = 0.0752, wR_2 = 0.2149	R_1 = 0.0545, wR_2 = 0.1504	R_1 = 0.0428, wR_2 = 0.1077	R_1 = 0.0343, wR_2 = 0.0912
Final R indexes [all data]	R_1 = 0.0617, wR_2 = 0.1201	R_1 = 0.0919, wR_2 = 0.2303	R_1 = 0.0595, wR_2 = 0.1565	R_1 = 0.0555, wR_2 = 0.1161	R_1 = 0.0445, wR_2 = 0.0997
Largest diff. peak and hole [e.$Å^{-3}$]	1.27/-1.06	0.66/-0.79	1.14/-0.67	0.80/-0.65	0.53/-0.42

Identification code	[Ni^{II}(pyr-bu)][ClO$_4$] (**46**)	[Zn^{II}(py)(pyr-MePEG)][OTf] (**49**)
Empirical formula	$C_{60}H_{50}Cl_2N_{12}Ni_2O_9$	$C_{40}H_{33}F_3N_8O_5SZn$
Formula weight	1271.44	860.17
Temperature/K	183(1)	183(1)
Crystal system	monoclinic	monoclinic
Space group	C2/c	P2$_1$/n
a [Å]	13.5619(11)	13.5524(4)
b [Å]	31.5748(15)	12.8033(3)
c [Å]	13.6087(11)	22.6427(7)
α [°]	90	90
β [°]	114.082(10)	105.460(3)
γ [°]	90	90
Volume [Å^3]	5320.2(8)	3786.70(19)
Z	4	4
Density (calculated) [Mg/m^3]	1.587	1.509
Absorption coefficient [mm^{-1}]	0.883	0.776
F(000)	2624	1768
Crystal size [mm^3]	0.4 × 0.08 × 0.06	0.50 × 0.21 × 0.12
Radiation [nm]	MoKα (λ = 0.71073)	MoKα (λ = 0.71073)
2Θ range for data collection [°]	5.08 to 52.746	5.3 to 61.0
Index ranges	$-16 \le h \le 13$, $-39 \le k \le 38$, $-16 \le l \le 17$	$-19 \le h \le 19$, $-18 \le k \le 18$, $-31 \le l \le 32$
Reflections collected	16108	41952
Independent reflections	5439 [R_{int} = 0.0386, R_{sigma} = 0.0484]	11558 [R_{int} = 0.0325, R_{sigma} = 0.0341]
Data/restraints/parameters	5439/68/395	11558/184/599
Goodness-of-fit on F^2	1.03	1.035
Final R indexes [I>=2σ (I)]	R_1 = 0.0510, wR_2 = 0.1195	R_1 = 0.0699, wR_2 = 0.1856
Final R indexes [all data]	R_1 = 0.0788, wR_2 = 0.1382	R_1 = 0.0841, wR_2 = 0.1968
Largest diff. peak and hole [e.Å^{-3}]	0.58/-0.53	2.05/-1.36

5.2 pH dependent CV measurements (BRB)

Electrochemical measurements were performed with a Metrohm 797 VA Computrace with a hanging mercury drop electrode (HMDE) and a Pt counter electrode versus a Ag/AgCl reference electrode. Prior to each measurement methyl viologen dichloride hydrate (MVCl2; MVCl2 • 2.5 H2O according to elemental analysis) was measured at 1 mM concentration and the potentials referenced to the standard hydrogen electrode (NHE) according to a reported value (-440 mV vs. NHE). The peak current of the reduction wave (usually 400-800 nA) was taken as the reference current flow for a one electron reduction. The onset potential for each WRC was defined as the corresponding 4 fold electron flow.

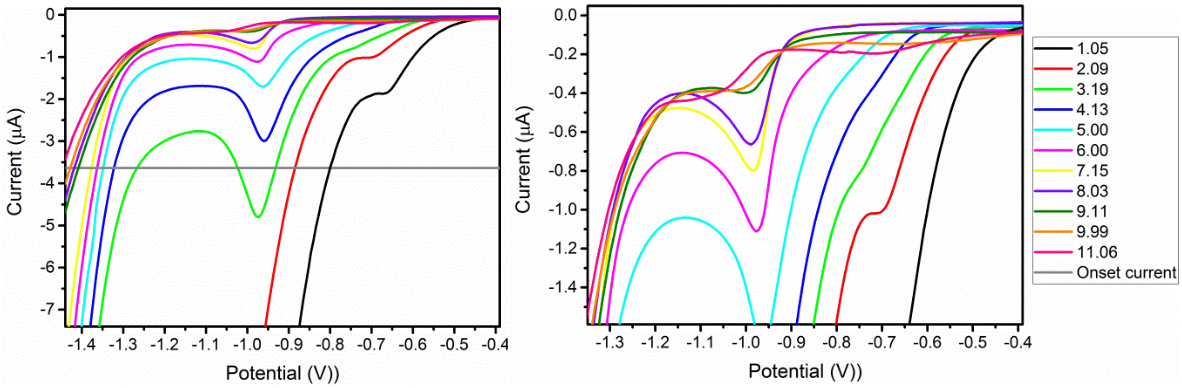

***Figure SI 1**: Cathodic waves of cyclic voltammograms of 1 mM [CoBr(tpy)]Br (**80**) at various pH values determined in 40 mM BRB and 0.1 M NaOTf. The pH was adjusted with 10-20 µL 5 M aqueous NaOH per pH unit. The onset current was defined as the 4 fold current flow of a one electron reduction (see above).*

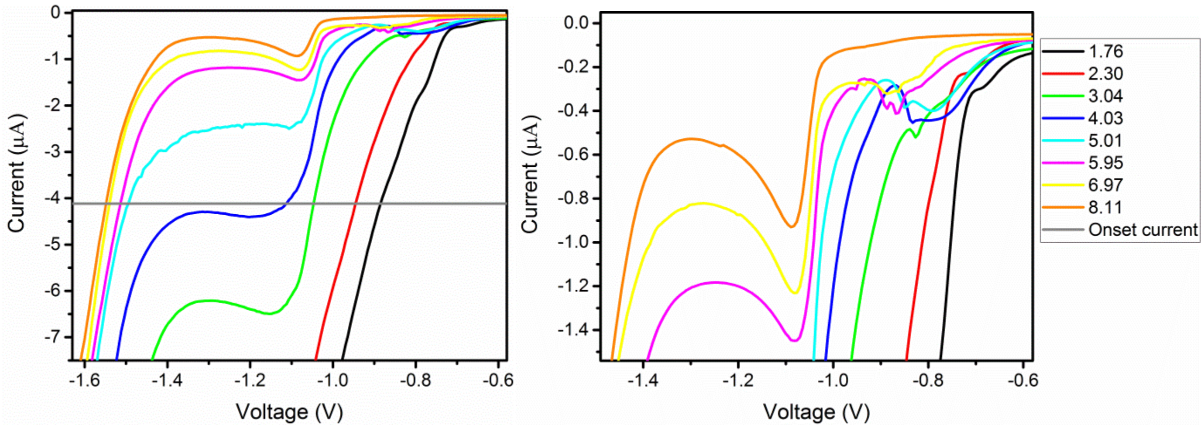

***Figure SI 2**: Cathodic waves of cyclic voltammograms of 1 mM [CoBr((MeO)$_2$tpy)]Br (**81**) at various pH values determined in 40 mM BRB and 0.1 M NaOTf. The pH was adjusted with 10-20 µL 5 M aqueous NaOH per pH unit. The onset current was defined as the 4 fold current flow of a one electron reduction (see above).*

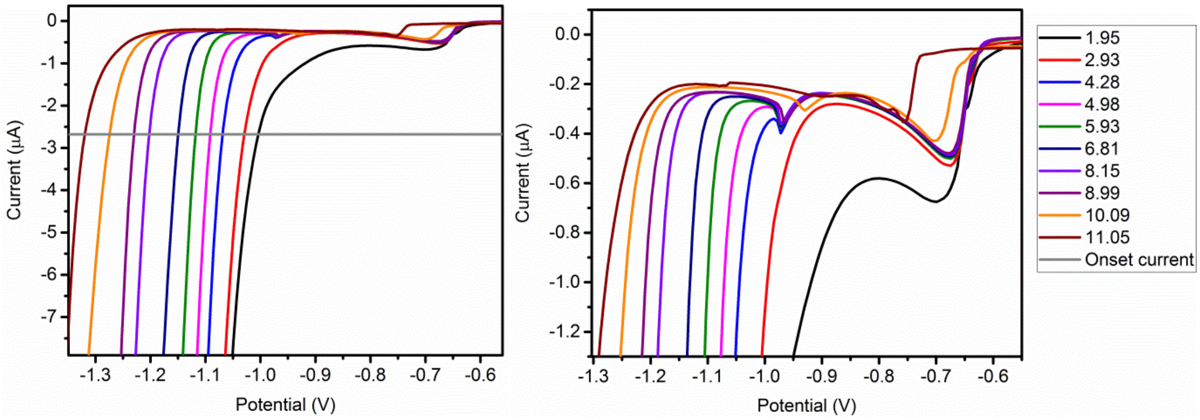

Figure SI 3*: Cathodic waves of cyclic voltammograms of 1 mM [CoBr(appy)]Br (****82****) at various pH values determined in 40 mM BRB and 0.5 M NaOTf. The pH was adjusted with 10-20 µL 5 M aqueous NaOH per pH unit. The onset current was defined as the 4 fold current flow of a one electron reduction (see above).*

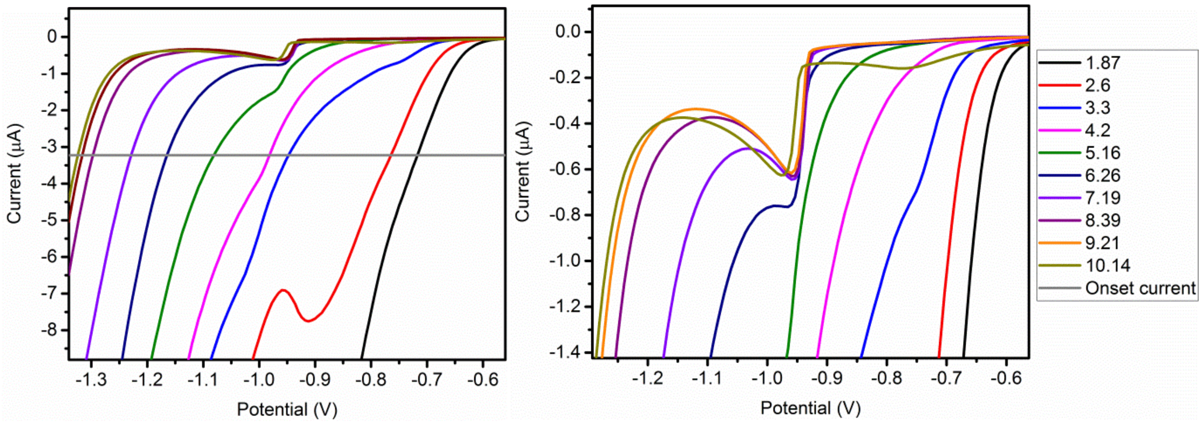

Figure SI 4*: Cathodic waves of cyclic voltammograms of 1 mM [CoBr((MeO)$_4$appy)]Br (****83****) at various pH values determined in 40 mM BRB. The pH was adjusted with 10-20 µL 5 M aqueous NaOH per pH unit. The onset current was defined as the 4 fold current flow of a one electron reduction (see above).*

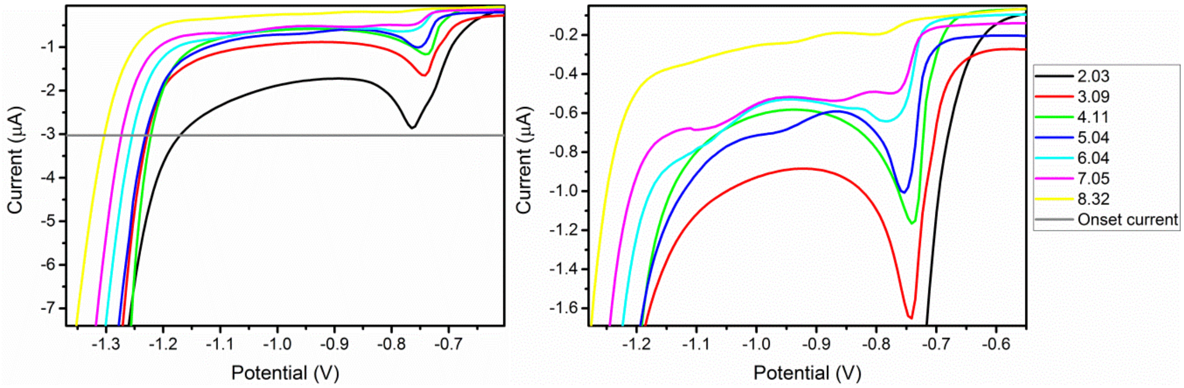

Figure SI 5*: Cathodic waves of cyclic voltammograms of 1 mM [CoBr(C-appy)]Br (****84****) at various pH values determined in 40 mM BRB and 0.1 M NaOTf. The pH was adjusted with 10-20 µL 5 M aqueous NaOH per pH unit. The onset current was defined as the 4 fold current flow of a one electron reduction (see above).*

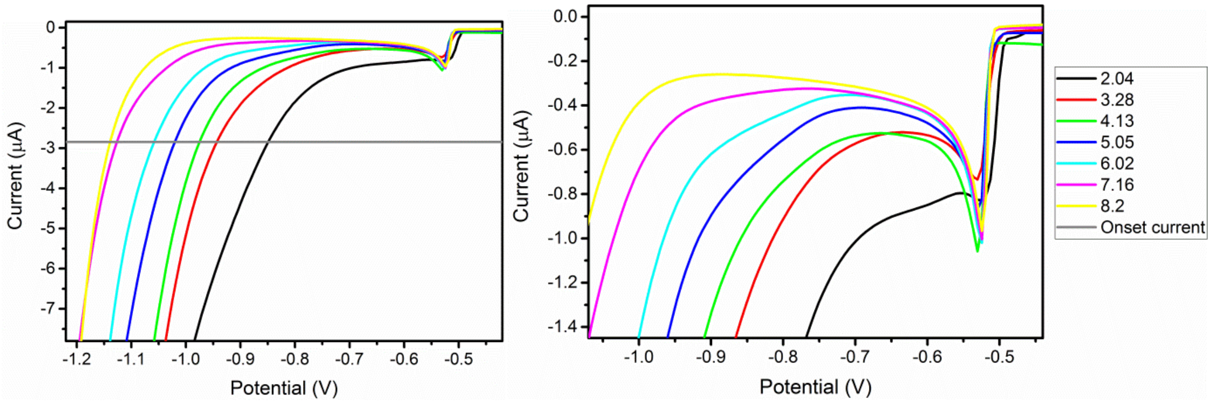

***Figure SI 6**: Cathodic waves of cyclic voltammograms of 1 mM [Co(hpy)]Br$_2$ (**85**) at various pH values determined in 40 mM BRB and 0.1 M KNO$_3$. The pH was adjusted with 10-20 µL 5 M aqueous NaOH per pH unit. The onset current was defined as the 4 fold current flow of a one electron reduction (see above).*

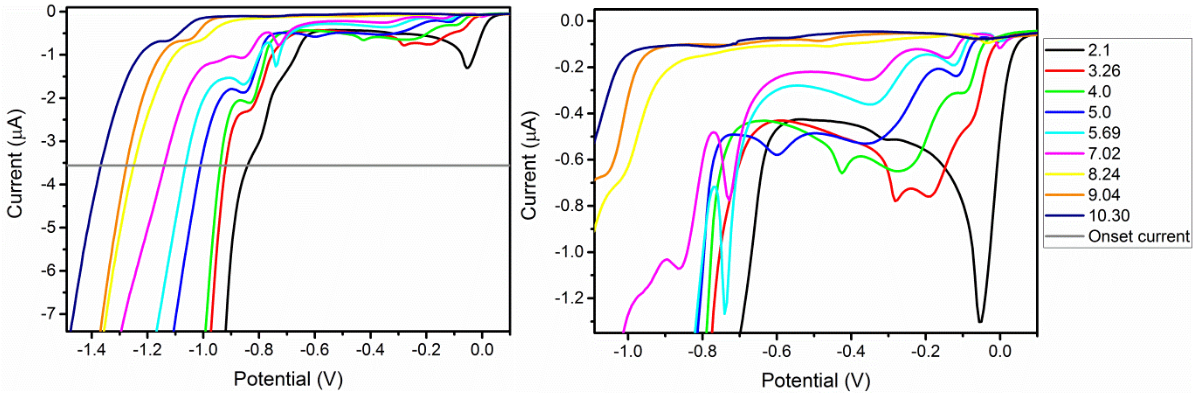

***Figure SI 7**: Cathodic waves of cyclic voltammograms of 1 mM [Co(bpy$_2$CO)]OTf$_2$ (**86**) at various pH values determined in 40 mM BRB and 0.1 M NaOTf. The pH was adjusted with 10-20 µL 5 M aqueous NaOH per pH unit. The onset current was defined as the 4 fold current flow of a one electron reduction (see above).*

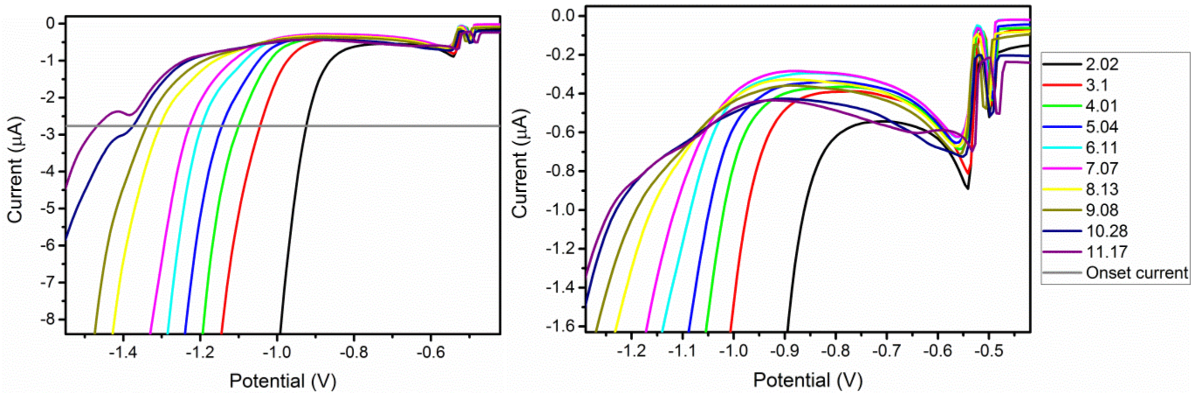

***Figure SI 8**: Cathodic waves of cyclic voltammograms of 1 mM [CoBr$_2$(bpy$_2$NH)] (**87**) at various pH values determined in 40 mM BRB and 0.1 M NaOTf. The pH was adjusted with 10-20 µL 5 M aqueous NaOH per pH unit. The onset current was defined as the 4 fold current flow of a one electron reduction (see above).*

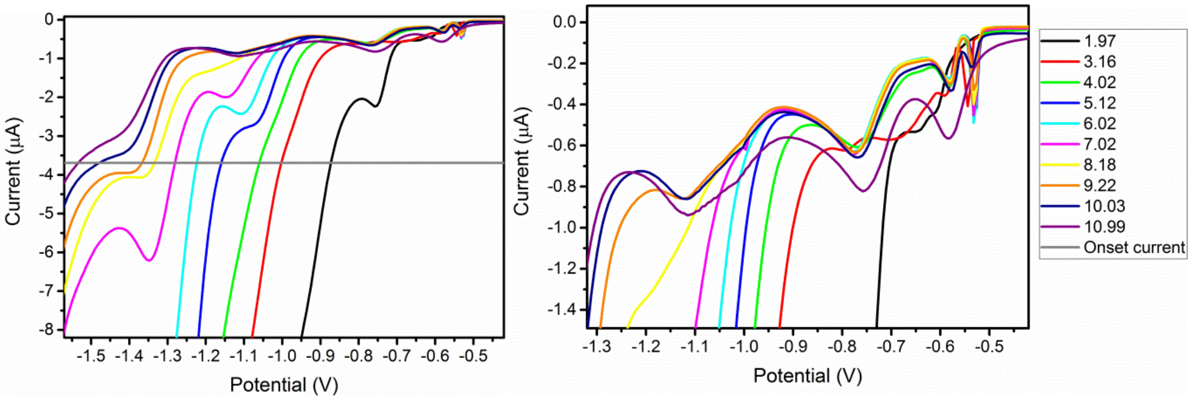

***Figure SI 9**: Cathodic waves of cyclic voltammograms of 1 mM [CoBr$_2$(N-appy)] (**88**) at various pH values determined in 40 mM BRB and 0.1 M NaOTf. The pH was adjusted with 10-20 µL 5 M aqueous NaOH per pH unit. The onset current was defined as the 4 fold current flow of a one electron reduction (see above).*

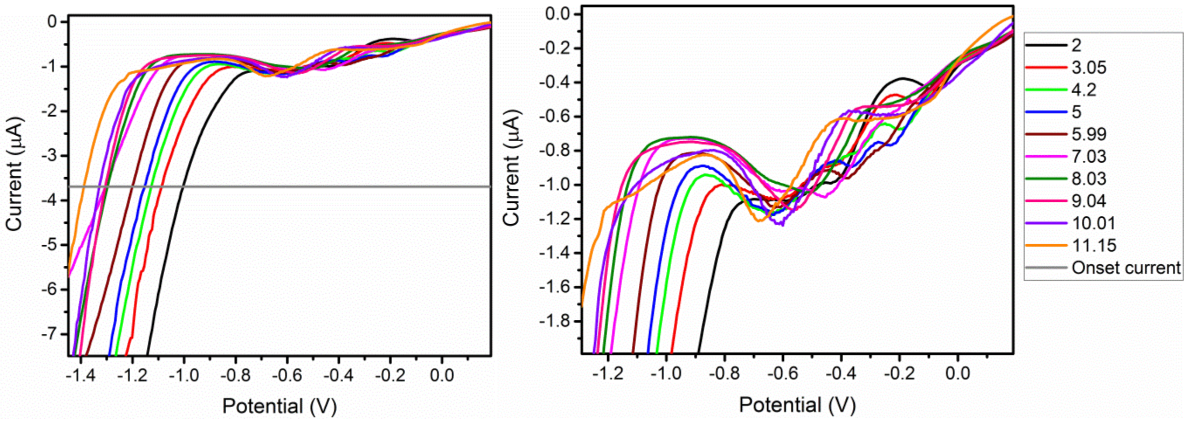

***Figure SI 10**: Cathodic waves of cyclic voltammograms of 1 mM [CoBr(pyr-bu)(MeOH)]Br (**44**) at various pH values determined in 40 mM BRB. The pH was adjusted with 10-20 µL 5 M aqueous NaOH per pH unit. The onset current was defined as the 4 fold current flow of a one electron reduction (see above).*

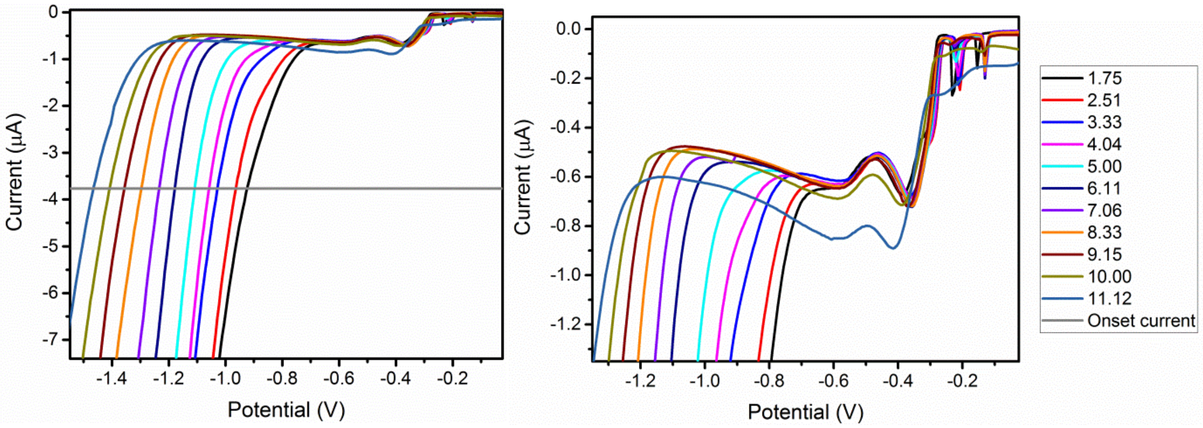

***Figure SI 11**: Cathodic waves of cyclic voltammograms of 1 mM [CoBr$_2$(cis-pyr-bu$_2$)] (**50**) at various pH values determined in 40 mM BRB. The pH was adjusted with 10-20 µL 5 M aqueous NaOH per pH unit. The onset current was defined as the 4 fold current flow of a one electron reduction (see above).*

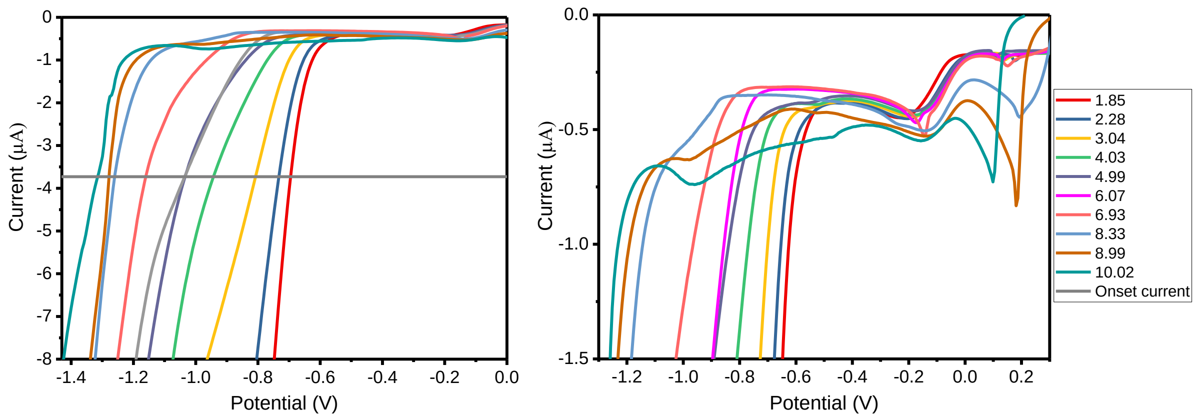

***Figure SI 12**: Cathodic waves of cyclic voltammograms of 1 mM [Co^{II}(ac)$_2$(aza-pyr)] (**55**) at various pH values determined in 40 mM BRB and 0.1 M NaOTf. The pH was adjusted with 10-20 µL 5 M aqueous NaOH per pH unit. The onset current was defined as the 4 fold current flow of a one electron reduction (see above).*

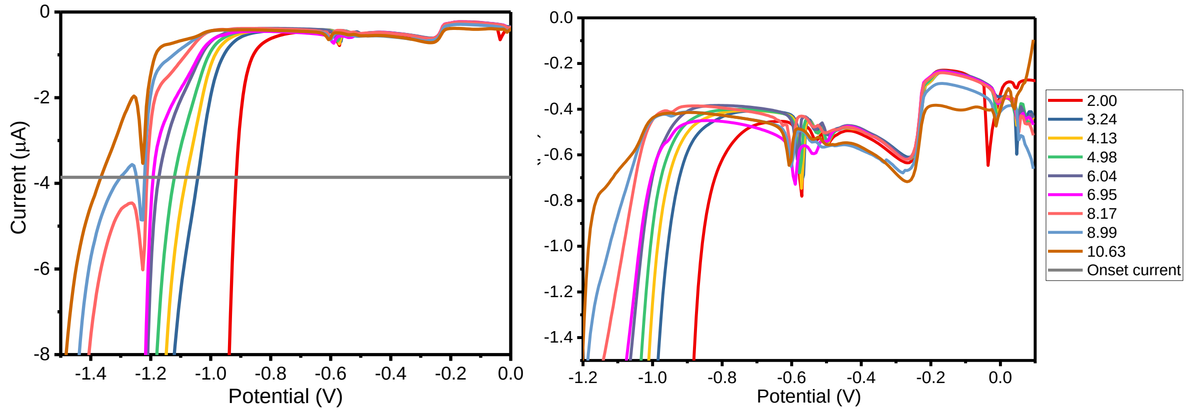

***Figure SI 13**: Cathodic waves of cyclic voltammograms of 1 mM [Co^{II}(ac)$_2$(Me$_2$-aza-pyr)] (**56**) at various pH values determined in 40 mM BRB and 0.1 M NaOTf. The pH was adjusted with 10-20 µL 5 M aqueous NaOH per pH unit. The onset current was defined as the 4 fold current flow of a one electron reduction (see above).*

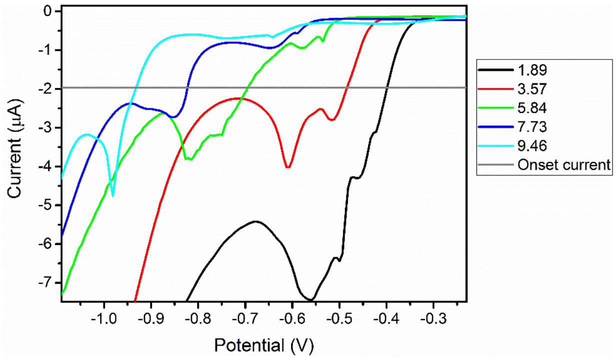

***Figure SI 14**: Cathodic waves of cyclic voltammograms of 1 mM [[CoBr$_2$((DO)(DOH)pn)] at various pH values determined in 40 mM BRB and 0.1 M NaOTf. The pH was adjusted with 10-20 µL 5 M aqueous NaOH per pH unit. The onset current was defined as the 4 fold current flow of a one electron reduction (see above).*

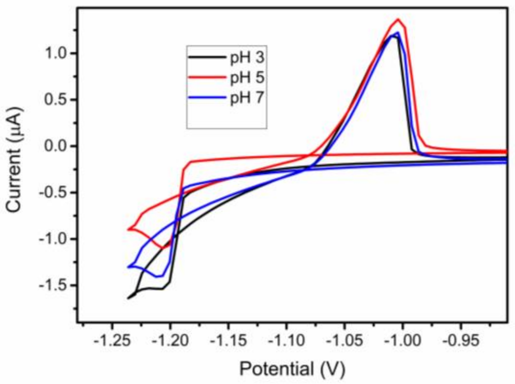

***Figure SI 15**: Cyclic voltammograms of [Ru(bpy)$_3$]Cl$_2$ (**RuPS**) at various pH values determined in 40 mM BRB and 0.1 M NaOTf.*

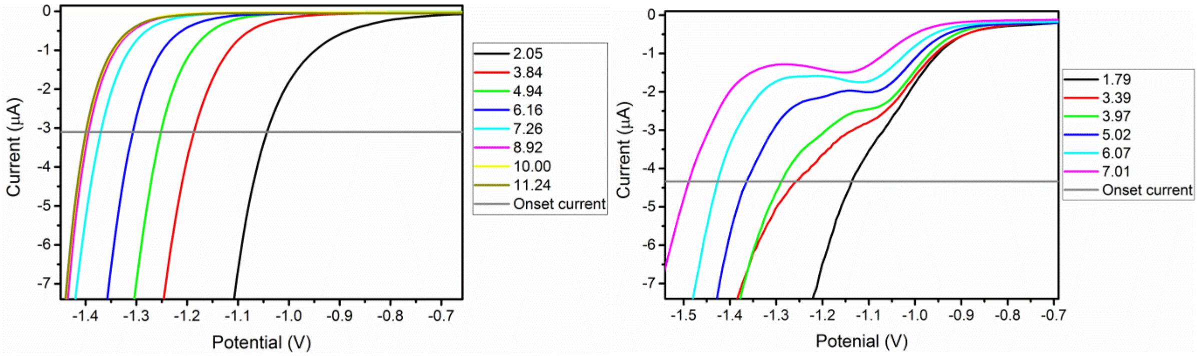

***Figure SI 16**: Cathodic waves of cyclic voltammograms of the plain HMDE (left) and 1 mM [Co(H$_2$O)$_6$]Br$_2$ (right) at various pH values determined in 40 mM BRB and 0.5 M KNO$_3$ (left) or 0.1 M NaOTf (right). The pH was adjusted with 10-20 µL 5 M aqueous NaOH per pH unit. The onset current was defined as the 4 fold current flow of a one electron reduction (see above).*

6. References

(1) Office of Energy Efficiency & Renewable Energy: 2017; Vol. 2017.

(2) Farrugia, L. J. *J. Appl. Cryst.* **1997**, *30*, 565.

(3) Joliat, E. *dissertation*, University of Zurich, 2017.

(4) *BP Energy Outlook*, BP, 2017.

(5) *A Shifting Global Economic Landscape*, International Monetary Fund, 2017.

(6) *BP Statistical Review of World Energy*, 2016.

(7) Styring, S. *Faraday Discuss.* **2012**, *155*, 357.

(8) *Bundesverfassung Schweiz, Artikel 732.44*, Switzerland, 1983.

(9) *Überprüfung der Beitragsbemessung in die Stilllegungs- und Entsorgungsfonds auf Basis der Kostenstudie 2016*, Schweizerische Energie-Stiftung, 2017.

(10) *World Energies Scenarios 2016*, World Energy Council, 2016.

(11) Sukhatme, S. P., Nayak, J. K. *Solar Energy Principle of Thermal Collection and Storage*; 3th ed.; Tata McGraw-Hill Publishing Company Limited, 2007.

(12) Garg, H. P., Prakash, J. *Solar Energy: Fundamentals and Applications*; 1st ed.; Tata McGraw-Hill publishing Company Limited, 2000.

(13) Administration, U. S. E. I. *International Energy Outlook 2016*, 2016.

(14) Papadopoulou, E. *Green Energy and Technology: Photovoltaic Industrial Systems – An Environmental Approach*; 1st ed.; Springer, 2011.

(15) Baxter, R. *Energy Storage: A Nontechnical Guide*; 1st ed.; PennWell Corporation, 2005.

(16) Collings, A. F., Critchley C. *Artificial Photosynthesis*; 1st ed.; WILEY-VCH, 2005.

(17) Lewis, N. S.; Nocera, D. G. *P. Natl. Acad. Sci. USA* **2006**, *103*, 15729.

(18) Jahangiri, H.; Bennett, J.; Mahjoubi, P.; Wilson, K.; Gu, S. *Catal. Sci. Technol.* **2014**, *4*, 2210.

(19) Olah, G. A. *Angew. Chem. Int. Ed.* **2005**, *44*, 2636.

(20) Guttentag, M.; Rodenberg, A.; Bachmann, C.; Senn, A.; Hamm, P.; Alberto, R. *Dalton T.* **2013**, *42*, 334.

(21) Berardi, S.; Drouet, S.; Francas, L.; Gimbert-Surinach, C.; Guttentag, M.; Richmond, C.; Stoll, T.; Llobet, A. *Chem. Soc. Rev.* **2014**, *43*, 7501.

(22) Nocera, D. G. *Acc. Chem. Res.* **2012**, *45*, 767.

(23) Blakemore, J. D.; Crabtree, R. H.; Brudvig, G. W. *Chemical Reviews* **2015**, *115*, 12974.

(24) Evangelisti, F.; Car, P.-E.; Blacque, O.; Patzke, G. R. *Catal. Sci. Technol.* **2013**, *3*, 3117.

(25) Conrad, F.; Bauer, M.; Sheptyakov, D.; Weyeneth, S.; Jaeger, D.; Hametner, K.; Car, P.-E.; Patscheider, J.; Gunther, D.; Patzke, G. R. *RSC Adv.* **2012**, *2*, 3076.

(26) Brown, G. M.; Brunschwig, B. S.; Creutz, C.; Endicott, J. F.; Sutin, N. *J. Am. Chem. Soc.* **1979**, *101*, 1298.

(27) Hawecker, J.; Lehn, J. M.; Ziessel, R. *New J. Chem.* **1983**, *7*, 271.

(28) Queyriaux, N.; Jane, R. T.; Massin, J.; Artero, V.; Chavarot-Kerlidou, M. *Coord. Chem. Rev.* **2015**, *304–305*, 3.

(29) DiSalle, B. F.; Bernhard, S. *J. Am. Chem. Soc.* **2011**, *133*, 11819.

(30) Fihri, A.; Artero, V.; Pereira, A.; Fontecave, M. *Dalton T.* **2008**, 5567.

(31) Fihri, A.; Artero, V.; Razavet, M.; Baffert, C.; Leibl, W.; Fontecave, M. *Angew. Chem. Int. Ed.* **2008**, *47*, 564.

(32) Probst, B.; Rodenberg, A.; Guttentag, M.; Hamm, P.; Alberto, R. *Inorg. Chem.* **2010**, *49*, 6453.

(33) Guttentag, M.; Rodenberg, A.; Kopelent, R.; Probst, B.; Buchwalder, C.; Brandstätter, M.; Hamm, P.; Alberto, R. *Eur. J. Inorg. Chem.* **2012**, 59.

(34) Luo, S.-P.; Mejía, E.; Friedrich, A.; Pazidis, A.; Junge, H.; Surkus, A.-E.; Jackstell, R.; Denurra, S.; Gladiali, S.; Lochbrunner, S.; Beller, M. *Angew. Chem. Int. Ed.* **2013**, *52*, 419.

(35) Windisch, J.; Orazietti, M.; Hamm, P.; Alberto, R.; Probst, B. *Chemsuschem* **2016**, *9*, 1719.

(36) Natali, M.; Argazzi, R.; Chiorboli, C.; Iengo, E.; Scandola, F. *Chem.-Eur. J.* **2013**, *19*, 9261.

(37) Lazarides, T.; Delor, M.; Sazanovich, I. V.; McCormick, T. M.; Georgakaki, I.; Charalambidis, G.; Weinstein, J. A.; Coutsolelos, A. G. *Chem. Commun.* **2014**, *50*, 521.

(38) Martindale, B. C. M.; Hutton, G. A. M.; Caputo, C. A.; Reisner, E. *J. Am. Chem. Soc.* **2015**, *137*, 6018.

(39) Lazarides, T.; McCormick, T.; Du, P.; Luo, G.; Lindley, B.; Eisenberg, R. *J. Am. Chem. Soc.* **2009**, *131*, 9192.

(40) Joliat, E.; Schnidrig, S.; Probst, B.; Bachmann, C.; Spingler, B.; Baldridge, K. K.; von Rohr, F.; Schilling, A.; Alberto, R. *Dalton T.* **2016**, *45*, 1737.

(41) Singh, N.; Prasad, L. B. *Synth. React. Inorg. Met.-Org. Chem.* **1996**, *26*, 627.

(42) Probst, B.; Guttentag, M.; Rodenberg, A.; Hamm, P.; Alberto, R. *Inorg. Chem.* **2011**, *50*, 3404.

(43) Cline, E. D.; Adamson, S. E.; Bernhard, S. *Inorg. Chem.* **2008**, *47*, 10378.

(44) Lazarides, T.; McCormick, T.; Du, P. W.; Luo, G. G.; Lindley, B.; Eisenberg, R. *J. Am. Chem. Soc.* **2009**, *131*, 9192.

(45) Eckenhoff, W. T.; Eisenberg, R. *Dalton T.* **2012**, *41*, 13004.

(46) Artero, V.; Chavarot-Kerlidou, M.; Fontecave, M. *Angew. Chem. Int. Edit.* **2011**, *50*, 7238.

(47) Losse, S.; Vos, J. G.; Rau, S. *Coord. Chem. Rev.* **2010**, *254*, 2492.

(48) Jacques, P. A.; Artero, V.; Pecaut, J.; Fontecave, M. *Proc. Natl. Acad. Sci. USA* **2009**, *106*, 20627.

(49) Bachmann, C.; Guttentag, M.; Spingler, B.; Alberto, R. *Inorg. Chem.* **2013**, *52*, 6055.

(50) Han, Z.; Shen, L.; Brennessel, W. W.; Holland, P. L.; Eisenberg, R. *J. Am. Chem. Soc.* **2013**, *135*, 14659.

(51) Karunadasa, H. I.; Chang, C. J.; Long, J. R. *Nature* **2010**, *464*, 1329.

(52) Eckenhoff, W. T.; Brennessel, W. W.; Eisenberg, R. *Inorg. Chem.* **2014**, *53*, 9860.

(53) Gloaguen, F.; Rauchfuss, T. B. *Chem. Soc. Rev.* **2009**, *38*, 100.

(54) Goldsmith, J. I.; Hudson, W. R.; Lowry, M. S.; Anderson, T. H.; Bernhard, S. *J. Am. Chem. Soc.* **2005**, *127*, 7502.

(55) Bachmann, C.; Probst, B.; Guttentag, M.; Alberto, R. *Chem.Commun.* **2014**, *50*, 6737.

(56) Dolphin, D., Wijesekera, T. *Porphyrins, Encyclopedia of Science and Technology*; McGraw-Hill Publishing Company, 1992; Vol. 14.

(57) Hückel, E. *Z. Phys.* **1931**, *70*, 204.

(58) Hückel, E. *Z. Phys.* **1931**, *72*, 310.

(59) Berg, J. M., Tymoczko, J. L., Stryer, L. *Biochemie*; 5th ed. ed.; Spektrum, 2008.

(60) Wang, S.; Tabata, I.; Hisada, K.; Hori, T. *Dyes and Pigments* **2002**, *55*, 27.

(61) Natali, M.; Luisa, A.; Iengo, E.; Scandola, F. *Chem. Commun.* **2014**, *50*, 1842.

(62) Kadish, K. M., Smith, K. M., Guilard, R. *the porphyrin handbook*; Academic Press, 1999; Vol. 1-3.

(63) Wang, S.; Hori, T. *J. Porphyrins Phthalocyanines* **2003**, *07*, 37.

(64) Zhang, L.; Lu, Y.; Du, Y.; Yang, P.; Wang, X. *J. Porphyrins Phthalocyanines* **2010**, *14*, 540.

(65) Kellett, R. M.; Spiro, T. G. *Inorg. Chem.* **1985**, *24*, 2373.

(66) Kellett, R. M.; Spiro, T. G. *Inorg. Chem.* **1985**, *24*, 2378.

(67) Bhugun, I.; Lexa, D.; Savéant, J.-M. *J. Am. Chem. Soc.* **1996**, *118*, 3982.

(68) Ogawa, S.; Uchida, T.; Uchiya, T.; Hirano, T.; Saburi, M.; Uchidac, Y. *J. Chem. Soc., Perkin Trans. 1* **1990**, 1649.

(69) Ogawa, S.; Shiraishi, S. *J. Chem. Soc., Perkin Trans. 1* **1980**, 2527.

(70) Wang, W.-J.; Sengul, A.; Luo, C.-F.; Kao, H.-C.; Cheng, Y.-H. *Tetrahedron Lett.* **2003**, *44*, 7099.

(71) Ogawa, S.; Kishii, N.; Shiraishi, S. *J. Chem. Soc., Perkin Trans. 1* **1984**, 2023.

(72) Pierre, C.; Vincent, J.-M.; Verlhac, J.-B.; Courseille, C.; Dautant, A.; Mathoniere, C. *New J. Chem.* **2001**, *25*, 522.

(73) Ibrahim, R.; Tsuchiya, S.; Ogawa, S. *J. Am. Chem. Soc.* **2000**, *122*, 12174.

(74) Isaacs, M.; Canales, J. C.; Aguirre, M. J.; Estiú, G.; Caruso, F.; Ferraudi, G.; Costamagna, J. *Inorg. Chim. Acta* **2002**, *339*, 224.

(75) Cheng, C.-C.; Kuo, Y.-N.; Chuang, K.-S.; Luo, C.-F.; Wang, W. J. *Angew. Chem. Int. Ed.* **1999**, *38*, 1255.

(76) Bünzli, C. *Investigation of N-Bridged Phenanthroline Macrocycles and their 3d-Transition Metal Complexes as Water Reduction Catalysts, master thesis*, University of Zurich, 2015.

(77) Bai, X.-L.; Liu, X.-D.; Wang, M.; Kang, C.-Q.; Gao, L.-X. *Synthesis* **2005**, *2005*, 458.

(78) Shimada, H.; Sakurai, T.; Kitamura, Y.; Matsuura, H.; Ihara, T. *Dalton T.* **2013**, *42*, 16006.

(79) Manfred Hesse, H. M., Bernd Zeeh *Thieme* **2005**.

(80) Spingler, B.; Schnidrig, S.; Todorova, T.; Wild, F. *CrystEngComm* **2012**, *14*, 751.

(81) Rodriguez-Ubis, J. C.; Sedano, R.; Barroso, G.; Juanes, O.; Brunet, E. *Helv. Chim. Acta* **1997**, *80*, 86.

(82) Nettekoven, M.; Jenny, C. *Org. Process Res. Dev.* **2003**, *7*, 38.

(83) Bachmann, C. *Polypyridine Based Transition Metal Complexes for Homo- and Heterogeneous Photocatalytic Hydrogen Production from Water, dissertation, dissertation*, University of Zurich, 2015.

(84) Amb, C. M.; Rasmussen, S. C. *J. Org. Chem.* **2006**, *71*, 4696.

(85) Uchida, Y.; Echikawa, N.; Oae, S. *Heteroatom Chem.* **1994**, *5*, 409.

(86) Newkome, G. R.; Joo, Y. J.; Fronczek, F. R. *J. Chem. Soc., Chem. Commun.* **1987**, 854.

(87) Ogawa, S.; Narushima, R.; Arai, Y. *J. Am. Chem. Soc.* **1984**, *106*, 5760.

(88) Nierengarten, H.; Rojo, J.; Leize, E.; Lehn, J.-M.; Van Dorsselaer, A. *Eur. J. Inorg. Chem.* **2002**, *2002*, 573.

(89) Guo, H. C.; Zheng, R. H.; Jiang, H. J. *Org. Prep. Proced. Int.* **2012**, *44*, 392.

(90) Wang, W.-J.; Chuang, K.-S.; Luo, C.-F.; Liu, H.-Y. *Tetrahedron Lett.* **2000**, *41*, 8565.

(91) Ogawa, S. *J. Chem. Soc., Perkin Trans. 1* **1977**, 214.

(92) Miwa Hirai , K. S., Hiroaki Sawai , Shojiro Ogawa *Chem. Lett.* **1992**, *21*, 2023.

(93) Newkome, G. R.; Taylor, H. C. R.; Fronczek, F. R.; Delord, T. J. *J. Org. Chem.* **1984**, *49*, 2961.

(94) Li, X.; Gibb, C. L. D.; Kuebel, M. E.; Gibb, B. C. *Tetrahedron* **2001**, *57*, 1175.

(95) Schnidrig, S. *Investigation of New Polypyridine Macrocycle (Pyrphyrin) Based Complexes as Water Reduction Catalyst and/or Photosensitiser, master thesis*, University of Zurich, 2013.

(96) Abraham, R. J.; Eivazi, F.; Pearson, H.; Smith, K. M. *J. Chem. Soc., Chem. Commun.* **1976**, 699.

(97) Batsanov, S. S. *Inorg. Mater.* **2001**, *37*, 871.

(98) Lide, D. R. *Handbook of Chemistry and Physics*; CRC, 2014.

(99) Kotz, J. C., Treichel, P. M., Weaver, G. C. *Chemistry and Chemical Reactivity, Enhanced Review Edition*; 6th edition ed.; Thomson Books/Cole, 2006.

(100) Abrahams, S. C.; Collin, R. L.; Lipscomb, W. N. *Acta Cryst.* **1951**, *4*, 15.

(101) Schmidt, S.; Heinemann, Frank W.; Grohmann, A. *Eur. J. Inorg. Chem.* **2000**, *2000*, 1657.

(102) Kumar, S.; Gupta, R. *Eur. J. Inorg. Chem.* **2014**, *2014*, 5567.

(103) Groom, C. R.; Bruno, I. J.; Lightfoot, M. P.; Ward, S. C. *Acta Cryst.* **2016**, *B72*, 171.

(104) Bruno, I. J.; Cole, J. C.; Edgington, P. R.; Kessler, M.; Macrae, C. F.; McCabe, P.; Pearson, J.; Taylor, R. *Acta Cryst.* **2002**, *B58*, 389.

(105) Macrae, C. F.; Bruno, I. J.; Chisholm, J. A.; Edgington, P. R.; McCabe, P.; Pidcock, E.; Rodriguez-Monge, L.; Taylor, R.; van de Streek, J.; Wood, P. A. *J. Appl. Crystallogr.* **2008**, *41*, 466.

(106) Zhenxia, Z.; Keiko, T.; Ayako, F.; Shojiro, O.; Shinji, T. *Bull. Chem. Soc. Jpn.* **2007**, *80*, 686.

(107) Xie, Y.; Hamann, T. W. *J. Phys. Chem. Lett.* **2013**, *4*, 328.

(108) Matsumoto, J.; Suzuki, T.; Kajita, Y.; Masuda, H. *Dalton T.* **2012**, *41*, 4107.

(109) Das, U. K.; Bobak, J.; Fowler, C.; Hann, S. E.; Petten, C. F.; Dawe, L. N.; Decken, A.; Kerton, F. M.; Kozak, C. M. *Dalton T.* **2010**, *39*, 5462.

(110) Linke, K. H.; Dürholz, F.; Hädicke, P. *Z. Anorg. Allg. Chem.* **1968**, *356*, 113.

(111) Schrauzer, G. N.; Lee, L.-P. *J. Am. Chem. Soc.* **1968**, *90*, 6541.

(112) Collman, J. P.; Brauman, J. I.; Doxsee, K. M.; Halbert, T. R.; Hayes, S. E.; Suslick, K. S. *J. Am. Chem. Soc.* **1978**, *100*, 2761.

(113) Ebsworth, E. A. V., Rankin, D. W. H., Cradock, S. *Structural Methods in Inorganic Chemistry*; 2nd edition ed.; Blackwell Scientific Publications, 1991.

(114) Fulmer, G. R.; Miller, A. J. M.; Sherden, N. H.; Gottlieb, H. E.; Nudelman, A.; Stoltz, B. M.; Bercaw, J. E.; Goldberg, K. I. *Organometallics* **2010**, *29*, 2176.

(115) Singh, W. M.; Mirmohades, M.; Jane, R. T.; White, T. A.; Hammarstrom, L.; Thapper, A.; Lomoth, R.; Ott, S. *Chem. Commun.* **2013**, *49*, 8638.

(116) Olmstead, W. N.; Margolin, Z.; Bordwell, F. G. *J. Org. Chem.* **1980**, *45*, 3295.

(117) Bordwell, F. G.; McCallum, R. J.; Olmstead, W. N. *J. Org. Chem.* **1984**, *49*, 1424.

(118) Bordwell, F. G.; Drucker, G. E.; Fried, H. E. *J. Org. Chem.* **1981**, *46*, 632.

(119) Radha R. Gupta, M. K., V. Gupta *Heterocyclic Chemistry: Volume II: Five-Membered Heterocycles*; 1th Ed. ed., 1999.

(120) R. Crampton, M.; A. Robotham, I. *J. Chem. Res., Synop.* **1997**, 22.

(121) Zanello, P. **2003**.

(122) Park, J. B. *Biochim. Biophys. Acta Gen. Sub.* **2001**, *1525*, 173.

(123) Wechtersbach, L.; Cigić, B. *J. Biochem. Biophys. Methods* **2007**, *70*, 767.

(124) Lykkesfeldt, J. *Anal. Biochem.* **2000**, *282*, 89.

(125) Krężel, A.; Latajka, R.; Bujacz, G. D.; Bal, W. *Inorg. Chem.* **2003**, *42*, 1994.

(126) Rountree, E. S.; McCarthy, B. D.; Eisenhart, T. T.; Dempsey, J. L. *Inorg. Chem.* **2014**, *53*, 9983.

(127) Costentin, C.; Drouet, S.; Robert, M.; Savéant, J.-M. *J. Am. Chem. Soc.* **2012**, *134*, 11235.
(128) Artero, V.; Saveant, J.-M. *Energy Environ. Sci.* **2014**, *7*, 3808.
(129) Costentin, C.; Savéant, J.-M. *ChemElectroChem* **2014**, *1*, 1226.
(130) Dempsey, J. L.; Brunschwig, B. S.; Winkler, J. R.; Gray, H. B. *Acc. Chem. Res.* **2009**, *42*, 1995.
(131) McCrory, C. C. L.; Uyeda, C.; Peters, J. C. *J. Am. Chem. Soc.* **2012**, *134*, 3164.
(132) Bachmann, C.; Probst, B.; Fox, T.; Alberto, R. *Chem. Sci.* **2016**, *7*, 436.
(133) Khnayzer, R. S.; Thoi, V. S.; Nippe, M.; King, A. E.; Jurss, J. W.; El Roz, K. A.; Long, J. R.; Chang, C. J.; Castellano, F. N. *Energy Environ. Sci.* **2014**, *7*, 1477.
(134) Krishnan, C. V.; Creutz, C.; Mahajan, D.; Schwarz, H. A.; Sutin, N. *Isr. J. Chem.* **1982**, *22*, 98.
(135) Costentin, C.; Drouet, S.; Robert, M.; Saveant, J. M. *J. Am. Chem. Soc.* **2012**, *134*, 11235.
(136) McKone, J. R.; Marinescu, S. C.; Brunschwig, B. S.; Winkler, J. R.; Gray, H. B. *Chem. Sci.* **2014**, *5*.
(137) Pourbaix, M. *Atlas of Electrochemical Equilibria in Aqueous Solutions,* 2nd ed.; National Association of Corrosion Engineers: Houston, Texas, 1974.
(138) Kirch, M.; Lehn, J. M.; Sauvage, J. P. *Helv. Chim. Acta* **1979**, *62*, 1345.
(139) Costentin, C.; Dridi, H.; Savéant, J.-M. *J. Am. Chem. Soc.* **2014**, *136*, 13727.
(140) Nippe, M.; Khnayzer, R. S.; Panetier, J. A.; Zee, D. Z.; Olaiya, B. S.; Head-Gordon, M.; Chang, C. J.; Castellano, F. N.; Long, J. R. *Chem. Sci.* **2013**, *4*, 3934.
(141) Krishnan, C. V.; Brunschwig, B. S.; Creutz, C.; Sutin, N. *J. Am. Chem. Soc.* **1985**, *107*, 2005.
(142) Knight, J. C.; Alvarez, S.; Amoroso, A. J.; Edwards, P. G.; Singh, N. *Dalton T.* **2010**, *39*, 3870.
(143) Connelly, N. G.; Geiger, W. E. *Chem. Rev.* **1996**, *96*, 877.
(144) Dutton, P. L. In *Methods Enzymol.*; Academic Press, Inc.: 1978; Vol. 54.
(145) Kaeffer, N.; Morozan, A.; Fize, J.; Martinez, E.; Guetaz, L.; Artero, V. *ACS Catalysis* **2016**, *6*, 3727.
(146) system, C. S.; 171.32 ed.; Oxford Diffraction Ltd.: Oxford, UK, 2007.
(147) Altomare, A.; Burla, M. C.; Camalli, M.; Cascarano, G. L.; Giacovazzo, C.; Guagliardi, A.; Moliterni, A. G. G.; Polidori, G.; Spagna, R. *J. Appl. Crystallogr.* **1999**, *32*, 115.
(148) Sheldrick, G. *Acta Cryst.* **2008**, *A64*, 112.
(149) Farrugia, L. *J. Appl. Crystallogr.* **2012**, *45*, 849.

7. Curriculum Vitae

Personal Information

First Name: Stephan Thomas
Last Name: Schnidrig
Date/Place of Birth: 07.04.1984, Zürich, ZH
Place of Origin Grächen, VS
Adress: Arbentalstrasse 323
8045 Zurich
Phone number: +41 79 423 60 55
E-Mail Adress: schniste@gmail.com

Education and Work Experience

04.2013 – 06.2017	**PhD Thesis** Group of Prof. Dr. Roger Alberto, Department of Chemistry, University of Zurich, Switzerland
05.2013	**Master Graduation** Group of Prof. Dr. Roger Alberto, Department of Chemistry, University of Zurich, Switzerland, Title: “Investigation of New Polypyridine Macrocycle (Pyrphyrin) Based Complexes as Water Reduction Catalyst and/or Photo Sensitiser”
09.2010 – 05.2013	**Master Studies** Master of Science UZH in Chemistry, University of Zurich, Switzerland
04.2009-01.2010	**Scientific employee** Group of PD Dr. Bernhard Spingler, Department of Chemistry, University of Zurich, Zürich, Suzuki Cross Coupling of Biaryls and Porphyrin Synthesis
09.2008	**Bachelor thesis in organic chemistry** Givaudan, Dübendorf, Group of Prof. Dr. Roger Marti, ZHAW Winterthur Hydrogenation of Small Molecules in a Flow-Through System
09.2004 – 09.2008	**Bachelor studies in chemistry** University of Applied Science, Zürcher Hochschule für Angewandte Wissenschaften (ZHAW), Winterthur
07.2001-07.2004	**Apprenticeship as chemistry laboratory assistent** Organic Chemistry, ETH Zürich, Zürich, Enantioselective Synthesis of Chiral Nitrones
07.2001-07.2004	**Professional certification in chemistry (BMS)** Gewerblich-Industrielle Berufsschule Winterthur (BMS), Winterthur
2000-2001	**School in England** English Education, Harrow House College, Swanage UK
1991-2000	**Basic education** Sekundarschule (Döltschi, ZH), Primarschule (Friesenberg, ZH)

Publications

- On-surface metalation and 2D self- assembly of pyrphrin molecules into metal- coordinated networks on Cu(111), Li, J., Waeckerlin, C., Schnidrig, S., Joliat, E., Alberto, R., Ernst, K.-H., *Helv. Chim. Acta*, **2017**, 100, e1600278.

- Cobalt complexes of tetradentate, bipyridine- based macrocycles: their structures, properties and photocatalytic proton reduction; Schnidrig, S., Joliat, E., Probst, B.; Bachmann, C.; Spingler, B.; Baldridge, K. K.; von Rohr, F.; Schilling, A.; Alberto, R., *Dalton Trans.*, **2016**, 45, 1737-1745.

- From porphyrins to pyrphyrins: adsorption study and metalation of a molecular catalyst on Au(111), Mette, G., Sutter, D., Gurdal, Y., Schnidrig, S., Probst, B., Iannuzzi, M., Hutter, J., Alberto, R., Osterwalder, J., *Nanoscale*, **2016**, 8, 7958-7968.

- Some thoughts about the single crystal growth of small molecules; Spingler, B., Schnidrig, S., Todorova, T. and Wild, F., *CrystEngComm*, **2012**, 14, 751-757.

Languages

German: first language
English: good
French: basics
Japanese: beginner

2001-2002 **CAE, FCE and PET English certificates**

Software

Chem Draw, ISIS Draw, Origin, Sci Finder,
MS-Word, MS-Excel, MS-Powerpoint,
Adobe Lightroom, Adobe Photoshop, Adobe Premier Pro

Instrument Usage

HPLC, UPLC-MS, NMR, IR, UV/Vis, TLC, GC, Column Chromatography
Electrochemistry and Spectroelectrochemistry

Interests

Photography; Reading; Japanese; Computer; Video Cutting; Diving